Technische Universität München
Fakultät für Elektrotechnik und Informationstechnik
Lehrstuhl für Elektrische Antriebssysteme und Leistungselektronik

Predictive Control and Finite-Set Observers for Variable-Speed Wind Generators

Mohamed Abdelsater Swify Abdelrahem

Vollständiger Abdruck der von der Fakultät für Elektrotechnik und Informationstechnik der Technischen Universität München zur Erlangung des akademischen Grades eines

Doktor-Ingenieurs

genehmigten Dissertation.

Vorsitzender: Prof. Dr. Thomas Hamacher
Prüfer der Dissertation:
1. Prof. Dr.-Ing. Dr. h. c. Ralph Kennel
2. Prof. José Rodríguez, Ph.D.
Universidad Andrés Bello, Santiago, Chile.

Die Dissertation wurde am 02.10.2019 bei der Technischen Universität München eingereicht und durch die Fakultät für Elektrotechnik und Informationstechnik am 10.02.2020 angenommen.

To my wife Rofida and my sons:
Ibrahim & Hamza

Mohamed

Acknowledgment

This dissertation at hand is based on my research carried out at the Institute for Electrical Drive Systems and Power Electronics (EAL), Technische Universität München (TUM), supervised by Prof. Dr.-Ing. Ralph Kennel. I would like to express my deepest gratitude to Prof. Dr.-Ing. Ralph Kennel for his constant guidance, helpful comments, advice, continued efforts, and support during this work. Prof. kennel has been giving me the freedom to think and implement my ideas without restrictions. His guidance helped throughout the whole period of this work. I could not have imagined having a wonderful, flexible, and open-minded supervisor for my PhD work like him. In addition, Prof. Kennel gave me the chance to present the results of my research at many different international conferences. Furthermore, the international atmosphere of the institute that he is heading gives me the chance to learn from different cultures, and consequently, have friends/colleagues from various countries around the world. All of these made me feel lucky to have worked at this prestigious institute.

I would like to express my heartfelt gratitude to Prof. Dr.-Ing. José Rodríguez for being the second examiner of this thesis. He is one of the most respectable specialists in the filed of power electronics and electrical drives. Furthermore, he is the inventor of the finite-control-set model predictive control (FCS-MPC) technique. It was an honor for me to organize a workshop in predictive control with Prof. Rodríguez and hosted him for two days in our institute from 18 to 19 September 2017. With the guidance of Prof. Rodríguez , we have already published several papers in IEEE journals and conferences; some more are still under preparation. It is my great honor to have Prof. Rodríguez as my co-supervisor. I wish we may have more cooperation in my future career and life.

My sincere thanks go to my mentor Prof. Dr.-Ing. Christoph Hackl, Munich University of Applied Sciences, and head of Control of renewable energy systems (CRES) group, TUM. His help and guidance particularly on how to transfer ideas and results precisely into readable (high quality) publications will benefit me forever. Furthermore, the cooperation with him and CRES group in the construction of the test benches that used for validating this work is highly appreciated. Throughout our collaboration, we have already published several papers in IEEE journals and conferences; some more are still under preparation. Without his precious support it would not be possible to conduct this research in its current form.

I am also greatly indebted to my colleagues: Dr.-Ing. Peter Stolze, Dr.-Ing. Peter Landsmann, Prof. Petros Karamanakos, Prof. Fengxiang Wang, Prof. Zhenbin Zhang, Prof. Felix Rojas, Dr.-Ing Esteban Fuentes, Dr.-Ing Ayman Ayad, Dr.-Ing Reza Fotouhi, Dr.-Ing Daniel Glose,

Dr. Ing Zhe Chen, Dr.-Ing Guangye Si, Dr.-Ing Xinbo Cai, Julien Cordier, Florian Bauer, Ali Hafni, Xiaonan Gao, Wei Tian, Hannes Börngen, Alexander Florian, Eyke Liegmann, Stefan Klaß, Sebastian Wendel, Simon Wiedemann, Issa Hammoud, Ahmed Soliman, Billel Kahia, Mostafa Ahmed, Ahmed Farhan, Yahia Asiri, Mohammed Azharuddin Shamshuddin, Haotian Xie, Dr. Mohamed Ali Ismeil, et al. I appreciate the cooperation with CRES group: Korbinian Schechner, Christian Dirscherl, Hisham Eldeeb, Julian Kullick, et al. Master students that I have supervised (Philipp Catterfeld, Prodyut Das, et al.), have also helped me.
I would like to thank administrative and technical staff members of the chair who have been kind enough to advise and help in their respective roles. I thank Mr. Wolfgang Ebert, Mr. Dietmar Schuster, Mr. Günter Kopetschny, Mrs. Julia Menz, and Mrs. Heidi Jonas for their help and cooperation.
I am grateful to the Egyptian Ministry of Higher Education and Scientific Research (MHESR) and the German Academic Exchange Service (DAAD) for funding my PhD project from 01.04.2014 to 30.09.2017 by awarding a highly prestigious scholarship within the program "German-Egyptian Research Long Term Scholarship (GERLS)".
My deepest gratitude goes to my parents for forgetting themselves and dedicating their life for us. My father, you are the greatest man I have ever known taking care of all the annoying details in our life. My Mother, your blessing and prayer for me is what keeps me going. I am also grateful to my lovely brothers and sisters for their support and kindness.
Finally, but most importantly, I would like to dedicate this dissertation to my wife *Rofida* for her love, patience, sacrifices, and understanding. I would like to deeply thank her for listening, helpful discussions, and encouraging me to finish this work on time. Thank you for giving me two handsome boys, *Ibrahim* and *Hamza*. They are really the light of my life.

Mohamed Abdelrahem
Munich, Germany
July 2019

Abstract

This dissertation presents several predictive control techniques and finite set observers for permanent-magnet synchronous generators (PMSGs) and doubly-fed induction generators (DFIGs) in variable-speed wind turbine systems (WTSs). Firstly, comprehensive mathematical models of wind energy conversion systems (WECSs) with PMSG and DFIG are presented. Then, the standard vector control (VC), deadbeat predictive control (DBPC), and finite-control-set model predictive control (FCS-MPC) techniques for PMSGs/DFIGs are implemented and compared. In these control techniques, the measurement of the rotor speed and position is essential. Therefore, in order to overcome the problems associated with encoders/speed transducers, novel finite-position-set (FPS) observers, which are based on the concept of FCS-MPC, are proposed for encoderless vector control of PMSGs/DFIGs. Furthermore, enhanced versions of these FPS observers to reduce the calculation burden and improve the accuracy are presented. Another solution is using the extended Kalman filter (EKF) to estimate the rotor speed and position. Moreover, the same EKF and a disturbance observer are employed to compensate the one sample delay caused by the digital controller and enhance the robustness of the DBPC against parameters variations of PMSGs/DFIGs. Subsequently, a deadbeat function and a discrete-time integral action are utilized to reduce the calculation burden of the traditional FCS-MPC and compensate against disturbances and uncertainties of the system. An efficient predictive direct torque control (PDTC) without weighting factors, i.e. no tuning effort is required, is then proposed for PMSGs/DFIGs. In order to enhance the dynamics of the speed control and eliminate the cascaded structure of the control loops, a simple predictive speed control (PSC) based on the FCS-MPC is presented for PMSGs/DFIGs. In addition to that, a multiple-vector (MV)-FCS-MPC is proposed to reduce the ripples in the output current of grid-connected voltage source converters (VSCs). Furthermore, a novel finite-inductance set observer is presented to enhance the robustness of the proposed MV-FCS-MPC. Finally, a low-voltage ride through (LVRT) technique is introduced for PMSGs/DFIGs to realize the modern grid code requirements. The performances of the proposed control techniques and observers aforementioned have been validated and compared with the traditional ones by experimental/simulation data. The results illustrate the superiority of the proposed control schemes and observers in comparison with the classical ones.

Zusammenfassung

Die vorliegende Dissertation stellt mehrere unterschiedliche Versionen der modellprädiktiven Regelung (MPC) und der so genannten Finite-Position-Set-Beobachter (FPSOs) sowohl für Synchrongeneratoren mit Permanentmagneterregung (PMSGs) als auch für doppelt gespeiste Asynchrongeneratoren (DFIGs) in Windkraftanlagen mit variabler Drehzahl (WTSs) vor und untersucht diese. Zunächst werden umfassende mathematische Modelle der Windenergie-Anlagen (WECSs) mit PMSGs und DFIGs entworfen. Anschließend werden die Standard-Vektorregelung (VC), die Deadbeat Prädiktiv-Regelung (DBPC) und die Finite-Control-Set Modell-Prädiktiv-Regelung (FCS-MPC) für PMSGs/DFIGs implementiert und miteinander verglichen. Bei diesen Regelungsverfahren spielt die Messung der Rotordrehzahl und Position eine wesentliche Rolle. Um Probleme in Zusammenhang mit Drehgebern/Geschwindigkeitswandlern zu vermeiden, werden neuartige Finite-Position-Set (FPS) Beobachter, die auf dem Konzept der FCS-MPC beruhen, für die geberlose Regelung der PMSGs/DFIGs verwendet. Zudem werden erweiterte Versionen dieses FPS-Beobachter beschrieben, die den Rechenaufwand verringern und die Genauigkeit erhöhen. Die Verwendung eines Erweiterten Kalman-Filters (EKF) zur Schätzung der Rotordrehzahl und –Position stellt eine weitere Möglichkeit dar Schwierigkeiten bei der Messung jener Gräßen zu verhindern. Darüber hinaus kann dieser EKF in Kombination mit einem Störungsbeobachter genutzt werden, um die vom digitalen Regler verursachte Verzögerung von einer Abtastperiode zu kompensieren und damit die Robustheit der DBPC gegenüber Parametervariationen von PMSGs/DFIGs zu erhöhen. Im Anschluss daran werden Deadbeat-Funktion und diskrete Zeitintegralaktion angewendet, um die Rechenzeit der herkömmlichen FCS-MPC zu reduzieren und Störungen sowie Unzuverlässigkeiten des Systems auszugleichen. Daraufhin wird für PMSGs und DFIGs eine effiziente Modellprädiktive Direkte Drehmomentregelung (PDTC) ohne Gewichtungsfaktoren präsentiert, die keine Abstimmung erfordert. Zur Verbesserung der Dynamik der Drehzahlregelung und zur Vermeidung der Kaskadierung der Regelkreise, wird eine einfache Modellprädiktive Drehzahlregelung (PSC) basierend auf der FCS-MPC eingeführt. Darüber hinaus wird ein Multi-Vektor (MV)-FCS-MPC zur Reduzierung der Welligkeiten im Ausgangsstrom von netzgekoppelten Spannungsquellenwandlern (VSCs) vorgeschlagen. Für eine verbesserte Robustheit dieser MV-FCS-MPC wird zusätzlich ein neuer Finite-Inductance-Set-Beobachter vorgestellt. Schließlich wird eine Low-Voltage Ride Through (LVRT) Technik für PMSGs und DFIGs eingeführt, um die modernen Netzanforderungen zu erfüllen. Die Leistungsfähigkeit der vorgestellten Regelungsverfahren und Beobachter wurden simulativ und experimentell validiert und mit

traditionellen Konzepten verglichen. Die Ergebnisse veranschaulichen die Überlegenheit der präsentierten Regelungsschemata und Beobachter im Vergleich zu den klassischen.

Table of Contents

CHAPTER 1

Introduction

This work focuses on control of permanent-magnet synchronous generators (PMSGs) and doubly-fed induction generators (DFIGs) in variable-speed wind turbine systems. In this chapter, the background, motivations, and contributions of this dissertation are presented.

1.1 Overview of installed wind power

Paris Agreement is aiming to keep the increase in global average temperature to be below $2°C$ above pre-industrial levels and pursuing efforts to limit it to $1.5\,°C$, which will significantly reduce the risks and impacts of climate change [1]. One of the main reasons of the global warming is the high emission of green house gases, in particularly, carbon dioxide CO_2. Generation of the electricity by burning of fossil fuels is still the most used method worldwide. However, this method of electricity generation causes a high amount of CO_2 emission, i.e. increase the global warming. Furthermore, the fossil fuels will vanish in the near future. Accordingly, electricity generation from renewable energy sources (RESs), which are environmentally friendly sources, has remarkably increased in the last few years. By 2017, the power generation from RESs reached $2195\,\mathrm{GW}$ worldwide, which represents approximately 26.5% of global energy consumption [2]. Furthermore, most of the countries around the world are planning to increase the share of RESs in their power grid.

Wind and solar energy are considered two promising power generation sources. The power generation from wind energy has been significantly increased in the last few years [3]. The cumulative installed wind power capacity from 2001 to 2017 is illustrated in Fig. 1.1, where the total installed capacity reached $539\,\mathrm{GW}$ in 2017, with $52.5\,\mathrm{GW}$ added in 2017. By 2020, it is expected that the total installed wind power generation will reach approximately $712\,\mathrm{GW}$, which makes this form of renewable energy a significant source of power generation. Thanks for the continuous development in this technology and the remarkably drop in the price per kW, which makes the wind power plant a strong competitor to the traditional power plants.

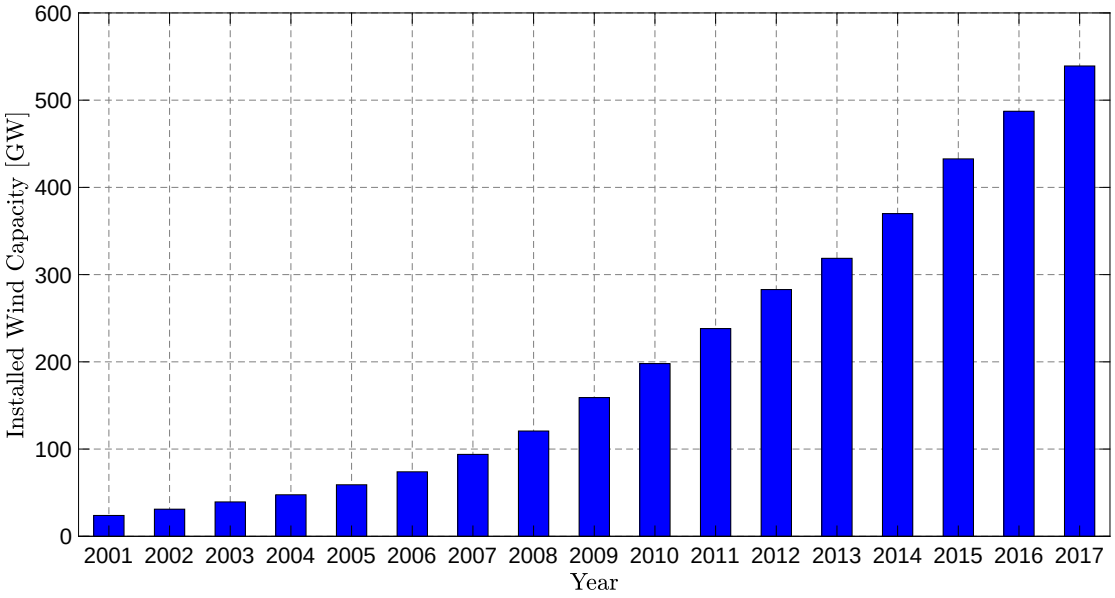

Figure 1.1: Global accumulative installed wind energy worldwide [3].

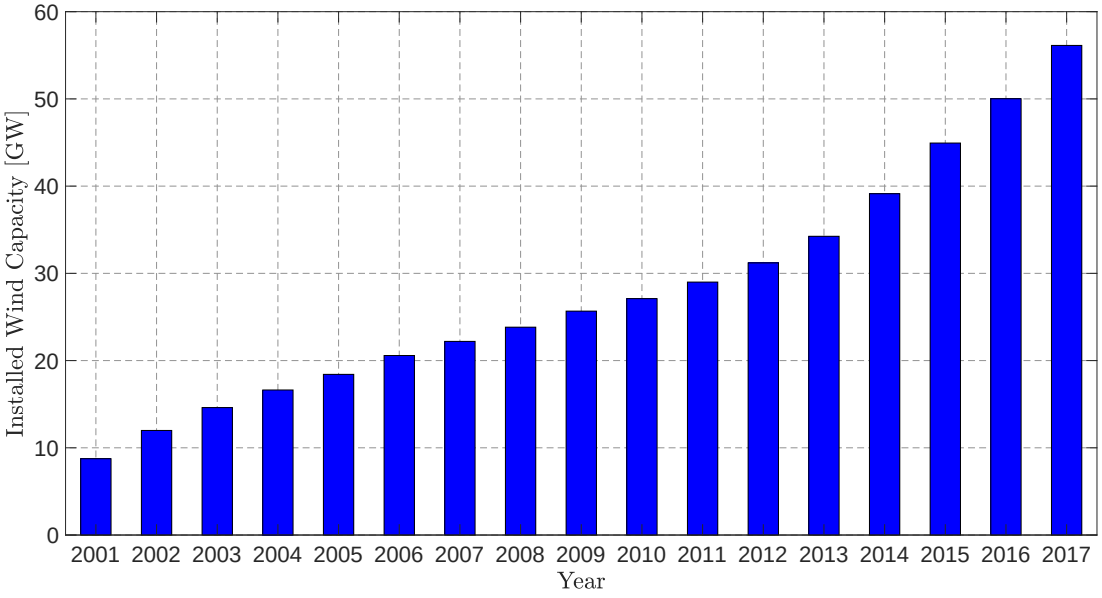

Figure 1.2: Accumulative installed wind energy in Germany [3].

In European Union (EU), $15.6\,\mathrm{GW}$ of new wind power capacity was installed in 2017. Germany led all markets in 2017 with $6.58\,\mathrm{GW}$ (a 15% higher than 2016) installed wind turbines. Fig. 1.2 illustrates the accumulative installed wind power in Germany from 2001 to 2017, which remarkably increased. In 2017, the wind power share in the total electricity consumption in Germany is 16.1%. In Egypt, the total installed wind power has been increased from $0.14\,\mathrm{GW}$ in 2004 to approximately $1\,\mathrm{GW}$ in 2017, which represents approximately 1.75% share in the total

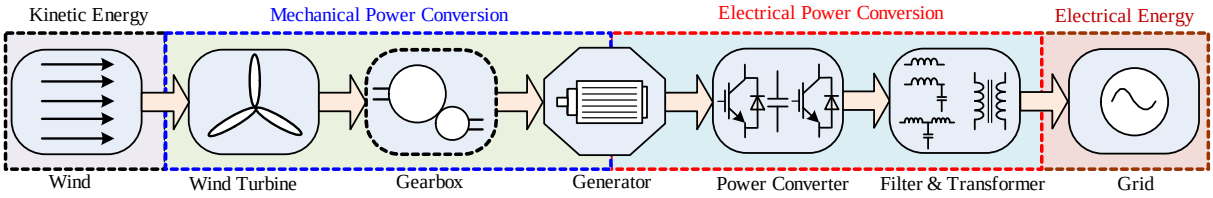

Figure 1.3: Basic components of grid-connected wind energy conversion systems (gearbox is eliminated in direct-drive topologies).

electricity consumption in Egypt [4]. Both countries (i.e. Germany and Egypt) are planning to increase the share of renewable energy in the future to fulfill Paris agreement goal.

The major parts of a grid-tied wind energy conversion system (WECS) are illustrated in Fig. 1.3. The WECS is consisted of different basic components, which can be classified to three categorizes [5]–[9]: Mechanical, electrical, and control part. The mechanical part includes tower, nacelle, rotor blades and hub, gearbox, pitch drives, yaw drives, wind speed and direction sensors, drive-train, and mechanical brakes. The electrical part includes generator, power converter, filter, step-up transformer, and grid. The control part contains the control of the pitch angle, yaw control, and power converter control. In the following sections, those components will be described in details.

1.2 Mechanical components of grid-connected WECSs

The wind kinetic-energy is converted to mechanical-energy with the help of the rotor blades. The efficiency of converting the kinetic energy to mechanical one is depending on several factors like the shape of rotor blades, angle of blades, speed of the wind, air density, etc. [5]–[9]. The speed and direction of the wind are measured with the help of mechanical sensors (anemometer and wind vane). The yaw drive is employed to move the rotor blades along with nacelle towards the wind to generate the maximum available power. The pitch angle of the rotor blades is kept at zero when the wind speed is below the rated value. If the wind speed is higher than the rated value, the pitch angle is increased to limit the output power of the wind turbine. Normally, the wind turbines, in particularly the big ones, rotate at very low speed. Therefore, multistage gearbox is employed to increase the rotation speed of the rotor. However, the gearbox has the following drawbacks: High initial cost, noise, reduced life span, reduces efficiency and reliability of the system, and need of regular maintenance. Accordingly, the direct-drive or gearless wind turbines overcome these problems. The mechanical brakes are installed directly on the generator drive-train (high-speed shaft) to stop the wind turbine during fault conditions or high wind gusts.

1.3 Electrical components of grid-connected WECSs

1.3.1 Generator

An electrical generator is employed to convert the mechanical-energy into electrical energy. Various types of generators such as squirrel-cage induction generator (SCIG), wound rotor in-

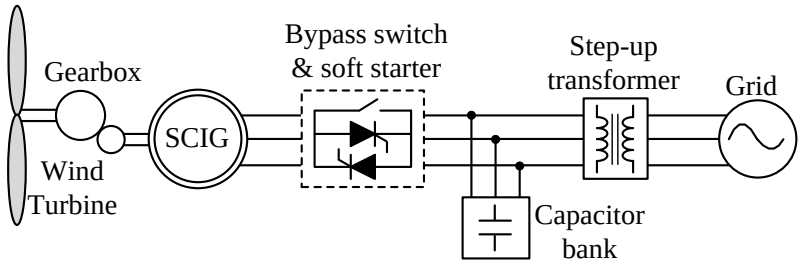

(a) Fixed-speed WECS

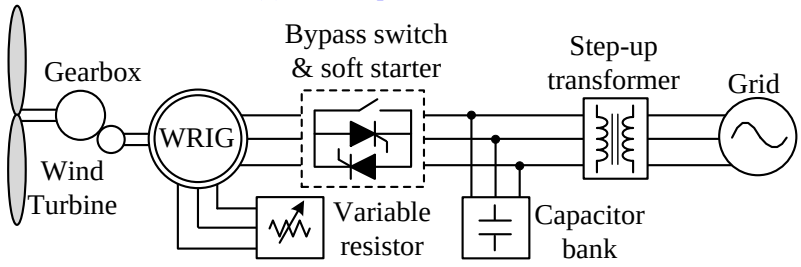

(b) Semi-variable speed (±10%) WECS

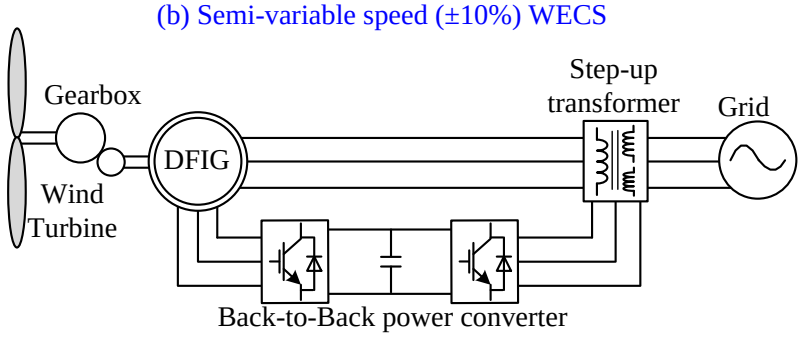

(c) Variable speed (±30%) WECS

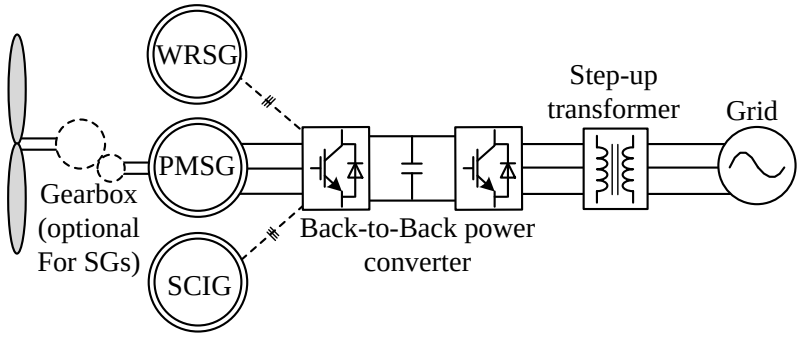

(d) Full-variable speed (0 to 100%) WECS

Figure 1.4: Different types of generators for grid-connected wind energy conversion systems.

duction generator (WRIG), doubly-fed induction generator (DFIG), permanent magnet synchronous generator (PMSG) and wound rotor synchronous generator (WRSG) have been used over the past years for wind turbine applications [5]–[9]. The first generation of grid-connected wind turbines was based on SCIG, which rotates at a high and fixed speed. Accordingly, this generation named "Fixed-speed wind turbines". Fixed-speed WECSs without power electronics converter are connected to the grid through a soft starter and step-up transformer, see Fig. 1.4(a). However, a multi-stage gearbox is essential to step-up the wind turbine speed to be suitable for

the SCIG. After the start-up procedure, the soft-starter is bypassed by a switch, and the system basically operates without any power converters. The SCIG draws reactive power from the grid, and accordingly, a capacitor bank is normally utilized to supply this reactive power. Fixed-speed WECSs have the advantages of simplicity and low initial cost. However, they have the following drawbacks: (1) Low wind energy conversion efficiency, (2) variations of the wind speed are directly reflected to the grid, (3) necessity for a multi-stage gearbox, and (4) very sensitive to grid faults. Due to these disadvantages, the fixed-speed WECSs are becoming seldom in the current wind turbines market. However, the fixed-speed wind turbines that already installed are still in operation.

In order to increase the wind energy conversion efficiency, the semi-variable speed WECSs using WRIG and variable resistor are utilized, see Fig. 1.4(b). The change in the rotor resistance affects the torque/speed characteristic of the WRIG, which enables variable-speed operation of the wind turbine. The variation range of the speed is typically limited to $\pm 10\%$ around the rated speed. Hence, the system can capture more power from the wind. However, the rotor resistance causes power losses. Furthermore, this configuration requires a gearbox, soft starter, and reactive power compensation. Therefore, semi-variable speed WECSs with WRIG are also becoming seldom in the current wind turbines market.

In order to overcome the power losses in the rotor resistance, the DFIG with partial-scale back-to-back (BTB) power converter is introduced in the wind turbines market, see Fig. 1.4(c). The power rating of the BTB power converter is approximately 30% of the generator power, which makes this concept attractive from a cost point of view. Furthermore, WECSs with DFIGs feature enhanced overall power conversion efficiency by performing maximum power point tracking (MPPT) algorithm and satisfactory speed variation range ($\pm 30\%$ speed change around the synchronous speed). Accordingly, the WECSs based on DFIG become one of the dominating technologies in today's wind industry with a market share of approximately 50% [5]–[9]. However, the fault-ride through (FRT) capability of DFIGs is limited due to the partial scale BTB power converter. Furthermore, a gearbox is essential in this configuration, which increases the cost, weight, and requires regular maintenance.

The wind energy conversion efficiency can be significantly improved by using of full-variable speed WECSs, see Fig. 1.4(d). Full-variables speed WECSs allow a speed variations range form 0 to 100%, which enables the application of MPPT algorithm for the whole wind speed operation range. Furthermore, due to the use of full-scale power converter, the generator is fully decoupled from the grid, and accordingly is robust to faults and disturbances in the grid. The power converter also enables the injection of reactive power to the grid in case of faults/voltage dips, which achieves the recent grid code requirements [9]. The gearbox can be eliminated by using a high-pole number PMSG/WRSG, which called direct-drive WECSs. Although, WRSGs can be used in this configuration, PMSGs are more suitable due to the elimination of slip rings and brushes, which simplify the design and eliminate the need for regular maintenance. Furthermore, PMSGs do not required reactive power like SCIG. Multi-pole PMSGs with full-scale BTB power converter sound to be the form to be adopted by most of the wind-turbine manufactures in the coming years, progressively replacing the DFIG as the main generator in the wind turbines market. Moreover, direct-drive WECSs reduces the noise level due to the elimination of the gearbox.

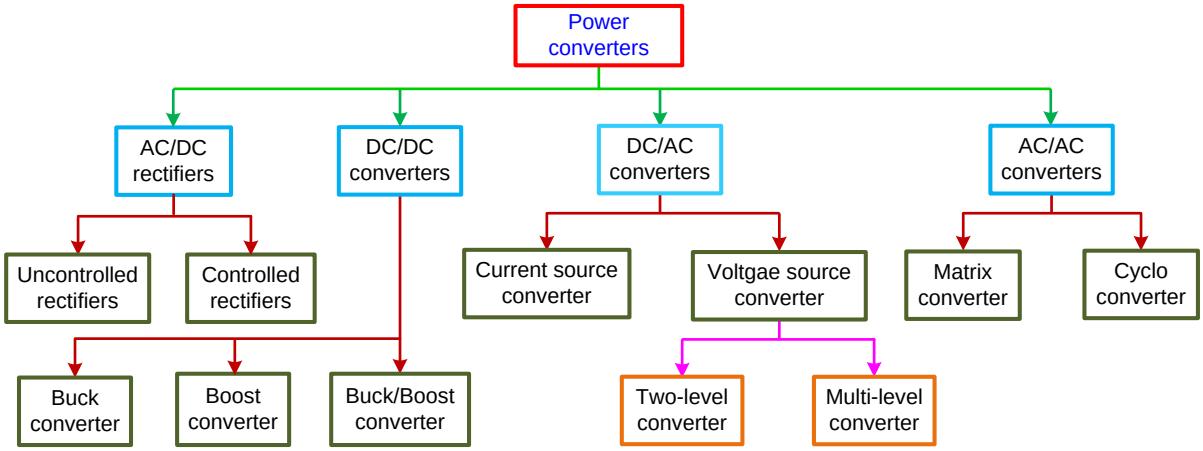

Figure 1.5: Different types of power electronics converters for WECSs.

1.3.2 Power electronics converter

Power electronics has changed speedily in the last few years and the number of applications has been significantly increasing, generally due to the developments of the semiconductor devices and the microprocessor technology. Thus, the performance of power electronics devices are steadily increasing, and at the same time, the price is continuously decreasing. According to Fig. 1.4, WECSs can be directly connected to the grid or they can be interfaced through power electronics converters [9]–[13]. The different types of power electronics rectifiers/converters that used in WECSs is illustrated in Fig. 1.5.

In fixed-speed speed WECSs, the power electronics is just a soft starter employed to initially tie the SCIG with the grid, where simple thyristors are used. A diode bridge with chopper are used to control the rotor resistance in semi-variable speed WECSs with WRIG. In variable-speed WECSs, a back-to-back (BTB) power converter is essential to enable the variable-speed operation and interface the system with the grid. By using a BTB power converter, it is possible to fully control the extracted power from the wind turbines and provide auxiliary services to the grid during normal and abnormal conditions. Power electronics progressively become more and more advanced and bring in considerable response enhancement for WECSs. They reduce the mechanical stress, increase the energy capture from the wind, and enable the whole WECS to behave like a completely controllable electricity generation unit. Hence, it is easy to integrate the wind power into the grid.

Normally, the most commonly used power converter in wind turbine applications is the two-level voltage source converter (2L-VSC) [9]–[13], which is a mature power converter topology in the market. The two level BTB power converter consists of two VSC that tied through a DC-link as shown in Fig. 1.6. The VSC is realized by Insulated Gate Bipolar Transistors (IGBTs) arranged in a matrix form. The DC-link is normally achieved using parallel/series string of capacitors to realize the required capacitance level and voltage. A technical feature of the two-level BTB converter is the full controllability (four quadrant operation) with a reasonably simple structure and few number of power electronics devices. However, the power rating of the modern wind turbines is really high (i.e. $6\,\mathrm{MW}$ or higher). Therefore, a single two-level BTB power converter topology at this power level (partial or full scale) will suffer from high

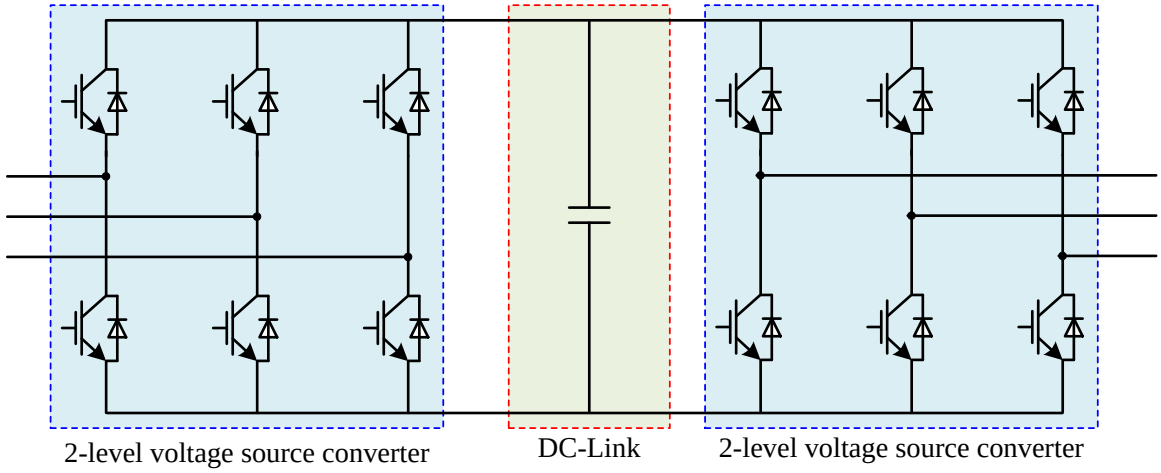

Figure 1.6: Two-level back-to-back power converter for wind turbine applications.

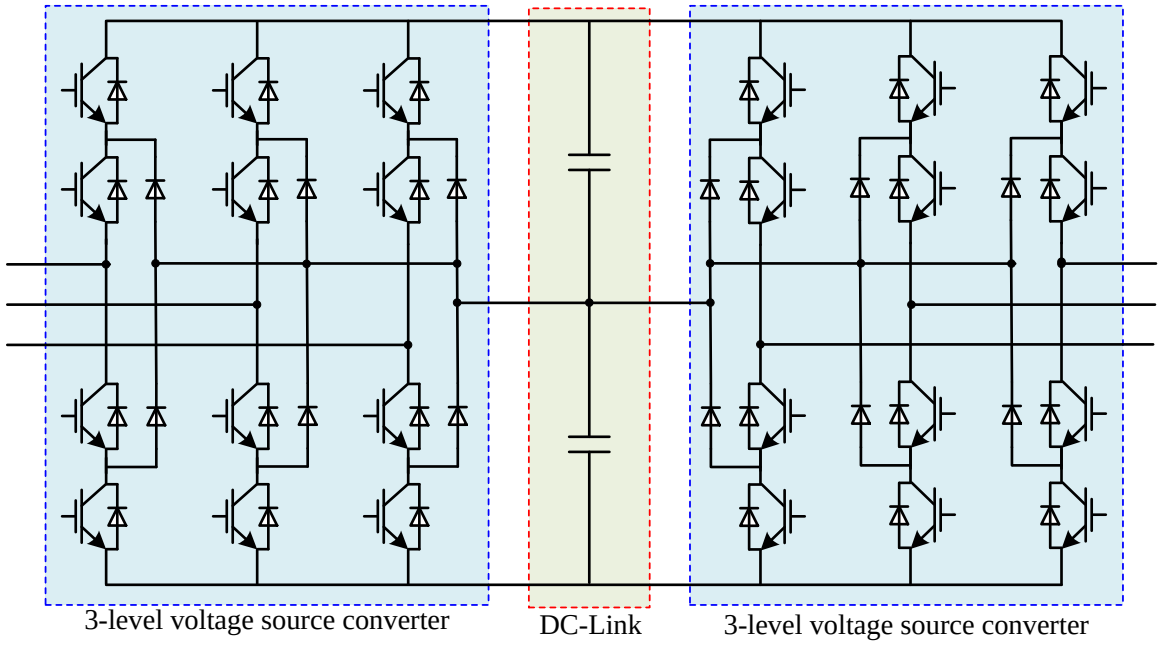

Figure 1.7: Three-level back-to-back power converter for wind turbine applications.

switching loss and numerous IGBTs need to be connected in parallel. Furthermore, the cabling in case of low voltage level can be a challenge. Accordingly, it becomes very difficult for a single two-level BTB converter to realize an acceptable response.

To handle the growing power with the exiting two-level BTB topology, parallel two-level BTB power converters with common/individual DC-Link have been presented by the wind turbines manufacturers. Another solution is the used of multi-level voltage source converters, which have the abilities of achieving higher voltage and power level. The three-level neutral point diode clamped (3L-NPC) topology is well-known and can be considered as the most commercialized multi-level power converter in the market. Similarly to the two-level BTB power converter, it is normally configured as a BTB structure in wind turbine systems, see Fig. 1.7.

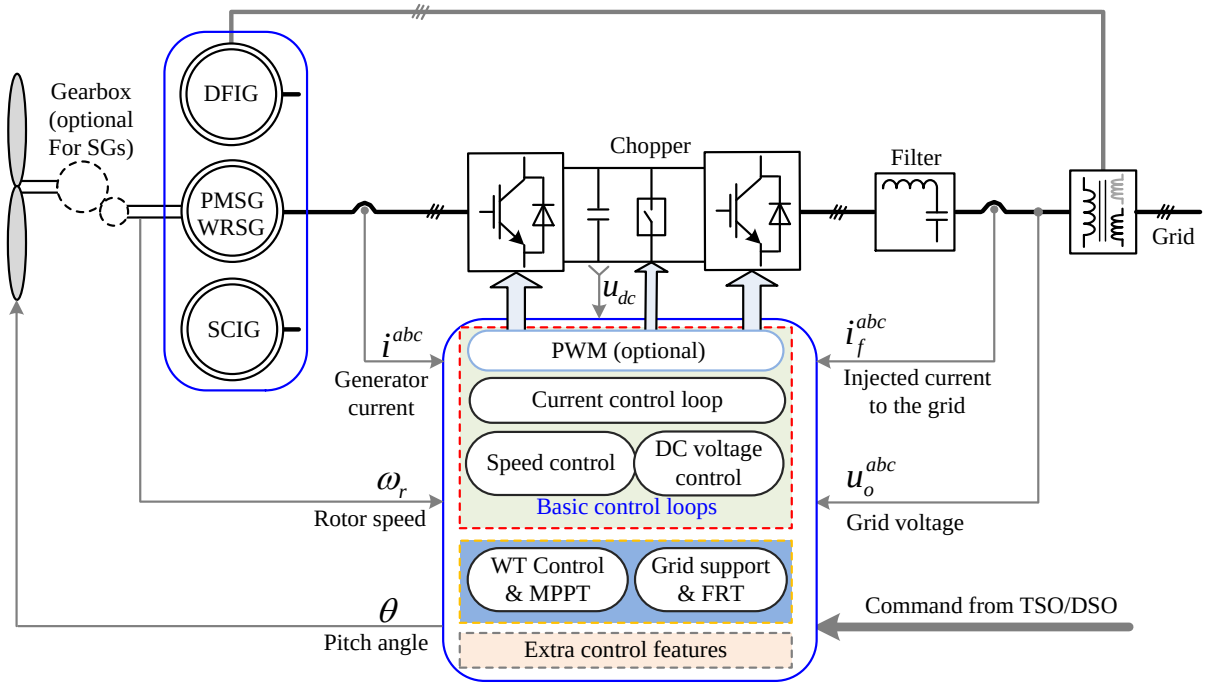

Figure 1.8: Structure of the control system for grid connected WECSs.

The 3L-NPC-BTB topology gives one more output voltage level and less dv/dt stress in comparison with the two level BTB converter. Therefore, 3L-NPC-BTB power converter can be used in the medium voltage range with lower current and smaller size of filters. However, the voltage fluctuation of the midpoint in the DC-link is a drawback of the 3L-NPC-BTB topology. Furthermore, the loss distribution between the outer and inner switching devices in a switching arm is not equal, and this problem might lead to a derated power capacity [10].

1.3.3 Filter and step-up transformer

Due to the use of power electronics converters, harmonics in the output voltage and current are inevitable. In order to meet the grid requirements, filters are employed to mitigate these harmonics. Normally, passive filters like L, LC, and LCL filters are used [12]. For LCL filters, damping of resonances is important and essential. The use of passive damping solves the resonances problem, however it causes power losses. Therefore, active damping techniques, which acting in the controller structure, are preferred for solving the resonances problem.

Usually, a step-up transformer is employed for connecting the WECS to the grid. However, the use of transformer increase the size, weight, and cost of the WECS. Therefore, it is highly desired to connect the WECS directly to the grid, i.e. avoiding the use of step-up transformer. This can be realized by operating the power electronics converter at the same voltage like the point of common coupling.

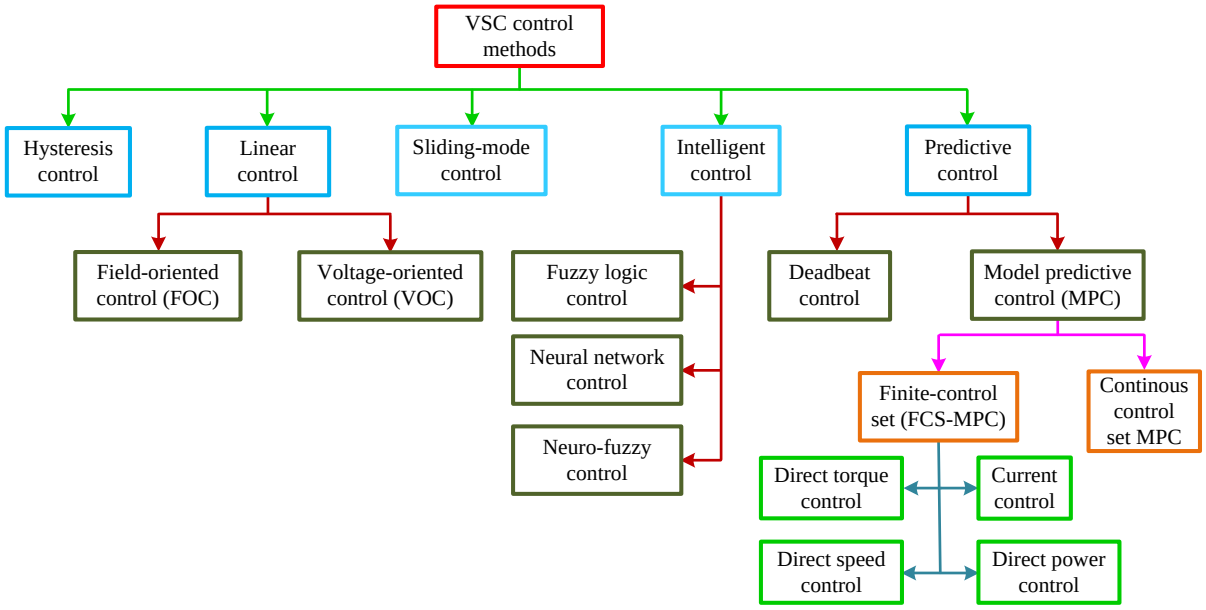

Figure 1.9: Classification of control methods for power electronics converters.

1.4 Control system for grid-connected WECSs

The structure of a general control system for grid connected variable-speed WECSs is illustrated in Fig. 1.8, which can be divided into the following parts: (1) Basic control loops, (2) wind turbine control and MPPT, (3) grid support and fault-ride through (FRT), and (4) extra control features. Note that the whole control system has to follow the power production commands given by transmission system operator (TSO)/distribution system operator (DSO).

1.4.1 Basic control loops

The basic control loops for VSCs consist of and inner (current) control loop and outer (speed or DC voltage) control loop. The two loops are usually implemented in a cascaded structure. Fig. 1.9 illustrates the the most established control schemes for power electronics converters. The structure of each control technique for current control of a VSC is shown in Fig. 1.10. The control variables are shown in the three-phase abc reference frame or in the rotating dq reference frame, but as demonstrated in the literature, it is also possible to control the variables in stationary $\alpha\beta$ reference frame.

1.4.1.1 Hysteresis control

The hysteresis current control, which is illustrated in Fig. 1.10(a), is a nonlinear control strategy for power converters [14]–[16]. The measured currents are compared with the reference ones and the gate signals S^{abc} are produced directly when the error exceeds a certain tolerance band. The main advantages of Hysteresis control are simplicity, robustness, and very good dynamics. However, the switching frequency of the power converter is variable due to the absence of modulator. Several modifications has been added to this technique to improve its performance and make the switching frequency constant [14]–[16].

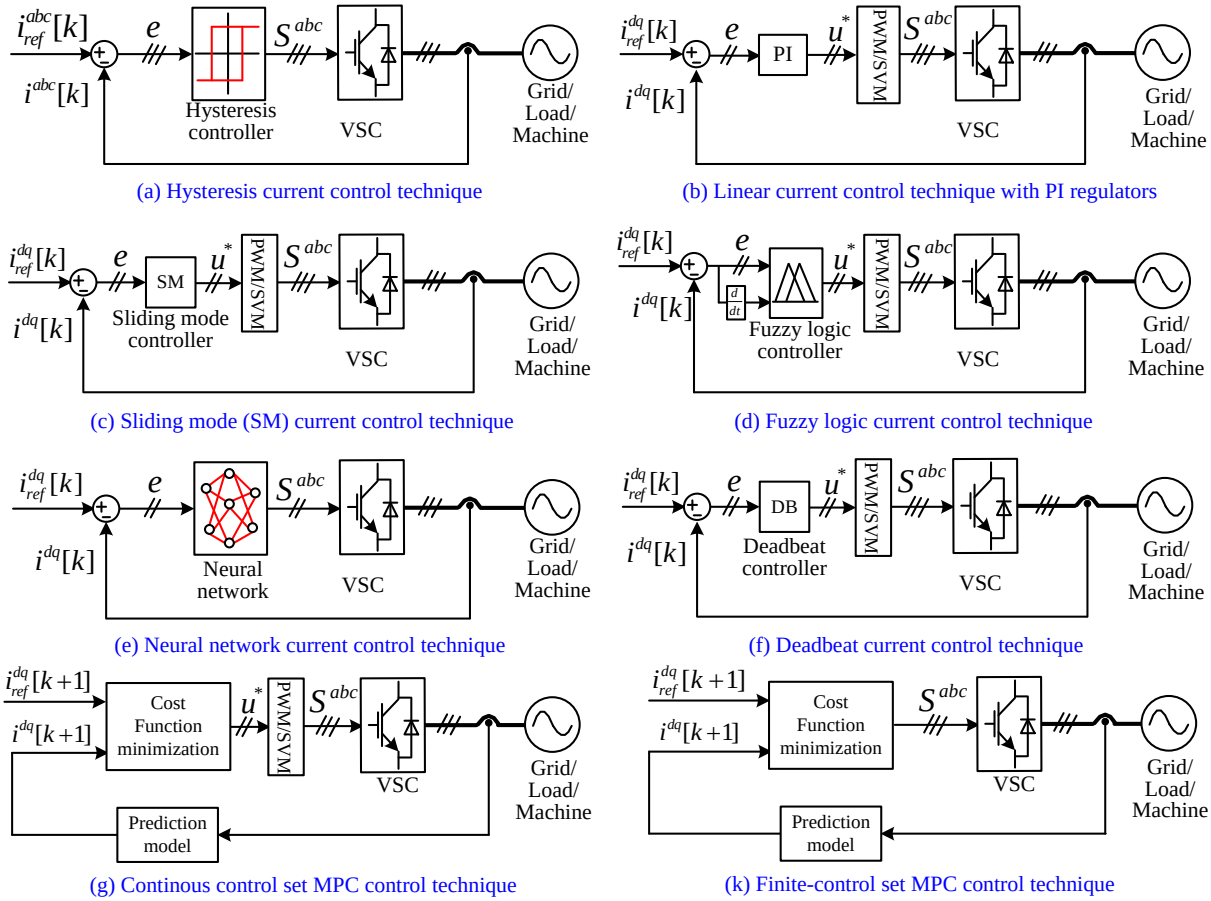

(a) Hysteresis current control technique

(b) Linear current control technique with PI regulators

(c) Sliding mode (SM) current control technique

(d) Fuzzy logic current control technique

(e) Neural network current control technique

(f) Deadbeat current control technique

(g) Continous control set MPC control technique

(k) Finite-control set MPC control technique

Figure 1.10: Structure of the different control schemes for power electronics converters.

1.4.1.2 Linear control

Linear control techniques have been widely used in industry and academia to control power electronics converters [14]–[17]. Fig. 1.10(b) illustrates a linear current control technique using proportional-integral (PI) controllers for a VSC, where the measured currents are compared to their references and the error is processed by PI regulators. The outputs of the PI regulators are the reference voltages and the switching signals S^{abc} are produced by employing a modulator stage. The most commonly used modulation methods are pulse width modulation (PWM) and space vector modulation (SVM). The switching frequency of the power converter is constant by using linear control techniques. Furthermore, the steady-state performance of the linear control methods is extremely good. However, the dynamics of the linear controllers is slow, which is the main drawback of these control techniques. Usually, to control AC machines, field-oriented control (FOC), which includes reference frame transformations, is used. Similar to FOC, voltage-oriented control (VOC) is utilized to control grid connected power converters.

With both hysteresis and linear control techniques, the system constraints, switching losses reduction and total harmonic distortion (THD) minimization, cannot be incorporated easily in the design of the control system.

1.4.1.3 Sliding mode control

The sliding mode control is an advanced and nonlinear control strategy for power electronics converters, see Fig. 1.10(c). The basic idea of this control technique is forcing the control variable (i.e. current, speed, etc.) to track/slide along a predefined trajectory [14]–[16]. The sliding mode control technique has several advantages like precise tracking and robustness against parameters variations and disturbances. However, the chattering problem is the main drawback of this control scheme.

1.4.1.4 Intelligent control

Fuzzy logic, neutral network, nero-fuzzy, genetic algorithm, and others are belonging to the family of intelligent control strategies [14]–[16]. Fig. 1.10(d) illustrates a fuzzy current control technique for power electronics converters, where the tracking error and its derivative are the input variables. By designing suitable membership functions, the reference voltage to apply in the next sampling instant can by selected. Since the exact model of the power converter is not required for the fuzzy controller, the robustness of the system to parameter variations is improved.

Neural network uses the processing of the human brain as a basis to develop/design algorithms that can be used to model/control different systems such as power converters. The neural network based current control is shown in Fig. 1.10(e). Based on the tracking error, the neural network can produce the switching signals of the power converter. Furthermore, a constant switching frequency can be realized by this method.

1.4.1.5 Predictive control

Predictive control (PC) was firstly used in 1970s for systems with very large time constant such as oil and chemical industries [18]–[24]. Predictive control is a powerful non-linear control technique for multi-variable constrained control problems, which encourages the industry to adopt it for slow process control systems. The application of predictive control for electrical drive and power electronics was a challenge due to the small time constant of such systems [19]–[24]. However, due to the evolution in the digital signal processors (DSPs), several types of predictive control techniques (e.g deadbeat PC, hysteresis-based PC, trajectory-based PC, and model predictive control (MPC)) have been applied for power electronics and electrical drive systems [19]–[24].

Deadbeat PC (DBPC) uses the system model and the reference variables (i.e currents) to compute the reference voltage, which applied to the power converter by using a modulator as shown in Fig. 1.10(f). Note, DBPC is also classified in the literature as a branch from the model predictive control techniques. DBPC gives better dynamic response than that of the linear control techniques. Furthermore, a comparable steady-state performance to that of the linear control techniques is obtained. However, problems with DBPC scheme are delays in the digital control system, and sensitivity to parameter variations of the model. Moreover, constraints/non-linearities of the system cannot be incorporated in a simple way in the controller design.

Model Predictive control (MPC) can be classified into two categories [20]–[24]: 1) Continuous-control-set model predictive control (CCS-MPC) and 2) finite-control-set model predictive control (FCS-MPC). The CCS-MPC takes into account the model of the system to predict

its future behavior over a given prediction horizon. Then, the best voltage vector is selected which minimizes a certain cost function. Finally, a modulator generates the switching states as illustrated in Fig. 1.10(g). However, its high calculation burden is the main disadvantage.

The FCS-MPC is a simple and powerful control technique for power electronics and electrical drive systems. The structure of FCS-MPC for current control of a power converter is illustrated in Fig. 1.10(k). FCS-MPC technique eliminates the PI regulators and modulation stage in comparison with the linear controllers. Furthermore, it offers a conceptually different control approach to control the power converters. The FCS-MPC approach takes advantage of the limited number of switching states of the power converter for solving the optimization problem. A discrete model is used to predict the behavior of the system for every admissible actuation sequence. The switching action that minimizes a predefined cost function is finally selected and applied in the next sampling instant. FCS-MPC techniques have been recently applied for several applications such as two-level power converters, multi-level power converters, induction motors (IMs), permanent-magnet synchronous machines (PMSMs), and others. Furthermore, it can be used for current control, direct torque control (DTC), direct power control (DPC), and direct speed control (DSC). The main features of FCS-MPC are:

- The concepts of FCS-MPC is simple and easy to understand.
- The discrete-natural of the power converter is exploited in the controller design.
- Non-linear control approach.
- Multi-variable control problems can be easily controlled by the FCS-MPC.
- The optimization problem is simplified due to the use of finite number of switching states.
- Constraints/non-linearities can be easily included in the controller design.
- Additional control requirements can be easily included in the optimization criteria.
- Direct application of the control action to the converter without requiring a modulation stage.

The main challenges of FCS-MPC are:

- Its applications are limited to power converters (i.e the concept of FCS-MPC is not used in observers).
- High calculation burden.
- The control performance is deteriorated due to variations of the model parameters.
- Selection of weighting factors is usually achieved by trail and error method.
- High ripples in the output current/torque/power due to the variable switching frequency.

1.4.2 Wind turbine control and MPPT

The control systems of the wind turbine can be classified to [25]–[27]: 1) Yaw control, and 2) pitch angle control system. Yaw control is employed to adjust the wind turbine to face the wind direction, which increases the energy capture of the wind turbine. Almost in all modern horizontal-axis wind turbines, an active yaw control system is utilized, i.e. an electric motors and gearboxes are employed to keep the turbine yawed against the wind.

Pitch angle control system [25]–[27], which is a feature of almost all modern horizontal-axis wind turbines, is employed to adjust the blade attack angle according to wind speed by changing the pitch angle and rotating the blades about their axis with respect to the hub. When the wind speed is higher than the cut-in value and lower than the rated value, the pitch angle is kept constant at its optimal value (i.e zero degree). When the wind speed is higher than the rated value, pitch control system adjusts the blade pitch to keep the rotor speed within operating limits. Finally, when the wind speed is higher than the cut-out value or during emergency cases, the wind turbine blades are completely pitched out of the wind (fully pitched or feathering) and no power will be captured by the blades. Then, The wind turbine is shut down and protected.

In order to extract the maximum energy from the wind turbine, the rotational speed of the rotor must be regulated by a MPPT algorithm. The MPPT control is applied when the wind speed is higher than the cut-in value and lower than the rated value (i.e. pitch angle is zero). Techniques adopted by MPPT controller can be classified into [25]–[27]: regulation of the tip speed ratio (TSR), using power signal feedback (PSF) control, Perturb and Observe (P&O) method, and optimal torque control (OTC) method.

TSR is a function of the wind speed, rotor diameter of the wind turbine, and rotor angular speed. By keeping the TSR constant at its optimal value, the optimal (reference) value of the rotational speed of the rotor can be computed. However, the wind speed must be measured by an anemometer. In PSF, the maximum power versus the rotational speed of the rotor is obtain firstly from the experimental results and recorded in a look-up table. Then, the rotational speed of the rotor is measured and feed-backed to this look-up table to find the value of the reference active power, which compared with the actual generated power from the WECS and based on the error the control action can be adjusted. P&O is a mathematical optimization technique used to search for the maximum power point of a given function, which is widely used in WECSs and PVs to find the optimal operating point that maximizes the extracted power. P&O technique is based on perturbing a certain control parameter such as the rotational speed of the rotor in small step-size and observing the resulting changes in the target function (i.e extracted power from the WECS), until the slope becomes zero. In OTC, the optimal torque of the generator is calculated as a quadratic function of the rotational speed of the rotor multiplied by the optimal torque coefficient. Through the feedback control, the generator torque will be regulated to its optimal value, and accordingly, the MPPT is realized. Note that there is no use of the wind speed signal in this scheme.

1.4.3 Grid support and fault-ride through control

Due to the high penetration of the wind power in the current power systems, WECSs have to achieve the new grid code requirements [10]–[13]. Supporting the grid during normal and abnormal conditions is highly desirable. Furthermore, the WECS must stay connected to the grid

during fault operations. Accordingly, fault-ride through control technique must be considered to protected the WECS during faults and inject active/reactive power to the grid.

1.4.4 Extra control features

Additional control features may be also included in the control system of the modern WECSs such as power quality improvement of the injected power to the grid (i.e reducing the harmonics in the current/voltage waveforms) [10]–[13]. Furthermore, in some WECSs, an energy storage system such as batteries is installed. Accordingly, the control system of this energy storage system is incorporated in the control system of the WECS.

1.5 Motivation and objectives

The main motivations and objectives of this dissertation are to closely investigate (and trying to solve) the problems associated with deadbeat predictive control and FCS-MPC listed in Sec. 1.4.1.5, respectively. More specifically, the objectives of this dissertation are:

- Development of thorough mathematical models for WECSs with PMSG and DFIG using two-level back-to-back power converter for theoretical analysis and controller design.
- Realization/experimental evaluation of the traditional FCS-MPC for PMSGs and DFIGs and comparing its performance with the DBPC and FOC/VOC techniques.
- Extension of the FCS-MPC concept to be used in observers for estimating mechanical/electrical parameters of the PMSG/DFIG such as rotor speed/position or resistance/inductance.
- Improving the robustness of the deadbeat predictive control for PMSGs/DFIGs to variations of the model parameters and compensating the delay due to the digital controller.
- Reducing the computational load of the traditional FCS-MPC scheme for PMSGs/DFIGs with two-level back-to-back power converter and enhancing its robustness to uncertainties/mismatches in the machine parameters.
- Solving the problem of weighting factors selection in predictive direct torque control for PMSGs/DFIGs.
- Extension of the FCS-MPC principles to control the speed/current in one control law, which eliminates the cascaded loop structure that normally used for electrical drive.
- Enhancing the steady-state performance and robustness of the FCS-MPC for grid connected power converters by reducing the ripples in the output current/power and estimating the model parameters.
- Improvement of the fault-ride through ability for WECSs with PMSGs/DFIGs by using FCS-MPC.

1.6 Contributions

This dissertation focuses on advanced/sensorless control techniques for WECSs with PMSGs and DFIGs using two-level back-to-back power converter. Two test benches (one for PMSG and the second for DFIG) to experimentally validate the theoretical finding have been constructed. More than 50 peer reviewed journal & conference papers (see Appendix A) have been published, contributing in the field of control for both PMSGs/DFIGs with two-level back-to-back power converter, grid tied power converter (active front end), AC motor drives, multilevel power converters, and six-phase PMSMs. More specifically, within my work the following have been realized:

- Comprehensive models of WECSs based on PMSGs/DFIGs with two-level back-to-back power converter are developed in details. Two test benches (PMSG and DFIG) have been constructed to validate the theoretical results (See Chapter 2).
- The conventional control techniques including FOC/VOC with SVM, deadbeat predictive control with SVM, and FCS-MPC are revisited in details, simulated, and experimentally implemented (See Chapter 3).
- The principles of the FCS-MPC have been extended to observers for estimating the rotor speed/position of PMSGs/DFIGs. A search-based algorithm is developed to discretize the position of the rotor, which produces a finite number of rotor position angles similar to the finite switching states of the power converter. The new algorithm is applied for phase-locked loop (PLL) based observers and model reference adaptive system (MRAS) estimators (See Chapter 4).
- The proposed search-based algorithm in Chapter 4 requires high computational burden (64 iterations). Therefore, this search-based algorithm is modified to reduce the computational load and enhance its accuracy. Two efficient search-based algorithms (one requires 36 iterations and the second calls for 24 iterations) are developed and experimentally validated (See Chapter 5).
- Enhancing the robustness of the deadbeat predictive control to variations of the machine parameters is realized by designing a disturbance observer. Furthermore, to further improve the control performance and achieve encoderless control for PMSGs and DFIGs, an extended kalman filter (EKF) is designed for compensating the one sample delay due to the digital controller and estimating the rotor speed/position of the machine (See Chapter 6).
- The deadbeat principles are combined with the FCS-MPC to reduce the computational burden of the classical DMPC for PMSGs and DFIGs. Furthermore, a (novel) discrete time integral action is added to the deadbeat function to improve the robustness of the proposed FCS-MPC to any mismatches in the model parameters (See Chapter 7).
- Predictive direct torque control (PDTC) without weighting factors is proposed and experimentally implemented for PMSGs and DFIGs in variable-speed wind turbine applications (see Chapter 8).

- Control of the rotor speed and current in one control law has been realized and experimentally implemented for PMSGs and DFIGs in wind turbine systems, which significantly improved the dynamic performance and eliminated the cascaded structure of the inner and outer control loops (see Chapter 9).
- A computationally efficient multiple-vector FCS-MPC to improve the steady-state response is proposed for grid connected two-level power converters. Furthermore, a (novel) finite set inductance estimation observer is proposed to enhance the robustness of the proposed multiple-vector FCS-MPC (see Chapter 10).
- A new fault-ride through (FRT) strategy based on using the rotor inertia of the wind turbine and generator is proposed for PMSGs and DFIGs in wind turbine applications. Furthermore, the FCS-MPC is combined with the prosed FRT technique to improve the dynamics of the WECS (see Chapter 11).

CHAPTER 2

System Modeling and Experimental System Description

Firstly, this chapter summarizes the mathematical symbols used in this dissertation. Then, the mathematical basics of the system modeling are highlighted in Sec. 2.1, which includes coordinate transformations, and continuous/discrete time system descriptions. Subsequently, the mathematical models for both the PMSG and DFIG in variable-speed wind turbine systems are developed in Sec 2.2 and Sec. 2.3, respectively. Then, the constructed test-benches of the PMSG and DFIG for validation of the proposed speed/position observers and control algorithms are described in Sec 2.4. Finally, the Simulink models of the PMSG and DFIG are briefly presented in Sec. 2.5.

Notation

$\mathbb{N}, \mathbb{R}, \mathbb{C}$ are the sets of natural, real and complex numbers. $x \in \mathbb{R}$ or $x \in \mathbb{C}$ is a real or complex scalar. $\boldsymbol{x} \in \mathbb{R}^n$ (bold) is a real valued vector with $n \in \mathbb{N}$. $\boldsymbol{x}^\top$ is the transpose and $\|\boldsymbol{x}\| = \sqrt{\boldsymbol{x}^\top \boldsymbol{x}}$ is the Euclidean norm of $\boldsymbol{x}$. $\mathbf{0}_n = (0, \ldots, 0)^\top$ is the n-th dimensional zero vector. $\boldsymbol{X} \in \mathbb{R}^{n \times m}$ (capital bold) is a real valued matrix with $n \in \mathbb{N}$ rows and $m \in \mathbb{N}$ columns. $\boldsymbol{O}_{n \times m} \in \mathbb{R}^{n \times m}$ is the zero matrix. $\boldsymbol{x}_z^y \in \mathbb{R}^2$ is a space vector of a rotor (r), stator (s) or filter (f) quantity, i.e. $z \in \{r, s, f\}$. The space vector is expressed in either phase abc-, stator fixed s-, rotor fixed r-, or arbitrarily rotating k-coordinate system, i.e. $y \in \{abc, s, r, k\}$, and may represent voltage $\boldsymbol{u}$, flux linkage $\boldsymbol{\psi}$ or current $\boldsymbol{i}$, i.e. $\boldsymbol{x} \in \{\boldsymbol{u}, \boldsymbol{\psi}, \boldsymbol{i}\}$.

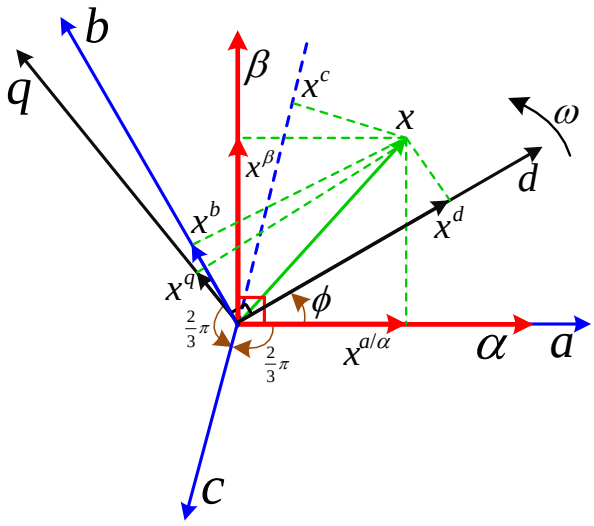

Figure 2.1: Coordinate systems

2.1 Mathematical basics for system modeling

2.1.1 Coordinate Systems

In Fig. 2.1, the following coordinate systems are illustrated: 1) Natural three-phase (abc) in blue, 2) stationary two-phase ($\alpha\beta$) in red, and 3) synchronously rotating two-phase (dq) in black, respectively. The vector $\boldsymbol{x}$ can be expressed in the $\alpha\beta$ or dq coordinate system by the corresponding quantities in the abc reference frame $\boldsymbol{x}^{abc}$ as fellow:

$$\boldsymbol{x}^{dq} = \boldsymbol{T}_P(\phi)^{-1}\boldsymbol{x}^{\alpha\beta} = \boldsymbol{T}_P(\phi)^{-1}\boldsymbol{T}_C\boldsymbol{x}^{abc}, \tag{2.1}$$

by using the Clarke and Park transformation, respectively, given by

$$\boldsymbol{x}^{\alpha\beta} = \underbrace{\gamma_C \begin{bmatrix} 1 & -\frac{1}{2} & -\frac{1}{2} \\ 0 & \frac{\sqrt{3}}{2} & -\frac{\sqrt{3}}{2} \end{bmatrix}}_{=:\boldsymbol{T}_C} \boldsymbol{x}^{abc} \;\&\; \boldsymbol{x}^{dq} = \underbrace{\begin{bmatrix} \cos(\phi) & \sin(\phi) \\ -\sin(\phi) & \cos(\phi) \end{bmatrix}}_{=:\boldsymbol{T}_P(\phi)^{-1}} \boldsymbol{x}^{\alpha\beta} \tag{2.2}$$

In (2.2), $\gamma_C = \frac{2}{3}$ for an amplitude-invariant transformation or $\gamma_C = \sqrt{2/3}$ for a power-invariant transformation. ϕ is the angle between the α/a-axis and the d-axis (in $[\mathrm{rad}]$).

2.1.2 Continuous-time state-space system representation

For a linear time-invariant (LTI) systems, the continuous-time differential equations can be written in state-space form of

$$\left.\begin{aligned} \tfrac{d}{dt}\boldsymbol{x}(t) &= \boldsymbol{A}\boldsymbol{x}(t) + \boldsymbol{B}\boldsymbol{u}(t), \\ \boldsymbol{y}(t) &= \boldsymbol{C}\boldsymbol{x}(t) + \boldsymbol{D}\boldsymbol{u}(t), \end{aligned}\right\} \tag{2.3}$$

where $\boldsymbol{x}$, $\boldsymbol{u}$, and $\boldsymbol{y}$ are the state, input, and output vectors, respectivey. In (2.3), $\boldsymbol{A}$, $\boldsymbol{B}$, $\boldsymbol{C}$, and $\boldsymbol{D}$ are the state, input, output, and feed-through matrices, respectively.

2.1.3 Discrete-time state-space system representation

For implementing control algorithms and observers on digital control systems, the discretization of the continuous-time system with a sampling time $T_s \ll 1$[s] is essential. Usually, the discrete-time form of (2.3) in state space can be written as

$$\left.\begin{aligned} \boldsymbol{x}[k+1] &= \boldsymbol{A}_d\boldsymbol{x}[k] + \boldsymbol{B}_d\boldsymbol{u}[k], \\ \boldsymbol{y}[k] &= \boldsymbol{C}_d\boldsymbol{x}[k] + \boldsymbol{D}_d\boldsymbol{u}[k], \end{aligned}\right\} \tag{2.4}$$

where $k = \frac{t}{T_s}$ is the current sampling instant.

2.1.4 Exact discretization and approximations

Various techniques for discretization of continous-time systems are exist [28]-[30]. Usually, it is necessary to make a trade-off between modeling accuracy and complexity.The following sections present the mostly-used discretization methods for power electronics and electrical drive.

2.1.4.1 Euler-forward discretization

The Euler-forward discretization is the most simple approximation method. For sufficiently small sampling time $T_s \ll 1$, the following holds $\boldsymbol{x}[k] := \boldsymbol{x}(kT_s) \approx \boldsymbol{x}(t)$ and

$$\frac{d}{dt}\boldsymbol{x}(t) = \frac{\boldsymbol{x}[k+1] - \boldsymbol{x}[k]}{T_s} \tag{2.5}$$

for all $t \in [kT_s,\ [k+1]T_s)$ and $k \in \mathbb{N}\cup\{0\}$. Accordingly, The discrete-time state-space matrices for the Euler-forward approximation are given by

$$\left.\begin{aligned} \boldsymbol{A}_d &= \boldsymbol{I} - \boldsymbol{A}\cdot T_\mathrm{s}, \\ \boldsymbol{B}_d &= \boldsymbol{B}\cdot T_\mathrm{s}, \\ \boldsymbol{C}_d &= \boldsymbol{C} \text{ and} \\ \boldsymbol{D}_d &= \boldsymbol{D} \end{aligned}\right\} \tag{2.6}$$

where $\boldsymbol{I}$ is the unity matrix.

2.1.4.2 Euler-backwards discretization

The Euler-backwards discretization is very similar to the previously mentioned Euler-forward method. The approximation of the time differentiation is given by

$$\frac{d}{dt}\boldsymbol{x}(t) = \frac{\boldsymbol{x}[k] - \boldsymbol{x}[k-1]}{T_s} \tag{2.7}$$

This approximation is numerically more stable than the Euler-forward method but in some cases it is not possible to calculate the discrete-time state-space matrices explicitly.

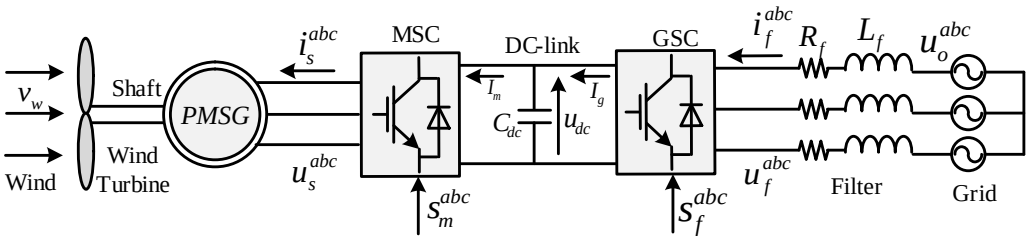

Figure 2.2: Structure of the variable-speed wind energy conversion system with PMSG.

2.1.4.3 Series Expansion

The idea of using Taylor series expansion for the discretization of nonlinear systems was successfully used in [28]-[30]. According to the Taylor series expansion $\boldsymbol{x}[k+1]$ can be written as

$$\boldsymbol{x}[k+1] = \boldsymbol{x}[k] + \sum_{i=1}^{\infty} \frac{T_s^i}{i!} \frac{d^i \boldsymbol{x}(t)}{dt^i}. \tag{2.8}$$

This method gives accurate discrete-model in comparsion with Euler techniques. However, its required high computational power due to the complexity of the result discrete model.

2.2 PMSG wind turbine system

The block diagram of the variable-speed wind energy conversion system with PMSG is shown in Fig. 2.2. It consists of a PMSG mechanically coupled to the wind turbine directly via a stiff shaft. The stator windings of the PMSG are connected via a back-to-back full-scale voltage source converter (VSC), a filter and a transformer to the grid. The transformer will be neglected in the upcoming modeling. The machine side converter (MSC) and the grid side converter (GSC) share a common DC-link with capacitance $C_{\mathrm{dc}}\,[\mathrm{As/V}]$ with DC-link voltage $u_{\mathrm{dc}}\,[\mathrm{V}]$.

2.2.1 Wind turbine

Wind turbines convert wind energy into mechanical energy and, via a generator, into electrical energy. The mechanical (turbine) power of a WECS is given by [27], [31]–[34]

$$p_t = c_p(\lambda, \beta) \underbrace{\frac{1}{2} \rho \pi r_t^2 v_w^3}_{\text{wind power}} \tag{2.9}$$

where $\rho > 0\,[\mathrm{kg/m^3}]$ is the air density, $r_t > 0\,[\mathrm{m}]$ is the radius of the wind turbine rotor (πr_t^2 is the turbine swept area), $c_p \geq 0\,[1]$ is the power coefficient, and $v_w \geq 0\,[\mathrm{m/s}]$ is the wind speed. The power coefficient c_p is a measure for the "efficiency" of the WECS. It is a nonlinear function of the tip speed ratio

$$\lambda = \frac{\omega_m r_t}{v_w} \geq 0 \qquad [1] \tag{2.10}$$

and the pitch angle $\beta \geq 0\,[^\circ]$ of the rotor blades. The Betz limit $c_{p,\mathrm{Betz}} = 16/27 \approx 0.59$ is an upper (theoretical) limit of the power coefficient, i.e. $c_p(\lambda, \beta) \leq c_{p,\mathrm{Betz}}$ for all $(\lambda, \beta) \in \mathbb{R} \times \mathbb{R}$.

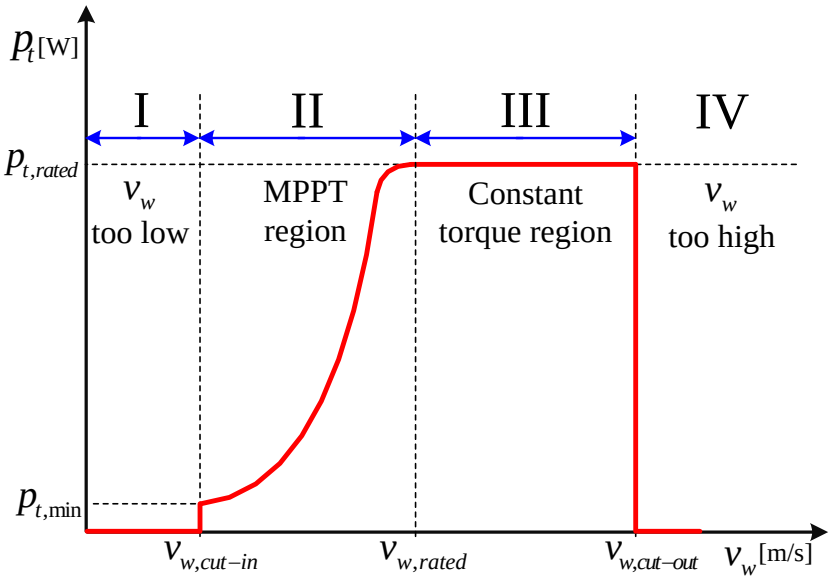

Figure 2.3: Operation regions of variable-speed wind turbines.

For typical WECS, the power coefficient ranges from 0.4 to 0.48 [27], [31]–[33]. Many different (data-fitted) approximations for c_p have been reported in the literature. This work uses the power coefficient from [33], i.e.

$$\begin{aligned} c_p(\lambda,\beta) &= 0.5176\left(\frac{116}{\lambda_i}-0.4\beta-5\right)^{\frac{-21}{\lambda_i}}+0.0068\lambda \\ \frac{1}{\lambda_i} &:= \frac{1}{\lambda+0.08\beta}-\frac{0.035}{\beta^3+1}. \end{aligned} \tag{2.11}$$

Generally, the operation regions of the variable-speed wind turbines can be classified into four regions [27], [31]–[34], depending on the wind speed $v_w[\mathrm{m/s}]$ as shown in Fig. 2.3.

- **Operation region I:** The wind speed in this region is lower than the cut-in value $v_w < v_{w,cut-in}$ of the wind turbine. Therefore, the wind turbine will stay in standstill and no power is generated (i.e. $p_t = 0[\mathrm{W}]$).

- **Operation region II:** The wind velocity in this zone is between the cut-in value $v_{w,cut-in}$ and the rated wind speed $v_{w,rated}$ of the wind turbine. Therefore, the wind turbine is operating in this region and the maximum power can be produced. A maximum power point tracking (MPPT) algorithm is employed to operate the wind turbine at its optimal tip speed ratio $\lambda^\star$ (a given constant) where the power coefficient has its maximum $c_p^\star := c_p(\lambda^\star,0) = \max_\lambda c_p(\lambda,0)$, see Fig. 2.4. Only then, the wind turbine can extract the maximally available power as

$$p_t^\star := \frac{1}{2}c_p^\star\rho\pi r_t^2 v_w^3. \tag{2.12}$$

Invoking (2.10), the output mechanical power of the wind turbine can be written as

$$p_t^\star := \frac{1}{2}c_p^\star\rho\pi r_t^2\left(\frac{\omega_m^\star r_t}{\lambda^\star}\right)^3. \tag{2.13}$$

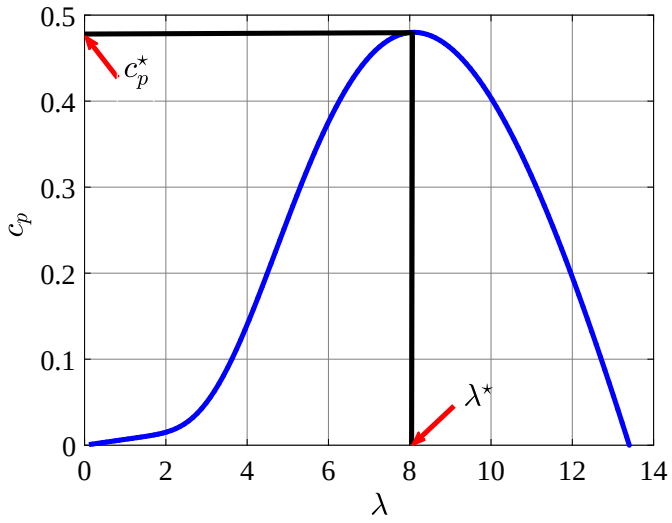

Figure 2.4: Power coefficient curve for $\beta = 0$.

Accordingly, the optimum mechanical torque of the wind turbine can be expressed as

$$T_m^\star = \frac{p_t^\star}{\omega_m^\star} = k_p^\star(\omega_m^\star)^2, \qquad k_p^\star := \frac{1}{2}\rho\pi r_t^5 \frac{c_p^\star}{(\lambda^\star)^3} \tag{2.14}$$

The MPPT is achieved by the nonlinear speed controller

$$T_e^\star = k_p^\star \omega_m^2, \tag{2.15}$$

which assures that the PMSG mechanical angular speed ω_m is adjusted to the actual wind speed v_w such that $\frac{\omega_m r_t}{v_w} \stackrel{!}{=} \lambda^\star$ holds. This method called *optimal torque control (OTC)*. Another alternative is *regulation of the tip speed ratio (TSR)* of the wind turbine, i.e. the optimal angular speed of the generator can be calculated as:

$$\omega_m^\star = \frac{\lambda^\star v_w}{r_t}. \tag{2.16}$$

In (2.16), the wind speed v_w is essential to calculate $\omega_m^\star$, which can be measured using anemometer. However, this technique increases cost and reduces the reliability of the overall system.

- **Operation region III:** The wind velocity in this zone is between the rated value $v_{w,rated}$ and the cut-out wind speed $v_{w,cut-out}$ of the wind turbine. Accordingly, the wind turbine will operate at the rated power $p_{t,rated}$ and the generator is producing its nominal torque $T_{e,rated}$. The control system regulates the input power (or torque) through changing (increasing) the pitch angle β to maintain the overall generated power not goes beyond its safety range.

- **Operation region IV:** The wind velocity in this zone is higher than the cut-out wind speed $v_w > v_{w,cut-out}$. The pitch angle control (to reduce the input power) is not enough to keep the system in safety mode, then the turbine will be shut-down (i.e. $p_t = 0[\mathrm{W}]$).

2.2.2 Permanent-Magnet Synchronous Generator (PMSG)

The PMSG can be constructed with a large number of poles and operate at a speed that directly matches the turbine blade speed. Such a direct-drive system does not need a gearbox as illustrated in Fig. 2.2. This results a reduction in installation and maintenance costs and provides an advantage over DFIG based turbines where the usage of a gearbox is a must [27], [31]–[34]. Furthermore, the rotor magnetic flux is generated by permanent magnets, and these generators are, therefore, brushless. Because of the absence of the rotor windings, a high power density can be achieved, reducing the size and weight of the generator. In addition, there are no rotor winding losses, reducing the thermal stress on the rotor. The drawbacks of these generators lie in the fact that permanent magnets are more expensive and prone to demagnetization. Generally, for direct-drive variable-speed wind turbine systems, a surface-mounted PMSG is employed, where the permanent magnets are placed on the rotor surface separated by non-ferrite materials between two adjacent magnets. Since the permeability of the magnets is very close to that of the non-ferrite materials, the effective air gap between the rotor core and stator is uniformly distributed around the surface of the rotor. This type of configuration is known as a non-salient-pole PMSG. Accordingly, the d- and q-axis inductance are approximately equal (i.e. $L_s^d = L_s^q =: L_s$ no anisotropy).

The stator voltage equation of the PMSG is given by [27, 34]

$$\boldsymbol{u}_s^{abc}(t) = R_s \boldsymbol{i}_s^{abc}(t) + \frac{\mathrm{d}\boldsymbol{\psi}_s^{abc}}{\mathrm{d}t}(t), \quad \boldsymbol{\psi}_s^{abc}(0) = \mathbf{0}_3 \tag{2.17}$$

where

$$\frac{\mathrm{d}\boldsymbol{\psi}_s^{abc}}{\mathrm{d}t}(t) = L_s \frac{\mathrm{d}\boldsymbol{i}_s^{abc}}{\mathrm{d}t}(t) + \boldsymbol{e}_s^{abc}(t). \tag{2.18}$$

Here $\boldsymbol{u}_s^{abc} = (u_s^a, u_s^b, u_s^c)^\top$ [V], $\boldsymbol{i}_s^{abc} = (i_s^a, i_s^b, i_s^c)^\top$ [A], $\boldsymbol{\psi}_s^{abc} = (\psi_s^a, \psi_s^b, \psi_s^c)^\top$ [Vs], and $\boldsymbol{e}_s^{abc} = (e_s^a, e_s^b, e_s^c)^\top$ [V] are the stator voltages, currents, fluxes, and back electro-motive forces respectively, all in the abc-reference frame (three-phase system). R_s [Ω] and L_s [Vs/A] are the stator resistance and inductance, respectively.

Note that the PMSG rotor rotates with mechanical angular frequency ω_m [rad/s]. Hence, for a machine with pole pair number n_p [1], the electrical angular frequency of the rotor is given by $\omega_r = n_p \omega_m$ and the rotor reference frame is shifted by the rotor angle

$$\phi_r(t) = \int_0^t \omega_r(\tau)\mathrm{d}\tau + \phi_r^0, \quad \phi_r^0 \in \mathbb{R} \tag{2.19}$$

with respect to the stator reference frame (ϕ_r^0 is the initial rotor angle). Equation (2.17) can be expressed in the stationary reference frame $s = (\alpha, \beta)$ as follows

$$\boldsymbol{u}_s^s(t) = R_s \boldsymbol{i}_s^s(t) + \frac{\mathrm{d}\boldsymbol{\psi}_s^s}{\mathrm{d}t}(t), \quad \boldsymbol{\psi}_s^s(0) = \mathbf{0}_2 \tag{2.20}$$

and (2.20) can be rewritten in the rotating reference frame $k = (d, q)$ as follows

$$\boldsymbol{u}_s^k(t) = R_s \boldsymbol{i}_s^k(t) + \frac{\mathrm{d}\boldsymbol{\psi}_s^k}{\mathrm{d}t}(t) + \omega_r \boldsymbol{J} \boldsymbol{\psi}_s^k(t), \quad \boldsymbol{\psi}_s^k(0) = \mathbf{0}_2 \tag{2.21}$$

where

$$\boldsymbol{J} = \begin{bmatrix} 0 & -1 \\ 1 & 0 \end{bmatrix}. \tag{2.22}$$

The PMSG flux in the dq frame can be expressed as

$$\boldsymbol{\psi}_s^k(t) = \begin{pmatrix} \psi_s^d(t) \\ \psi_s^q(t) \end{pmatrix} = L_s \begin{pmatrix} i_s^d(t) \\ i_s^q(t) \end{pmatrix} + \begin{pmatrix} \psi_{pm} \\ 0 \end{pmatrix}. \tag{2.23}$$

The dynamics of the mechanics of the wind turbine system are given by

$$\frac{d\omega_m(t)}{dt} = \frac{1}{\Theta}\Big(T_m(t) - T_e(t) + \nu\omega_m(t)\Big), \quad \omega_m(0) = \omega_m^0 \in \mathbb{R} \tag{2.24}$$

where

$$T_e(t) = \tfrac{3}{2} n_p \psi_{pm} i_s^q(t) \tag{2.25}$$

is the electro-magnetic machine torque (moment) and $T_m\,[\mathrm{Nm}]$ is the mechanical torque produced by the wind turbine acting on the PMSG shaft. $\Theta\,[\mathrm{kg/m^2}]$ is the rotor inertia, $n_p\,[1]$ is the pole pair number, and $\nu\,[\mathrm{N\,m\,s}]$ is the viscous friction coefficient.

2.2.3 Back-to-back converter and DC-Link

As shown in Fig. 2.2, a balanced generator and grid are considered in this work. The output voltage of the MSC and GSC can be calculated as follows [34]:

$$\boldsymbol{u}_s^{abc} = \frac{1}{3} u_{\mathrm{dc}} \boldsymbol{T}^{abc} \boldsymbol{s}_m^{abc} \;\text{ and }\; \boldsymbol{u}_f^{abc} = \frac{1}{3} u_{\mathrm{dc}} \boldsymbol{T}^{abc} \boldsymbol{s}_f^{abc} \tag{2.26}$$

where $\boldsymbol{s}_m^{abc} = (s_m^a, s_m^b, s_m^c)^\top \in \{0,1\}$ and $\boldsymbol{s}_f^{abc} = (s_f^a, s_f^b, s_f^c)^\top \in \{0,1\}$ are the switching state vectors of the MSC and GSC, respectively, and $\boldsymbol{T}^{abc}$ is the transformation matrix

$$\boldsymbol{T}^{abc} = \begin{bmatrix} 2 & -1 & -1 \\ -1 & 2 & -1 \\ -1 & -1 & 2 \end{bmatrix} \tag{2.27}$$

describing the relation between switching state vector and output phase voltage vector of the converter.

The DC-link dynamics are given by (neglecting resistive losses)

$$\frac{d}{dt} u_{dc}(t) = \frac{1}{C_{dc}} (I_g(t) - I_m(t)), \quad u_{dc}(0) = 0 \in \mathbb{R} \tag{2.28}$$

where

$$I_m(t) = \boldsymbol{i}_s^{abc}(t)^\top \boldsymbol{s}_m^{abc} \quad \text{and} \quad I_g(t) = \boldsymbol{i}_f^{abc}(t)^\top \boldsymbol{s}_f^{abc}. \tag{2.29}$$

are the machine and grid side DC-link currents (see Fig. 2.2).

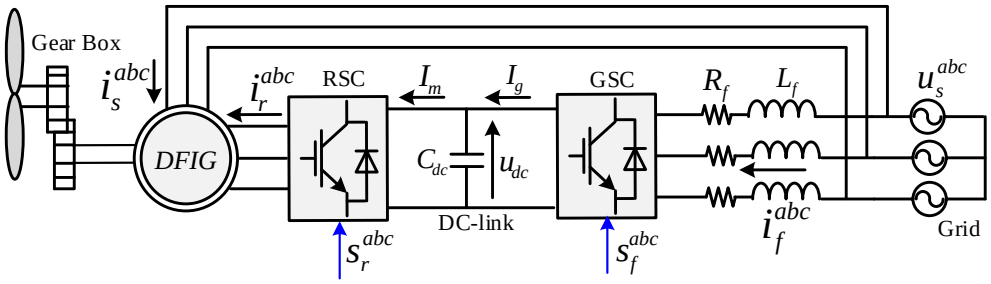

Figure 2.5: Structure of the variable-speed wind energy conversion system with DFIG.

2.2.4 Filter and grid

In Fig. 2.2, a grid-connected voltage source converter is shown. It is connected to the grid via a RL-filter with resistance $R_f\,[\Omega]$ and inductance $L_f\,[\mathrm{Vs/A}]$. The grid is represented as ideal voltage source with grid voltage $\boldsymbol{u}_o^{abc} = (u_o^a, u_o^b, u_o^c)^\top\,[\mathrm{V}]$ and the currents $\boldsymbol{i}_f^{abc} = (i_f^a, i_f^b, i_f^c)^\top\,[\mathrm{A}]$ flow from the grid to the GSC. Invoking Kirchhoff's voltage law at the AC side of the GSC [34] yields

$$\boldsymbol{u}_o^{abc}(t) = R_f \boldsymbol{i}_f^{abc}(t) + L_f \frac{\mathrm{d}\boldsymbol{i}_f^{abc}}{\mathrm{d}t}(t) + \boldsymbol{u}_f^{abc}(t) \quad \boldsymbol{i}_f^{abc}(0) = \boldsymbol{0}_3. \tag{2.30}$$

Here $\boldsymbol{u}_f^{abc} = (u_f^a, u_f^b, u_f^c)^\top\,[\mathrm{V}]$ is the output voltage of the GSC. The voltage equation (2.30) can be rewritten in the $s = (\alpha, \beta)$ reference frame as follows

$$\boldsymbol{u}_o^s(t) = R_f \boldsymbol{i}_f^s(t) + L_f \frac{\mathrm{d}\boldsymbol{i}_f^s}{\mathrm{d}t}(t) + \boldsymbol{u}_f^s(t), \quad \boldsymbol{i}_f^s(0) = \boldsymbol{0}_2. \tag{2.31}$$

Voltage orientation is achieved by aligning the d-axis of the synchronous (rotating) reference frame with the grid voltage vector $\boldsymbol{u}_o^s$ which rotates with the grid angular frequency ω_e (under ideal conditions, i.e. for a constant grid frequency $f_e > 0$, it holds that $\omega_e = 2\pi f_e\,[\mathrm{rad/s}]$ is constant). Applying the (inverse) Park transformation with $\boldsymbol{T}_P(\phi_e)^{-1}$ as in (2.2) with

$$\phi_e(t) = \int_e^t \omega_e(\tau)\mathrm{d}\tau + \phi_e^0, \quad \phi_e^0 \in \mathbb{R}$$

to the voltage equation (2.31) yields the description in the rotating reference frame (neglecting initial values)

$$\boldsymbol{u}_o^k(t) = R_f \boldsymbol{i}_f^k(t) + L_f \frac{\mathrm{d}\boldsymbol{i}_f^k}{\mathrm{d}t}(t) + \omega_e \boldsymbol{J} L_f \boldsymbol{i}_f^k(t) + \boldsymbol{u}_f^k(t). \tag{2.32}$$

2.3 DFIG wind turbine system

Among various configurations of variable-speed WECSs, doubly-fed induction generator (DFIG) is the most commonly used form in present wind power plants, due to its attractive advantages of variable-speed operation with a partial-scale back-to-back converter with only 30% of the generator rating and lower power loss [35, 36]. In Fig. 2.5, the doubly-fed induction generator is mechanically coupled to the wind turbine via a shaft and gearbox with ratio $g_r \geq 1$.

The stator windings of the DFIG are directly coupled to the grid, whereas the rotor winding is coupled via a back-to-back partial-scale voltage source converter (VSC), and a filter to the grid. The grid side converter (GSC) and the rotor side converter (RSC) share a common DC-link with capacitance $C_{\mathrm{dc}}\,[\mathrm{As/V}]$ with DC-link voltage $u_{\mathrm{dc}}\,[\mathrm{V}]$.

The model of the wind turbine, filter and grid are the same like in the PMSG wind turbine system. Therefore, the model of those components will not repeated here again.

2.3.1 Gearbox

The gearbox transmits the mechanical power of the wind turbine to the rotor of the DFIG. In variable-speed wind turbines, the angular speed of the shaft $\omega_t(t)\,[\mathrm{rad/s}]$ is significantly lower than the rated angular speed $\omega_m(t)\,[\mathrm{rad/s}]$ of the DFIG. Therefore, the use of an step-up gearbox with ratio $g_r \geq 1$ is essential.

2.3.2 Doubly-Fed Induction Generator (DFIG)

The stator and rotor voltage equations of the DFIG can be written in the abc reference frame as follows [35, 36]:

$$\boldsymbol{u}_s^{abc}(t) = R_s \boldsymbol{i}_s^{abc}(t) + \tfrac{d}{dt}\boldsymbol{\psi}_s^{abc}(t) \qquad \text{and} \qquad \boldsymbol{u}_r^{abc}(t) = R_r \boldsymbol{i}_r^{abc}(t) + \tfrac{d}{dt}\boldsymbol{\psi}_r^{abc}(t) \tag{2.33}$$

where (considering *linear* flux linkage relations)

$$\boldsymbol{\psi}_s^{abc}(t) = L_s \boldsymbol{i}_s^{abc}(t) + L_m \boldsymbol{i}_r^{abc}(t) \qquad \text{and} \qquad \boldsymbol{\psi}_r^{abc}(t) = L_r \boldsymbol{i}_r^{abc}(t) + L_m \boldsymbol{i}_s^{abc}(t). \tag{2.34}$$

Here $\boldsymbol{u}_s^{abc}(t) = \big(u_s^a(t), u_s^b(t), u_s^c(t)\big)^\top\,[\mathrm{V}]$, $\boldsymbol{u}_r^{abc}(t) = \big(u_r^a(t), u_r^b(t), u_r^c(t)\big)^\top\,[\mathrm{V}]$, $\boldsymbol{i}_s^{abc}(t) = \big(i_s^a(t), i_s^b(t), i_s^c(t)\big)^\top\,[\mathrm{A}]$, $\boldsymbol{i}_r^{abc}(t) = (i_r^a(t), i_r^b(t), i_r^c(t))^\top\,[\mathrm{A}]$, $\boldsymbol{\psi}_s^{abc}(t) = \big(\psi_s^a(t), \psi_s^b(t), \psi_s^c(t)\big)^\top\,[\mathrm{Vs}]$, and $\boldsymbol{\psi}_r^{abc}(t) = \big(\psi_r^a(t), \psi_r^b(t), \psi_r^c(t)\big)^\top\,[\mathrm{Vs}]$ are the stator and rotor voltages, currents and flux linkages, respectively, all in the abc-reference frame (three-phase system). L_s, L_r, and $L_m\,[\mathrm{Vs/A}]$ are the stator, rotor and mutual inductances. $R_s\,[\Omega]$ and $R_r\,[\Omega]$ are stator and rotor winding resistances. The DFIG rotor rotates with mechanical angular frequency $\omega_m(t)\,[\mathrm{rad/s}]$. Hence, for a machine with pole pair number $n_p\,[1]$, the electrical angular frequency of the rotor is given by $\omega_r(t) = n_p\omega_m(t)$ and the rotor reference frame is shifted by the rotor angle $\phi_r(t) = \int_0^t \omega_r(\tau)\mathrm{d}\tau + \phi_r^0$, $\phi_r^0 \in \mathbb{R}$, with respect to the stator reference frame (ϕ_r^0 is the initial rotor angle). Equation (2.33) can be written in the stationary/rotating reference frame as follows $\boldsymbol{x}^k = \boldsymbol{T}_P(\phi)^{-1}\boldsymbol{x}^s = \boldsymbol{T}_P(\phi)^{-1}\boldsymbol{T}_C\boldsymbol{x}^{abc}$ by using the Clarke and Park transformation, respectively, where $\boldsymbol{x}^k = (x^d, x^q)^\top$, and $\boldsymbol{x}^s = (x^\alpha, x^\beta)^\top$. The rotor voltage equation (2.33) with respect to the stationary reference frame (i.e. $\boldsymbol{u}_r^s = \boldsymbol{T}_P(\phi_r)^{-1}\boldsymbol{T}_C\boldsymbol{u}_r^{abc}$) can be expressed as

$$\boldsymbol{u}_s^s(t) = R_s \boldsymbol{i}_s^s(t) + \tfrac{d}{dt}\boldsymbol{\psi}_s^s(t), \qquad \text{and} \qquad \boldsymbol{u}_r^s(t) = R_r \boldsymbol{i}_r^s(t) + \tfrac{d}{dt}\boldsymbol{\psi}_r^s(t) - \omega_r(t)\boldsymbol{J}\boldsymbol{\psi}_r^s(t). \tag{2.35}$$

The flux linkages in the $\alpha\beta$ reference frame can be expressed as follows:

$$\boldsymbol{\psi}_s^s(t) = L_s \boldsymbol{i}_s^s(t) + L_m \boldsymbol{i}_r^s(t) \qquad \text{and} \qquad \boldsymbol{\psi}_r^s(t) = L_r \boldsymbol{i}_r^s(t) + L_m \boldsymbol{i}_s^s(t). \tag{2.36}$$

The stator voltage orientation (SVO) is realized by aligning the d-axis of the synchronous (rotating) reference frame with the stator voltage vector $\boldsymbol{u}_s^s$ which rotates with the stator (grid)

angular frequency ω_s (under ideal conditions, i.e. constant grid frequency $f_0 > 0$, it holds that $\omega_s = 2\pi f_0$ is constant). Applying the (inverse) Park transformation with $\boldsymbol{T}_P(\phi_s)^{-1}$ as in (2.2) with $\phi_s(t) = \int_0^t \omega_s(\tau)\mathrm{d}\tau + \phi_s^0$, $\phi_s^0 \in \mathbb{R}$, to the voltage equations (2.35) yields the description in the rotating reference frame

$$\boldsymbol{u}_s^k(t) = R_s\boldsymbol{i}_s^k(t) + \tfrac{d}{dt}\boldsymbol{\psi}_s^k(t) + \omega_s\boldsymbol{J}\boldsymbol{\psi}_s^k(t), \quad \text{and} \quad \boldsymbol{u}_r^k(t) = R_r\boldsymbol{i}_r^k(t) + \tfrac{d}{dt}\boldsymbol{\psi}_r^k(t) + \omega_{sl}(t)\boldsymbol{J}\boldsymbol{\psi}_r^k(t), \tag{2.37}$$

where $\omega_{sl}(t) := \omega_s - \omega_r(t)$ is the slip angular frequency. Since, e.g., $\boldsymbol{\psi}_s^k = \boldsymbol{T}_P(\phi_s)^{-1}\boldsymbol{\psi}_s^s = \boldsymbol{T}_P(\phi_s)^{-1}\boldsymbol{T}_C\boldsymbol{\psi}_s^{abc}$, the flux linkages are given by

$$\boldsymbol{\psi}_s^k(t) = L_s\boldsymbol{i}_s^k(t) + L_m\boldsymbol{i}_r^k(t) \qquad \text{and} \qquad \boldsymbol{\psi}_r^k(t) = L_r\boldsymbol{i}_r^k(t) + L_m\boldsymbol{i}_s^k(t). \tag{2.38}$$

For a stiff shaft and a step-up gear with ratio $g_r \geq 1$, the dynamics of the mechanical system are given by

$$\tfrac{d}{dt}\omega_m(t) = \tfrac{1}{\Theta}\Big(\underbrace{\tfrac{T_t(t)}{g_r}}_{=:T_m(t)} - T_e(t)\Big), \qquad \omega_m(0) = \omega_m^0 \in \mathbb{R} \tag{2.39}$$

where

$$T_e(t) = \frac{3}{2}n_p\boldsymbol{i}_s^k(t)^\top\boldsymbol{J}\boldsymbol{\psi}_s^k(t) = -\frac{3}{2}n_p\frac{L_m}{L_s}\boldsymbol{i}_r^k(t)^\top\boldsymbol{J}\boldsymbol{\psi}_s^k(t) = \frac{3}{2}n_pL_m\boldsymbol{i}_s^k(t)^\top\boldsymbol{J}\boldsymbol{i}_r^k(t). \tag{2.40}$$

is the electro-magnetic machine torque (moment), $T_t\,[\mathrm{Nm}]$ is the turbine torque produced by the wind and $T_m = \frac{T_t}{g_r}\,[\mathrm{Nm}]$ is the mechanical torque acting on the DFIG shaft. $\Theta\,[\mathrm{kg/m^2}]$ is the rotor inertia and $n_p\,[1]$ is the pole pair number.

2.3.3 Back-to-back converter and DC-Link

As illustrated in Fig. 2.5, the back-to-back converter is connected to the rotor of the DFIG not to the stator like the PMSG. The output voltage of the GSC is the same as given above. For the RSC, the notation is different, therefore the model will be repeated here. The output voltage of the RSC can be expressed as

$$\boldsymbol{u}_r^{abc} = \frac{1}{3}u_{\mathrm{dc}}\boldsymbol{T}^{abc}\boldsymbol{s}_r^{abc}, \tag{2.41}$$

where $\boldsymbol{s}_r^{abc} = (s_r^a, s_r^b, s_r^c)^\top \in \{0,1\}$ is the switching state vector of the RSC. The DC-link dynamics is the same like in (2.28). Only, the expression of DC-current $I_m(t)$ is different and can be written as

$$I_m(t) = \boldsymbol{i}_r^{abc}(t)^\top\boldsymbol{s}_r^{abc}. \tag{2.42}$$

2.4 Laboratory setups

This section describes the constructed test-benches for PMSG and DFIG based variable-speed WECSs, which include the power electronics circuits, PMSG, DFIG, interface circuits, and the real-time system.

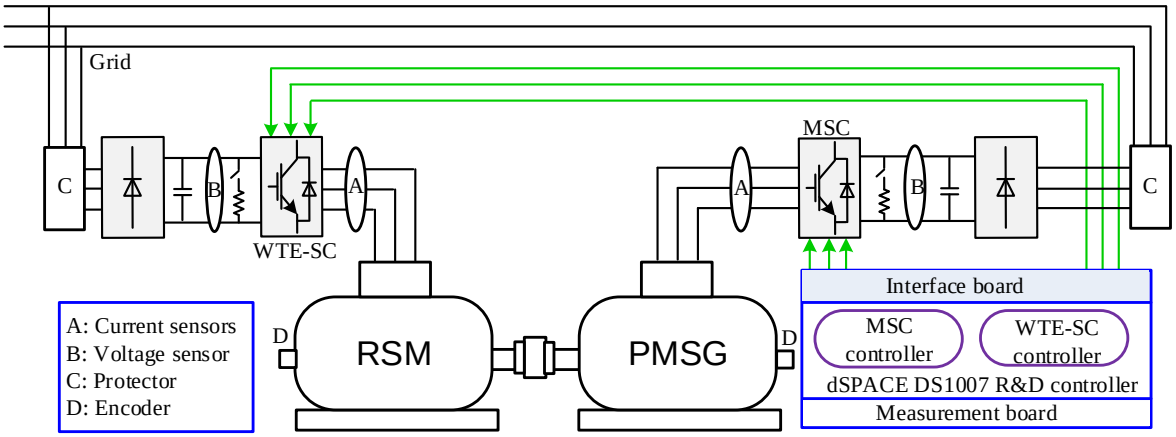

Figure 2.6: Schematic diagram of the laboratory setup for PMSG based variable-speed wind energy conversion systems.

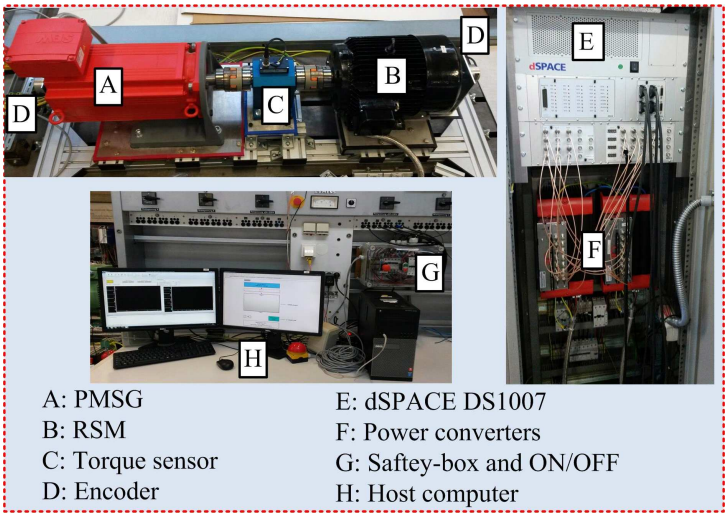

Figure 2.7: Laboratory setup of the PMSG.

2.4.1 Test bench of the PMSG

In reality, the stator of the PMSG is connected to the grid via a two-level back-to-back power converter as illustrated in Fig. 2.2. However, due to limitations in the hardware components, the schematic diagram of the constructed test bench for PMSG is illustrated in Fig. 2.6. The setup consists of a $14.5\,\mathrm{kW}$ PMSG driven by a two-level power converter [machine-side converter (MSC)], which connected to the grid via a three-phase diode rectifier. The DC-link contains a chopper circuit to dissipate the generated power from the PMSG. A $9.5\,\mathrm{kW}$ reluctance synchronous machine (RSM) driven by another two-level power converter, which called wind-turbine emulator side converter (WTE-SC), is employed to emulate the wind turbine dynamics. The RSM is controlled using a nonlinear PI-based FOC technique [37]. The two machines (i.e. PMSG and RSM) are coupled through a torque sensor as illustrated in Fig. 2.7. A dSPACE DS1007 real-time platform with Control Desk and MATLAB/Simulink is utilized for implementing the different control schemes and observers of the PMSG. An incremental encoder

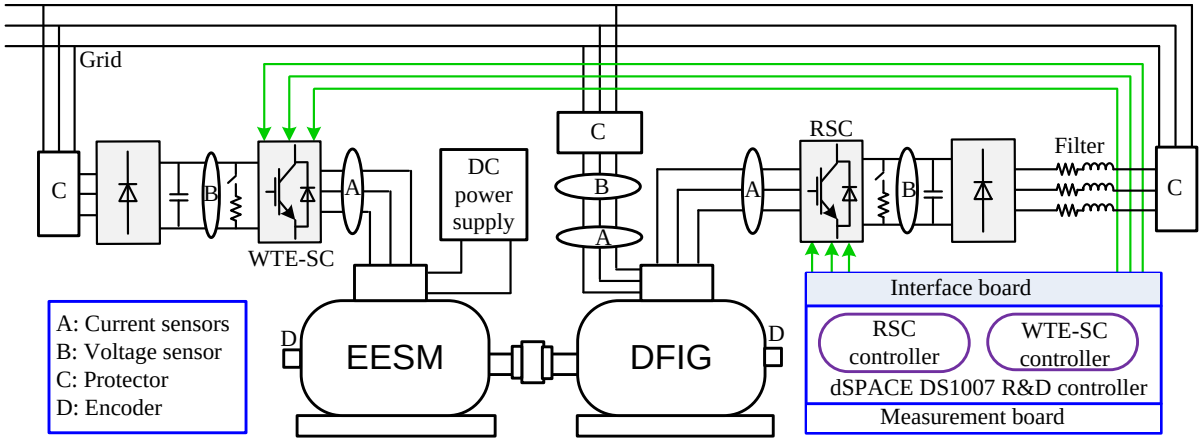

Figure 2.8: Schematic diagram of the laboratory setup for DFIG based variable-speed wind energy conversion systems.

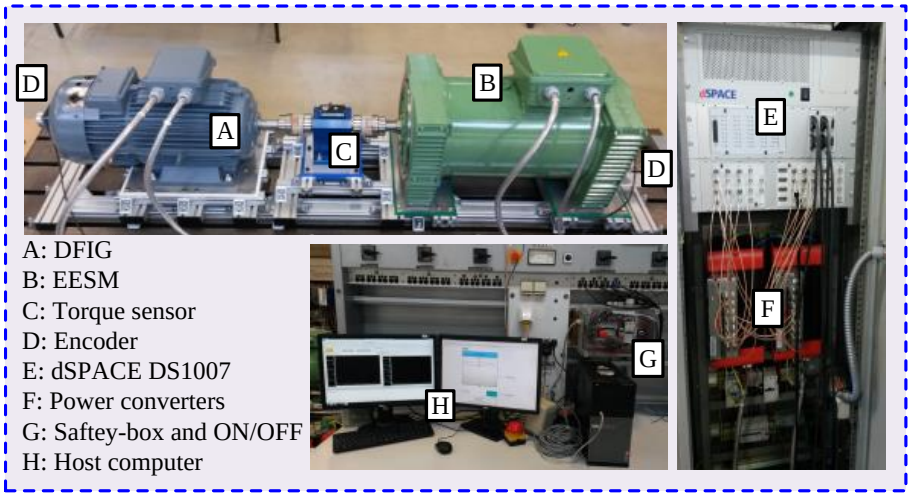

Figure 2.9: Laboratory setup of the DFIG.

with 2048 pulses per revolution (ppr) is used to measure the rotor position of the PMSG, which is fed to dSPACE using a DS3002 incremental encoder board. Three current sensors and one voltage sensor are used to measure the stator currents of the PMSG and the DC-link voltage, respectively. The measured currents and voltage are available in dSPACE via a DS2004 analog to digital converter (A/D) board. The power converters are controlled by dSPACE through a DS5101 pulse-width-modulation board. The constructed test-bench for PMSG is illustrated in Fig. 2.7. Further description of the constructed test bench for PMSG and its parameters are given in Appendix B.

2.4.2 Test bench of the DFIG

Usually, the rotor of the DFIG is tied to the grid via a two-level back-to-back power converter as illustrated in Fig. 2.5. However, due to limitations in the hardware components, the schematic diagram of the constructed test bench for DFIG is illustrated in Fig. 2.8. The setup consists of

$10\,\mathrm{kW}$ DFIG, where the stator of the DFIG is connected directly to the grid, while the rotor is connected to a voltage source converter [Rotor-side converter (RSC)]. Then, the RSC is tied to the grid via a three-phase diode rectifier. The DC-link contains a chopper circuit to dissipate the generated power from the rotor of the DFIG. A $10\,\mathrm{kW}$ electrical-excited synchronous machine (EESM) driven by another two-level power converter, which called wind-turbine emulator side converter (WTE-SC), is employed to emulate the wind turbine dynamics. The EESM is controlled using a PI-based FOC technique. The two machines (i.e. DFIG and EESM) are coupled through a torque sensor as illustrated in Fig. 2.9. The dSPACE DS1007 real-time platform with Control Desk and MATLAB/Simulink is utilized for implementing the different control schemes and observers of the DFIG. An incremental encoder with 2048 pulses per revolution (ppr) is used to measure the rotor position of the DFIG, which is fed to dSPACE using a DS3002 incremental encoder board. Six current sensors and four voltage sensor are used to measure the stator/rotor currents of the DFIG and the DC-link voltage/stator voltages of the DFIG, respectively. The measured currents and voltages are available in dSPACE via a DS2004 analog to digital converter (A/D) board. The power converters are controlled by dSPACE through a DS5101 pulse-width-modulation board. The constructed test-bench for DFIG is illustrated in Fig. 2.9. Further description of the constructed test bench for DFIG and its parameters are given in Appendix B.

2.5 Simulink models

This section describes the simulation models of the PMSG and DFIG based variable-speed WECSs, which have been implemented in Matlab/Simulink.

2.5.1 Simulation model of the PMSG

A $20\,\mathrm{kW}$ WECS with PMSG is implemented in Matlab/Simulink. The system parameters are given in Appendix B and the implementation is illustrated in Fig. 2.2.

2.5.2 Simulation model of the DFIG

A simulation model of a $50\,\mathrm{kW}$ WECS with DFIG is implemented in Matlab/Simulink. The system parameters are listed in Appendix B and the implementation is illustrated in Fig. 2.5.

2.6 Summary

In this chapter, the mathematical symbols used in this dissertation are summarized. Furthermore, the mathematical basics of the system modeling are explained, which incorporates coordinate transformations, and continuous/discrete time system descriptions. The mathematical models for both the PMSG/DFIG in variable-speed wind turbine systems are developed in details. Finally, the laboratory set-ups of the PMSG and DFIG for validation of the proposed speed/position observers and control algorithms are described. Moreover, the simulink models for PMSG and DFIG are highlighted.

CHAPTER 3

Conventional control systems

This chapter describes and summarizes the classical control techniques for PMSG and DFIG based variable-speed WECSs, which include:

- **Conventional control schemes for PMSG**
  - **Field-oriented-control (FOC)** for the machine-side converter (MSC) and **voltage-oriented control (VOC)** for the grid side converter (GSC). All with space-vector modulator (SVM), see Sec. 3.2.1.
  - **Deadbeat predictive control (DBPC)** for MSC and GSC with SVM, see Sec. 3.2.2.
  - **Direct-model predictive current control (DMPCC)** for MSC and GSC without modulator, see Sec. 3.2.3.
- **Conventional control schemes of DFIG**
  - **Voltage-oriented control (VOC)** for the rotor-side converter (RSC) and GSC, both with SVM, see Sec. 3.3.1.
  - **Deadbeat predictive control (DBPC)** for RSC and GSC with SVM, see Sec. 3.3.2.
  - **Direct-model predictive current control (DMPCC)** for RSC and GSC without modulator, see Sec. 3.3.3.

Their basic principles are explained and discussed. The digital realizations of those control schemes are presented in details and the performances are evaluated with experimental data (Sec. 3.4) and simulation (Sec. 3.5). Finally, the chapter is summarized in Sec. 3.6.

3.1 Introduction

A controller which gives a continuous actuation signal requires a modulator to generate the gate signals of the power converters' switches. Two well-known modulators can be used for

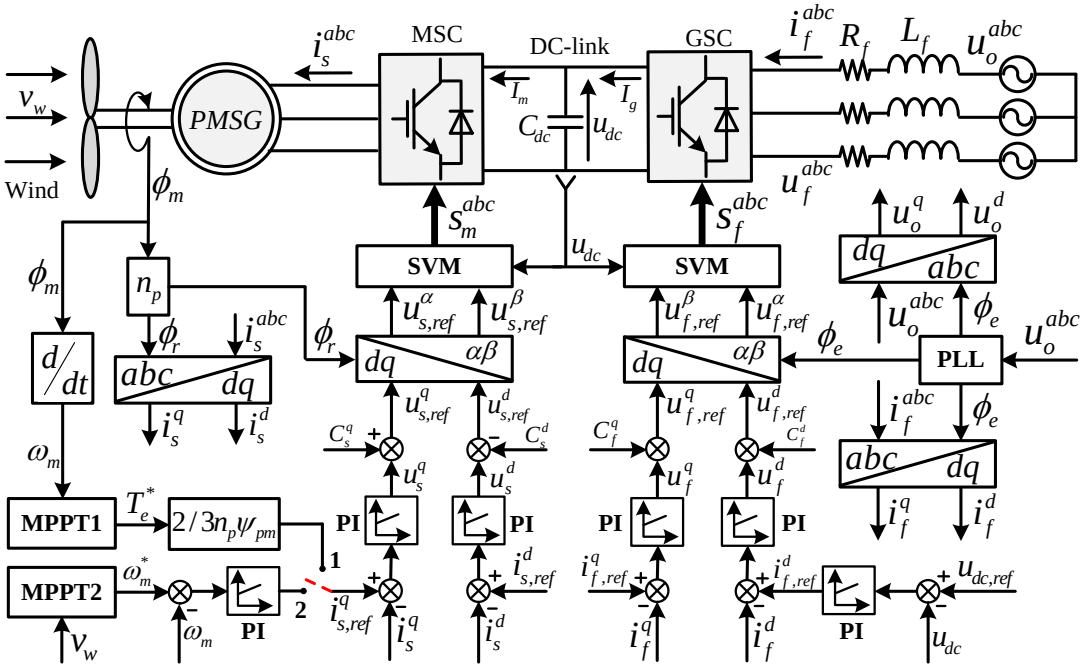

Figure 3.1: Schematic diagram of the field and voltage oriented control schemes for PMSGs.

such purpose: 1) Pulse-width modulator (PWM), and 2) space vector modulator (SVM). SVM have the advantages of better DC-link utilization, smaller total harmonic distortions (THDs), and ease for embedded system realizations. Accordingly, SVM is utilized in this work. As the SVM is already a well-known technique, its design and implementation are not presented in this dissertation.

3.2 Conventional control schemes for PMSG

In this section, FOC, VOC, DBPC, and DMPCC for PMSGs will be explained in details.

3.2.1 Field and voltage oriented control for PMSG

The basic concept of VOC/FOC is the so-called *vector orientation*, which is achieved by transferring the system to a *synchronously rotating* frame [38]–[40]. Accordingly, the control variables will be *DC components* and the inner part of the system (both the grid and machine sides) can be simplified as a one-order system. For such system, proportional integration (PI) controller can achieve good dynamic/steady-state performances. In the following sections, system dynamics of both the machine and grid sides in the synchronously rotating frame are revisited to ease the controller descriptions. Their respective controller design processes are briefly presented.

3.2.1.1 Field-oriented control for MSC

The FOC of the MSC consists of two loops [38]–[40]: 1) Inner (current) control loop, and 2) outer (speed) control loop as shown in Fig. 3.1.

1) Inner (current) control loop: The dynamics of the stator currents of the PMSG can be obtained be inserting (2.23) into (2.21), which is solved for $\frac{d}{dt}\boldsymbol{i}_s^k$ leading to [41]

$$\left.\begin{aligned}\tfrac{d}{dt}i_s^d(t) &= -\tfrac{R_s}{L_s}i_s^d(t) + \omega_r(t)i_s^q(t) + \tfrac{1}{L_s}u_s^d(t)\\ \tfrac{d}{dt}i_s^q(t) &= -\tfrac{R_s}{L_s}i_s^q(t) - \omega_r i_s^d(t) - \tfrac{\omega_r(t)}{L_s}\psi_{pm} + \tfrac{1}{L_s}u_s^q(t).\end{aligned}\right\} \tag{3.1}$$

Rearranging (3.1), gives the PMSG' stator voltage in the dq-frame, as

$$\left.\begin{aligned}u_s^d(t) + \underbrace{\omega_r(t)L_s i_s^q(t)}_{C_s^d(t)} &= L_s\tfrac{d}{dt}i_s^d(t) + R_s i_s^d(t),\\ u_s^q(t) - \underbrace{\omega_r(t)(L_s i_s^d(t) + \psi_{pm})}_{C_s^q(t)} &= L_s\tfrac{d}{dt}i_s^q(t) + R_s i_s^q(t).\end{aligned}\right\} \tag{3.2}$$

By neglecting the compensation terms $C_s^d(t)$ and $C_s^q(t)$, the transfer function $\boldsymbol{TF}_s^i(S)$ between the currents $\boldsymbol{I}_s^{dq}(S)$ and their control voltages $\boldsymbol{U}_s^{dq}(S)$ can be expressed as

$$\boldsymbol{TF}_s^i(S) = \frac{I_s^d(S)}{U_s^d(S)} = \frac{I_s^q(S)}{U_s^q(S)} = \frac{1}{R_s + L_s S}. \tag{3.3}$$

The currents $I_s^d(S)$ and $I_s^q(S)$ are DC variables due to the transformation to the dq-frame. Accordingly, a proportional-integral (PI) controller with the following transfer function

$$\boldsymbol{TF}_{PI}^i(S) = K_{PI}^i\frac{1 + ST_{PI}^i}{ST_{PI}^i}. \tag{3.4}$$

can be employed for making the currents (i.e. $I_s^d(S)$ and $I_s^q(S)$) follow the reference values with a zero steady-state tracking error. In (3.4), K_{PI}^i and T_{PI}^i are the gain and time constant of the PI controller. These PI controllers produce the control voltages $\boldsymbol{u}_s^{dq}$. Then, the compensation terms $C_s^d(t)$ and $C_s^q(t)$ will be added to those voltages as

$$\left.\begin{aligned}u_{s,ref}^d(t) &= u_s^d(t) - \omega_r(t)L_s i_s^q(t),\\ u_{s,ref}^q(t) &= u_s^q(t) + \omega_r(t)(L_s i_s^d(t) + \psi_{pm}).\end{aligned}\right\} \tag{3.5}$$

Finally, the SVM produces the switching signals of the MSC according to the reference voltages $u_{s,ref}^d(t)$ and $u_{s,ref}^d(t)$ as shown in Fig. 3.1.

2) Outer (speed) control loop: The outer (speed) control loop for PMSGs in wind turbine application can be implemented in two different ways: i) Non-linear speed controller, and ii) linear (PI) speed controller.

i) Non-linear speed controller This control technique is based on calculating the reference electro-magnetic torque $T_e^\star$ from (2.15). Invoking (2.24) and neglecting ν, the dynamics of the mechanical system can be expressed as

$$\frac{d}{dt}\omega_m(t) = \frac{1}{\Theta}(T_m(t) - k_p^\star\omega_m^2). \tag{3.6}$$

The mechanical torque T_m of the wind turbine can be calculated as

$$T_m = \frac{p_t}{\omega_m} = \frac{1}{2}\rho\pi r_t^5 \frac{c_p}{(\lambda)^3}\omega_m^2. \tag{3.7}$$

Inserting (3.7) into (3.6), gives

$$\frac{d}{dt}\omega_m(t) = \frac{1}{2}\frac{1}{\Theta}\rho\pi r_t^5 \omega_m^2 \left(\frac{c_p}{(\lambda)^3} - \frac{c_p^\star}{(\lambda^\star)^3}\right). \tag{3.8}$$

Since the rotor inertia Θ, air density ρ, rotor radius r_t, and squared rotor speed ω_m^2 are positive, the sign of $\frac{d}{dt}\omega_m(t)$ depends on the sign of the difference in (3.8). In one hand, when the tip-speed ratio $\lambda > \lambda^\star$, c_p will be lower than $c_p^\star$ and $\frac{d}{dt}\omega_m(t)$ will be negative. Accordingly, the rotor decelerates toward $\lambda = \lambda^\star$. On the other hand, when $\lambda < \lambda^\star$, $\frac{d}{dt}\omega_m(t)$ will be positive positive. Therefore, the rotor accelerates toward $\lambda = \lambda^\star$. Finally, when $\lambda = \lambda^\star$, c_p will be equal to $c_p^\star$ and $\frac{d}{dt}\omega_m(t)$ will be zero, i.e the rotor will rotate at constant speed and the maximum power from the wind turbine will be generated.
Finally, the reference value of the q-axis current $i_{s,ref}^q$ can be computed from the reference electro-magnetic torque $T_e^\star$ as follows

$$i_{s,ref}^q = \frac{2}{3}\frac{T_e^\star}{n_p\psi_{pm}}. \tag{3.9}$$

ii) Linear (PI) speed controller This control method is based on calculating the optimal rotor speed $\omega_m^\star$ from (2.16) and then a PI controller will be employed to make the actual rotor speed ω_m follow its optimal value $\omega_m^\star$. The dynamics of the mechanical system in Laplace domain can be driven from (2.24) as

$$S\Omega_m(S) = \frac{1}{\Theta}(T_m(S) - T_e(S) + \nu\Omega_m(S) \tag{3.10}$$

Similarly, the speed loop transfer function $TF_s^{\omega_m}(S)$ can be expressed as

$$TF_s^{\omega_m}(S) = \frac{\Omega_m}{T_m(S) - T_e(S)} = \frac{1}{\Theta S + \nu}. \tag{3.11}$$

It can be observed that the transfer function between the rotor speed of the PMSG and the input torque is again one-order system. Accordingly, a PI controller with the following transfer function

$$\boldsymbol{TF}_{PI}^{\omega_m}(S) = K_{PI}^{\omega_m}\frac{1 + ST_{PI}^{\omega_m}}{ST_{PI}^{\omega_m}}. \tag{3.12}$$

can be used for regulating the rotor speed. In (3.12), $K_{PI}^{\omega_m}$ and $T_{PI}^{\omega_m}$ are the gain and time constant of the PI controller. The output of the PI controller is the reference electro-magnetic torque $T_e^\star$. Note that, the output of the PI controller can also be regarded as $i_{s,ref}^q$ since the difference between the torque and the current is simply a constant [27, 41, 42], see (3.9).

The two methods for controlling the rotor speed of the PMSG are illustrated in Fig. 3.1.

3.2.1.2 Voltage-oriented control for GSC

The VOC of the GSC consists of two loops [27, 41, 42]: 1) Inner (current) control loop, and 2) outer (voltage) control loop as shown in Fig. 3.1.

1) Inner (current) control loop: The dynamics of the GSC can be obtain from (2.32) as

$$\left.\begin{aligned} u_f^d(t) + \underbrace{u_o^d(t) - \omega_e(t) L_f i_f^q(t)}_{C_f^d(t)} &= -\big(L_f \tfrac{d}{dt} i_f^d(t) + R_f i_f^d(t)\big), \\ u_f^q(t) + \underbrace{u_o^q(t) + \omega_e(t) L_f i_f^d(t)}_{C_f^q(t)} &= -\big(L_f \tfrac{d}{dt} i_f^q(t) + R_f i_f^q(t)\big). \end{aligned}\right\} \tag{3.13}$$

Similarly to the MSC, by neglecting the compensation terms $C_f^d(t)$ and $C_f^q(t)$, the transfer function $\boldsymbol{TF}_f^i(S)$ between the currents $\boldsymbol{I}_f^{dq}(S)$ and their control voltages $\boldsymbol{U}_f^{dq}(S)$ can be expressed as

$$\boldsymbol{TF}_f^i(S) = \frac{I_f^d(S)}{U_f^d(S)} = \frac{I_f^q(S)}{U_f^q(S)} = \frac{1}{R_f + L_f S}. \tag{3.14}$$

Accordingly, a PI controller with the following transfer function,

$$\boldsymbol{TF}_{PI}^{i_f}(S) = K_{PI}^{i_f} \frac{1 + S T_{PI}^{i_f}}{S T_{PI}^{i_f}}, \tag{3.15}$$

can be employed for regulating the currents i_f^d and i_f^q. In (3.15), $K_{PI}^{i_f}$ and $T_{PI}^{i_f}$ are the gain and time constant of the PI controller. These PI controller produce the control voltages $\boldsymbol{u}_f^{dq}$. Then, the compensation terms $C_f^d(t)$ and $C_f^q(t)$ will be added to those voltages as

$$\left.\begin{aligned} u_{f,ref}^d(t) &= u_f^d(t) - u_o^d(t) + \omega_e(t) L_f i_f^q(t), \\ u_{f,ref}^q(t) &= u_f^q(t) - u_o^q(t) - \omega_e(t) L_f i_f^d(t). \end{aligned}\right\} \tag{3.16}$$

Finally, the SVM produces the switching signals of the GSC according to the reference voltages $u_{f,ref}^d(t)$ and $u_{f,ref}^d(t)$ as shown in Fig. 3.1.

2) Outer (voltage) control loop: Considering the current flow in the DC-link that illustrated in Fig. 3.1, the DC-link dynamics can be expressed as

$$I_{dc} = C_{dc} \frac{du_{dc}}{dt} = I_g - I_m. \tag{3.17}$$

Furthermore, by considering an ideal GSC, the power in the AC side of the GSC is equal to the power of the DC side as

$$u_{dc} I_g = \frac{3}{2}\left(u_f^d i_f^d + u_f^q i_f^q\right). \tag{3.18}$$

The GSC is controlled by aligning the d-axis of the rotating reference frame with the grid voltage vector, and accordingly, $u_f^d = \hat{u}_o$ and $u_f^q = 0$. Inserting the value of I_g from (3.17) into (3.18) gives

$$u_{dc}\left(C_{dc} \frac{du_{dc}}{dt} + I_m\right) = \frac{3}{2} \hat{u}_o i_f^d. \tag{3.19}$$

Re-arranging (3.19) and considering the current I_m as a disturbance, the dynamics of the DC-link voltage can be written as

$$\frac{du_{dc}}{dt} = \frac{3}{2}\frac{1}{C_{dc}}\frac{\hat{u}_o}{u_{dc}}i_f^d. \tag{3.20}$$

In (3.20), assuming $\hat{u}_o = u_{dc}/2$, the transfer function of the DC-link voltage $TF_f^{u_{dc}}$ can be expressed as

$$TF_f^{u_{dc}}(S) = \frac{U_{dc}(s)}{I_f^d(S)} = \frac{3}{4}\frac{1}{C_{dc}S}. \tag{3.21}$$

Therefore, a PI controller with the following transfer function,

$$\boldsymbol{TF}_{PI}^{u_{dc}}(S) = K_{PI}^{u_{dc}}\frac{1+ST_{PI}^{u_{dc}}}{ST_{PI}^{u_{dc}}}, \tag{3.22}$$

can be employed for regulating the DC-link voltage. In (3.22), $K_{PI}^{u_{dc}}$ and $T_{PI}^{u_{dc}}$ are the gain and time constant of the PI controller. The output of this PI controller is the reference value of the d-axis current $i_{f,ref}^d$, which is an input of the inner (current) control loop as illustrated in Fig. 3.1.

3.2.2 Deadbeat Control for PMSG

Deadbeat control aims to manipulate the system to fully reach certain references in a finite number of control intervals (ideally in one sampling period) by assigning to the plant (i.e voltage source converter) an input (e.g., reference voltage vector). The deadbeat control uses the discrete system model to compute the input of the plants and due to the delay in the digital controller, one step state prediction is required. Therefore, it is also called *predictive control* in some publications. The deadbeat predictive control gives a continuous output, and accordingly, a modulator is essential to generate the switching signals of the power converter. In the following sections, the deadbeat current control scheme for the MSC and GSC is presented.

3.2.2.1 Deadbeat current control for MSC

The objective of the deadbeat current controller is to manipulate the current to reach its reference value until the end of (one or several) sampling period(s) [43]–[45]. The main idea is to calculate the required input of the power converter/plant from the discrete system model. Inserting (2.23) into (2.21) and using Euler-forward discretization, the discrete-time model can be written as [46]

$$\left.\begin{aligned} u_s^d[k] &= R_s i_s^d[k] + L_s\tfrac{i_s^d[k+1]-i_s^d[k]}{T_s} - \omega_r[k]L_s i_s^q[k], \\ u_s^q[k] &= R_s i_s^q[k] + L_s\tfrac{i_s^q[k+1]-i_s^q[k]}{T_s} + \omega_r[k]L_s i_s^d[k] + \omega_r[k]\psi_{pm}, \end{aligned}\right\} \tag{3.23}$$

where k is the current sampling instant and T_s is the sampling time. The aim of the deadbeat control system is to find a reference voltage vector $\boldsymbol{u}_{s,ref}^{dq}[k] = (u_{s,ref}^d[k], u_{s,ref}^q[k])^\top$, which renders the predicted current vector $\boldsymbol{i}_s^{dq}[k+1] = (i_s^d[k+1], i_s^q[k+1])^\top$ equal or close to the reference current vector $\boldsymbol{i}_{s,ref}^{dq}[k+1] = (i_{s,ref}^d[k+1], i_{s,ref}^q[k+1])^\top$ in the next sampling instant.

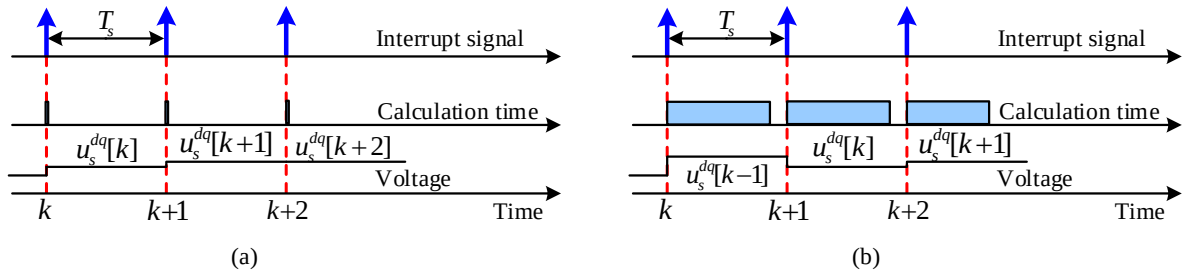

Figure 3.2: Timing sequence of the discrete-time current controller [47] (from top to bottom): Interrupt signal, calculation time, and stator voltage of the PMSG): (a) Ideal case, and (b) real case.

According to the DB principles [43]–[45], the reference voltage vector $\boldsymbol{u}_{s,ref}^{dq}[k]$ can be calculated directly by replacing the predicted currents $\boldsymbol{i}_s^{dq}[k+1]$ by the reference currents $\boldsymbol{i}_{s,ref}^{dq}[k+1]$ in (3.23) as follows

$$\left.\begin{aligned} u_{s,ref}^{d}[k] &= R_s i_s^d[k] + L_s \frac{i_{s,ref}^{d}[k+1]-i_s^d[k]}{T_s} - \omega_r[k] L_s i_s^q[k], \\ u_{s,ref}^{q}[k] &= R_s i_s^q[k] + L_s \frac{i_{s,ref}^{q}[k+1]-i_s^q[k]}{T_s} + \omega_r[k] L_s i_s^d[k] + \omega_r[k]\psi_{pm}. \end{aligned}\right\} \tag{3.24}$$

For the ideal case [47], the calculation time of the reference voltage vector $\boldsymbol{u}_{s,ref}^{dq}[k]$ is almost zero as shown in Fig. 3.2a. Therefore, at the current sampling instant k, the reference voltage $\boldsymbol{u}_{s,ref}^{dq}[k]$ is calculated and immediately applied. For the real case, the digital signal processor (DSP) needs some time to compute the reference voltage vector $\boldsymbol{u}_{s,ref}^{dq}[k]$ as seen in Fig. 3.2b, and accordingly, the voltage vector of the previous sampling instant $\boldsymbol{u}_{s,ref}^{dq}[k-1]$ is still applied in the current sampling instant k. The reference voltage $\boldsymbol{u}_{s,ref}^{dq}[k]$ is calculated at the current sampling instant k and applied in the next sampling instant $k+1$ as shown in Fig. 3.2b, and accordingly, a one-step sampling delay is inevitable. Therefore, in order to compensate this delay [44, 47], (3.24) is modified to

$$\left.\begin{aligned} u_{s,ref}^{d}[k+1] &= R_s i_s^d[k+1] + L_s \frac{i_{s,ref}^{d}[k+2]-i_s^d[k+1]}{T_s} - \omega_r[k+1] L_s i_s^q[k+1], \\ u_{s,ref}^{q}[k+1] &= R_s i_s^q[k+1] + L_s \frac{i_{s,ref}^{q}[k+2]-i_s^q[k+1]}{T_s} + \omega_r[k+1]\big(L_s i_s^d[k+1] + \psi_{pm}\big). \end{aligned}\right\} \tag{3.25}$$

In (3.25), at the current sampling instant k, the voltages for the next sampling instant $k+1$ are calculated. Therefore, the correct voltages will be applied in the next sampling instant. However, correct prediction of the currents $i_s^d[k+1]$ and $i_s^q[k+1]$ is essential. Using a Smith predictor [44], the currents $i_s^d[k+1]$ and $i_s^q[k+1]$ can be predicted from (3.24) as follows

$$\left.\begin{aligned} i_s^d[k+1] &= (1-\tfrac{T_s R_s}{L_s}) i_s^d[k] + T_s \omega_r[k] i_s^q[k] + \tfrac{T_s}{L_s} u_s^d[k], \\ i_s^q[k+1] &= (1-\tfrac{T_s R_s}{L_s}) i_s^q[k] - T_s \omega_r[k] i_s^q[k] - T_s \omega_r[k]\psi_{pm} + \tfrac{T_s}{L_s} u_s^q[k]. \end{aligned}\right\} \tag{3.26}$$

Then, the reference currents

$$i_{s,ref}^{dq}[k+2] = 3 i_{s,ref}^{dq}[k] - 3 i_{s,ref}^{dq}[k-1] + i_{s,ref}^{dq}[k-2] \tag{3.27}$$

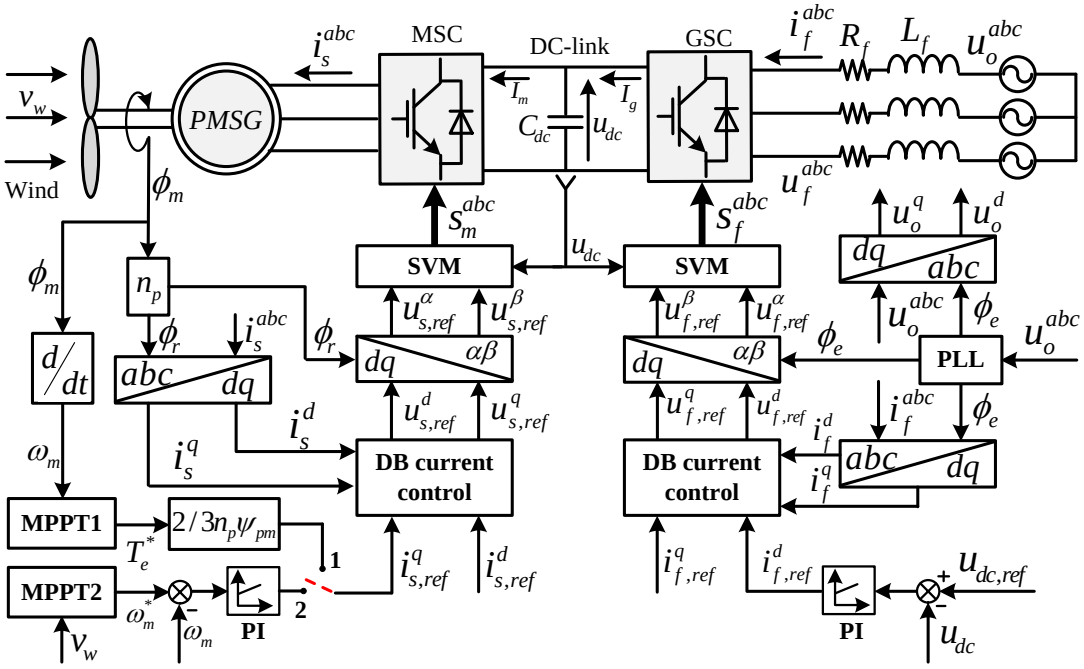

Figure 3.3: Schematic diagram of the deadbeat predictive control scheme for PMSGs.

are calculated using Lagrange extrapolation. The rotor speed $\omega_r[k+1]$ can be calculated using also Lagrange extrapolation as follows

$$\omega_r[k+1] = 2\omega_r[k] - \omega_r[k-1]. \tag{3.28}$$

The schematic diagram of the deadbeat predictive current control for MSC is illustrated in Fig 3.3.

3.2.2.2 *Deadbeat current control for GSC*

Applying Euler-forward discretization method to the continuous-time model in (2.32) gives the discrete-time model of the GSC and output filter as [46]

$$\left.\begin{aligned} u_f^d[k] &= -R_f i_f^d[k] - L_f \tfrac{i_f^d[k+1]-i_f^d[k]}{T_s} + \omega_e L_f i_f^q[k] + u_o^d[k], \\ u_f^q[k] &= -R_f i_f^q[k] - L_f \tfrac{i_f^q[k+1]-i_f^q[k]}{T_s} - \omega_e L_f i_f^d[k] + u_o^q[k]. \end{aligned}\right\} \tag{3.29}$$

Similarly to the MSC, considering the one-sample delay due to the digital controller, the reference voltage vector $\boldsymbol{u}_{f,ref}^{dq}[k+1]$ can be calculated as follows

$$\left.\begin{aligned} u_{f,ref}^d[k+1] &= -R_f i_f^d[k+1] - L_f \tfrac{i_{f,ref}^d[k+2]-i_f^d[k+1]}{T_s} + \omega_e L_f i_f^q[k+1] + u_o^d[k+1], \\ u_{f,ref}^q[k+1] &= -R_f i_f^q[k+1] - L_f \tfrac{i_{f,ref}^q[k+2]-i_f^q[k+1]}{T_s} - \omega_e L_f i_f^d[k+1] + u_o^q[k+1]. \end{aligned}\right\} \tag{3.30}$$

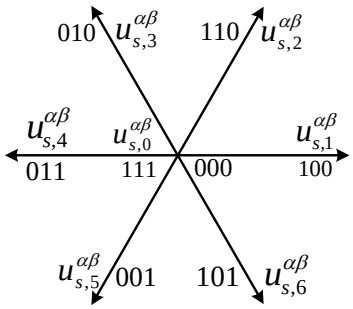

Figure 3.4: All the candidates VVs for 2-level power converter.

The currents $i_f^d[k+1]$ and $i_f^q[k+1]$ can be predicted as

$$\left.\begin{array}{rcl} i_f^d[k+1] & = & (1-\frac{T_s R_f}{L_f})i_f^d[k] + \omega_e T_s i_f^q[k] + \frac{T_s}{L_f}(u_o^d[k] - u_f^d[k]), \\ i_f^q[k+1] & = & (1-\frac{T_s R_f}{L_f})i_f^q[k] - \omega_e T_s i_f^d[k] + \frac{T_s}{L_f}(u_o^q[k] - u_f^q[k]). \end{array}\right\} \quad (3.31)$$

The currents $i_{f,ref}^d[k+2]$ and $i_{f,ref}^q[k+2]$ can be computed using Lagrange extrapolation as explained in the above section. The schematic diagram of the deadbeat predictive current control for GSC is illustrated in Fig 3.3.

3.2.3 Direct-model predictive current control for PMSG

Predictive control presents several advantages [20]–[24]: Concepts are intuitive and easy to understand, it can be applied to a variety of systems, constraints and nonlinearities can be easily included, and the multi-variable case can be considered. The MPC techniques have been classified into two main categories: continuous control set (CCS-MPC) and finite control set MPC (FCS-MPC), also called direct-model predictive control (DMPC). In the first group, a modulator generates the switching states, starting from the continuous output of the predictive controller. On the other hand, the FCS-MPC approach takes advantage of the limited number of switching states of the power converter for solving the optimization problem. A discrete model is used to predict the behavior of the system for every admissible actuation sequence. The switching action that minimizes a predefined cost function is finally selected to be applied in the next sampling instant. The main advantage of FCS-MPC lies in the direct application of the control action to the converter, without requiring a modulation stage. In the following sections, the direct-model predictive current control (DMPCC) for the MSC and GSC is presented.

3.2.3.1 Direct-model predictive current control for MSC

The DMPC approach uses a discrete-time model for the prediction of the currents at a future sample period. Furthermore, the one sample delay due to the digital controller that explained in the above section must be considered. Accordingly, the prediction model can be expressed as [23]

$$\left.\begin{array}{rcl} i_s^d[k+2] & = & (1-\frac{T_s R_s}{L_s})i_s^d[k+1] + \omega_r[k+1]T_s i_s^q[k+1] + \frac{T_s}{L_s}u_s^d[k+1], \\ i_s^q[k+2] & = & (1-\frac{T_s R_s}{L_s})i_s^q[k+1] - \omega_r[k+1]T_s i_s^d[k+1] - \frac{T_s}{L_s}\omega_r[k+1]\psi_{pm} + \frac{T_s}{L_s}u_s^d[k+1]. \end{array}\right\} \quad (3.32)$$

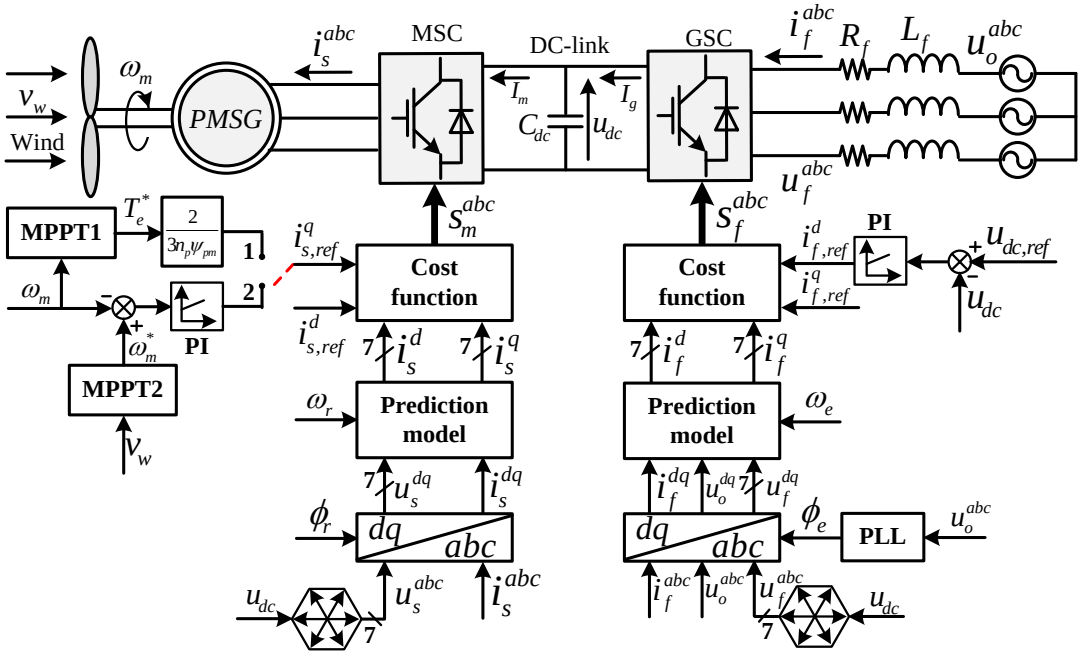

Figure 3.5: Schematic diagram of the DMPCC scheme for PMSGs.

In (3.32), $u_s^{dq}[k+1]$ is the actuation in the next sampling instant to be evaluated and the currents $i_s^d[k+1]$ and $i_s^q[k+1]$ can be computed from (3.26).

For two-level power converter, Considering all the possible combinations of the switching state vector $\boldsymbol{s}_m^{abc}$ or $\boldsymbol{s}_f^{abc}$: eight switching states, and consequently, eight voltage vectors (VVs) are obtained (Note that two *different* zero voltage vectors are available.), see Fig. 3.4. Accordingly, the stator voltage can be expressed as

$$\boldsymbol{u}_s^{dq}[k+1] = \underbrace{\begin{bmatrix} \cos(\phi_r) & \sin(\phi_r) \\ -\sin(\phi_r) & \cos(\phi_r) \end{bmatrix}}_{=:\boldsymbol{T}_P(\phi_r)^{-1}} \underbrace{\frac{2}{3}\begin{bmatrix} 1 & -\frac{1}{2} & -\frac{1}{2} \\ 0 & \frac{\sqrt{3}}{2} & -\frac{\sqrt{3}}{2} \end{bmatrix}}_{=:\boldsymbol{T}_C} \underbrace{\frac{1}{3}u_{dc}[k]\begin{bmatrix} 2 & -1 & -1 \\ -1 & 2 & -1 \\ -1 & -1 & 2 \end{bmatrix}\boldsymbol{s}_m^{abc}[k+1]}_{=:\boldsymbol{u}_s^{abc}[k+1]}, \tag{3.33}$$

Using those seven VVs and the prediction model (3.32), seven different values of the currents can be predicted. Then, a quality function in the form,

$$g_{MSC} = \left|i_{s,ref}^d[k+2] - i_s^d[k+2]\right| + \left|i_{s,ref}^q[k+2] - i_s^q[k+2]\right|, \tag{3.34}$$

is evaluated for each VV. Finally, the VV, which its prediction minimizes the cost function, is selected and applied in the next sampling instant. The schematic diagram of the direct-model predictive current control for MSC is shown in Fig 3.5.

3.2.3.2 *Direct-model predictive current control for GSC*

Similarly to the MSC, the prediction model can be expressed as follows

$$\left.\begin{array}{rcl} i_f^d[k+2] & = & (1-\frac{T_s R_f}{L_f})i_f^d[k+1]+\omega_e[k+1]T_s i_f^q[k+1]+\frac{T_s}{L_f}(u_o^d[k+1]-u_f^d[k+1]), \\ i_f^q[k+2] & = & (1-\frac{T_s R_f}{L_f})i_f^q[k+1]-\omega_e[k+1]T_s i_f^d[k+1]+\frac{T_s}{L_f}(u_o^q[k+1]-u_f^q[k+1]). \end{array}\right\} \tag{3.35}$$

The cost function of the GSC can be written as

$$g_{GSC} = \left|i_{f,ref}^d[k+2]-i_f^d[k+2]\right| + \left|i_{f,ref}^q[k+2]-i_f^q[k+2]\right|. \tag{3.36}$$

Again, (3.35) is evaluated for each of the possible seven voltage vectors, giving seven different current predictions. The voltage vector whose current prediction is minimizing the cost function (3.36) will be applied at the next sampling period. The schematic diagram of the direct-model predictive current control for GSC is shown in Fig 3.5.

3.3 Conventional control schemes for DFIG

In this section, the different control schemes for DFIGs in variable-speed wind turbines will be detailed.

3.3.1 Voltage-oriented control for DFIG

In this section the VOC for RSC will be presented. For the GSC, the VOC is the same like that of the GSC in PMSGs, see Sec 3.2.1. Therefore, the VOC of the GSC in DFIGs will not repeated here again.

3.3.1.1 *Voltage-oriented control for RSC*

Similarly to the PMSG, the VOC of the RSC consists of two loops: 1) Inner (current) control loop, and 2) outer (speed) control loop as shown in Fig. 3.6.
1) Inner (current) control loop: By substituting the value of $\boldsymbol{\psi}_r^k(t)$ from (2.38) in (2.37), the rotor voltage of the DFIG $\boldsymbol{u}_r^k(t)$ can be expressed as [48]

$$\boldsymbol{u}_r^k(t) = R_r\boldsymbol{i}_r^k(t)+L_r\tfrac{d}{dt}\boldsymbol{i}_r^k(t)+L_m\tfrac{d}{dt}\boldsymbol{i}_s^k(t)+\omega_{sl}(t)L_r\boldsymbol{J}\boldsymbol{i}_r^k(t)+\omega_{sl}(t)L_m\boldsymbol{J}\boldsymbol{i}_s^k(t) \tag{3.37}$$

From (2.38), the stator current $\boldsymbol{i}_s^k(t)$ can be written as

$$\boldsymbol{i}_s^k(t) = \tfrac{1}{L_s}\boldsymbol{\psi}_s^k(t)-\tfrac{L_m}{L_s}\boldsymbol{i}_r^k(t) \tag{3.38}$$

substitute (3.38) in (3.37) yields

$$\boldsymbol{u}_r^k(t) = R_r\boldsymbol{i}_r^k(t)+\sigma L_r\tfrac{d}{dt}\boldsymbol{i}_r^k(t)+\tfrac{L_m}{L_s}\tfrac{d}{dt}\boldsymbol{\psi}_s^k(t)+\omega_{sl}(t)\sigma L_r\boldsymbol{J}\boldsymbol{i}_r^k(t)+\omega_{sl}(t)\tfrac{L_m}{L_s}\boldsymbol{J}\boldsymbol{\psi}_s^k(t). \tag{3.39}$$

where $\sigma = 1-\frac{L_m^2}{L_s L_r}$. Substituting $\frac{d}{dt}\boldsymbol{\psi}_s^k(t)$ from (2.37) and $\boldsymbol{\psi}_s^k(t)$ from (2.38) in (3.39) gives

$$\boldsymbol{u}_r^k(t) = R_r\boldsymbol{i}_r^k(t)+\sigma L_r\tfrac{d}{dt}\boldsymbol{i}_r^k(t)+(\omega_{sl}(t)L_r-\omega_s(t)\tfrac{L_m^2}{L_s})\boldsymbol{J}\boldsymbol{i}_r^k(t)-(R_s\tfrac{L_m}{L_s}+\omega_r(t)L_m\boldsymbol{J})\boldsymbol{i}_s^k(t)+\tfrac{L_m}{L_s}\boldsymbol{u}_s^k(t). \tag{3.40}$$

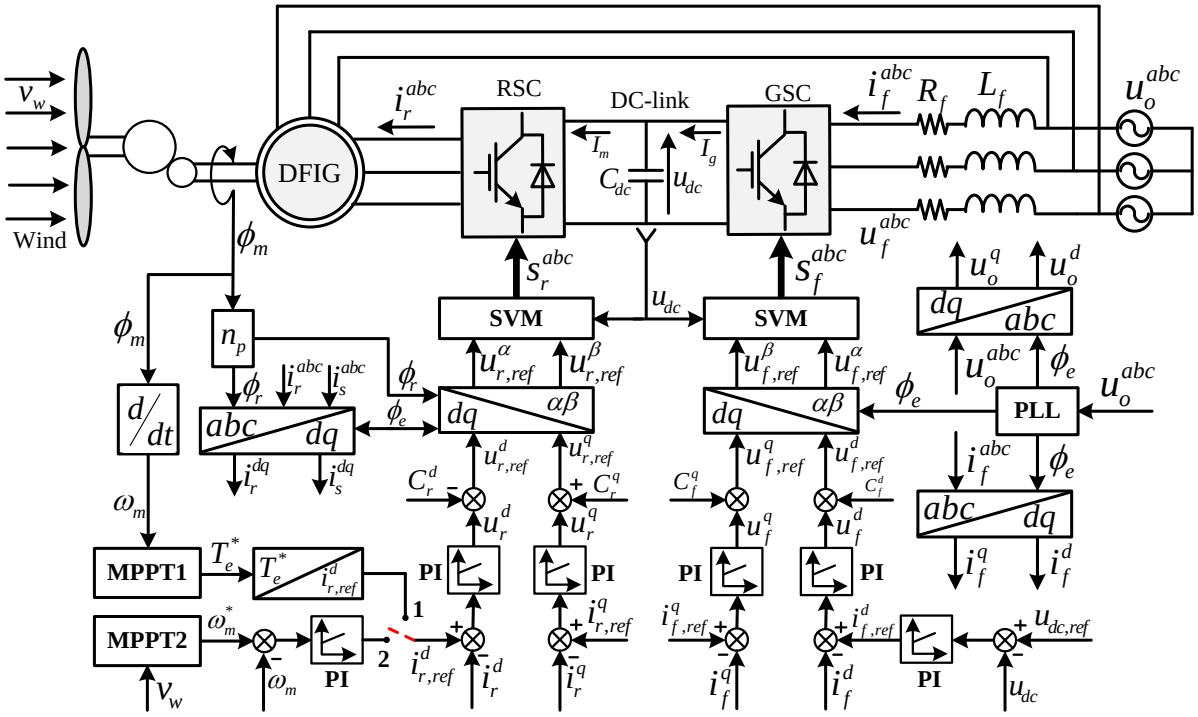

Figure 3.6: Schematic diagram of the voltage oriented control scheme for DFIGs.

By writing out both components, i.e. d and q, gives

$$\left.\begin{aligned} u_r^d(t) &= R_r i_r^d(t) + \sigma L_r \tfrac{d}{dt} i_r^d(t) - \underbrace{(\omega_{sl}(t)L_r - \omega_s(t)\tfrac{L_m^2}{L_s})i_r^q(t) - R_s\tfrac{L_m}{L_s}i_s^d(t) + \omega_r(t)L_m i_s^q(t) + \tfrac{L_m}{L_s}\boldsymbol{u}_s^q(t)}_{C_r^d(t)}, \\ u_r^q(t) &= R_r i_r^q(t) + \sigma L_r \tfrac{d}{dt} i_r^q(t) + \underbrace{(\omega_{sl}(t)L_r - \omega_s(t)\tfrac{L_m^2}{L_s})i_r^d(t) - R_s\tfrac{L_m}{L_s}i_s^d(t) - \omega_r(t)L_m i_s^d(t) + \tfrac{L_m}{L_s}\boldsymbol{u}_s^q(t)}_{C_r^q(t)}. \end{aligned}\right\} \tag{3.41}$$

By neglecting the compensation terms $C_r^d(t)$ and $C_r^q(t)$, the transfer function $\boldsymbol{TF}_r^i(S)$ between the currents $\boldsymbol{I}_r^{dq}(S)$ and their control voltages $\boldsymbol{U}_r^{dq}(S)$ can be expressed as

$$\boldsymbol{TF}_r^i(S) = \frac{I_r^d(S)}{U_r^d(S)} = \frac{I_r^q(S)}{U_r^q(S)} = \frac{1}{R_r + \sigma L_r S}. \tag{3.42}$$

In analogy to the PMSG, a proportional-integral (PI) controller is employed for making the currents (i.e. $I_r^d(S)$ and $I_r^q(S)$) follow the reference values with a zero steady-state tracking error. These PI controller produce the control voltages $\boldsymbol{u}_r^{dq}$. Then, the compensation terms $C_r^d(t)$ and $C_r^q(t)$ will be added to those voltages as

$$\left.\begin{aligned} u_{r,ref}^d(t) &= u_r^d(t) - (\omega_{sl}(t)L_r - \omega_s(t)\tfrac{L_m^2}{L_s})i_r^q(t) - R_s\tfrac{L_m}{L_s}i_s^d(t) + \omega_r(t)L_m i_s^q(t) + \tfrac{L_m}{L_s}\boldsymbol{u}_s^q(t), \\ u_{r,ref}^q(t) &= u_r^q(t) + (\omega_{sl}(t)L_r - \omega_s(t)\tfrac{L_m^2}{L_s})i_r^d(t) - R_s\tfrac{L_m}{L_s}i_s^d(t) - \omega_r(t)L_m i_s^d(t) + \tfrac{L_m}{L_s}\boldsymbol{u}_s^q(t). \end{aligned}\right\} \tag{3.43}$$

Finally, the SVM produces the switching signals of the RSC according to the reference voltages $u_{r,ref}^d(t)$ and $u_{r,ref}^d(t)$ as shown in Fig. 3.6.

2) Outer (speed) control loop: Similarly to the PMSG,the outer (speed) control loop for DFIGs in wind turbine application can be implemented in two different ways: i) Non-linear speed controller, and ii) linear (PI) speed controller.
i) Non-linear speed controller: This control technique is based on calculating the reference electro-magnetic torque T_e^* from (2.15), which is used to compute the reference value of the rotor d-axis current $i_{r,ref}^d$. In steady-state (i.e. $\frac{d}{dt}\boldsymbol{\psi}_s^k(t) = 0$), by substituting the value of $\boldsymbol{\psi}_s^k(t)$ from (2.37) in (2.40), the electro-magnetic torque T_e can be expressed as [27]

$$T_e(t) = -\frac{3}{2} n_p \frac{L_m}{L_s} \boldsymbol{i}_r^k(t)^\top \frac{\boldsymbol{u}_s^k(t) - R_s \boldsymbol{i}_s^k(t)}{\omega_s}. \tag{3.44}$$

With $u_s^q = 0$ for the stator voltage oriented control, equation (3.44) can be simplified to

$$T_e(t) = -\frac{3}{2} n_p \frac{L_m}{\omega_s L_s} \Big(i_r^d(t) u_s^d(t) - R_s (i_r^q(t) i_s^q(t) + i_r^d(t) i_s^d(t)) \Big). \tag{3.45}$$

The stator resistance is normally very low value, in particularity for large machines, the electro-magnetic torque T_e can be further simplified to

$$T_e(t) = -\frac{3}{2} n_p \frac{L_m}{\omega_s L_s} i_r^d(t) u_s^d(t). \tag{3.46}$$

Accordingly, the d-axis reference current of the rotor can be computed as

$$i_{r,ref}^d(t) = -\frac{2}{3} \frac{\omega_s L_s}{n_p L_m} \frac{T_e^*(t)}{u_s^d(t)}. \tag{3.47}$$

ii) linear (PI) speed controller: The linear (PI) speed control loop for DFIGs in wind turbine application is the same like that of the PMSG, see Sec. 3.2.1.1. Therefore, it will not repeated here again.

3.3.2 Deadbeat Control for DFIG

The structure of the DBPC of RSC/GSC for DFIGs is illustrated in Fig. 3.7. In this section, the deadbeat predictive control for the RSC will be explained. The deadbeat predictive control for GSC is already explained in Sec. 3.2.2.

3.3.2.1 Deadbeat current control for RSC

By applying the forward Euler discretization method to (3.40), the discrete-time model of the DFIG can be expressed as [49]

$$\left.\begin{aligned} u_r^d[k] &= R_r i_r^d[k] + \sigma L_r \tfrac{i_r^d[k+1] - i_r^d[k]}{T_s} - \omega_{sl}[k] L_r i_r^q[k] + \omega_s \tfrac{L_m^2}{L_s} i_r^q[k] - R_s \tfrac{L_m}{L_s} i_s^d[k] \\ &\quad + \omega_r[k] L_m i_s^q[k] + \tfrac{L_m}{L_s} u_s^d[k], \\ u_r^q[k] &= R_r i_r^q[k] + \sigma L_r \tfrac{i_r^q[k+1] - i_r^q[k]}{T_s} + \omega_{sl}[k] L_r i_r^d[k] - \omega_s \tfrac{L_m^2}{L_s} i_r^d[k] - R_s \tfrac{L_m}{L_s} i_s^q[k] \\ &\quad - \omega_r[k] L_m i_s^d[k] + \tfrac{L_m}{L_s} u_s^q[k]. \end{aligned}\right\} \tag{3.48}$$

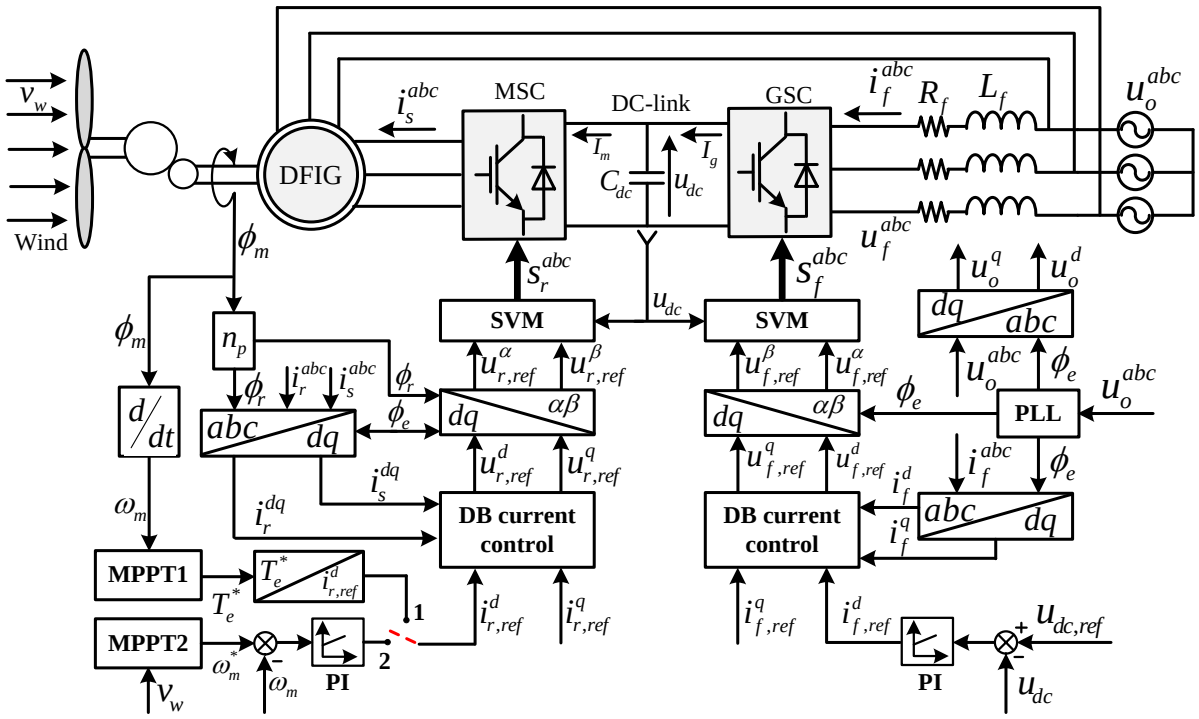

Figure 3.7: Schematic diagram of the deadbeat predictive control for DFIGs.

Similarly to the PMSG, by considering the one sample delay due to the digital controller, the reference voltage vector $\boldsymbol{u}^{dq}_{r,ref}[k+1]$ can be computed directly by replacing the predicted currents $\boldsymbol{i}^{dq}_{r}[k+2]$ by the reference currents $\boldsymbol{i}^{dq}_{r,ref}[k+2]$ in (3.48) as follows

$$\left.\begin{aligned} u^d_{r,ref}[k+1] &= R_r i^d_r[k+1] + \sigma L_r \tfrac{i^d_{r,\mathrm{ref}}[k+2]-i^d_r[k+1]}{T_s} - \omega_{sl}[k+1]L_r i^q_r[k+1] + \omega_s \tfrac{L_m^2}{L_s} i^q_r[k+1] \\ &\quad -R_s \tfrac{L_m}{L_s} i^d_s[k+1] + \omega_r[k+1]L_m i^q_s[k+1] + \tfrac{L_m}{L_s} u^d_s[k+1], \\ u^q_{r,ref}[k+1] &= R_r i^q_r[k+1] + \sigma L_r \tfrac{i^q_{r,\mathrm{ref}}[k+2]-i^q_r[k+1]}{T_s} + \omega_{sl}[k+1]L_r i^d_r[k+1] - \omega_s \tfrac{L_m^2}{L_s} i^d_r[k+1] \\ &\quad -R_s \tfrac{L_m}{L_s} i^q_s[k+1] - \omega_r[k+1]L_m i^d_s[k+1] + \tfrac{L_m}{L_s} u^q_s[k+1]. \end{aligned}\right\} \tag{3.49}$$

The currents $i^d_r[k+1]$ and $i^q_r[k+1]$ can be predicted from (3.48) as follows

$$\left.\begin{aligned} i^d_r[k+1] &= i^d_r[k] + \tfrac{T_s}{\sigma L_s L_r}\Big(- R_r L_s i^d_r[k] + (\omega_{sl}[k] L_r L_s - \omega_s[k] L_m^2) i^q_r[k] + R_s L_m i^d_s[k] \\ &\quad -\omega_r[k] L_m L_s i^q_s[k] + L_s u^d_r[k] - L_m u^d_s[k]\Big) \\ i^q_r[k+1] &= i^q_r[k] + \tfrac{T_s}{\sigma L_s L_r}\Big(- R_r L_s i^q_r[k] - (\omega_{sl}[k] L_r L_s - \omega_s[k] L_m^2) i^d_r[k] + R_s L_m i^q_s[k] \\ &\quad +\omega_r[k] L_m L_s i^d_s[k] + L_s u^q_r[k] - L_m u^q_s[k]\Big). \end{aligned}\right\} \tag{3.50}$$

In (3.49), $i^d_{r,\mathrm{ref}}[k+2]$, $i^q_{r,\mathrm{ref}}[k+2]$, $\omega_r[k+1]$, $\omega_{sl}[k+1]$, $i^d_s[k+1]$, $i^q_s[k+1]$, $u^d_s[k+1]$, and $u^q_s[k+1]$ can be computed using Lagrange extrapolation as explained before.

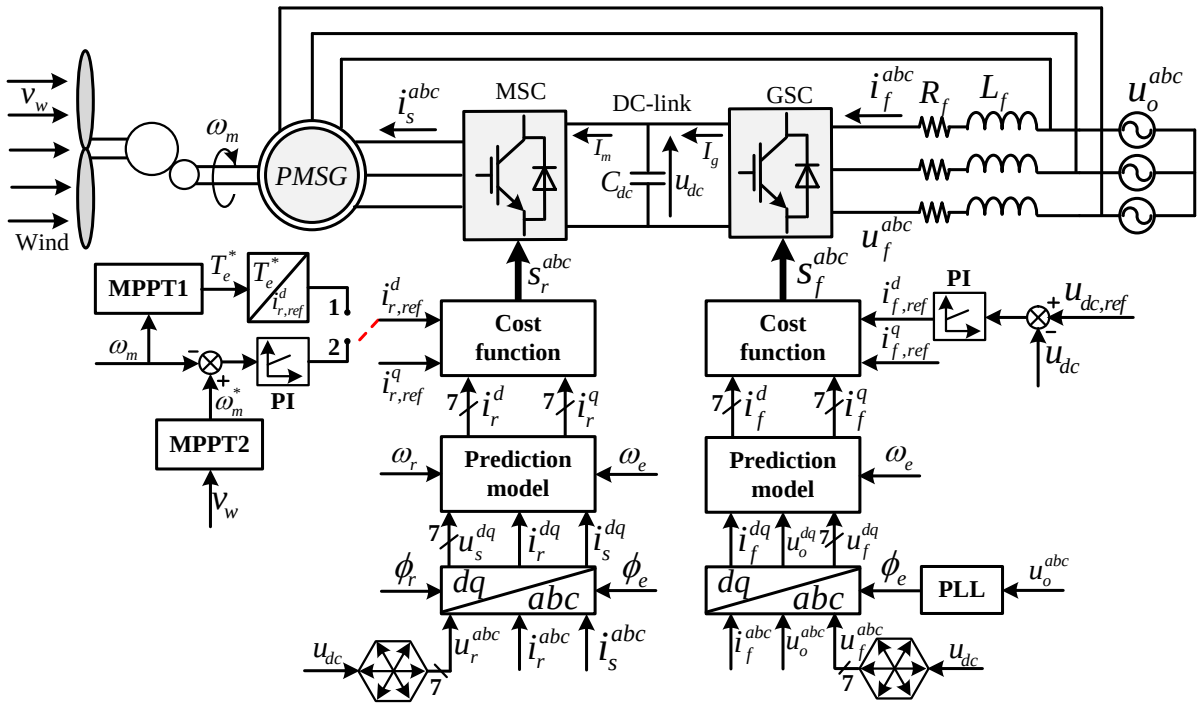

Figure 3.8: Schematic diagram of the DMPCC technique for DFIGs.

3.3.3 Direct-model predictive current control for DFIG

The structure of the direct-model predictive current control (DMPCC) of RSC/GSC for DFIGs is illustrated in Fig. 3.8. In this section the DMPCC for the RSC will be explained. The DMPCC for GSC is already explained in Sec. 3.2.3.

3.3.3.1 Direct-model predictive current control for RSC

The prediction model of the rotor currents of the DFIG can be written as [49]

$$\left.\begin{aligned} i_r^d[k+2] &= i_r^d[k+1] + \tfrac{T_s}{\sigma L_s L_r}\Big(- R_r L_s i_r^d[k+1] + (\omega_{sl}[k+1] L_r L_s - \omega_s[k+1] L_m^2) i_r^q[k+1] \\ &\quad + R_s L_m i_s^d[k+1] - \omega_r[k+1] L_m L_s i_s^q[k+1] + L_s u_r^d[k+1] - L_m u_s^d[k+1]\Big) \\ i_r^q[k+2] &= i_r^q[k+1] + \tfrac{T_s}{\sigma L_s L_r}\Big(- R_r L_s i_r^q[k+1] - (\omega_{sl}[k+1] L_r L_s - \omega_s[k+1] L_m^2) i_r^d[k+1] \\ &\quad + R_s L_m i_s^q[k+1] + \omega_r[k+1] L_m L_s i_s^d[k+1] + L_s u_r^q[k+1] - L_m u_s^q[k+1]\Big). \end{aligned}\right\} \tag{3.51}$$

Seven values of the currents $i_r^d[k+2]$ and $i_r^q[k+2]$ can be predicted by considering the seven voltage vectors of the RSC. Then, a cost function in the form

$$g_{RSC} = \left|i_{r,ref}^d[k+2] - i_r^d[k+2]\right| + \left|i_{r,ref}^q[k+2] - i_r^q[k+2]\right|, \tag{3.52}$$

is utilized to find the optimal actuation to apply in the next sampling instant.

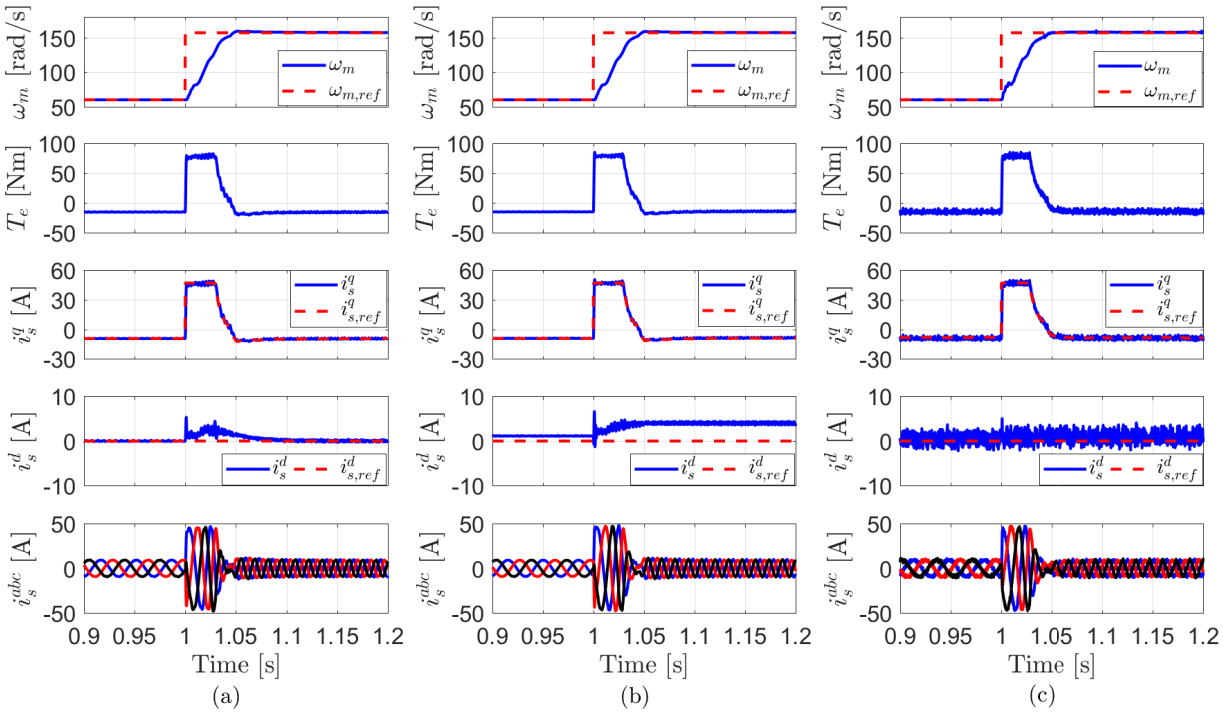

Figure 3.9: Experimental results for the PMSG at step change in the rotor speed ω_m: (a) Field-oriented control, (b) deadbeat predictive control, and (c) FCS-MPC.

3.4 Experimental results

In the constructed test benches for PMSGs and DFIGs, another machine is employed to mimic the wind turbine. Accordingly, its not possible to implement the outer speed control loop using the non-linear speed control method. Therefore, a linear PI controller is implemented to regulate the speed of the generator.

3.4.1 Experimental results for PMSGs

The switching frequency as well as the sampling frequency are set to $4\,\mathrm{kHz}$ in case of using FOC and DBPC, while the sampling frequency for FCS-MPC is set to $10\,\mathrm{kHz}$. The PMSG is employed to control the speed of the rotor and the RSM is utilized to control the load torque.

Fig. 3.9 shows the performance of FOC, DBPC, and FCS-MPC for PMSGs at step change in the rotor speed. At the time instant $t = 1\mathrm{s}$, a step change in the reference value of the rotor mechanical speed $\omega_{m,ref}$ from $60\mathrm{rad/s}$ to $157\mathrm{rad/s}$ (rated speed of the PMSG). The load torque is kept constant at $-20\mathrm{Nm}$ by the RSM control strategy. From top to bottom, the plotted signals are reference $\omega_{m,ref}$ and measured speed ω_m of the PMSG rotor, electro-magnetic torque T_e of the PMSG, reference $i_{s,ref}^q$ and measured q-axis current i_s^q of the PMSG stator, reference $i_{s,ref}^d$ and measured d-axis current i_s^d of the PMSG stator, three-phase currents i_s^{abc} of the PMSG stator, respectively.

According to Fig. 3.9, it can be firstly observed that the dynamic performance of the DBPC and FCS-MPC are slightly better than that of the FOC due to the replacement of the inner

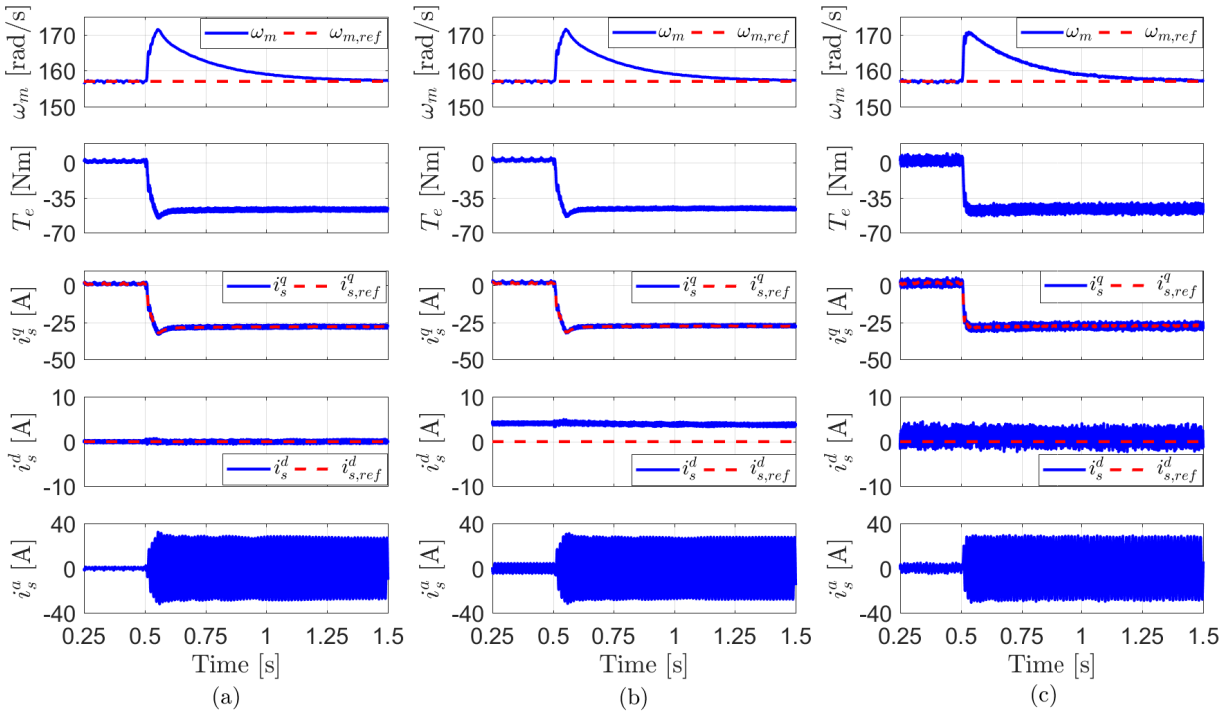

Figure 3.10: Experimental results for the PMSG at step change in load torque: (a) Field-oriented control, (b) deadbeat predictive control, and (c) FCS-MPC.

(current) control loop with the predictive algorithm. However, due to the use of an (slow) outer PI control for regulating the speed of the rotor, the effect of using predictive control in the inner loop is not clear. Secondly, A clear difference in the dynamic performance of the controllers is the decoupling capability between the d and q axes. Using FOC and DBPC, the d-axis current is disturbed during the step change in the rotor speed. This effect is not noticeable in the performance of the FCS-MPC. Thirdly, a small overshoot in the speed/torque can be observed using FOC and DBPC, while no any overshoot in the speed is observed using the FCS-MPC. Fourthly, it can by observed that, with FOC, the steady-state error (SSE) of the speed and current tracking is almost zero due to the exist of the integral term of the PI controller. The SSE of the DBPC is significantly higher than that of the FCS-MPC due to its high sensitivity to parameters variations. Finally, it can be seen that the ripples in the currents/torque waveforms of the FOC and DBPC are lower than that of the FCS-MPC. The high ripples of the FCS-MPC are due to the direct application of the switching signals to the power converter, while FOC and DBPC use a modulator to generate the switching signals. Furthermore, in FCS-MPC technique, only one voltage vector is applied for the whole sampling instant. Finally, The execution times of the different control algorithms in the real-time system dSPACE DS1007 platform have been measured to assess the computing power requirement of each technique. It has been found that the execution times of FOC, DBPC, and FCS-MPC are $24\mu s$, $29\mu s$, and $43\mu s$, respectively. Accordingly, the computational load of the FCS-MPC scheme is the highest. However, due to the continuous development of powerful digital signal processors (DSPs) and field-programmable gate arrays (FPGAs), implementation of this control technique is not a problem anymore.

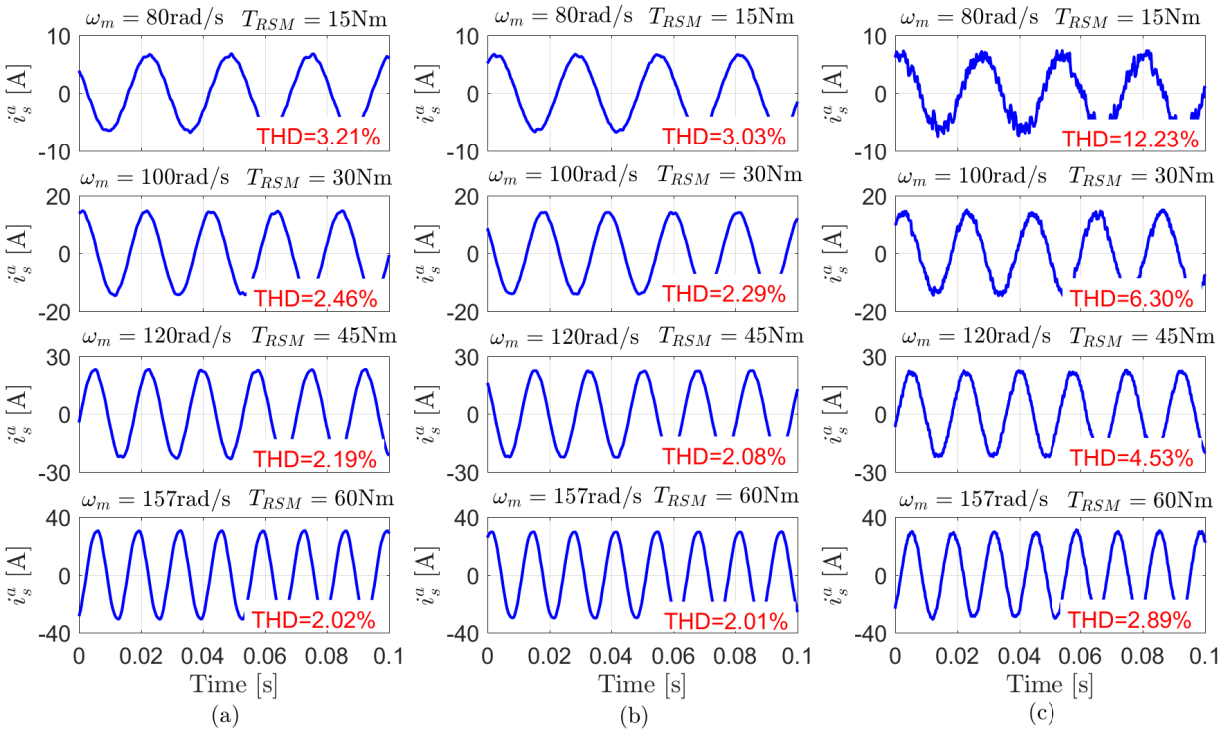

Figure 3.11: Experimental results for the PMSG at steady-state operation: (a) Field-oriented control, (b) deadbeat predictive control, and (c) FCS-MPC.

Fig. 3.10 illustrates the response of the different control techniques at step change in the load torque. At the time instant $t = 0.5\,\mathrm{s}$, a step change in the load torque of the PMSG from $0\mathrm{Nm}$ to $-50\mathrm{Nm}$ is applied o the RSM control system. The mechanical speed of the rotor is controlled to be constant at $157\mathrm{rad/s}$ by the PMSG control technique. According to Fig. 3.10, the same differences between FOC, DBPC, and FCS-MPC are observed.

Finally, in order to closely investigate the steady-state performance of the different control techniques, the waveforms of phase a current of the PMSG stator i_s^a at different speed values of the rotor are shown in Fig. 3.11. The mechanical speed of the rotor is set to 80, 100, 120, and $157\mathrm{rad/s}$ by the PMSG, while the load torque is set to -15, -30, -45, and $-60\mathrm{Nm}$ by the RSM, respectively. It can be observed that, with FOC and DBPC, almost the same values of the total harmonic distortion (THD) at the different values of the rotor speed is obtained, while the FCS-MPC gives higher values of the THD. However, at higher values of the rotor speed, the THD of the FCS-MPC is close to that of FOC/DBPC.

3.4.2 Experimental results for DFIGs

The switching frequency as well as the sampling frequency are set to $8\,\mathrm{kHz}$ in case of using FOC and DBPC, while the sampling frequency for FCS-MPC is set to $16\,\mathrm{kHz}$. The DFIG is employed to control the speed of the rotor and the EESM is utilized to control the load torque T_l. Fig. 3.12 shows the performance of FOC, DBPC, and FCS-MPC for DFIGs at change of the rotor speed. At the time instant $t = 2\mathrm{s}$, a change in the reference value of the rotor mechanical speed $\omega_{m,ref}$ from $130\mathrm{rad/s}$ to $190\mathrm{rad/s}$ (i.e. from sub-synchronous to super-synchronous operation)

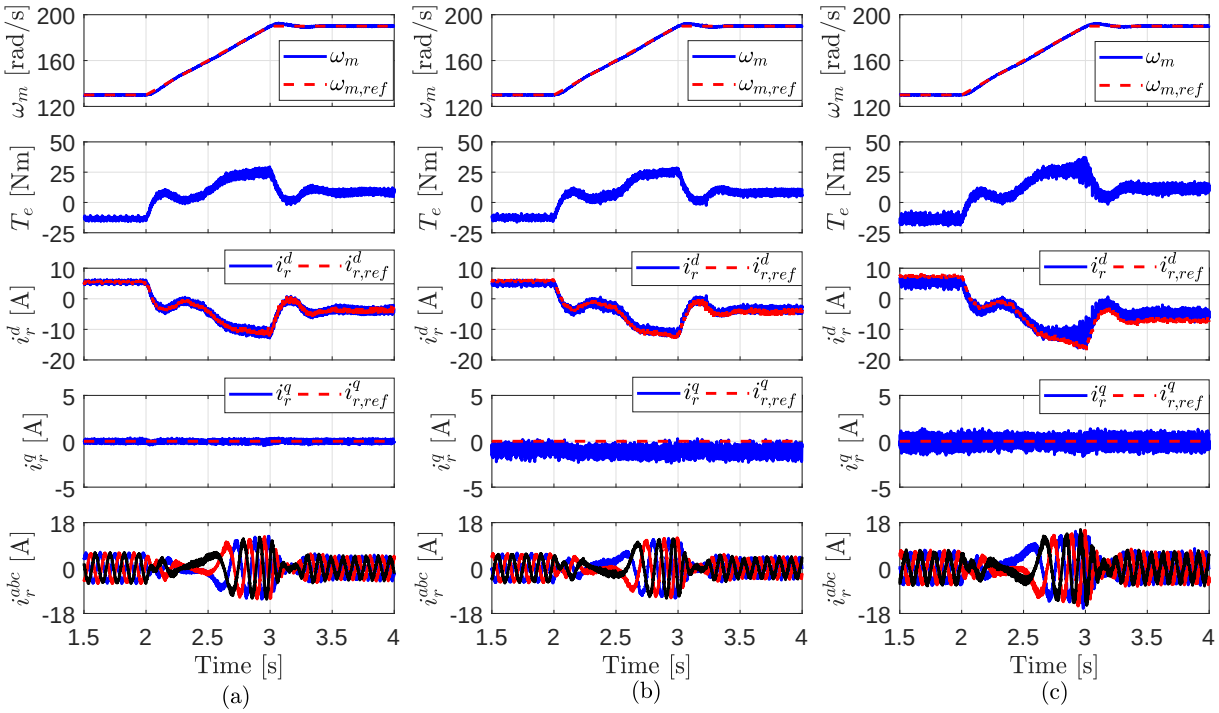

Figure 3.12: Experimental results for the DFIG at change of the rotor mechanical speed ω_m: (a) Field-oriented control, (b) deadbeat predictive control, and (c) FCS-MPC.

is applied. The load torque is kept constant at $-15\mathrm{Nm}$ by the EESM control strategy. From top to bottom, the plotted signals are reference $\omega_{m,ref}$ and measured speed ω_m of the DFIG rotor, electro-magnetic torque T_e of the DFIG, reference $i_{r,ref}^d$ and measured d-axis current i_r^d of the DFIG rotor, reference $i_{r,ref}^q$ and measured q-axis current i_r^q of the DFIG rotor, three-phase currents i_r^{abc} of the DFIG rotor, respectively. Similarly to the PMSG and according to Fig. 3.12, the same differences in the dynamic/steady-state performances of FOC, DBPC, and FCS-MPC can be observed.

Furthermore, the performance of the different control techniques is investigated at step change in the load torque, see Fig. 3.13. At the time instant $t = 1\,\mathrm{s}$, a step change in the load torque of the DFIG from $-5\mathrm{Nm}$ to $-40\mathrm{Nm}$ is applied o the EESM control system. The mechanical speed of the rotor is controlled to be constant at $140\mathrm{rad/s}$ by the DFIG control technique, i.e the DFIG is operating in the sub-synchronous region. According to Fig. 3.13, the same differences in the dynamic/steady-state performances of FOC, DBPC, and FCS-MPC are observed.

Finally, the steady-state waveforms of phase a of the rotor current i_r^a at various operation conditions are illustrated in Fig. 3.14. The mechanical speed of the rotor is set to 125, 150, and $175\mathrm{rad/s}$ by the DFIG, while the load torque is set to -15, -55, and $-18\mathrm{Nm}$ by the EESM, respectively. According to Fig. 3.14, the same differences in the steady-state performance of FOC, DBPC, and FCS-MPC are observed.

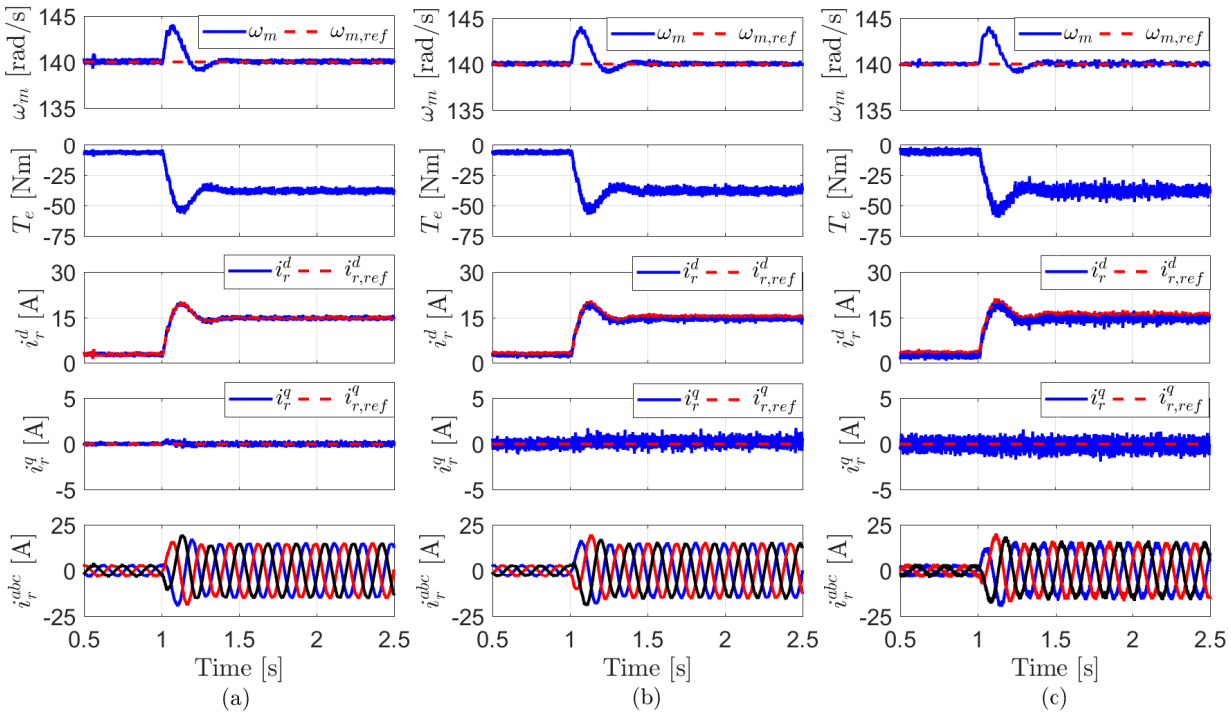

Figure 3.13: Experimental results for the DFIG at step change in the load torque: (a) Field-oriented control, (b) deadbeat predictive control, and (c) FCS-MPC.

3.5 Simulation results

In the constructed experimental test benches, it is not possible to investigate the ability of the different control techniques in tracking the maximum power point, i.e. the ability of the tip speed ratio λ and power coefficient c_p to track their optimal values $c_p^\star$ and $\lambda^\star$, respectively. Furthermore, the performance of the grid-side converter (GSC) in tracking the DC-link voltage is not investigated by experiments due to the fact that only one VSC is installed in the machine/rotor side. Accordingly, in this section, simulation results are given for both PMSG and DFIG. Note that in the Simulink model, the non-linear speed controller is employed to regulate the rotor speed of the PMSG/DFIG, see Sec. 3.2.1.

3.5.1 Simulation results for PMSGs

Fig. 3.15 illustrates the performances of the various control techniques (i.e. vector control, DBPC, and FCS-MPC) at step changes in the wind speed, which started at $8\,\mathrm{m/s}$, increased gradually to $20\,\mathrm{m/s}$ (the rated speed of the wind turbine), and reduce gradually to $14\,\mathrm{m/s}$, respectively. It can be seen from this figure that the different control techniques can track the optimal rotor speed $\omega_m^\star$, which ensure the MPPT capability. The tip speed ratio λ is kept close to its optimal value $\lambda^\star \approx 8.11$. Accordingly, the power coefficient c_p is tracking its maximal (optimal) value $c_p^\star \approx 0.48$. Finally, the different control schemes illustrate good tracking per-

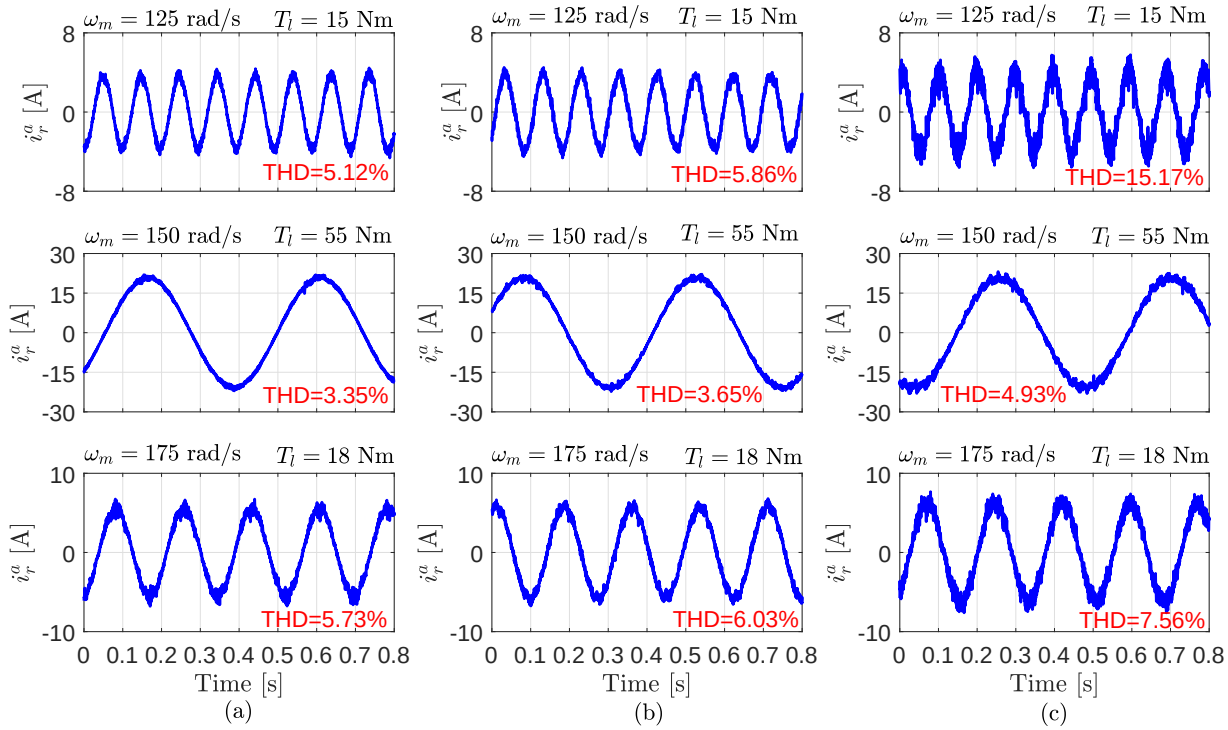

Figure 3.14: Experimental results for the DFIG at steady-state operation: (a) Field-oriented control, (b) deadbeat predictive control, and (c) FCS-MPC.

formance for the DC-link voltage u_{dc}. However, it can be observed that the dynamic response of the DC-link voltage u_{dc} is better by using DBPC and FCS-MPC in the inner-current control loop.

3.5.2 Simulation results for DFIGs

Fig. 3.16 shows the performances of the different control techniques (i.e. vector control, DBPC, and FCS-MPC) at step changes in the wind speed, which started at $8\,\mathrm{m/s}$, increased gradually to $14\,\mathrm{m/s}$ (the rated speed of the wind turbine), and reduce gradually to $11\,\mathrm{m/s}$, respectively. It can be observed that at $v_w = 8\,\mathrm{m/s}$, the DFIG is working in the sub-synchronous region and at $v_w = 14\,\mathrm{m/s}$, the DFIG is working in the super-synchronous area. Similary to the PMSG, it can be seen that the different control techniques can track realize the MPPT by regulation the tip speed ration λ and power coefficient c_p to their optimal values $\lambda^\star \approx 8.16$ and $c_p^\star \approx 0.48$. Again, the dynamic performance of the DC-link voltage u_{dc} is better by using DBPC and FCS-MPC in the inner-current control loop.

3.6 Summary

In this chapter, the conventional control techniques for PMSGs and DFIGs have been described and implemented. These control techniques include: vector control (FOC/VOC for PMSGs and VOC for DFIGs), DBPC, and FCS-MPC. The performances of those different control tech-

niques have been validated and compared by experimental and simulation results. The results illustrated that: 1) Vector control gives a satisfactory dynamic performance, very good steady-state response, and is robust to parameters variations, 2) DBPC enhances the dynamic performance of the system and gives good steady-state response; however, its sensitivity to parameters variations and the one-sample delay due to the digital controller are the main drawbacks, 3) FCS-MPC gives excellent dynamic response; however the high ripples in the current/torque and sensitivity to parameters variations are the main disadvantages.

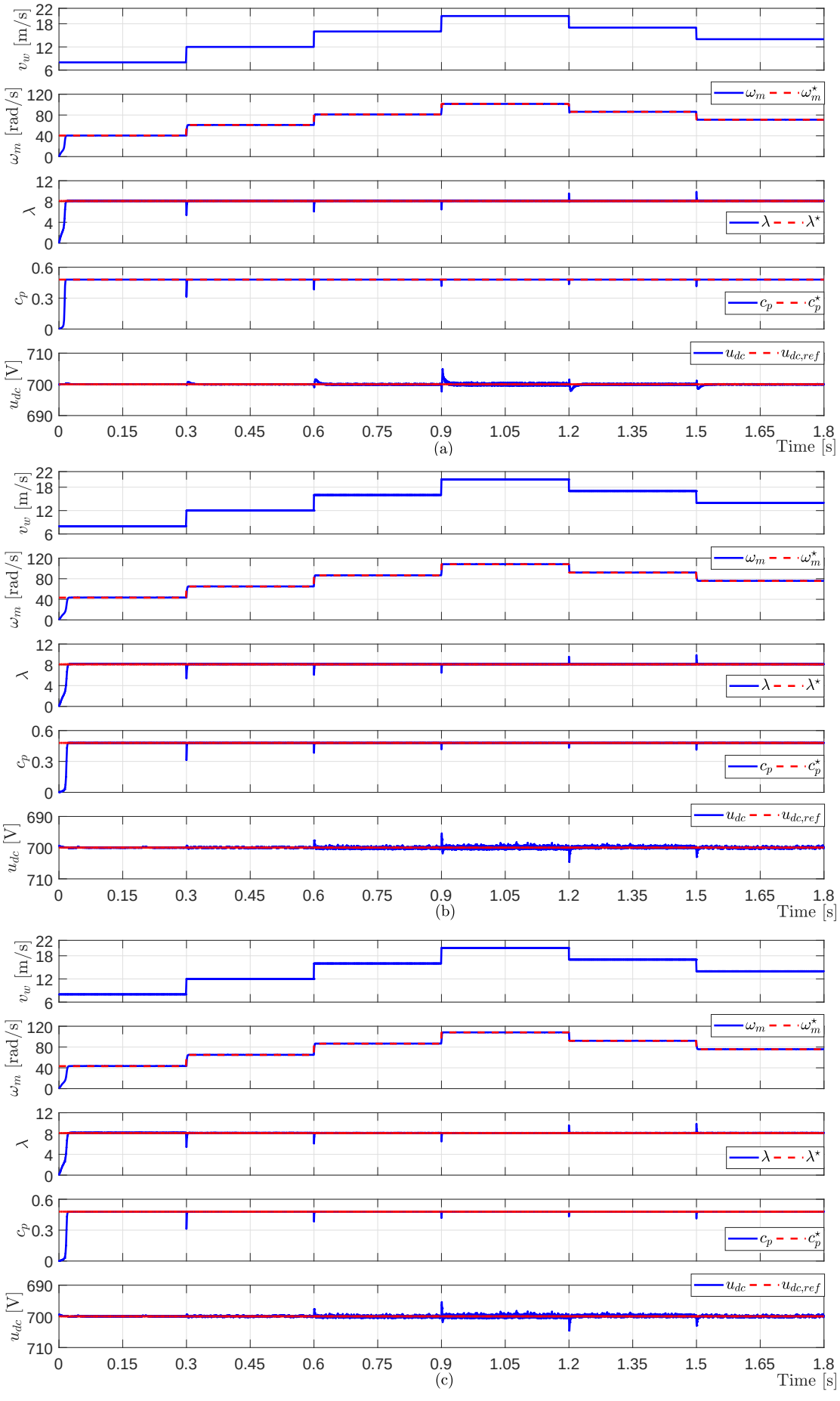

Figure 3.15: Simulation results for the PMSG at step changes in the wind speed v_w: (a) Vector control, (b) deadbeat predictive control, and (c) FCS-MPC.

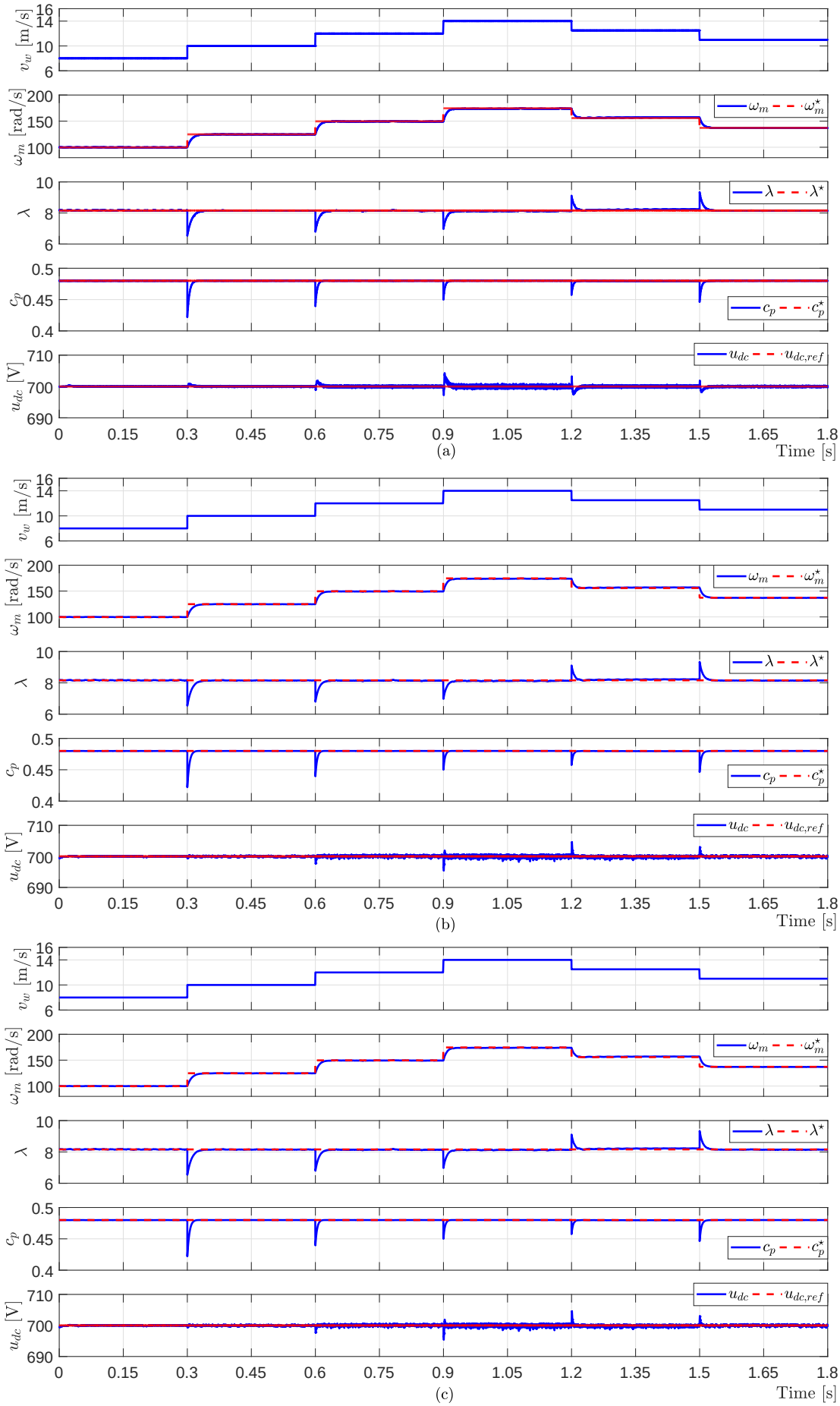

Figure 3.16: Simulation results for the DFIG at step changes in the wind speed v_w: (a) Vector control, (b) deadbeat predictive control, and (c) FCS-MPC.

CHAPTER 4

Finite-Position-set observers for PMSGs and DFIGs

This chapter proposes novel finite-position-set (FPS) observers for sensorless control of PMSGs and DFIGs, where the finite-control-set MPC (FCS-MPC) principles are extended to replace the fixed-gain PI controllers in the conventional observers for estimating the speed/position of the rotor. Firstly, review of the literature of the different observers for estimation of the rotor speed and position is given in Sec. 4.1. Then, two well-known observers are presented in this chapter: 1) Phase-locked loop (PLL) for PMSGs (see Sec. 4.2), and 2) model reference adaptive system (MRAS) for PMSGs/DFIGs (see Sec. 4.3). In these sections, the conventional PLL/MRAS observers are firstly explained and then the proposed FPS-PLL/FPS-MRAS are detailed. Subsequently, the experimental results of the proposed FPS-PLL and FPS-MRAS observers are illustrated in Sec. 4.4. Finally, a summary of this chapter is given in Sec. 4.5.

4.1 Introduction

Installations of variable-speed wind turbine systems with PMSGs and DFIGs have steadily increased over the last years. Normally, rotor speed/position of the generator are required, not only for a safe operation, but also for torque and current control of the wind energy conversion system. Consequently, mechanical sensors, such as incremental-encoders/speed-transducers, are essential for detecting the rotor position/speed. However, those mechanical sensors require wiring, precise mounting, and result in lower reliability. These problems can be overcome by utilizing position/speed sensorless control strategies.

Several speed and position observers have been proposed for induction machines (IMs), Permanent Magnet Synchronous Machines (PMSMs), and recently, was applied successfully to variable-speed WECSs [46], [47], [50]–[57]. Among those observers, the Model Reference Adaptive System (MRAS) observers and phase locked loop (PLL)-based observers attracted attention due to their simplicity and direct physical interpretation. MRAS and PLL observers

have been utilized for controlling and estimating the rotor speed and position of IM and PMSM drives [53]–[56]. They have been also applied for variable-speed WECSs based on DFIG and PMSG [34], [48], [57]–[61].

Generally, fixed-gain proportional-integral (PI) controllers are employed in MRAS/PLL observers for estimating the rotor speed/position. Linearization of the MRAS/PLL observer is essential to tune this linear natural PI controller. Otherwise, tuning of this PI controller can be realized by trial and error which is a time-consuming process. Moreover, due to the continuous variation in the machine parameters and the operating conditions, in addition to the nonlinearities present in the inverter, fixed-gain PI controller may not guarantee the desired performance. Therefore, several alternative controllers have been used in MRAS/PLL observers to enhance the performance of them. In [62]–[64], a neural network based controller was proposed to replace the fixed-gain PI adaption mechanism. In [65]–[68], the PI controller was replaced by a fuzzy logic based adaption algorithm. These two schemes (i.e. neural network and fuzzy logic) provide enhancement in the observer dynamic response. However, the computational burden of these controllers are the main drawback of these schemes. Moreover, fuzzy logic mandates tuning of some gains in the fuzzification and defuzzification steps. In [68]–[71], another solution was suggested where the fixed-gain PI controller was replaced by a sliding mode (SM) algorithm. The SM controller demonstrates good robustness and dynamic performance, however undesirable deterioration evolves within the estimated speed due to chattering.

As discussed in Sec. 1.4, model predictive control (MPC) is a promising control scheme for power converters/inverters and motor drives because of several features, such as good dynamic performance, absence of modulator, and direct consideration of nonlinearities/constraints of the adopted system [19]–[24]. MPC takes into account the model of the adopted system for predicting its future performance over a prediction horizon. Then, an optimization problem will be solved where a sequence of future switching actions is obtained by minimizing a cost function. The optimal switching actions are then applied, and the algorithm is repeated for each sampling instant. Power converters/inverters have a finite number of switching states. Therefore, the MPC optimization problem can be simplified to the prediction of the system performance for each admissible state. Then, each prediction is evaluated using the cost function, and the switching action that optimizes this cost function is selected to be applied in the next sampling period [24]. This scheme, called finite control set-model predictive control (FCS-MPC), has been successfully applied for various applications, including three phase converters/inverters, multi-level converters, and motor drives [19]–[24]. However, the rotor position/speed does not have a discrete natural like the power converter, and accordingly, a discretization algorithm is essential to use the FCS-MPC in MRAS/PLL observers.

In the following sections, novel PLL/MRAS observers based on the principles of the FCS-MPC are detailed and their performances have been experimentally investigated and compared with that of the conventional ones.

4.2 Phase-locked loop observer for PMSGs

PLL based observers are well-known for the synchronization of grid connected power converters [72]–[75]. Furthermore, they have been used for sensorless control of IMs [76]–[78] and are combined with signal-injextion based encoderless methods [79]–[81].

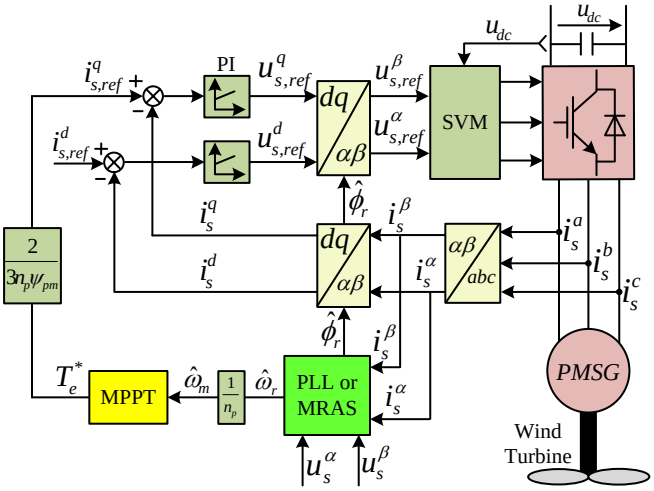

Figure 4.1: Sensorless field-oriented control (FOC) of a surface-mounted PMSG using PLL or MRAS observer.

Back electromotive force (EMF)-based PLL observers have been extensively studied for sensorless control of PMSMs and enhanced methods to estimate the back EMF have been presented in the literature [82]–[86]. A sliding-mode observer is combined with the PLL in [82]–[84] to improve the position estimation performance of the PMSM. An adaptive linear neural (ADALINE)-network-based filter to mitigate the harmonic ripple in the back EMF has been presented in [85]. A linear state observer, developed in the Laplace domain, to improve the back EMF estimation was presented in [86]. Furthermore, this back EMF based PLL is the most used type in the literature, and accordingly, it is adopted in this work. The PLL is employed to estimate the speed/position of the rotor and feed it back to the control algorithm as illus tared in Fig. 4.1.

4.2.1 Conventional PLL for sensorless control of PMSG

The conventional PLL for sensorless control of a PMSG was introduced in [87]. Fig. 4.2 shows the vector diagram of the permanent-magnet flux-oriented reference frame, where ϕ_r and $\hat{\phi}_r$ are the actual and estimated rotor position, respectively, and ψ_{pm} is the permanent-magnet flux linkage. The d-axis is supposed to be aligned with the permanent-magnet flux linkage. However, an initial error between ϕ_r and $\hat{\phi}_r$ (i.e. $\Delta\phi_r = \phi_r - \hat{\phi}_r$) will exist. For small $\Delta\phi_r$, it can be assumed that $e_s^d \approx \Delta\phi_r$. Accordingly, e_s^d can be employed as an indicator to show whether the d-axis and the permanent-magnet flux linkage are aligned or not. To do so, estimation of the back EMF components $(e_s^d, e_s^q)^\top$ is necessary. Rearranging (3.1) gives

$$\left.\begin{aligned} u_s^d(t) &= R_s i_s^d(t) + L_s \tfrac{d}{dt} i_s^d(t) - \omega_r(t) L_s i_s^q(t) + \underbrace{0}_{=:e_s^d(t)}, \\ u_s^q(t) &= R_s i_s^q(t) + L_s \tfrac{d}{dt} i_s^q(t) + \omega_r(t) L_s i_s^d(t) + \underbrace{\omega_r(t)\psi_{pm}}_{=:e_s^q(t)}, \end{aligned}\right\} \tag{4.1}$$

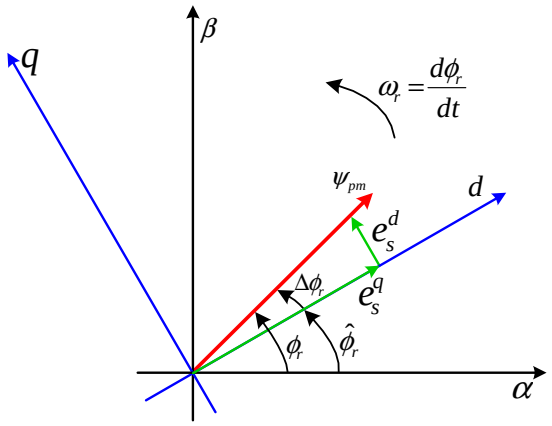

Figure 4.2: Vector diagram of a permanent-magnet flux-oriented reference frame.

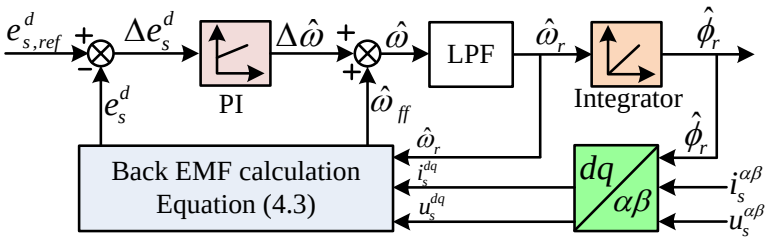

Figure 4.3: Block diagram of the conventional PLL for sensorless control of PMSG.

Therefore, a discrete-time model is required. For discretization the forward Euler method with sampling time T_s (in s) is applied to the time-continuous model (4.1). Hence, the discrete-time model of the PMSG can be written as

$$\left.\begin{aligned} u_s^d[k] &= R_s i_s^d[k] + L_s \tfrac{i_s^d[k+1]-i_s^d[k]}{T_s} - \omega_r[k] L_s i_s^q[k] + e_s^d[k], \\ u_s^q[k] &= R_s i_s^q[k] + L_s \tfrac{i_s^q[k+1]-i_s^q[k]}{T_s} + \omega_r[k] L_s i_s^d[k] + e_s^q[k], \end{aligned}\right\} \tag{4.2}$$

where k is the current sampling instant. Using (4.2), e_s^d and e_s^q can be calculated as

$$\left.\begin{aligned} e_s^d[k] &= -R_s i_s^d[k] - L_s \tfrac{i_s^d[k+1]-i_s^d[k]}{T_s} + \omega_r[k] L_s i_s^q[k] + u_s^d[k], \\ e_s^q[k] &= -R_s i_s^q[k] - L_s \tfrac{i_s^q[k+1]-i_s^q[k]}{T_s} - \omega_r[k] L_s i_s^d[k] + u_s^q[k]. \end{aligned}\right\} \tag{4.3}$$

Once e_s^d is computed from (4.3), the conventional PLL can be designed as shown in Fig. 4.3. As illustrated in this figure, e_s^d is fed back and compared to its reference $e_{s,ref}^d = 0$, while the estimation error $\Delta e_s^d = e_{s,ref}^d - e_s^d$ is processed by a fixed-gain PI controller to produce the compensation term $\Delta\hat{\omega}$ [87]. The q-axis component of the back EMF e_s^q is employed to compute the feed-forward term $\hat{\omega}_{ff}$ as follows

$$\hat{\omega}_{ff} = \frac{e_s^q[k]}{\psi_{pm}}. \tag{4.4}$$

Hence, the estimated rotor speed $\hat{\omega}$ is given by

$$\hat{\omega} = \Delta\hat{\omega} + \hat{\omega}_{ff}. \tag{4.5}$$

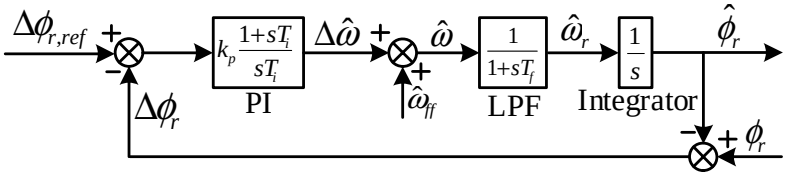

Figure 4.4: Simplified structure of the conventional PLL.

The estimated rotor speed $\hat{\omega}$ needs to be filtered by a low-pass filter (LPF) in order to reduce the impact of high-frequency noise (see Fig. 4.3). Then, the rotor position $\hat{\phi}_r[k]$ can be estimated/approximated by integrating $\hat{\omega}_r[k]$ as follows

$$\hat{\phi}_r[k] = \hat{\phi}_r[k-1] + T_s\hat{\omega}_r[k]. \tag{4.6}$$

For tuning of the PI controller, the conventional PLL (as illustrated in Fig. 4.3) can be simplified as shown in Fig. 4.4 [88]. The open-loop transfer function of the conventional PLL is

$$G_{ol}(s) = k_p\frac{1+sT_i}{sT_i}\frac{1}{1+sT_f}\frac{1}{s}, \tag{4.7}$$

where k_p and T_i are the PI controller parameters and T_f is the LPF time constant. This is a standard control problem similar to a speed control-loop of an electrical drive system. Various techniques can be utilized to select the PI controller parameters based on the desired performance criteria. In this work, the symmetrical optimum method [88, 89] was employed to compute the PI controller parameters.

4.2.2 Finite position set PLL for sensorless control of PMSG

The idea of the finite position set-phase locked loop (FPS-PLL) is based on the finite control set-model predictive control (FCS-MPC) principle. The FCS-MPC scheme utilizes the finite number of switching states of the power converter/inverter to predict its future behavior over a given prediction horizon. The switching state/action that minimizes a pre-defined cost function will be selected and applied in the next sampling interval. For a two-level power converter/inverter with a prediction horizon of one, eight switching states have to be evaluated [20].

The FCS-MPC scheme is employed in this work to replace the fixed-gain PI controller in the conventional PLL. A cost function is formulated to find the optimal rotor position from a finite number of rotor positions. However, the rotor position varies continuously between 0 and 2π rad and does not have discrete states such as the power converter/inverter. For that reason, a search-based strategy is presented to discretize the rotor position of the PMSG and to obtain a finite number of positions (eight positions for every iteration; similar to the eight switching states of a 2-level power converter). This search-based strategy is implemented as an iteration-based algorithm [90, 91]. The block diagram of the proposed FPS-PLL is illustrated in Fig. 4.5 and the flowchart of the proposed search algorithm is shown in Fig. 4.6.

The algorithm starts by reading the actual values of the currents $i_s^{\alpha\beta}[k]$ and voltages $u_s^{\alpha\beta}[k]$. Then, the initial rotor angle $\phi_{in,i}[k]$ and the cost function $g_{in}[k]$ (error) are defined. In order to obtain a finite number of rotor positions, two nested iteration loops with indices i and j are used

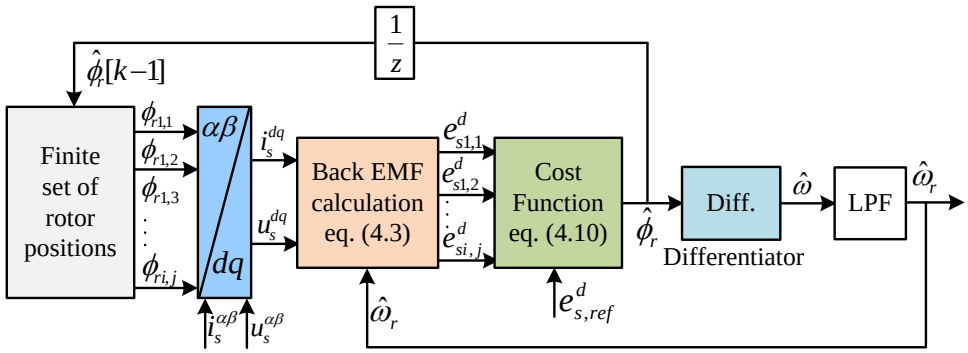

Figure 4.5: Block diagram of proposed FPS-PLL for sensorless control of PMSG.

(each linked to discrete values as indicated in Fig. 4.6). The discretized rotor position can be expressed as

$$\phi_{ri,j}[k] = \phi_{in,i}[k] + (j-4)\Delta\phi_i[k], \tag{4.8}$$

where

$$\Delta\phi_i[k] = \frac{\pi}{4} \cdot 2^{-i}. \tag{4.9}$$

Using theses rotor positions, the d-axis component of the back EMF $e^d_{si,j}$ can be calculated from (4.3) as illustrated in Fig. 4.5. Then, a cost function of the form

$$g_{i,j}[k] = e^d_{s,ref} - e^d_{si,j}, \tag{4.10}$$

is employed in the proposed FPS-PLL to select the optimal (estimated) rotor position. The rotor position whose back EMF prediction is minimizing the cost function is selected. According to Fig. 4.6, the optimal rotor position is obtained after 64 iterations during the execution of the two nested loops.

In order to clarify the proposed search-based algorithm, consider that $\phi_{in,0}[k] = \hat{\phi}_r[k-1] = 0$ rad and $g_{in}[k] = \infty$. The first iteration of the outer loop starts with $i = 0$ and $\Delta\phi_0[k] = \frac{\pi}{4}$ rad according to (4.9). Consequently, invoking (4.8), eight discrete values for the rotor position will be generated: 0, $\frac{\pi}{4}$, $\frac{\pi}{2}$, $\frac{3\pi}{4}$, π, $\frac{-3\pi}{4}$, $\frac{-\pi}{2}$, $-\frac{\pi}{4}$ rad (see also Fig. 4.7(a)). Each of these rotor positions $\phi_{ri,j}$ is employed to calculate the d-axis component of the back EMF $e^d_{si,j}$. Then, the rotor position that minimizes the cost function will be chosen to be the optimal rotor position angle $\phi_{r,opt}[k]$ and the initial angle of the second iteration $\phi_{in,1}[k]$ (i.e., $i = 1$).

Assume that the optimal angle calculated from the first iteration is $\frac{\pi}{2}$ rad. For the second iteration of the outer loop, we have $i = 1$ and $\Delta\phi_1[k] = \frac{\pi}{8}$ rad. Therefore, the accuracy of the search-based algorithm is improved by a factor of 2. Again, invoking (4.8), eight new values for the rotor position will be generated as shown in Fig. 4.7(b). Accordingly, the proposed search-based algorithm converges to the optimal rotor position as the number of iterations increases. Finally, during the last iteration (i.e., $i = 7$), the estimated rotor position is found with an accuracy of $\frac{1}{2} \times \frac{\pi}{4} \times 2^{-7} = \frac{\pi}{1024} = 0.003$ rad. Therefore, the proposed FPS-PLL estimates the rotor position with a rather high precision.

The output of the proposed FPS-PLL is the estimated rotor position. To compute the rotor speed, the change in rotor position over the last sampling period is calculated and divided by the sampling time T_s, i.e.

$$\hat{\omega}[k] = \frac{\hat{\phi}_r[k] - \hat{\phi}_r[k-1]}{T_s}, \tag{4.11}$$

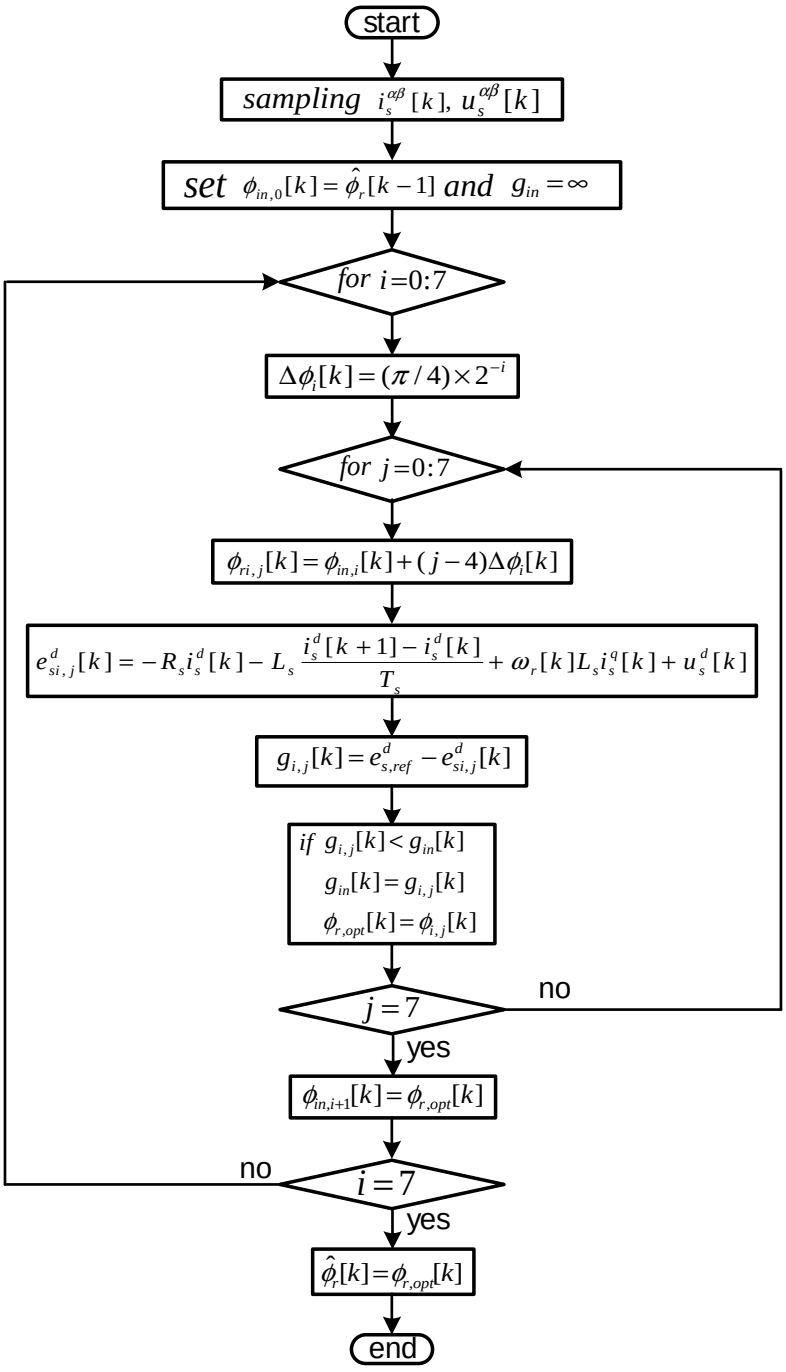

Figure 4.6: Flowchart of the proposed search-based algorithm.

where k and $k-1$ are the actual and previous sampling instant, respectively. A LPF is employed to filter this signal $\hat{\omega}[k]$. Its output is the rotor speed signal $\hat{\omega}_r[k]$ as illustrated in Fig. 4.5.

The main feature of the proposed FPS-PLL is the absence of the required effort to tune the PI controller. Consequently, the design and implementation of the proposed FPS-PLL is straightforward and can be extended to any type of electrical machines without changes in the algorithm. However, a relatively long execution time is to be expected, which is a limitation of

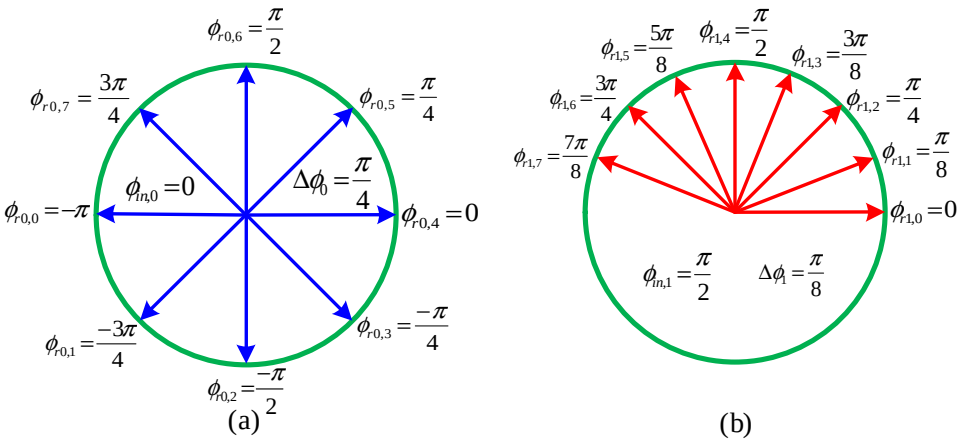

Figure 4.7: Graphical representation of the first two iterations of the proposed search-based strategy. (a) First iteration $i = 0$ and $j = 0 - 7$. (b) Second iteration $i = 1$ and $j = 0 - 7$.

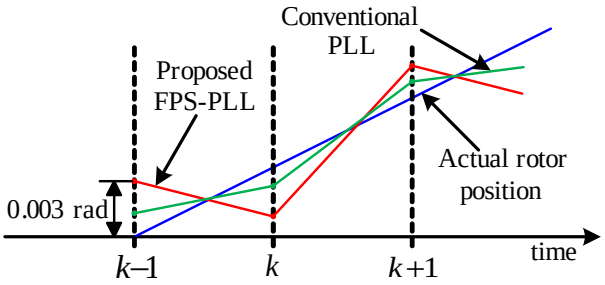

Figure 4.8: Ripples in rotor position for FPS-PLL and conventional PLL.

the proposed FPS-PLL compared to the conventional PLL. Fortunately, the sampling frequency of the control systems of WECSs is rather low ($\leq 5\,\mathrm{kHz}$) [31]; in particularly for large-scale wind turbines. Hence, the sampling period is sufficient to execute both, the control and the observer algorithm. Thanks to the continuous development of faster and more powerful digital signal processors (DSPs), execution of such algorithms will not be the bottleneck in the future.

Furthermore, the rotor position is a mechanical variable. Therefore, it varies slowly and, hence, it does not change significantly between two sampling instants. Accordingly, by initializing the proposed search-based algorithm with the output of the algorithm from the last sampling instant, i.e. $\phi_{in,0}[k] = \hat{\phi}_r[k-1]$, the number of required iterations by the search-based algorithm to estimate the rotor position can be significantly reduced as the search is performed only near the previous rotor position.

A well known disadvantage of FCS-MPC are the high ripples in the output current. Therefore, the estimated rotor position/speed using the proposed FPS-PLL contains also ripples in comparison to the estimated rotor position/speed via the conventional PLL. These ripples are produced due to the fact that the proposed FPS-PLL selects the optimal rotor position from a finite number of angles. Therefore, these angles may not represent the actual rotor position as shown in Fig. 4.8, which produces higher ripples in the estimated position. According to the proposed search algorithm, the maximum accuracy is $0.003\,\mathrm{rad}$. This means that at least ripples of $0.006\,\mathrm{rad}$ will appear in the estimated position (see Fig. 4.8). In contrast, the conventional

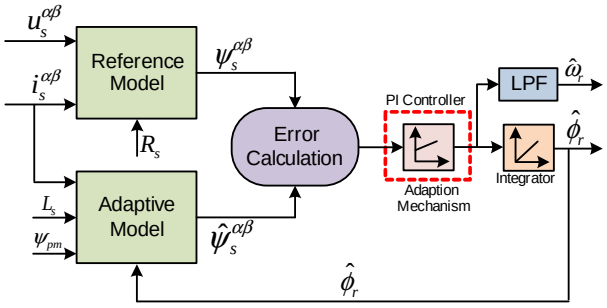

Figure 4.9: Structure of traditional MRAS observer for sensorless control of the PMSG.

PLL finds the actual rotor position from an infinite number of angles. Therefore, the estimated angle by the conventional PLL will contain (much) lower ripples.

Nevertheless, in view of (4.9), the accuracy of the proposed FPS-PLL can be improved by increasing the number of iterations, and accordingly, the ripples in the estimated position/speed can also be reduced. For example, if the indices i and j are selected from 0 to 9, the achievable accuracy will be $\frac{1}{2} \times \frac{\pi}{5} \times 2^{-9} = \frac{\pi}{5120} = 0.0006$ rad. Therefore, the ripples in the estimated position/speed will be significantly reduced. However, the computational load will increase (100 iterations are required for this case). Therefore, a trade-off between accuracy and computational load must be found. In this work, the number of iterations were fixed to $i, j \in [0, 7]$.

4.3 Model-reference adaptive system observer

In order to prove that the proposed search-based algorithm in Sec. 4.2.2 can be easily applied to other types of observers and machines, this section presents a MRAS observer based of finite position set for encoder-less control of PMSGs/DFIGs.

4.3.1 Conventional MRAS observer for sensorless control of PMSG

The traditional MRAS observer approach for encoderless control of IM and PMSM drives were first presented in [55] and [56], respectively. It is composed of two models, the reference and adaptive model, in addition to an adaption mechanism to estimate the rotor speed (see Fig. 4.9). The reference model, which is independent of the rotor speed, calculates the stator flux $\boldsymbol{\psi}_s^{\alpha\beta} = (\psi_s^{\alpha}, \psi_s^{\beta})^{\top}$ in the (α, β)-stationary reference frame as follows

$$\left.\begin{aligned} \psi_s^{\alpha}[k+1] &= \psi_s^{\alpha}[k] + T_s(u_s^{\alpha}[k] - R_s i_s^{\alpha}[k]), \\ \psi_s^{\beta}[k+1] &= \psi_s^{\beta}[k] + T_s(u_s^{\beta}[k] - R_s i_s^{\beta}[k]), \end{aligned}\right\} \tag{4.12}$$

from the PMSG stator voltages $\boldsymbol{u}_s^{\alpha\beta} = (u_s^{\alpha}, u_s^{\beta})^{\top}$ and currents $\boldsymbol{i}_s^{\alpha\beta} = (i_s^{\alpha}, i_s^{\beta})^{\top}$, where T_s is the sampling time (in s) of the discrete control system, and $k \in \mathbb{N}$ is the sampling instant.

The adaptive model, which depends on the rotor position, uses the currents $\boldsymbol{i}_s^{\alpha\beta}$ to estimate the stator flux $\hat{\boldsymbol{\psi}}_s^{\alpha\beta}$ as shown in Fig. 4.10, where the currents $\boldsymbol{i}_s^{\alpha\beta}$ are transformed to the synchronously rotating (d, q)-reference frame using the estimated rotor position $\hat{\phi}_r$. The flux in the rotating reference frame dq can be calculated as

$$\hat{\psi}_s^{d}[k] = L_s \hat{i}_s^{d}[k] + \psi_{pm} \quad \text{and} \quad \hat{\psi}_s^{q}[k] = L_s \hat{i}_s^{q}[k]. \tag{4.13}$$

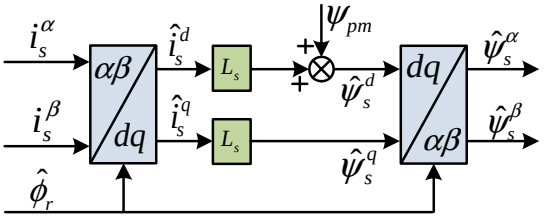

Figure 4.10: Adaptive model of the MRAS observer.

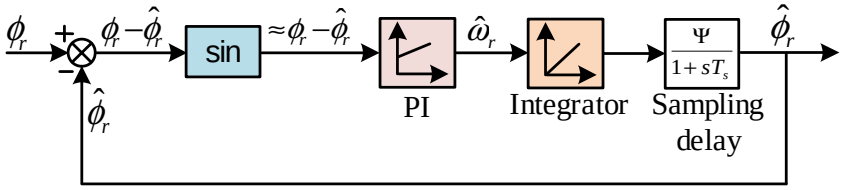

Figure 4.11: Simplified structure of the traditional MRAS observer for PMSGs.

Then this estimated flux linkage vector $\hat{\boldsymbol{\psi}}_s^{dq}$ is transformed back to the stationary (α, β)-reference frame as shown in Fig. 4.10. The error in the stationary reference frame between the reference and estimated value of the stator fluxes is defined as

$$\varepsilon[k] = \hat{\psi}_s^\alpha[k]\psi_s^\beta[k] - \hat{\psi}_s^\beta[k]\psi_s^\alpha[k] = \underbrace{|\hat{\boldsymbol{\psi}}_s^{\alpha\beta}[k]||\boldsymbol{\psi}_s^{\alpha\beta}[k]|}_{=:\Psi} \sin(\underbrace{\phi_r[k] - \hat{\phi}_r[k]}_{=:\Delta\phi_r[k]}), \tag{4.14}$$

where a correct estimation of rotor angle (and speed) is achieved when the angle difference is zero, i.e. $\Delta\phi_r[k] := \phi_r - \hat{\phi}_r = 0$.

In [55], the MRAS observer is treated as a vector Phase-Locked Loop (PLL), where the estimated rotor position $\hat{\phi}_r$ is found by controlling the angle between the the estimated flux $\hat{\boldsymbol{\psi}}_s^{\alpha\beta}$ and the computed stator flux $\boldsymbol{\psi}_s^{\alpha\beta}$. The estimated flux is varied till coinciding with the reference flux. This is because the error ε in (4.14) is defined as the cross product between the output of the adaptive model and that of the reference model. Therefore, the error ε is driven to zero when the phase angle between $\boldsymbol{\psi}_s^{\alpha\beta}$ and $\hat{\boldsymbol{\psi}}_s^{\alpha\beta}$ is also zero. The merits of using the cross product to define the error ε is discussed in [55], [56] and the interested reader can refer to these references.

For small difference between the actual and estimated rotor position $\Delta\phi_r[k]$, the following assumption

$$\sin(\Delta\phi_r[k]) \approx \Delta\phi_r[k] \tag{4.15}$$

is valid. A PI controller drives this error to zero by adjusting $\hat{\omega}_r$. Its output is the estimated rotor speed $\hat{\omega}_r$ which is integrated to obtain the estimated rotor angle $\hat{\phi}_r$ (see Fig. 4.11). Considering the sampling delay and the gain Ψ, the open-loop transfer function (TF) of the traditional MRAS adaptation mechanism shown in Fig. 4.11 can be written as

$$G_{ol}(s) = k_{pi}^M \frac{1 + sT_{pi}^M}{sT_{pi}^M} \frac{1}{1 + sT_s} \frac{\Psi}{s}, \tag{4.16}$$

where k_{pi}^M and T_{pi}^M are the PI controller parameters. Following the tuning procedure in [89], the PI controller parameters can be designed.

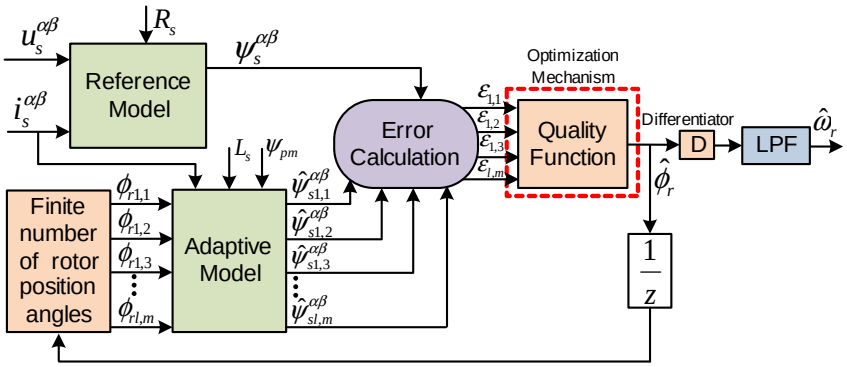

Figure 4.12: Structure of the proposed FPS-MRAS observer for encoderless control of PMSG.

Algorithm 1 : Proposed FPS-MRAS Observer for encoderless control of PMSG.

Step I: Read the currents $i_s^{\alpha\beta}[k]$ and voltages $u_s^{\alpha\beta}[k]$.
Step II: Compute $\boldsymbol{\psi}_s^{\alpha\beta}[k+1] = \boldsymbol{\psi}_s^{\alpha\beta}[k] + T_s(\boldsymbol{u}_s^{\alpha\beta}[k] - R_s \boldsymbol{i}_s^{\alpha\beta}[k])$.
Step III:
Initiate the angle $\phi_{in,0}[k] = \hat{\phi}_r[k-1]$ and error $\varepsilon_{in}[k] = \infty$
For $i = 0:1:7$
  calculate $\Delta\phi_i[k] = \frac{\pi}{4} \times 2^{-i}$
    For j=0:1:7
      calculate $\phi_{ri,j}[k] = \phi_{in,i}[k] + (j-4)\Delta\phi_i[k]$.
      calculate $\hat{\boldsymbol{i}}_{si,j}^{dq}[k] = \boldsymbol{T}_P(\phi_{ri,j}[k])^{-1} \boldsymbol{i}_s^{\alpha\beta}[k]$.
      calculate $\hat{\psi}_{si,j}^{d}[k] = L_s \hat{i}_{si,j}^{d}[k] + \psi_{pm}$ and $\hat{\psi}_{si,j}^{q}[k] = L_s \hat{i}_{si,j}^{q}[k]$.
      calculate $\hat{\boldsymbol{\psi}}_{si,j}^{\alpha\beta}[k] = \boldsymbol{T}_P(\phi_{ri,j}[k]) \hat{\boldsymbol{\psi}}_{si,j}^{dq}[k]$
      evaluate the quality function $\varepsilon_{i,j}[k] = \hat{\psi}_{si,j}^{\alpha}[k]\ \psi_s^{\beta}[k] - \hat{\psi}_{si,j}^{\beta}[k]\ \psi_s^{\alpha}[k]$.
        if $\varepsilon_{i,j}[k] < \varepsilon_{in}[k]$
          $\varepsilon_{in}[k] = \varepsilon_{i,j}[k]$
          $\phi_{r,opt}[k] = \phi_{i,j}[k]$
        end
    end
  set $\phi_{in,i+1}[k] = \phi_{r,opt}[k]$
end
Step IV: $\hat{\phi}_r[k] = \phi_{r,opt}[k]$
Step V: Return to **Step I**.

4.3.2 Finite Position Set-MRAS observer for sensorless control of PMSG

Similarly to the FPS-PLL, The search-based algorithm illustrated in Fig. 4.6 is applied to the conventional MRAS observer to replace the fixed-again PI controller in the adaption mechanism of MRAS observer. The proposed FPS-MRAS observer is shown in Fig. 4.12 and its algorithm is described in **Algorithm 1** [92], [93].

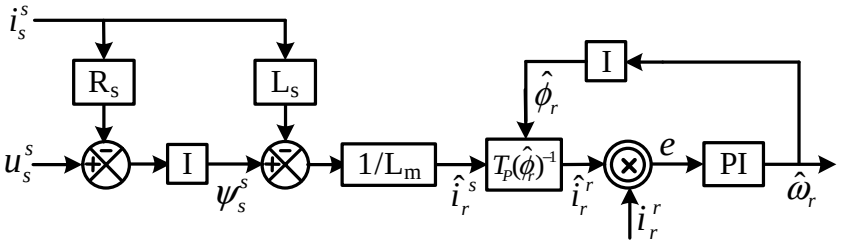

Figure 4.13: Traditional MRAS observer for encoderless control of DFIGs.

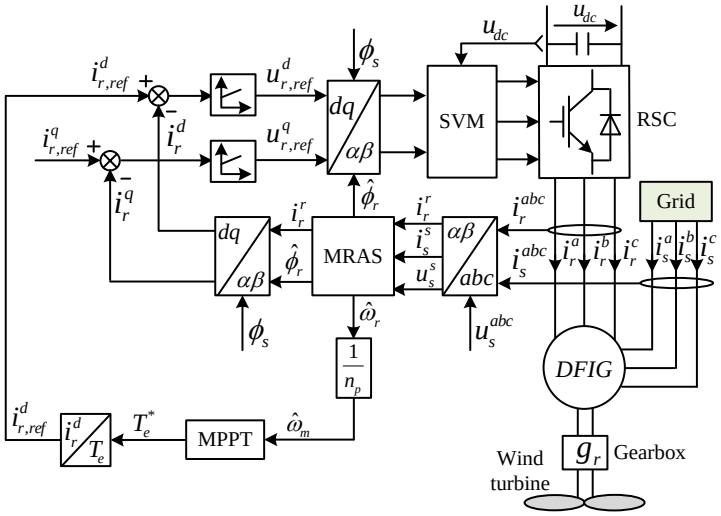

Figure 4.14: Sensorless voltage-oriented control (VOC) for DFIGs using MRAS observer.

4.3.3 Conventional MRAS observer for sensorless control of DFIG

It has been concluded in [57] that the rotor current based MRAS observer is the best option among the other types of MRAS estimators for encoder-less control of DFIGs. Therefore, this type of MRAS observers is selected in this work. As described before, the MRAS observer is based on two models: a reference model and an adaptive model, see Fig. 4.13. The adaptive model is fed by the measured stator current $\boldsymbol{i}_s^s$ and the measured stator (grid) voltage $\boldsymbol{u}_s^s$. From the adaptive model, the rotor current $\hat{\boldsymbol{i}}_r^s$ is estimated from (2.36) via

$$\hat{\boldsymbol{i}}_r^s(t) = \frac{1}{L_m}\big(\boldsymbol{\psi}_s^s(t) - L_s \boldsymbol{i}_s^s(t)\big), \tag{4.17}$$

where $\boldsymbol{\psi}_s^s(t)$ is computed from (2.35) as follows,

$$\boldsymbol{\psi}_s^s(t) = \int_0^t \big(\boldsymbol{u}_s^s(\tau) - R_s \boldsymbol{i}_s^s(\tau)\big)\mathrm{d}\tau. \tag{4.18}$$

The PI controller is fed by the estimated rotor current $\hat{\boldsymbol{i}}_r^s$ and the measured rotor current $\boldsymbol{i}_r^r$ in the *rotor reference frame*. The goal is to estimate rotor position $\hat{\phi}_r$ and rotor speed $\hat{\omega}_r$. To achieve that the estimated and the measured rotor current must be compared; to do so, the estimated rotor current $\hat{\boldsymbol{i}}_r^s$ (in the stator reference frame) must be expressed in the rotor reference frame,

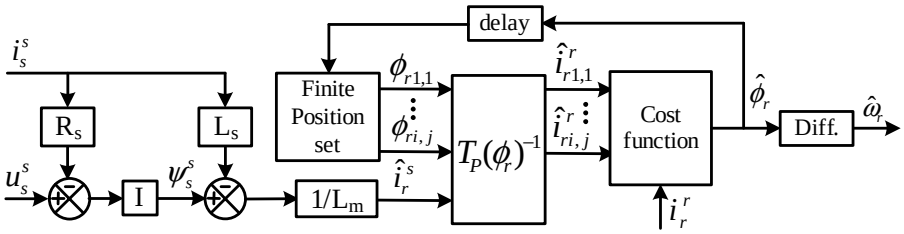

Figure 4.15: Proposed FPS-MRAS observer for encoderless control of DFIGs in variable speed WTSs.

Algorithm 2 : Proposed FPS-MRAS Observer for encoder-less control of DFIGs.

Step 1: Read the currents $\boldsymbol{i}_r^r$, $\boldsymbol{i}_s^s$ and voltages $\boldsymbol{u}_s^s$.
Step 2: calculate $\boldsymbol{\psi}_s^s(t) = \int_0^t \big(\boldsymbol{u}_s^s(\tau) - R_s \boldsymbol{i}_s^s(\tau)\big)\mathrm{d}\tau$.
Step 3: Estimate $\hat{\boldsymbol{i}}_r^s(t) = \frac{1}{L_m}\big(\boldsymbol{\psi}_s^s(t) - L_s \boldsymbol{i}_s^s(t)\big)$.
Step 4:
Initiate the angle $\phi_{in,0} = 0$ and error $J_{in} = \infty$
For $i = 0:1:7$
  calculate $\Delta\phi_i = \frac{\pi}{4} \cdot \frac{1}{2^i}$.
    For $j = 0:1:7$
      calculate $\phi_{ri,j} = \phi_{in,i} + (j-4)\Delta\phi_i$.
      calculate $\hat{\boldsymbol{i}}_{ri,j}^r = \boldsymbol{T}_P(\hat{\phi}_{ri,j})^{-1}\hat{\boldsymbol{i}}_r^s$.
      evaluate the cost function $J_{i,j} = \hat{i}_{ri,j}^{\alpha} i_r^{\beta} - \hat{i}_{ri,j}^{\beta} i_r^{\alpha}$.
        if $J_{i,j} < J_{in}$
          $J_{in} = J_{i,j}$
          $\phi_{r,opt} = \phi_{i,j}$
        end
    end
  set $\phi_{in,i+1} = \phi_{r,opt}$
end
Step 5: $\hat{\phi}_r = \phi_{r,opt}$
Step 6: Return to **Step 1**.

i.e. $\hat{\boldsymbol{i}}_r^r = \boldsymbol{T}_P(\hat{\phi}_r)^{-1}\hat{\boldsymbol{i}}_r^s$, where $\boldsymbol{T}_P(\hat{\phi}_r)^{-1}$ is the inverse Park transformation matrix. The "error" between estimated $\hat{\boldsymbol{i}}_r^r$ and measured rotor current $\boldsymbol{i}_r^r$ is defined as

$$\boldsymbol{e} := \hat{\boldsymbol{i}}_r^r \times \boldsymbol{i}_r^r = \|\hat{\boldsymbol{i}}_r^r\| \, \|\boldsymbol{i}_r^r\| \sin\big(\angle(\hat{\boldsymbol{i}}_r^r, \boldsymbol{i}_r^r)\big).$$

The PI controller drives this error to zero by adjusting $\hat{\omega}_r$. Its output is the estimated speed $\hat{\omega}_r$ which is integrated to obtain the estimated rotor angle $\hat{\phi}_r$, see Fig. 4.13. Finally, the estimated speed $\hat{\omega}_r$ and position $\hat{\phi}_r$ are feed backed to the control system of the DFIG as illustrated in Fig. 4.14.

4.3.4 Finite Position Set-MRAS observer for sensorless control of DFIG

The proposed search-based algorithm in Sec. 4.2.2 is employed to replace the fixed-gain PI controller in the conventional MRAS observer described in Sec. 4.3.3. The schematic diagram of the proposed finite-position-set (FPS-MRAS) observer for encoderless control of DFIGs is depicted in Figure 4.15 and its algorithm is described in **Algorithm 2** [93].

4.4 Experimental results and discussion

In this section the experimental results of the proposed finite-position-set observers are given and compared with that of the conventional ones.

4.4.1 Experimental results of PLL for sensorless control of PMSGs

In this section, the performance of the proposed FPS-PLL is compared to the conventional one. In general, for surface-mounted PMSGs, a good estimation performance of speed and position observers, and also of the proposed FPS-PLL, is challenging at low sampling rates and/or very low speeds (i.e. approaching zero) owing to the rotor isotropy which leads to an unobservable system [53], [94]. Fortunately, the variable-speed wind turbines operate only when the wind speed is higher than the cut-in wind speed [53], [87]. Consequently, zero speed is not within the discussed operation range. In this work, the mechanical speed operation range is selected from 4-$100\,\mathrm{rad/s}$ in order to present the performance of the proposed observer in low and medium speeds . The speed of the rotor is controlled by the RSM and the PMSG controls the electromagnetic torque. The torque command of the PMSG $T_e^\star$ is selected to be lower than the rated output mechanical torque of the RSM ($T_{RSM}^{rated} = 61\,\mathrm{N\,m}$). The PMSG is controlled using the FOC technique as shown in Fig. 4.1 and the RSM is controlled using a nonlinear PI-based FOC technique [37].

The power converter's switching frequencies as well as the sampling frequency are set to $4\,\mathrm{kHz}$ with a dead-time period of $1\,\mu\mathrm{s}$. The PI controller parameters of the conventional PLL are set to $k_p = 303$ and $T_i = 11\,\mathrm{ms}$, respectively, which are selected to obtain a controller bandwidth of $300\,\mathrm{rad/s}$ covering the selected speed range of the adopted PMSG. The measurements were exported from the dSPACE platform to MATLAB and plotted. In terms of execution time, it was found that the proposed FPS-PLL required $32\,\mu\mathrm{s}$, while the conventional one was carried out in $5\,\mu\mathrm{s}$.

Fig. 4.16 illustrates the transient response of the proposed FPS-PLL and conventional PLL for a step change in the rotor speed. From top to bottom, the plotted signals are measured speed ω_r, estimated speed $\hat{\omega}_r$; error $\Delta\omega_r = \omega_r - \hat{\omega}_r$ between measured and estimated speed; error $\Delta\phi_r = \phi_r - \hat{\phi}_r$ between measured and estimated rotor position. At the time instant $t = 5\,\mathrm{s}$, a step change in the reference mechanical speed $\omega_{m,ref}$ of the rotor from $5\,\mathrm{rad/s}$ to $80\,\mathrm{rad/s}$ has been applied to the RSM control system. The torque command $T_e^\star$ is set to $-30\,\mathrm{N\,m}$. According to Fig. 4.16, the proposed FPS-PLL gives a better transient performance than the conventional PLL. The oscillations in the estimated speed $\hat{\omega}_r$ are eliminated and the error $\Delta\omega_r$ converges quickly to zero. The maximum error $\Delta\omega_r$ using the proposed FPS-PLL is $12.8\,\mathrm{rad/s}$, while using the conventional PLL is $18.65\,\mathrm{rad/s}$.

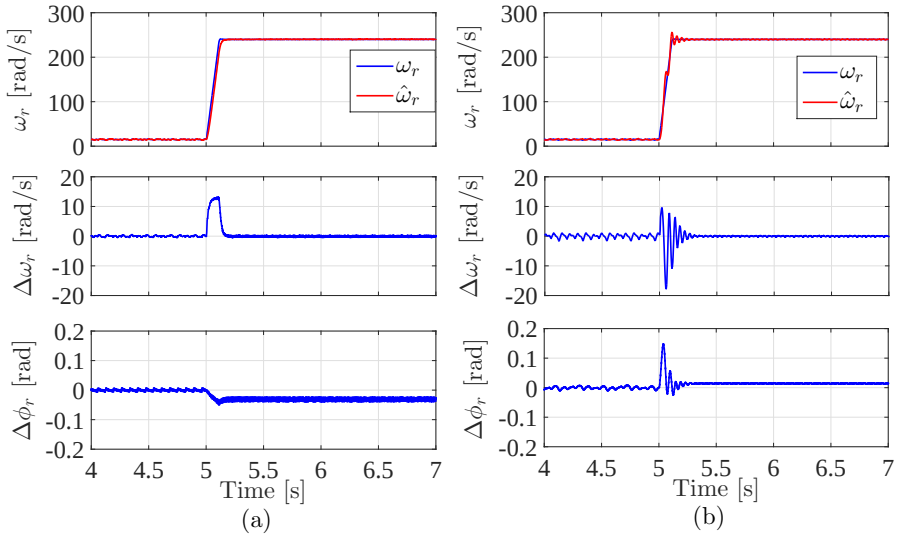

Figure 4.16: Experimental results for a step change in the rotor speed of the PMSG: (a) Proposed FPS-PLL and (b) conventional PLL.

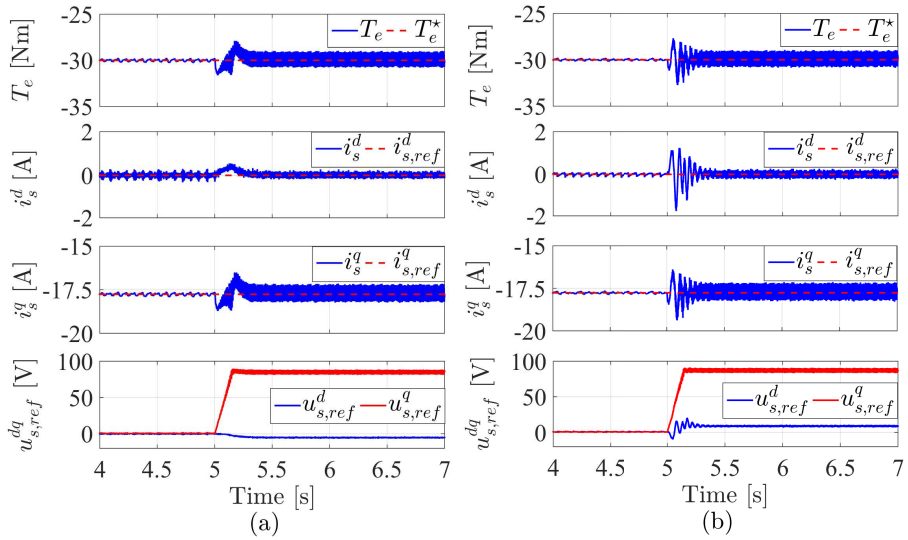

Figure 4.17: Performance of the FOC system of the PMSG for a step change in the rotor speed: (a) Using the proposed FPS-PLL and (b) using the conventional PLL.

According to the analysis presented in Sec. 4.2.2, the error $\Delta\phi_r$ should be $0.003\,\text{rad}$. However, in Fig. 4.16, it can be observed that the value of the estimation error $\Delta\phi_r$ during transients and steady-state is larger than the theoretical value (i.e. $\Delta\phi_r > 0.003\,\text{rad}$). This is due to unmodel dynamics of the machine, inverter nonlinearities, and harmonics in the estimated back EMF. Several solutions have been presented in the literature for those problems [82]–[86]. Nevertheless, the accuracy of the proposed FPS-PLL is still good and acceptable.

Fig. 4.17 shows the performance of the FOC scheme of the PMSG for a step change in the rotor speed (as illustrated in Fig. 4.16) with the proposed FPS-PLL and the conventional PLL. From top to bottom, the plotted signals are calculated electro-magnetic torque T_e, optimal

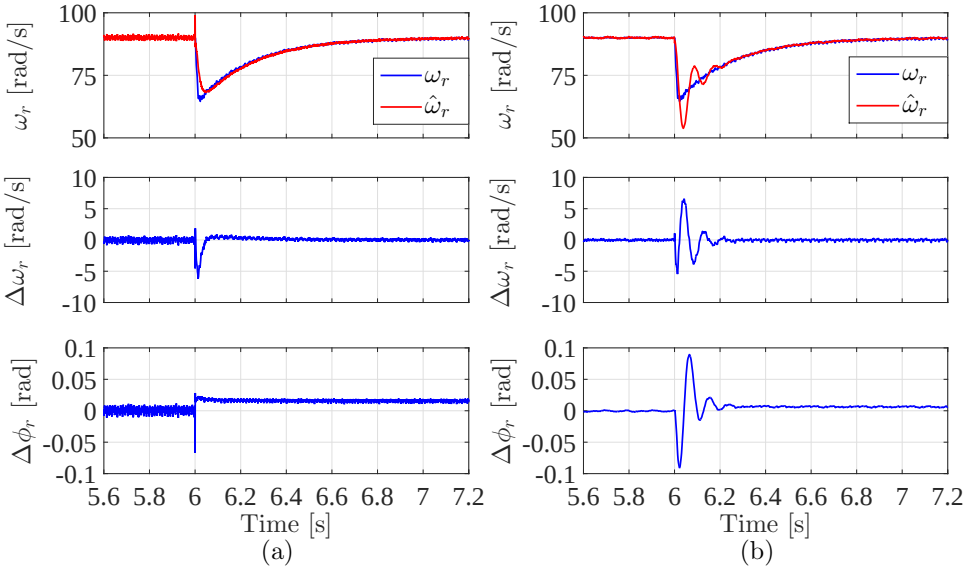

Figure 4.18: Experimental results for a step change in the reference torque $T_e^\star$ of the PMSG: (a) Proposed FPS-PLL and (b) conventional PLL.

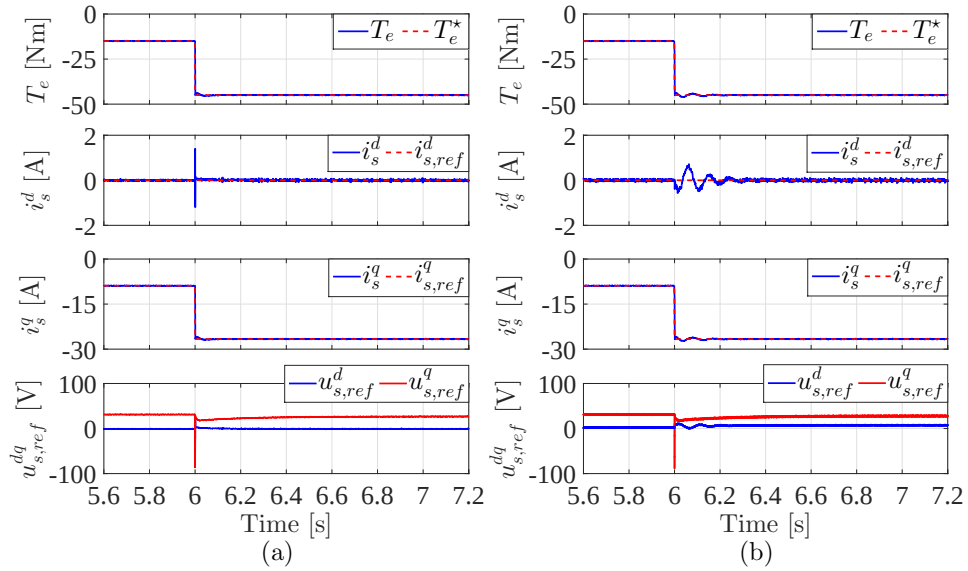

Figure 4.19: Performance of the FOC system of the PMSG for a step change in the reference torque $T_e^\star$: (a) Using the proposed FPS-PLL and (b) using the conventional PLL.

torque $T_e^\star$; measured and reference d-axis currents (i_s^d, $i_{s,ref}^d$); measured and reference q-axis currents (i_s^q, $i_{s,ref}^q$); reference d- and q-axis voltages ($u_{s,ref}^d$, $u_{s,ref}^q$). It can be observed from Fig. 4.17 that the performance of the FOC strategy using the proposed FPS-PLL is better than that with the conventional PLL. In contrast to the performance with the conventional PLL, no oscillations in the torque, currents, and voltage are produced by the proposed FPS-PLL.

Fig. 4.18 shows the dynamic response of the proposed FPS-PLL and the conventional PLL for a step change in the reference torque $T_e^\star$. At the time instant $t = 6\,\mathrm{s}$, a step change in the

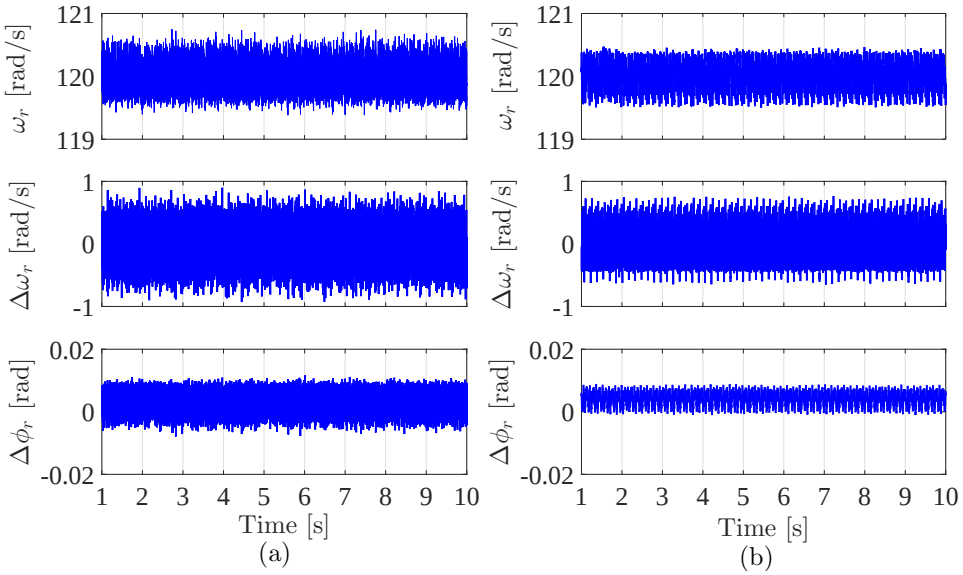

Figure 4.20: Experimental results at steady-state: (a) Proposed FPS-PLL and (b) conventional PLL.

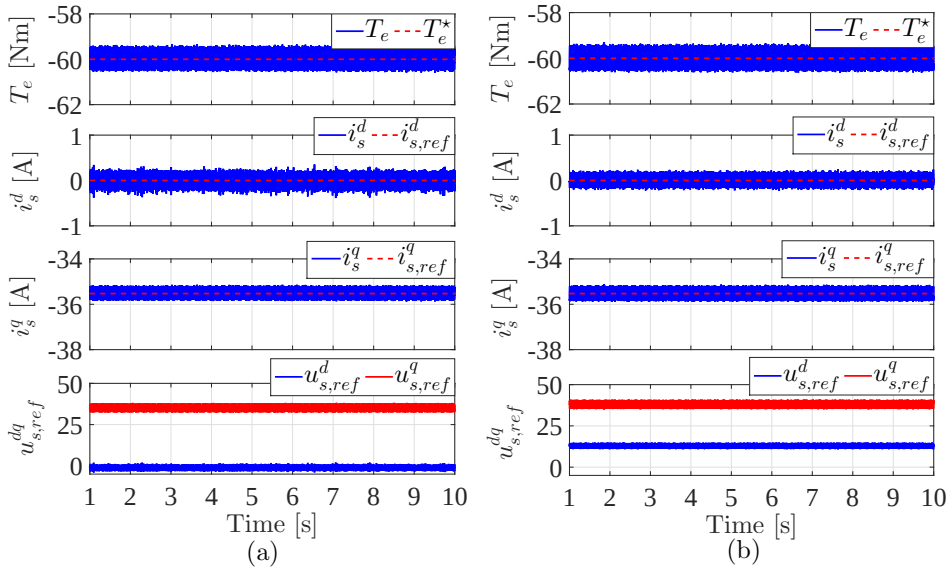

Figure 4.21: Performance of the FOC system of the PMSG for a steady-state: (a) Using the proposed FPS-PLL and (b) using the conventional PLL.

reference torque $T_e^\star$ from $-15\,\mathrm{N\,m}$ to $-45\,\mathrm{N\,m}$ has been applied to the PMSG control system. The mechanical speed ω_m of the rotor is set to $30\,\mathrm{rad/s}$ by the RSM control scheme. A gain, the proposed FPS-PLL yields a better dynamic performance than the conventional PLL. For the proposed FPS-PLL, no oscillations in the estimated speed and position are present. For the conventional PLL, oscillations in the estimated speed and position are visible. Due to the proposed search algorithm, the proposed FPS-PLL gives a faster dynamic performance in comparison to the conventional PLL. Fig. 4.19 illustrates the response of the FOC system of the PMSG dur-

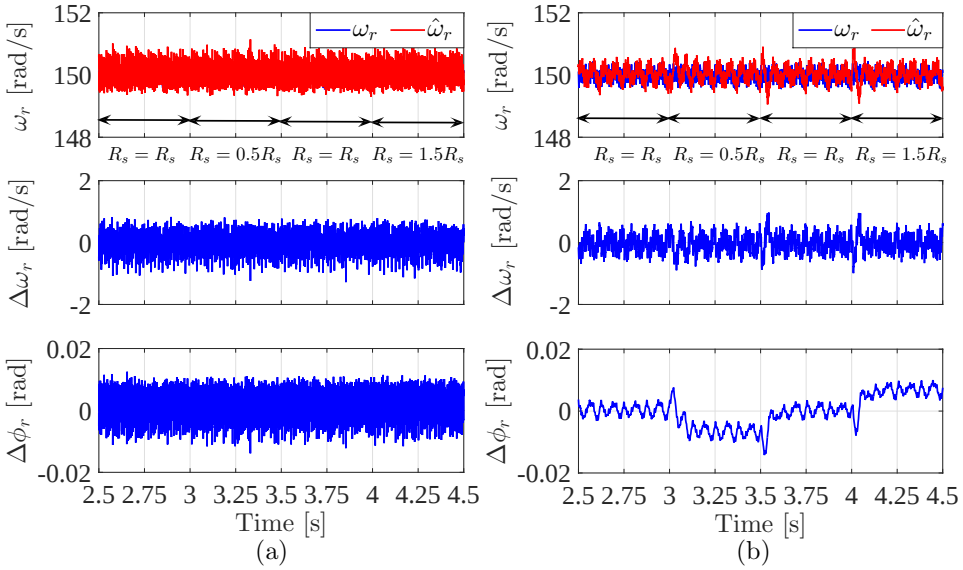

Figure 4.22: Experimental results for $\pm 50\%$ step changes in the stator resistance R_s of the PMSG: (a) Proposed FPS-PLL and (b) conventional PLL.

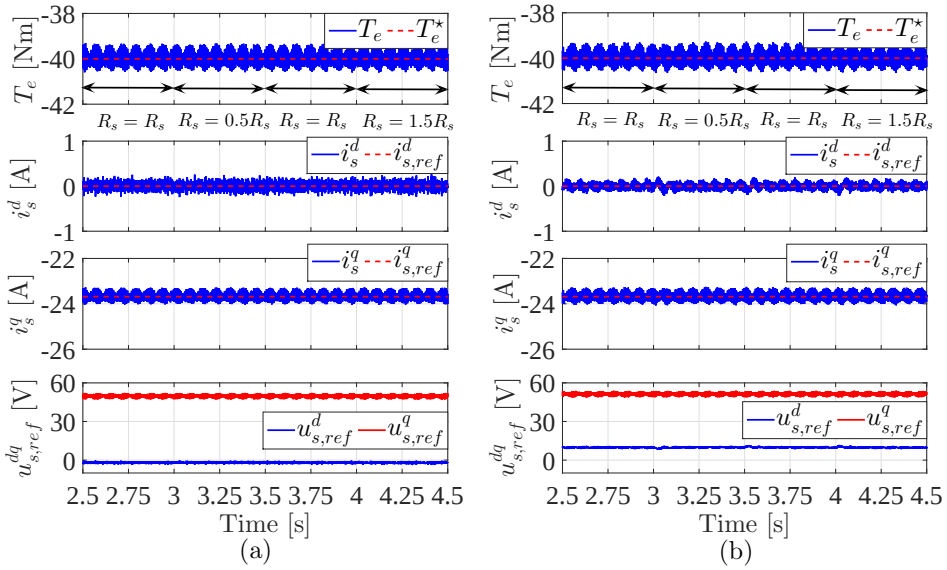

Figure 4.23: Performance of the FOC system of the PMSG for $\pm 50\%$ step changes in the stator resistance R_s : (a) Using the proposed FPS-PLL and (b) using the conventional PLL.

ing the step change in the reference torque $T_e^\star$ (as was shown in Fig. 4.18) using the proposed FPS-PLL and the conventional PLL. Again, the performance of FOC system with the proposed FPS-PLL is better than the response with the conventional PLL.

In order to also compare the steady-state performance of the proposed FPS-PLL and conventional PLL, the steady-state response of both observers are shown in Fig. 4.20. The mechanical speed ω_m of the rotor is set to $40\,\mathrm{rad/s}$ by the RSM control system and the reference torque $T_e^\star$ is set to $-60\,\mathrm{N\,m}$. At this torque (i.e. $T_e^\star = -60\,\mathrm{N\,m}$), the RSM operates (almost) at its

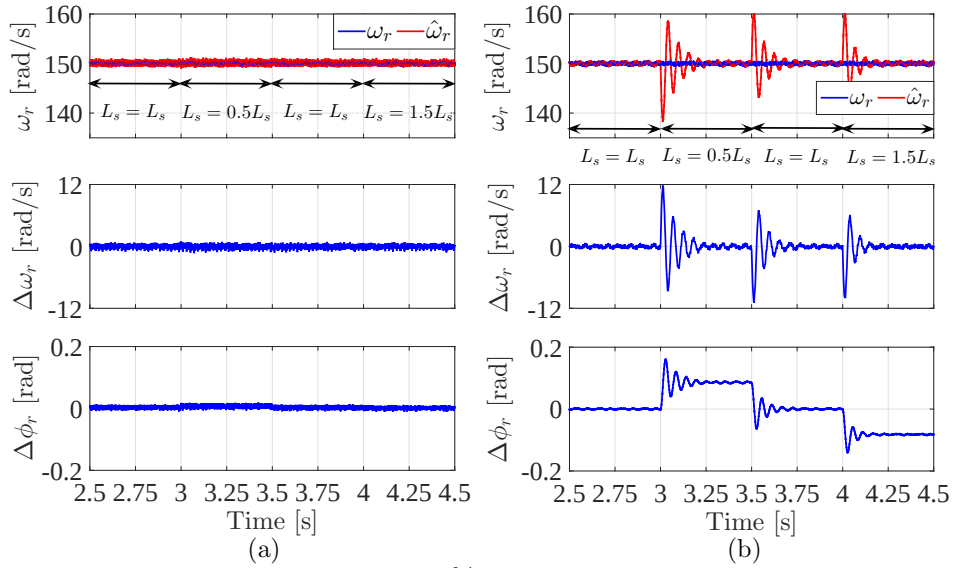

Figure 4.24: Experimental results for $\pm 50\%$ step changes in the stator inductance L_s of the PMSG: (a) Proposed FPS-PLL and (b) conventional PLL.

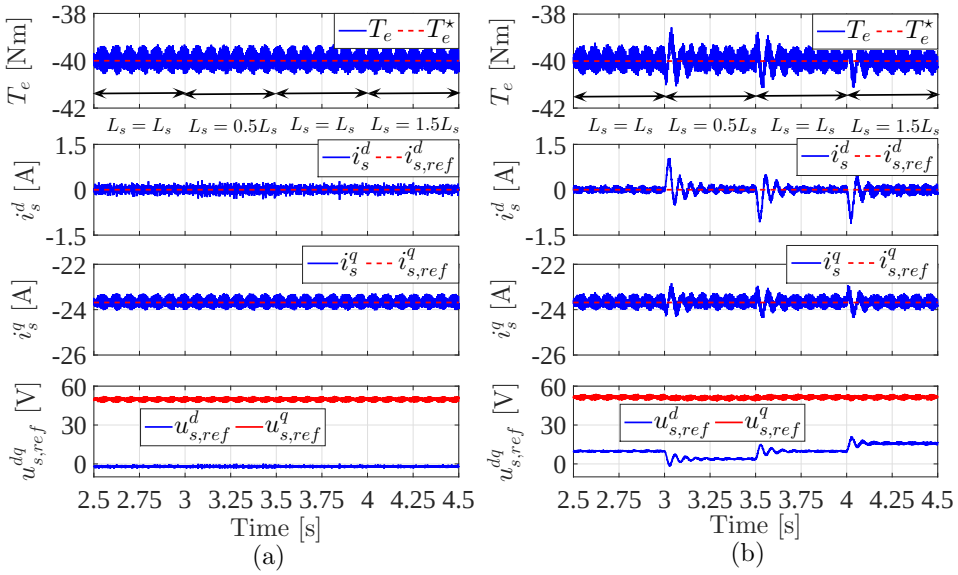

Figure 4.25: Performance of the FOC system of the PMSG for $\pm 50\%$ step changes in the stator inductance L_s : (a) Using the proposed FPS-PLL and (b) using the conventional PLL.

rated mechanical torque (i.e. $T_{RSM}^{rated} = 61\,\mathrm{N\,m}$). It can be observed that the proposed FPS-PLL gives slightly higher ripples in the estimated speed and position than the conventional PLL. However, its performance is still satisfactory. Fig. 4.21 shows the steady-state performance of the FOC system of the PMSG (as illustrated in Fig. 4.20) with the proposed FPS-PLL and the conventional PLL. It can be seen from this figure that the steady-state performances of the FOC systems are very similar for both PLLs.

The parameter sensitivities of the proposed FPS-PLL and the conventional PLL are also investigated and compared. Fig. 4.22 illustrates the performance of both PLLs for $\pm 50\%$ software step changes in the stator resistance R_s of the PMSG. The mechanical speed ω_m of the rotor is

set to $50\,\mathrm{rad/s}$ by the RSM control system and the reference torque $T_e^\star$ is set to $-40\,\mathrm{N\,m}$. It is clear that the variation of the stator resistance R_s has (almost) no effect on the response of the proposed FPS-PLL, while the conventional PLL is more sensitive to this parameter uncertainty and its response is slightly deteriorated. Fig. 4.23 shows the performance of the FOC system of the PMSG during the variation of the resistance R_s (as illustrated in Fig. 4.22) using the proposed FPS-PLL and the conventional PLL. In this case, a similar behavior can be observed.

The response of both PLLs (i.e. proposed FPS-PLL and conventional one) are also investigated when the stator inductance L_s of the PMSG is varied. At the time instants $t = 3\,\mathrm{s}$ and $t = 4\,\mathrm{s}$, a -50% and a $+50\%$ step change of the stator inductance L_s were applied within the real-time model. The mechanical speed and reference torque are the same as in Fig. 4.22 (i.e. $50\,\mathrm{rad/s}$ and $-40\,\mathrm{N\,m}$). According to Fig. 4.24, it can be observed that the proposed FPS-PLL gives a transient response without oscillation compared to the conventional PLL. The peak-to-peak oscillations in $\hat{\omega}_r$ using the proposed FPS-PLL are almost zero in contrast to $18\,\mathrm{rad/s}$ for the conventional PLL. Again, the variation of the stator inductance L_s generates a negligible error in the rotor position estimation using the proposed FPS-PLL, while a large error is produced using the conventional PLL (see Fig. 4.24). Accordingly, the enhancement in robustness against PMSG parameter variations is mainly due to the replacement of the fixed-gain PI controller by the proposed search-based approach. Fig. 4.25 illustrates the performance of the FOC system of the PMSG during variations of the stator inductance L_s (as illustrated in Fig. 4.24) with the proposed FPS-PLL and the conventional PLL. It can be observed from Fig. 4.25 that the performance of the FOC system with the proposed FPS-PLL is better than that of the conventional PLL.

4.4.2 Experimental results of MRAS observer for sensorless control of PMSGs

To practically implement both MRAS observers (i.e. proposed FPS-MRAS and conventional one), the integrator in the reference model was replaced by a low-pass filter with a cut-off frequency of $5\,\mathrm{Hz}$ to minimize drift/initial condition problems associated with pure integration. The PMSG is controlled using the FOC technique as shown in Fig. 4.1. The power converter's switching frequencies/sampling frequency are the same as in Sec. 4.4.1, i.e $4\,\mathrm{kHz}$. The PI controller proportional and integral gains of the traditional MRAS observer are set to $k_{pi}^M = 667$ and $T_{pi}^M = 9\,\mathrm{ms}$, respectively, which are selected to get a bandwidth of $630\,\mathrm{rad/s}$; covering the whole speed range of the adopted PMSG. Consequently, the damping factor value is 2.5, which is considered as a compromise between acceptable transient performance and sufficient bandwidth. The gain Ψ is selected to be equal to square of the permanent-magnet flux of the machine (i.e. $\Psi = \psi_{pm}^2$) because the flux of the PMSG is varying in a narrow range. Therefore, this assumption is valid and acceptable [56]. The proposed FPS-MRAS observer required $47\,\mu\mathrm{s}$ execution time, against $9\,\mu\mathrm{s}$ for the traditional one.

Fig. 4.26 shows the dynamic response of the proposed FPS-MRAS and traditional MRAS observer under step changes in the rotor speed. From top to bottom, the waveforms are measured speed ω_r, estimated speed $\hat{\omega}_r$; the error $\Delta\omega_r = \omega_r - \hat{\omega}_r$ between the measured speed and estimated speed; the error $\Delta\phi_r = \phi_r - \hat{\phi}_r$ between the measured and estimated rotor position. At the time instants $t = 2\,\mathrm{s}$ and $t = 4\,\mathrm{s}$, step changes in the reference mechanical speed ω_m of the rotor from $15\,\mathrm{rad/s}$ to $75\,\mathrm{rad/s}$ and then back to $45\,\mathrm{rad/s}$ have been applied to the RSM

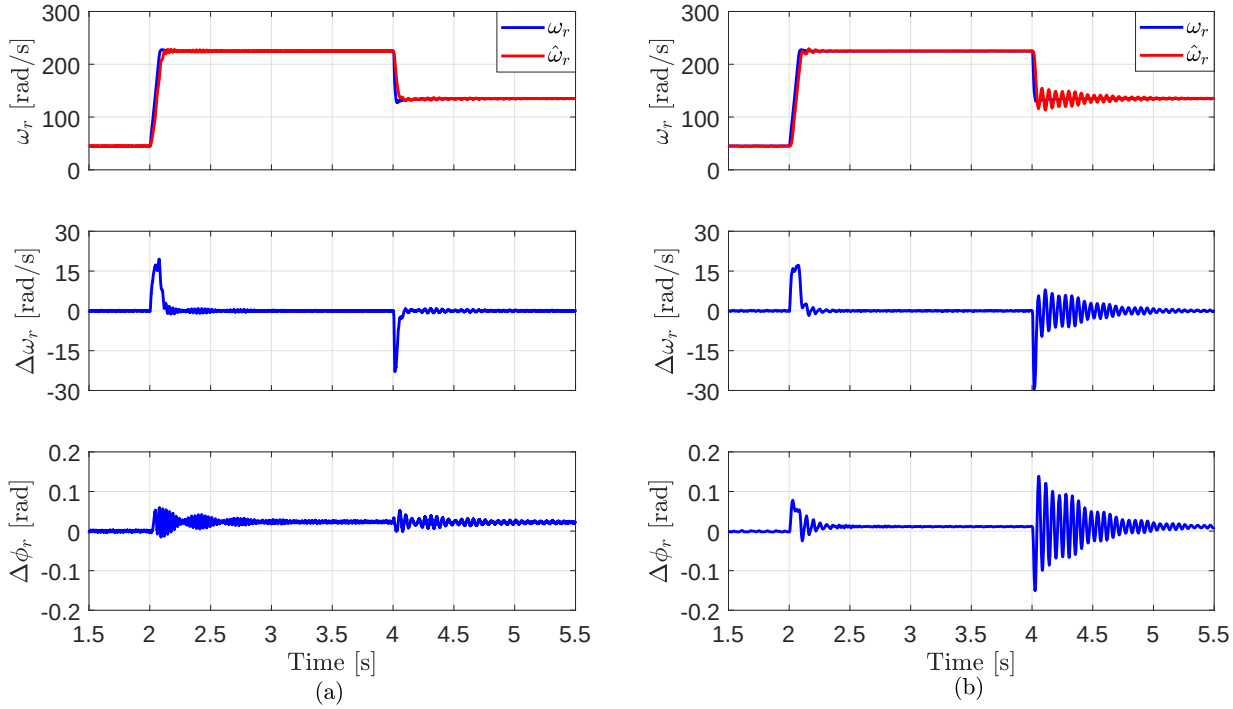

Figure 4.26: Experimental results for step changes in the rotor speed ω_r of the PMSG: (a) Proposed FPS-MRAS and (b) conventional MRAS.

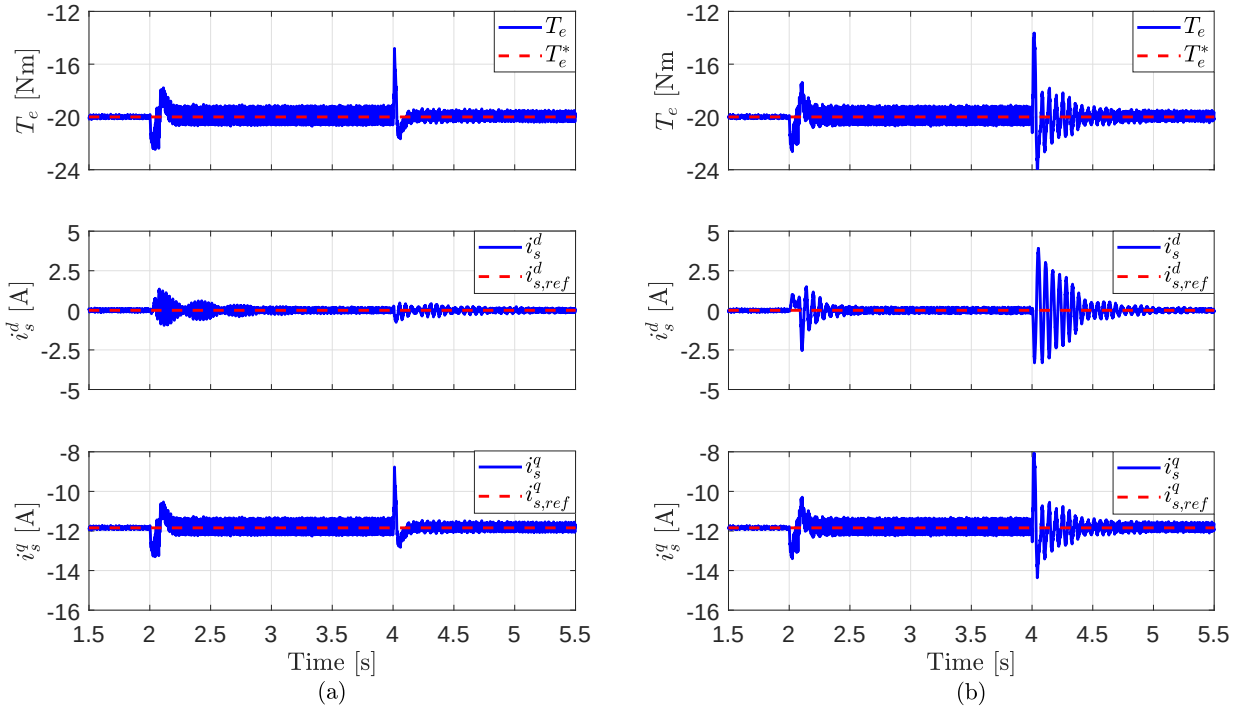

Figure 4.27: Performance of the FOC system of the PMSG for step changes in the rotor speed ω_r of the PMSG: (a) Proposed FPS-MRAS and (b) conventional MRAS.

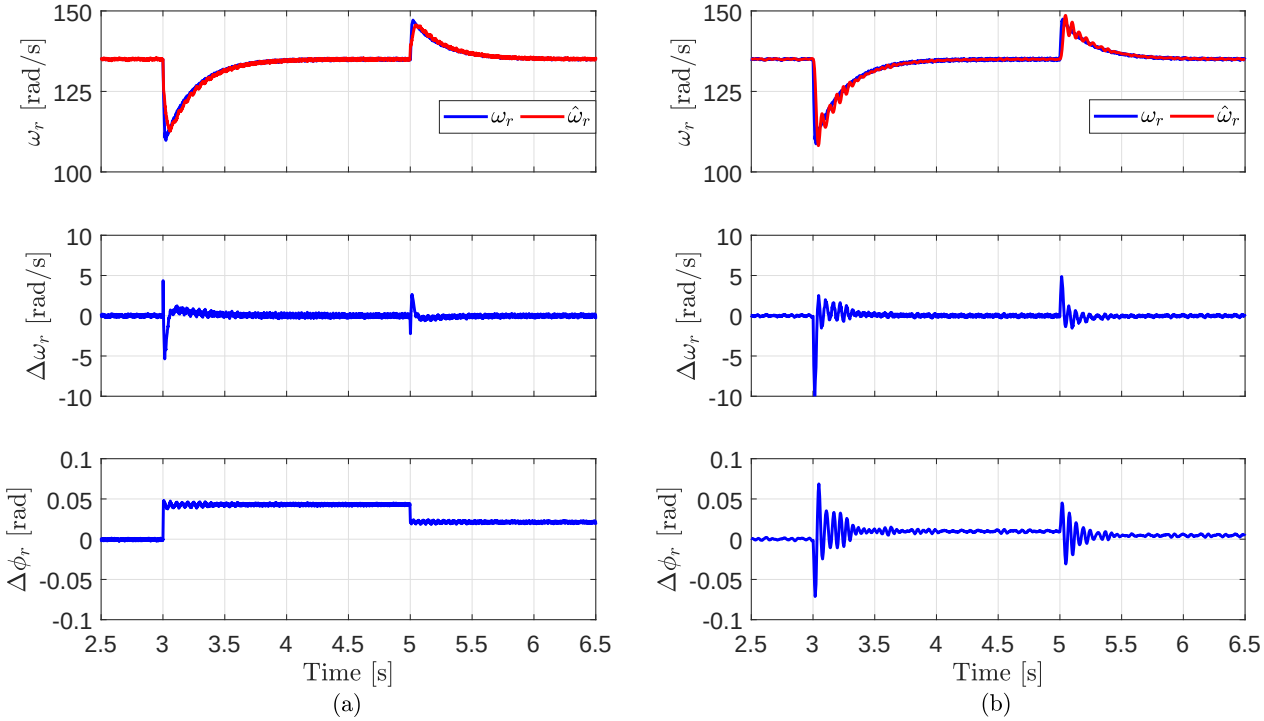

Figure 4.28: Experimental results for step changes in the electro-magnetic torque $T_e^\star$: (a) Proposed FPS-MRAS and (b) conventional MRAS.

control system. The torque command $T_e^\star$ is set to $-20\,\mathrm{N\,m}$. According to Fig. 4.26, the proposed FPS-MRAS observer demonstrates better dynamic performance than the traditional one. The oscillation in the estimated speed $\hat{\omega}_r$ is significantly reduced and the error $\Delta\omega_r$ converge quickly to zero. The maximum error $\Delta\omega_r$ using the proposed FPS-MRAS observer is $26\,\mathrm{rad/s}$, while using the traditional MRAS is $30\,\mathrm{rad/s}$. Moreover, The estimated rotor position $\hat{\phi}_r$ using the proposed FPS-MRAS observer tracks the measured position ϕ_r with better performance than that of the traditional one. Accordingly, the error $\Delta\phi_r$ using the proposed FPS-MRAS observer is significantly smaller than that when adopting the traditional MRAS observer.

Fig. 4.27 illustrates the response of the FOC scheme of the PMSG for the step changes in the rotor speed that given in Fig. 4.26 with the proposed FPS-MRAS observer and the traditional one. From top to bottom, the plotted signals are calculated and reference electro-magnetic torque (T_e, $T_e^\star$), measured and reference d-axis currents (i_s^d, $i_{s,ref}^d$), and measured and reference q-axis currents (i_s^q, $i_{s,ref}^q$). It can be observed from Fig. 4.27 that the response of the FOC strategy using the proposed FPS-MRAS observer is better than that with the traditional MRAS observer. In contrast to the performance with the traditional MRAS observer, negligible oscillations in the torque and currents are produced by the proposed FPS-MRAS observer.

Fig. 4.28 illustrates the dynamic response of the proposed FPS-MRAS observer and the traditional one under step changes in the reference torque $T_e^\star$. At the time instants $t = 3\,\mathrm{s}$ and $t = 5\,\mathrm{s}$, step changes in the reference reference torque $T_e^\star$ from $-10\,\mathrm{N\,m}$ to $-40\,\mathrm{N\,m}$ and then back to $-25\,\mathrm{N\,m}$ have been applied to the PMSG control scheme. The mechanical speed ω_m of the rotor is set to $45\,\mathrm{rad/s}$ by the RSM control system. It can be observed from this figure that the proposed FPS-MRAS observer gives a better dynamic response than that of the traditional MRAS observer. For the proposed FPS-MRAS observer, no oscillations in the estimated speed/position

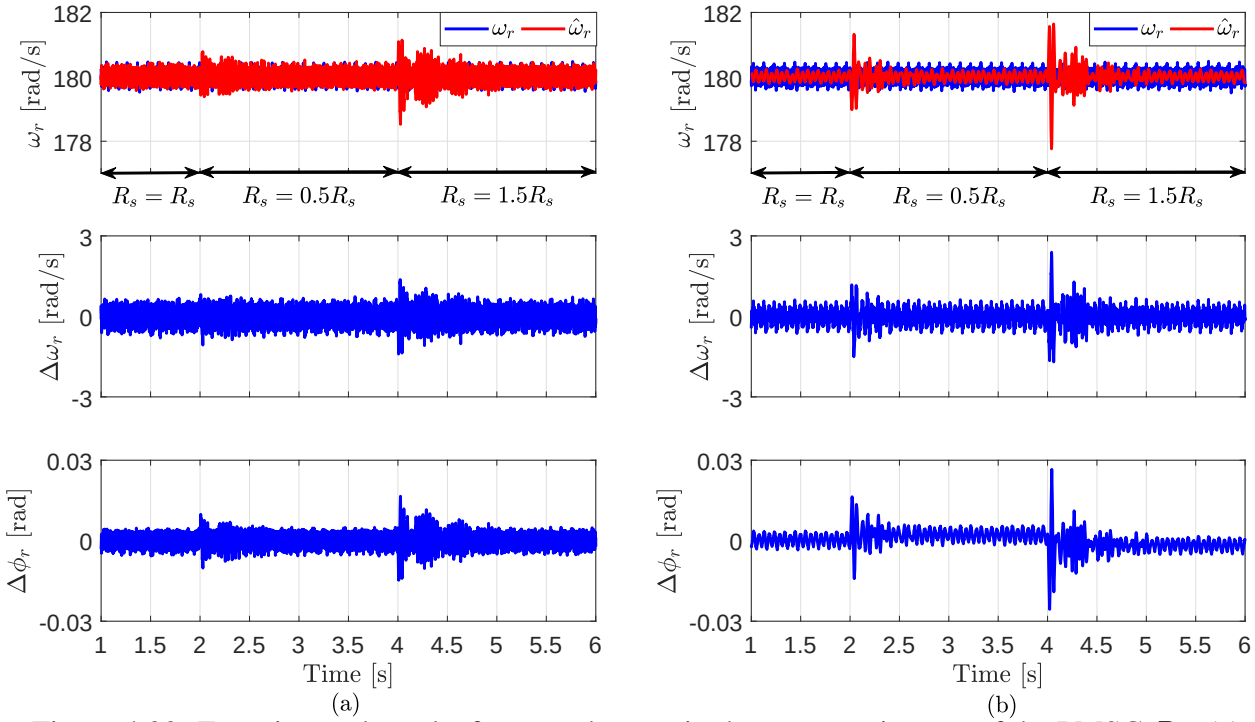

Figure 4.29: Experimental results for step changes in the stator resistance of the PMSG R_s: (a) Proposed FPS-MRAS and (b) conventional MRAS.

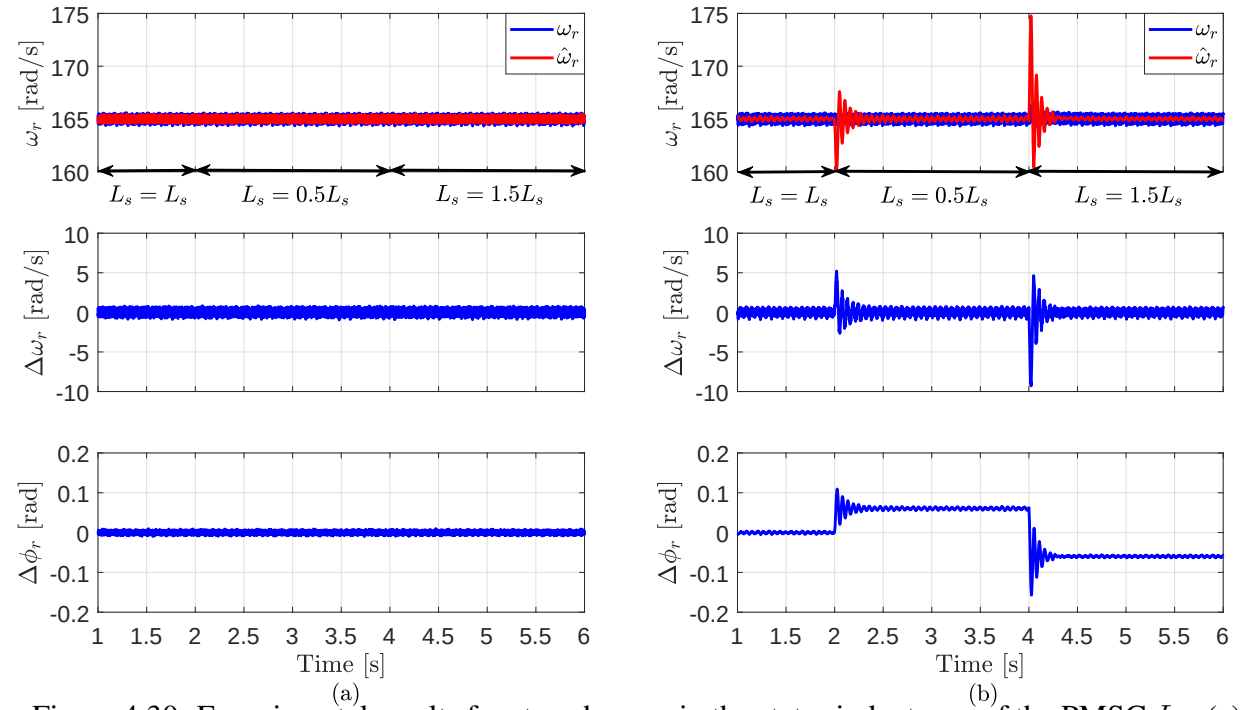

Figure 4.30: Experimental results for step changes in the stator inductance of the PMSG L_s: (a) Proposed FPS-MRAS and (b) conventional MRAS.

are exist. For the traditional MRAS observer, oscillations in the estimated speed/position are present. Due to the proposed search-based algorithm, the proposed FPS-MRAS observer gives a faster transient performance in comparison to the traditional one.

The parameter sensitivity of the proposed FPS-MRAS observer is also investigated and compared with the traditional MRAS observer. Fig. 4.29 shows the response of both observers at $\mp 50\%$ step changes in stator resistance R_s within the real-time model (i.e within the software model). The mechanical speed ω_m of the rotor is set to $60\,\mathrm{rad/s}$ by the RSM control system and the torque command $T_e^\star$ is set to $-30\,\mathrm{N\,m}$. It is clear that the variation of stator resistance R_s has a small effect in the performance of the proposed FPS-MRAS observer, while the traditional MRAS is less immune and the performance is deteriorated.

The performance of both observers were tested when varying the stator inductance L_s. At the time instants $t = 2\,\mathrm{s}$ and $t = 4\,\mathrm{s}$, $\mp 50\%$ *software* step changes in the stator inductance L_s within the real time model has been applied. According to Fig. 4.30, it can be observed that the proposed FPS-MRAS observer demonstrates better dynamics without oscillation during transients compared to the traditional MRAS observer. The peak-peak oscillations in $\hat{\omega}_r$ using the proposed FPS-MRAS is almost nulled compared to $14\,\mathrm{rad/s}$ for the traditional one. Again, the variation of the stator inductance L_s produces a negligible error in the rotor position estimation using the proposed FPS-MRAS observer, while a large error is generated using the traditional version, see Fig. 4.30. Hence, the enhancement in robustness against PMSG parameter variations is mainly because of the replacement of the fixed-gain PI controller in the adaptation mechanism of MRAS observer by the proposed search-based approach.

4.4.3 Experimental results of MRAS observer for sensorless control of DFIGs

The speed of the rotor is controlled by the EESM and the DFIG controls the electro-magnetic torque. The DFIG is controlled using the VOC technique as shown in Fig. 4.14 and the EESM is controlled using a nonlinear PI-based FOC technique. The power converter's switching frequencies as well as the sampling frequency are set to $8\,\mathrm{kHz}$ with a dead-time period of $1\,\mu\mathrm{s}$.

Fig. 4.31 illustrates the dynamic response of the proposed FPS-MRAS observer and conventional one at a change in the rotor mechanical speed ω_m from $120\,\mathrm{rad/s}$ to $170\,\mathrm{rad/s}$ (i.e. from sub-synchronous to super-synchronous operation) by the EESM. The plotted signals from top to bottom are: measured mechanical speed ω_m, estimated mechanical speed $\hat{\omega}_m$; error $\Delta\omega_m = \omega_m - \hat{\omega}_m$ between detected and estimated speed; error $\Delta\phi_m = \phi_m - \hat{\phi}_m$ between detected and estimated rotor position. The reference electro-magnetic torque of the DFIG T_e^* is set to $-25\,\mathrm{N\,m}$ and the reference q-axis current of the DFIG rotor $i_{r,ref}^q$ is set to $0\,\mathrm{A}$. It can be observed that the performance of the proposed FPS-MRAS observer is better than that of the conventional one. The peak-peak error in speed/position estimation using the proposed FPS-MRAS observer is lower than that of the conventional MRAS observer, see Fig. 4.31.

In Fig. 4.32, the performance of the proposed FPS-MRAS observer and traditional one under step changes in the optimal (electro-magnetic) torque $T_e^\star$ is illustrated. At $t = 2\,\mathrm{s}$ and $t = 4\,\mathrm{s}$, step changes in the optimal torque $T_e^\star$ from $-20\,\mathrm{N\,m}$ to $-40\,\mathrm{N\,m}$ and back to $-15\,\mathrm{N\,m}$ were applied to the DFIG control algorithm. The mechanical speed of the rotor is kept constant at $140\,\mathrm{rad/s}$ by the EESM control system. Again, it can be observed that the performance of the proposed FPS-MRAS estimator is better than that of the classical one.

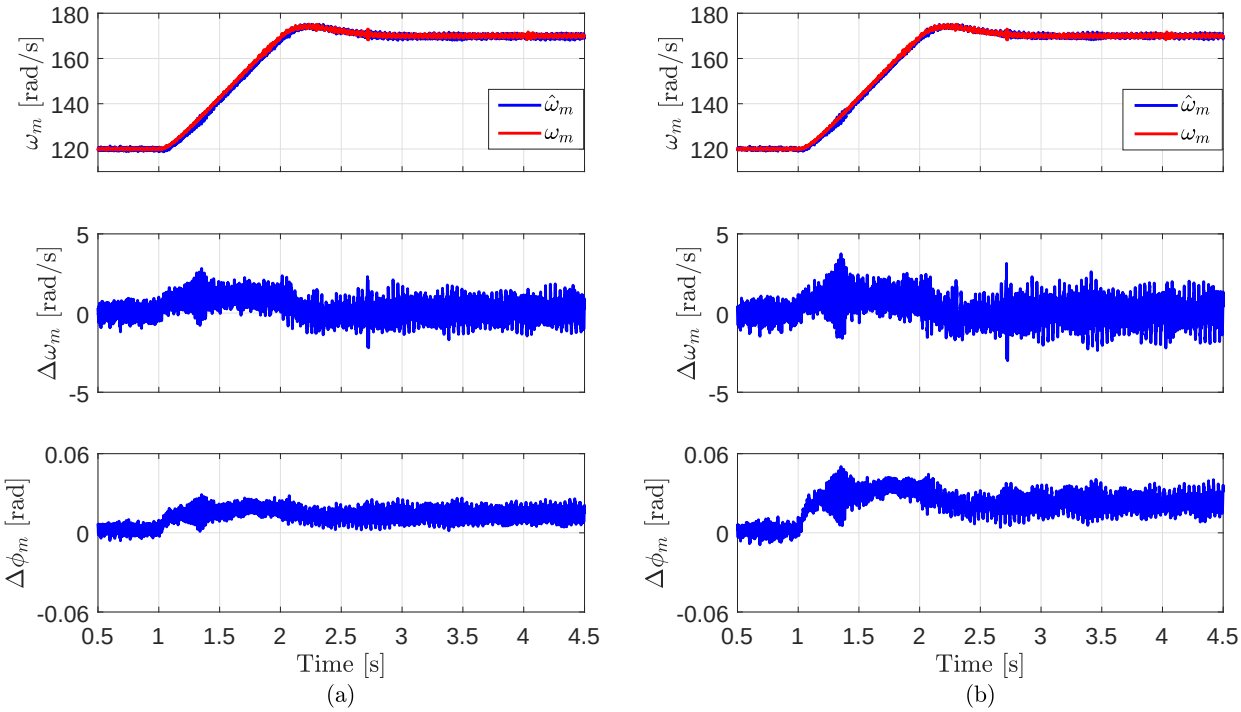

Figure 4.31: Experimental results under changing the rotor mechanical speed of the DFIG: (a) Proposed FPS-MRAS and (b) conventional MRAS.

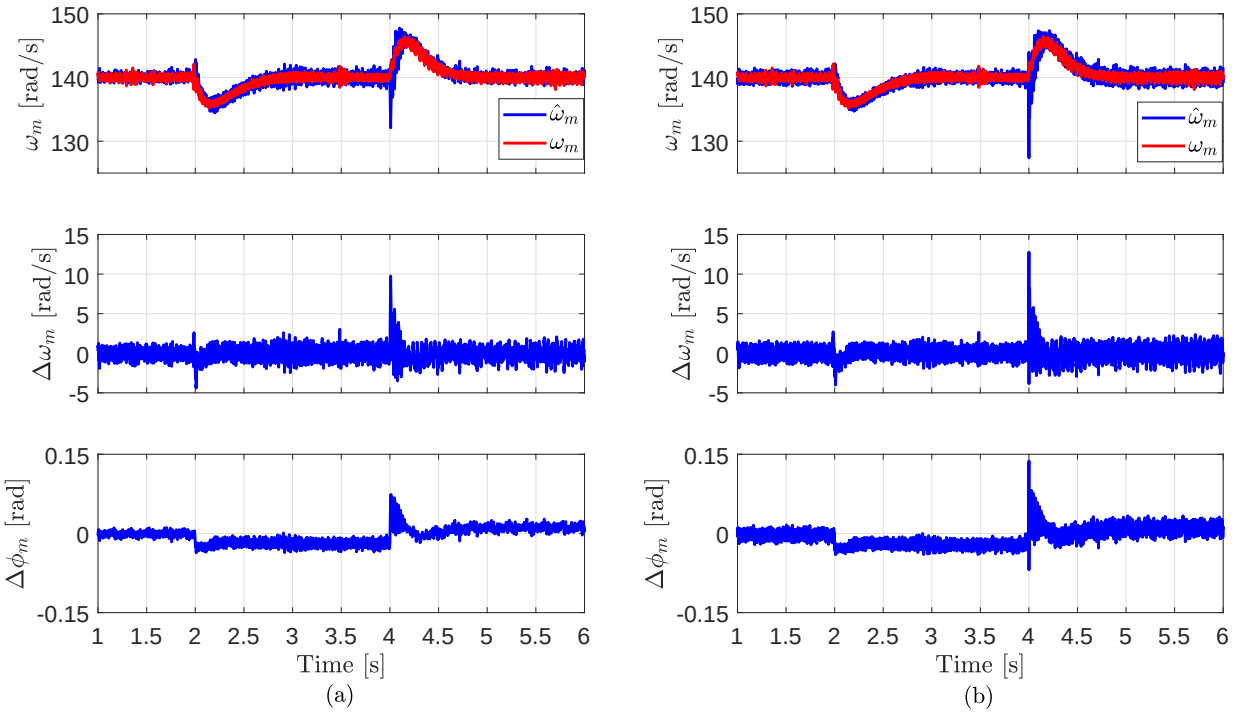

Figure 4.32: Experimental results at step changes in the electro-magnetic torque $T_e^\star$ of the DFIG $i_{r,ref}^d$: (a) Proposed FPS-MRAS and (b) conventional MRAS.

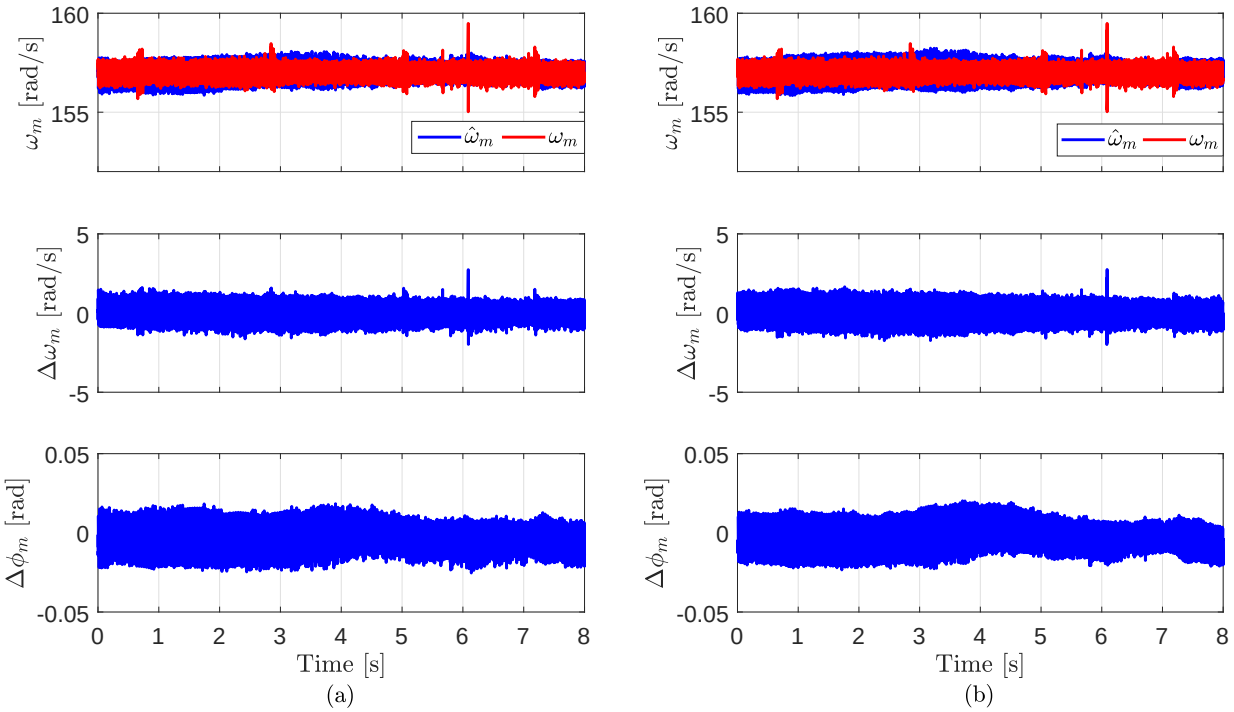

Figure 4.33: Experimental results at the synchronous speed of the DFIG: (a) Proposed FPS-MRAS and (b) conventional MRAS.

Furthermore, the performance of the proposed FPS-MRAS observer and traditional one has been investigated at the synchronous speed of the DFIG (i.e. at $\omega_m = 157\,\mathrm{rad/s}$). The reference electro-magnetic torque of the DFIG T_e^* is set to $-35\,\mathrm{N\,m}$. According to Fig. 4.33, the response of the proposed FPS-MRAS estimator is similar to that of the conventional one.

The robustness of the proposed FPS-MRAS observer and traditional one has been also tested under variations of the parameters of the DFIG. In Fig. 4.34, the performance of both observers under a $\mp 50\%$ software variation of the stator resistance R_s of the DFIG is illustrated. The mechanical speed of the rotor is kept constant at $145\,\mathrm{rad/s}$ by the EESM control system and electro-magnetic torque of the DFIG T_e^* is set to $-30\,\mathrm{N\,m}$. It can be observed that both estimators (i.e. proposed FPS-MRAS observer and traditional one) demonstrated good robustness to variations of the stator resistance R_s of the DFIG due to the fact that the stator resistance R_s is very small in particularly of large generators.

Finally, the response of both observers under a $\mp 50\%$ software variation of the mutual inductance L_m of the DFIG is shown in Fig. 4.35. The mechanical speed of the rotor is kept constant at $150\,\mathrm{rad/s}$ by the EESM control system and electro-magnetic torque of the DFIG T_e^* is set to $-33\,\mathrm{N\,m}$. According to Fig. 4.35, the proposed FPS-MRAS observer illustrated better robustness to variations of the mutual inductance L_m of the DFIG than the classical one. Thanks to the proposed search-based algorithm.

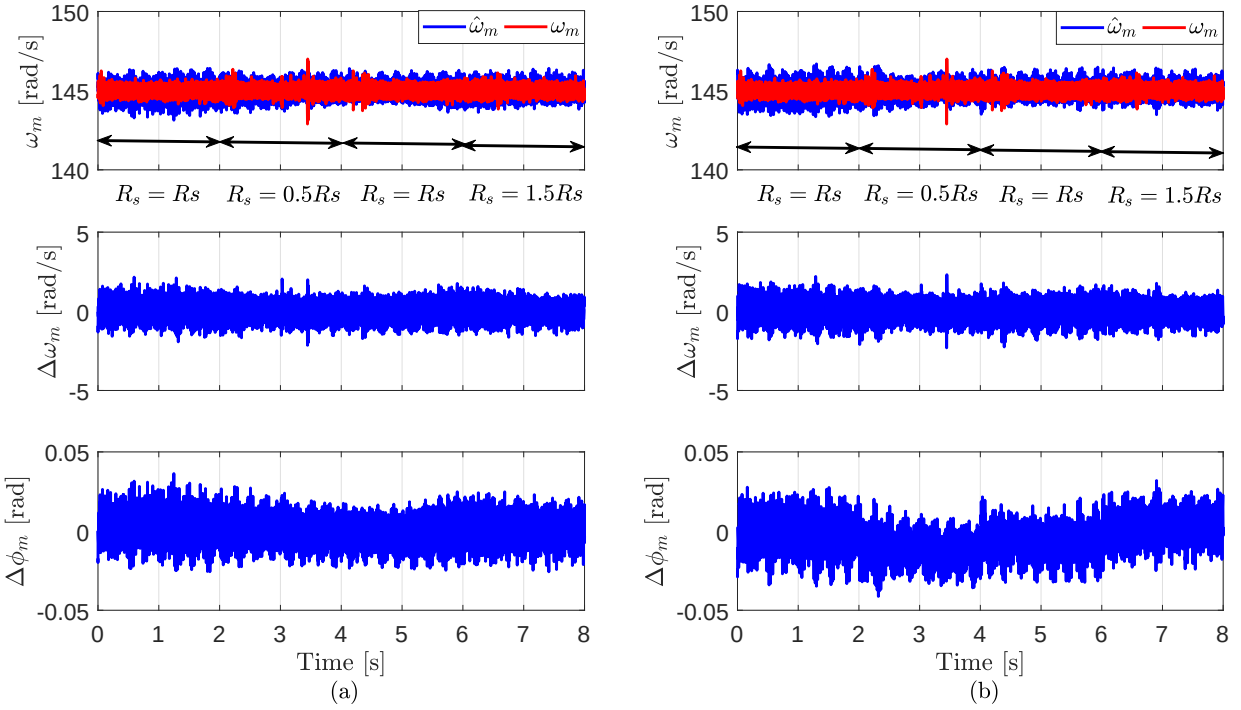

Figure 4.34: Experimental results for step changes in the stator resistance R_s of the DFIG: (a) Proposed FPS-MRAS and (b) conventional MRAS.

4.5 Summary

In this chapter, a search-based algorithm is proposed for extending the principles of the FCS-MPC to be applied for speed/position observers. The proposed algorithm is applied firstly to the well-known PLL based observer for sensorless control of PMSGs in variable-speed wind turbines applications. Then, it is extended to MRAS observer for PMSGs/DFIGs. The proposed finite-position-set (FPS) observers have been experimentally implemented and their performances have been compared with that of the traditional ones. The results illustrated that the FPS observers have the following advantages:

- The dynamic performance of the proposed FPS-PLL/FPS-MRAS observers is better than that of the conventional ones.
- The robustness of the proposed FPS-PLL/FPS-MRAS observers to variations of the machine parameters is better than that of the conventional estimators.
- The required effort to tune the PI controllers in the conventional PLL/MRAS observers is eliminated.
- The concept of the proposed search-based algorithm is simple and easy to understand.

However, the proposed FPS-PLL/FPS-MRAS observers have the following drawbacks:

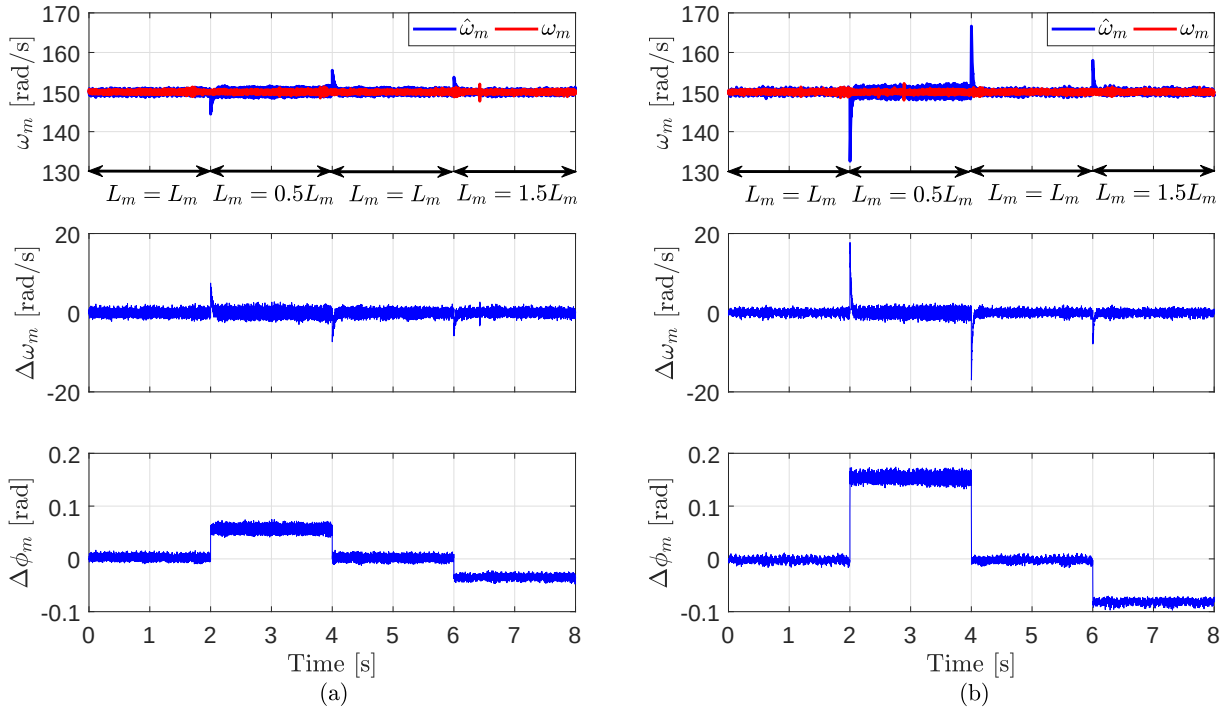

Figure 4.35: Experimental results for step changes in the mutual inductance L_m of the DFIG: (a) Proposed FPS-MRAS and (b) conventional MRAS.

- The computational burden of the proposed FPS-PLL/FPS-MRAS observers is significantly higher than that of the conventional ones, where 64 iterations are required to find the optimal rotor position.
- The accuracy of the proposed search-based algorithm is high due to the fact that it produces a limited number of rotor position angles.
- The ripples in the estimated speed/position using the proposed FPS-PLL/FPS-MRAS observers are higher than that of the traditional PLL/MRAS observers.

These problems have been further investigated and solutions were proposed in the next chapter (See chapter 5).

CHAPTER 5

Computationally-efficient finite-position-set Observers

In the previous chapter, the principles of the FCS-MPC have been extended to include the speed/position observers, which called finite-position-set (FPS) observers. However, 64 iterations are required to find the optimal rotor position (i.e. the calculation burden is high and a powerful DSP is essential to implement the algorithm). Furthermore, the accuracy of the proposed search-based algorithm (SBA) is slightly high, which causes high ripples in the estimated speed/position. This chapter presents two improved versions of the proposed search based algorithm that presented in Sec. 4.2.2. The first computationally efficient search-based algorithm (CE-SBA1) calls for 36 iterations and slightly improves the accuracy (see Sec. 5.2.1), while the second computationally efficient search-based algorithm (CE-SBA2) needs only 24 iterations and significantly enhances the accuracy (see Sec. 5.2.2). The proposed CE-SBA1&2 are applied for PLL/MRAS observers in sensorless control of PMSGs/DFIGs [95]–[98]. However, in order to declare the concept of the CE-SBA1&2 and avoid duplication, PLL based observers will be only detailed in this chapter. The experimental results of the proposed computationally efficient FPS-PLLs are compared with that of the FPS-PLL and the traditional PLL (See Sec. 5.3). Finally, a summary of this chapter is given in Sec. 5.4.

5.1 Introduction

In Fig. 4.6, the algorithm of the conventional FPS-PLL has been explained in details. The algorithm consists of two nested loops to discretize the rotor position into a limited number of angles. In the first iteration, $\Delta\phi_0 = \frac{\pi}{4}$ rad and 8 angles are produced as illustrated in Fig. 5.1a. Suppose that the optimal angle after the first iteration is $\frac{\pi}{2}$, which means that the right rotor position is located some where between $\frac{3\pi}{8}$ and $\frac{5\pi}{8}$. Accordingly, in the second iteration, the algorithm should search only in this area (marked with ellipse in Fig. 5.1b). However, the algorithm searches in larger area, where 5 angles are not belonging to the solution 0, $\frac{\pi}{8}$, $\frac{\pi}{4}$,

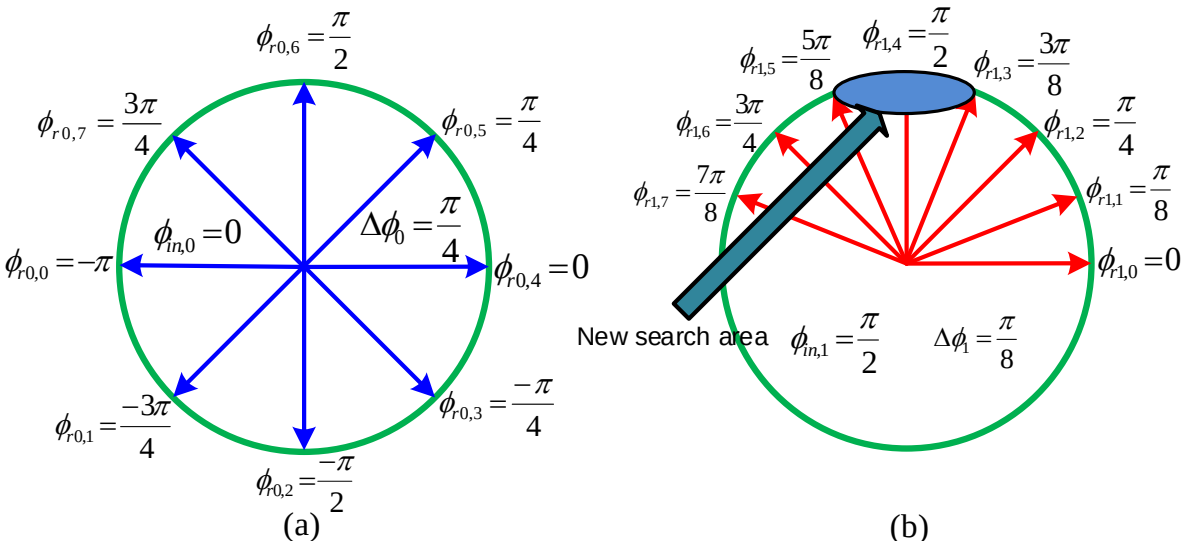

Figure 5.1: Graphical representation of the first two iterations of the FPS observers: (a) First iteration $i = 0$ and $j = 0 - 7$. (b) Second iteration $i = 1$ and $j = 0 - 7$.

$\frac{3\pi}{4}$, and $\frac{7\pi}{8}$ and significantly increase the computational load of the algorithm. Therefore, the algorithm must be modified to efficiently find the optimal angle, i.e to search only in the area marked with ellipse in Fig. 5.1b.

5.2 Computationally-efficient FPS-PLL (CE-FPS-PLL) for PMSGs

In order to reduce the computational burden of the FPS-PLL that presented in Sec. 4.2.2, two computationally efficient search-based algorithm (CE-SBA1&2) are proposed and explained in the next section.

5.2.1 Computationally efficient search-based algorithm 1

The main difference between the CE-FPS-PLL1 and FPS-PLL proposed in the last chapter is the number of required iteration to find the optimal rotor position. The proposed CE-SBA1 is illustrated in Fig. 5.2, where the modified items in comparison with the old SBA (Fig. 4.6) are marked in red color.

Similarly to the SBA, the CE-SBA1 consists of two nested loops with indices i and j. However, the discrete value that the indices i and j is lower than that in the SBA (i.e i and j have the range form $0 - 5$ instead of $0 - 7$). Furthermore, the displacement $\Delta\phi_i$ is modified to

$$\Delta\phi_i[k] = \frac{\pi}{3} \cdot \frac{2^{-i}}{i+1}. \tag{5.1}$$

Accordingly, consider that $\phi_{in,0}[k] = \hat{\phi}_r[k-1] = 0\,\text{rad}$ and $g_{in}[k] = \infty$. The first iteration of the outer loop starts with $i = 0$ and $\Delta\phi_0[k] = \frac{\pi}{3}\,\text{rad}$ according to (5.1). Consequently, six discrete

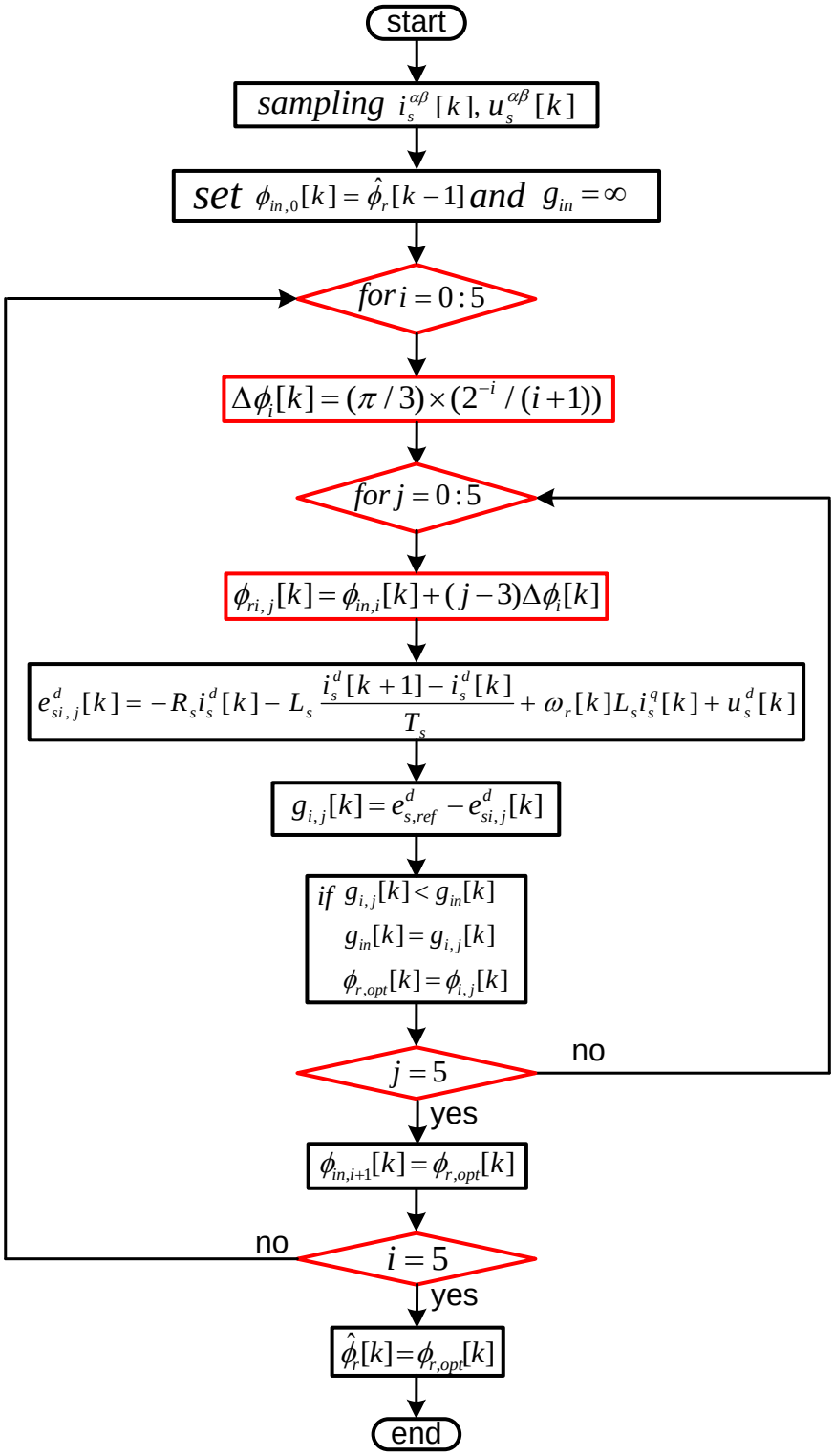

Figure 5.2: Flowchart of the proposed computationally-efficient search-based algorithm 1.

values for the rotor position will be generated: 0, $\frac{\pi}{3}$, $\frac{2\pi}{3}$, π, $\frac{-2\pi}{3}$, $\frac{-\pi}{3}$ (see also Fig. 5.3(a)). Each of these rotor positions $\phi_{ri,j}$ is employed to calculate the d-axis component of the back EMF

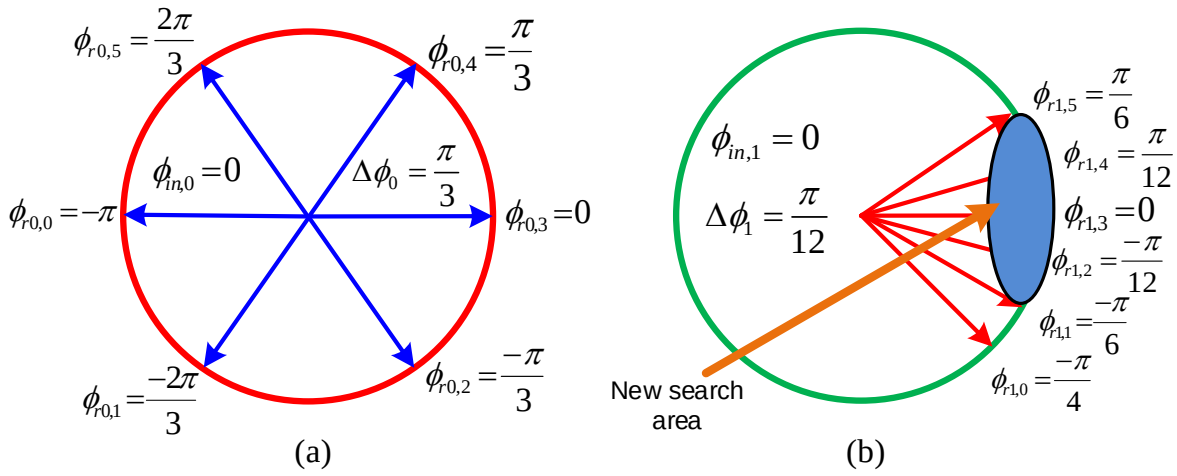

Figure 5.3: Graphical representation of the first two iterations of the proposed CE-SBA1: (a) First iteration $i = 0$ and $j = 0 - 5$. (b) Second iteration $i = 1$ and $j = 0 - 5$.

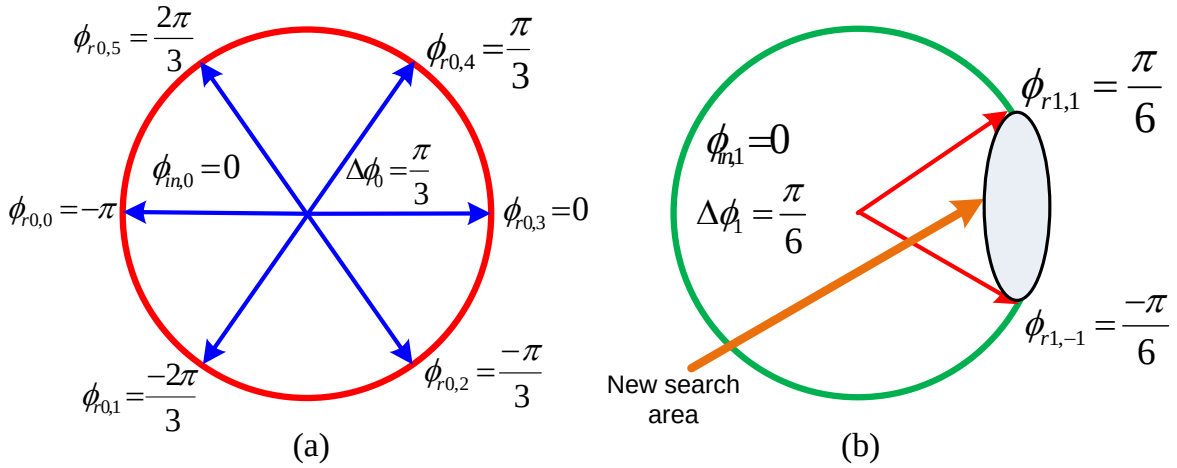

Figure 5.4: Graphical representation of the first two iterations of the proposed CE-SBA2: (a) First iteration $i = 0$ and $j = 0 - 5$. (b) Second iteration $i = 1$ and $j = -1, 1$.

$e^d_{si,j}$. Then, the rotor position that minimizes the cost function will be chosen to be the optimal rotor position angle $\phi_{r,opt}[k]$ and the initial angle of the second iteration $\phi_{in,1}[k]$ (i.e., $i = 1$).

Assume that the optimal angle calculated from the first iteration is 0 rad. Accordingly, the right rotor position is located somewhere between $\frac{\pi}{6}$ and $\frac{-\pi}{6}$ and this what the new SBA do in the second iteration of the outer loop $i = 1$, see Fig. 5.3(b). Furthermore, in the second iteration of the outer loop, $\Delta\phi_1[k] = \frac{\pi}{12}$ rad, which means that the accuracy of the proposed CE-SBA1 is enhanced by factor 4 not 2 like the old SBA. Note: in the new CE-SBA1 algorithm, only one angle $\frac{\pi}{4}$ rad is not belonging to the solution. However, this single iteration will not significantly increase the calculation load. According to Fig. 5.2, the optimal rotor position will be found after 36 iterations. Finally, the accuracy of the proposed CE-SBA1 is $\frac{1}{2} \times \frac{\pi}{3} \times \frac{2^{-5}}{6} = \frac{\pi}{1152} = 0.0027$ rad, which is slightly better than the accuracy of the old SBA. Accordingly, the ripples in the estimated position and speed will be also slightly lower.

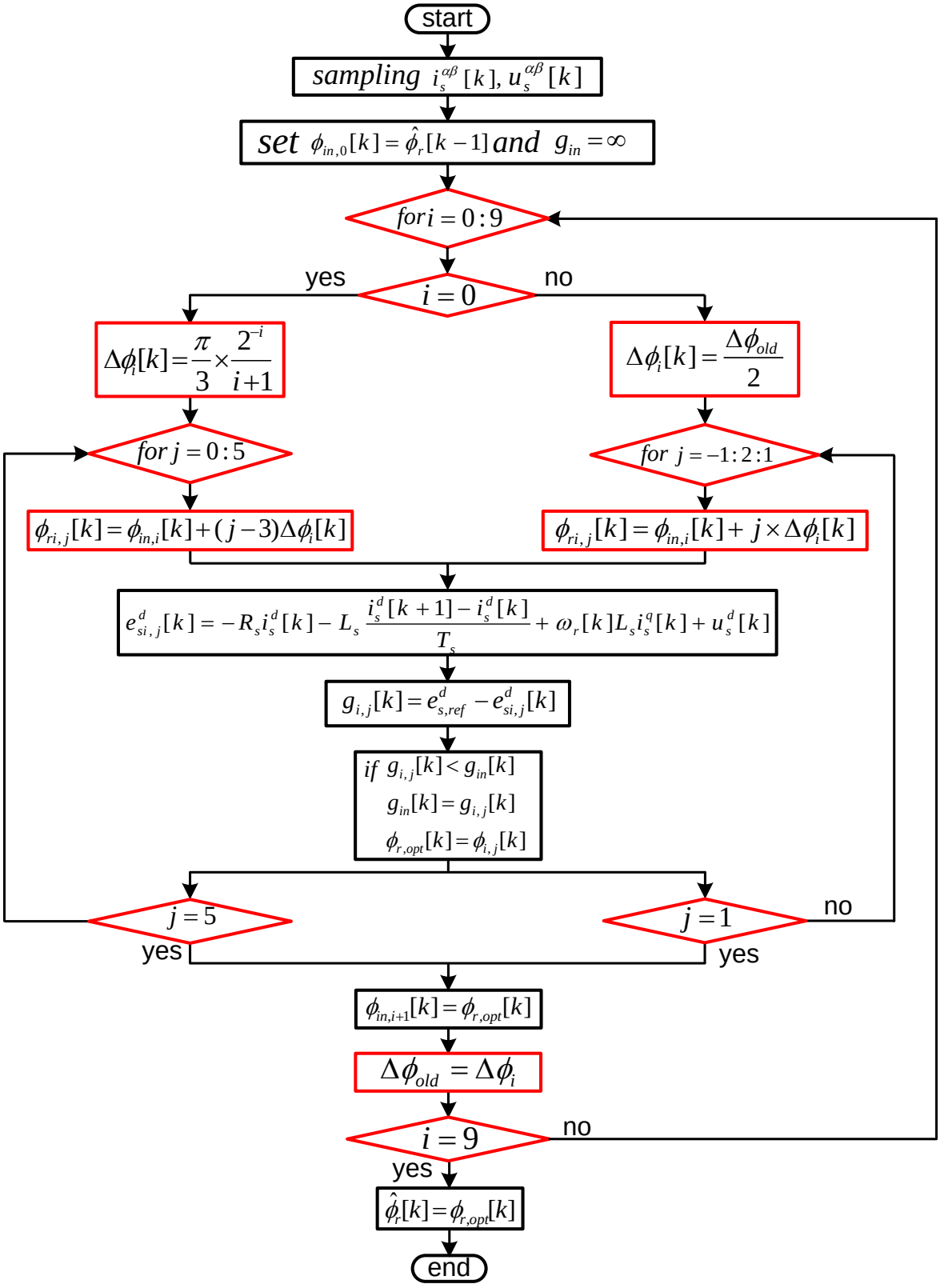

Figure 5.5: Flowchart of the proposed computationally-efficient search-based algorithm 2.

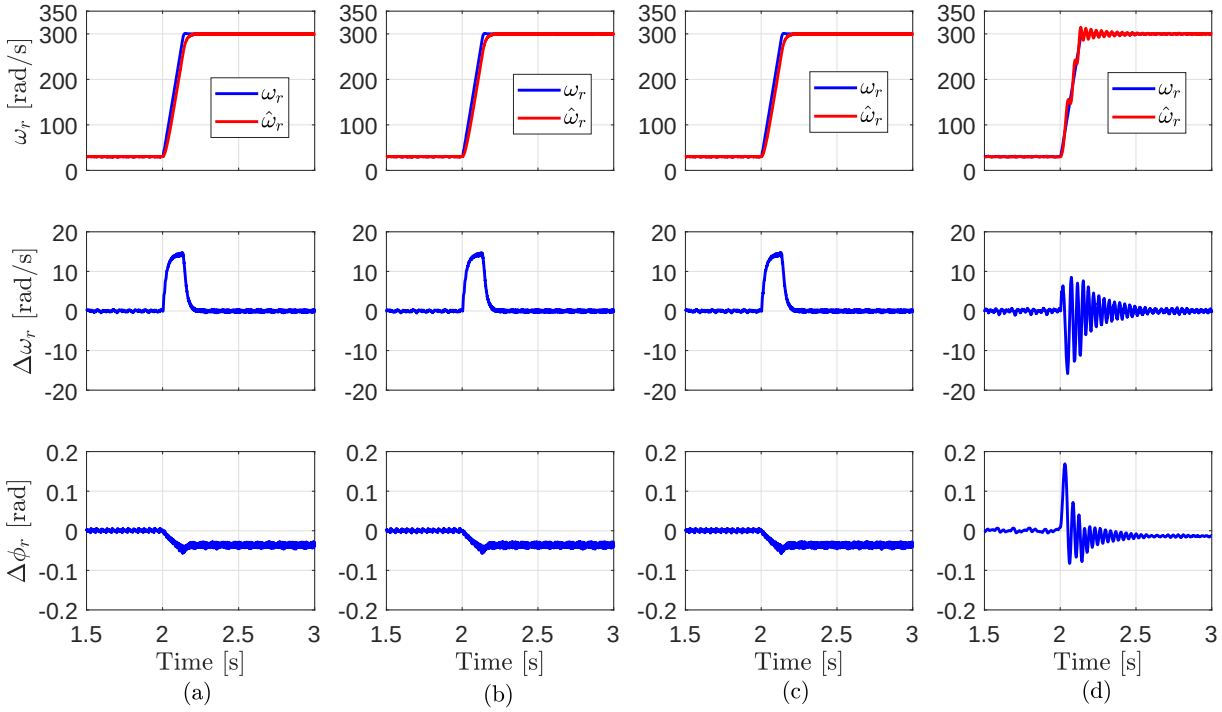

Figure 5.6: Experimental results for a step change in the rotor speed of the PMSG: (a) CE-FPS-PLL2 (b) CE-FPS-PLL1, (c) FPS-PLL and (d) TPLL.

5.2.2 Computationally efficient search-based algorithm 2

Although the CE-SBA1 significantly reduces the number of iterations to find the right rotor position, its accuracy is still relatively high. Therefore, another computationally efficient search-based algorithm (CE-SBA2) is proposed and illustrated in Fig. 5.5. In the first iteration of the outer loop $i = 0$, the CE-SBA2 is the same like CE-SBA1, i.e $\Delta\phi_0[k] = \frac{\pi}{3}$ rad and six discrete values for the rotor position are produced, see Fig. 5.4a. From those six angles, one angle will be selected based on the cost function to be the optimal value and the initial for the second iteration.

Assume that the optimal angle computed from the first iteration is 0 rad. In the second iteration of the outer loop $i = 1$, the displacement is differently computed as: $\Delta\phi_1[k] = \frac{\Delta\phi_{old}}{2} = \frac{\pi/3}{2} = \frac{\pi}{6}$. Furthermore, the discretized rotor position can be expressed as

$$\phi_{ri,j}[k] = \phi_{in,i}[k] + j \times \Delta\phi_i[k]. \tag{5.2}$$

Accordingly, due to the change of the index $j = -1 : 2 : 1$, only two angles will be produced $\frac{-\pi}{6}$ rad and $\frac{\pi}{6}$ rad as shown in Fig. 5.4b. Accordingly, the d-axis component of the back EMF $e^d_{si,j}$ and the cost function $g_{i,j}$ are evaluated for only two times, which significantly reduces the computational load. Furthermore, the discrete value of the outer loop index $i = 0 : 9$ is updated to improve the accuracy of the proposed CE-SBA2. The estimated rotor position is obtained after 24 iterations with an accuracy of 0.001 rad. Thanks to the proposed CE-SBA2.

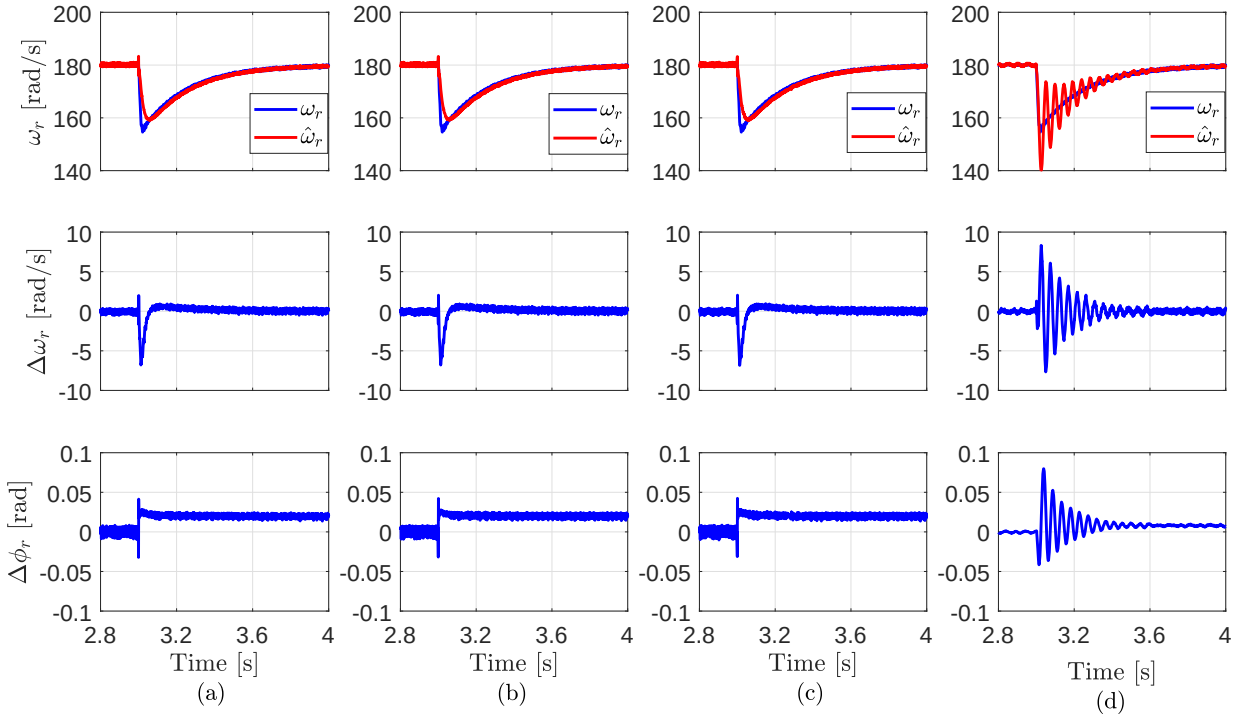

Figure 5.7: Experimental results for a step change in the torque: (a) CE-FPS-PLL2 (b) CE-FPS-PLL1, (c) FPS-PLL and (d) TPLL.

5.3 Experimental results

The CE-SBA1&2 are applied for the PLL based observer, they are called CE-FPS-PLL1 and CE-FPS-PLL2, respectively. Those two observers are experimentally implemented and compared with the FPS-PLL and traditional one. The PMSG is controlled using the FOC technique as shown in Fig. 4.1. Experimentally, it has been observed that the execution time of the CE-FPS-PLL2, CE-FPS-PLL1, FPS-PLL, and traditional PLL were $15\,\mu$s, $21\,\mu$s, $32\,\mu$s, and $5\,\mu$s, respectively. Accordingly, the computational load using CE-FPS-PLL2 and CE-FPS-PLL1 is reduced to $\frac{15}{32} \times 100 \approx 46.9\%$ and $\frac{21}{32} \times 100 \approx 65.6\%$, respectively, in comparison with the FPS-PLL.

Fig. 5.6 illustrates the dynamic performance of CE-FPS-PLL2, CE-FPS-PLL1, FPS-PLL, and traditional PLL under step change in the mechanical speed ω_m of the rotor. From top to bottom, the plotted signals are measured speed ω_r, estimated speed $\hat{\omega}_r$; error $\Delta\omega_r = \omega_r - \hat{\omega}_r$ between measured and estimated speed; error $\Delta\phi_r = \phi_r - \hat{\phi}_r$ between measured and estimated rotor position. At the time instant $t = 2\,\mathrm{s}$, a step change in the reference mechanical speed $\omega_{m,ref}$ of the rotor from $10\,\mathrm{rad/s}$ to $100\,\mathrm{rad/s}$ has been applied to the RSM control system. The torque command $T_e^\star$ of the PMSG is set to $-30.5\,\mathrm{N\,m}$. It can be seen that the transient performance of the CE-FPS-PLL2, CE-FPS-PLL1, and FPS-PLL are similar and better than that of the conventional PLL, which suffer from high oscillations in the estimated speed/position.

In order to further investigate and compare the transient response of the different observers, a step change in the reference electro-magnetic torque $T_e^\star$ of the PMSG from $-20\,\mathrm{N\,m}$ to $-50\,\mathrm{N\,m}$ has been applied at the time instant $t = 3\,\mathrm{s}$, see Fig. 5.7. The mechanical speed

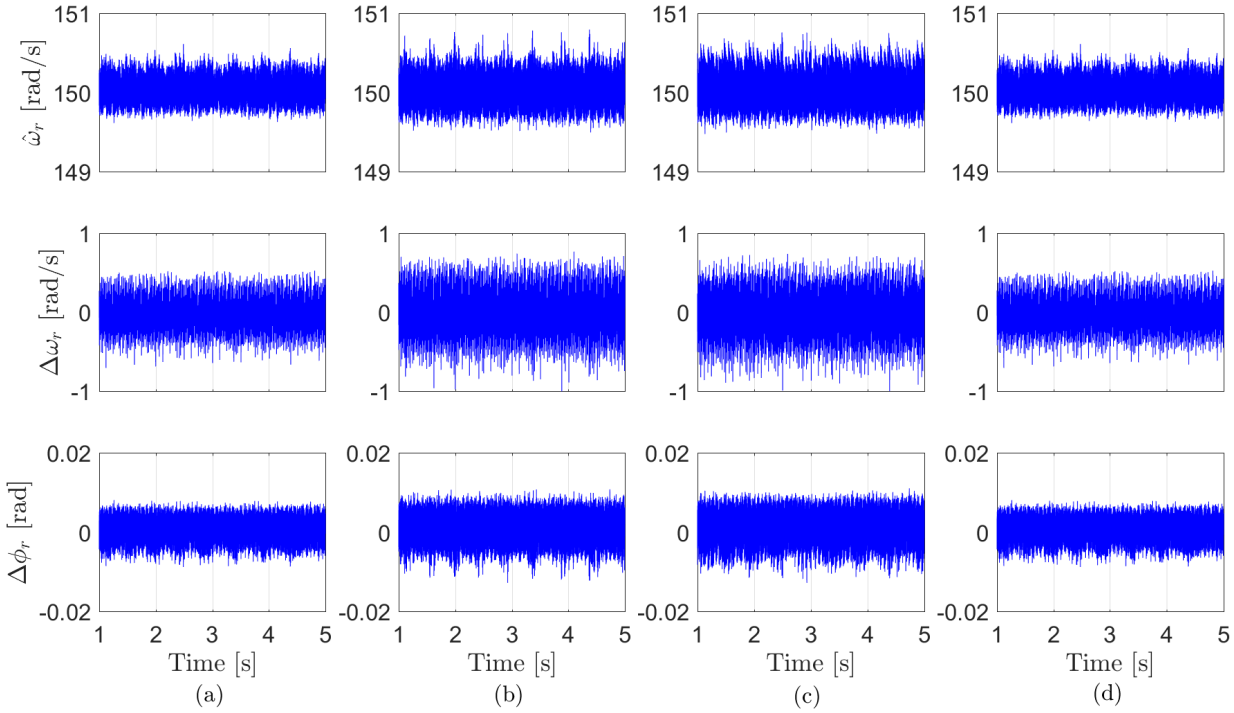

Figure 5.8: Experimental results at steady-state: (a) CE-FPS-PLL2 (b) CE-FPS-PLL1, (c) FPS-PLL and (d) TPLL.

ω_m of the rotor is kept constant at $60\,\mathrm{rad/s}$ by the RSM control scheme. Again, it can be observed that the dynamic performance of the CE-FPS-PLL2, CE-FPS-PLL1, and FPS-PLL are similar and better than that of the traditional PLL.

Fig. 5.8 illustrates the steady-state performance of CE-FPS-PLL2, CE-FPS-PLL1, FPS-PLL, and traditional PLL, respectively. The mechanical speed ω_m of the rotor is regulated to $50\,\mathrm{rad/s}$ by the RSM control technique, while the electro-magnetic torque $T_e^\star$ of the PMSG is set to $-45\,\mathrm{N\,m}$. It can be observed that the ripples in the estimated speed $\hat{\omega}_r$ and position $\hat{\phi}_r$ using the proposed CE-FPS-PLL2 are lower than the ripples in case of using the CE-FPS-PLL1 and FPS-PLL and almost similar to the ripples of the traditional PLL.

Finally, the robustness of the proposed CE-FPS-PLL2, CE-FPS-PLL1, FPS-PLL, and traditional PLL are investigated and compared. At the time instants $t = 2\,\mathrm{s}$ and $t = 4\,\mathrm{s}$, a -50% and a $+50\%$ step change of the stator inductance L_s were applied within the real-time model. The mechanical speed ω_m of the rotor is set to $65\,\mathrm{rad/s}$ by the RSM control system and the reference torque $T_e^\star$ is set to $-35\,\mathrm{N\,m}$. According to Fig. 5.9, it can be seen that the CE-FPS-PLL2, CE-FPS-PLL1, and FPS-PLL demonstrated good robustness to variations of the stator inductance L_s of the PMSG, while the traditional PLL is highly sensitive to mismatches in the stator inductance L_s.

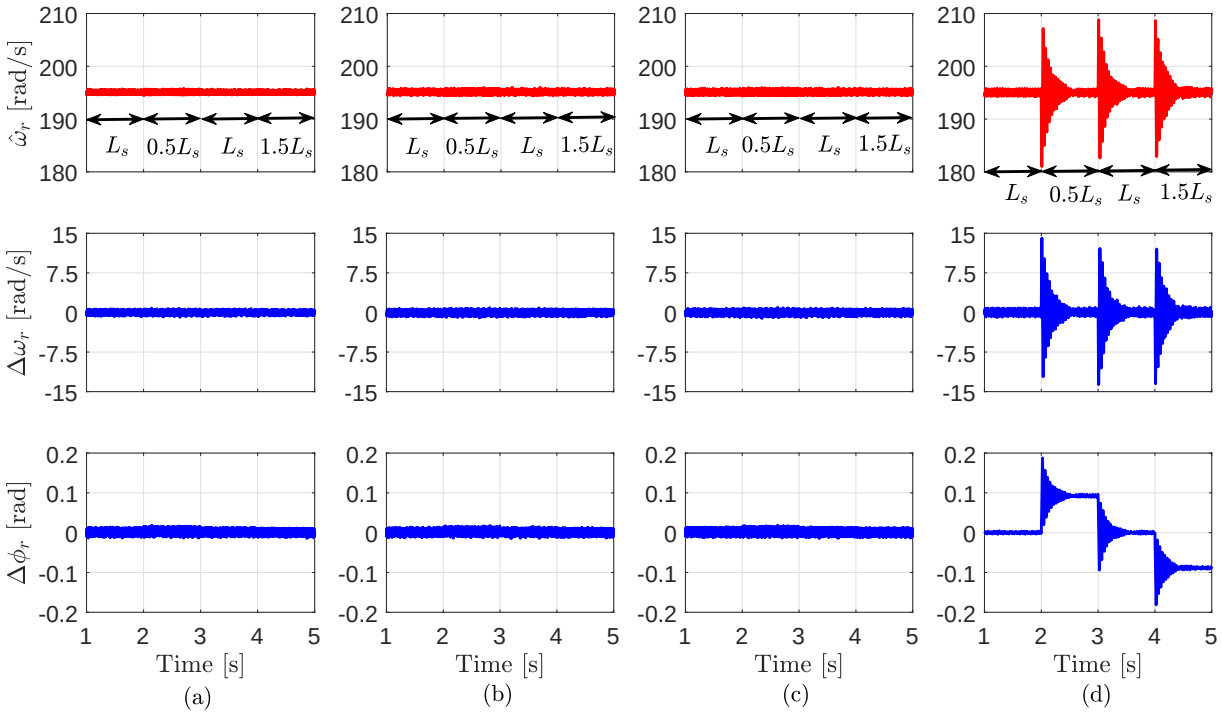

Figure 5.9: Experimental results at steady-state: (a) CE-FPS-PLL2 (b) CE-FPS-PLL1, (c) FPS-PLL and (d) TPLL.

5.4 Summary

In this chapter, two computationally-efficient finite-position-set phase looked loops (CE-FPS-PLLs1&2) are proposed to reduce the computational effort of the FPS-PLL presented in Sec. 4.2.2. The proposed CE-FPS-PLL2 and CE-FPS-PLL1 highly reduced the number of iterations requested to find the optimal rotor position, where 24 and 36 iterations, respectively, are required in comparison with 64 iterations for the FPS-PLL. Furthermore, the accuracy of the proposed CE-FPS-PLL2 is significantly better than that of CE-FPS-PLL1 and FPS-PLL. The proposed CE-FPS-PLL2, CE-FPS-PLL1, FPS-PLL, and traditional PLL were experimentally implemented and compared. The results illustrated that the dynamic response and robustness of the CE-FPS-PLL2, CE-FPS-PLL1, FPS-PLL are better than that of the traditional one. Furthermore, the steady-state response of the proposed CE-FPS-PLL2 is similar to the traditional PLL, i.e. the ripples in the estimated speed/position are almost comparable.

CHAPTER 6

Robust deadbeat control without mechanical sensors

This chapter presents a robust deadbeat predictive control strategy for PMSGs (Sec. 6.2) and DFIGs (Sec. 6.3) without mechanical sensors (i.e no position encoders or speed transducers). An extended Kalman filter is employed to estimate stator/rotor currents, rotor speed, rotor position, and mechanical torque of the PMSG/DFIG, see Sec. 6.2.2/Sec. 6.3.2. The estimated stator/rotor currents are fed back to the prediction model in order to compensate the one-step delay caused by the digital controller and to reduce the total harmonic distortion (THD) of the stator/rotor currents. Thus, the torque ripples are also reduced. Furthermore, a simple disturbance observer is presented which estimates the perturbations caused by parameter variations of the PMSG/DFIG or by any un-modeled dynamics in order to enhance the robustness of the proposed DB algorithm, see Sec. 6.2.2.1 and Sec. 6.3.2.1, respectively. The proposed DB control scheme is experimentally implemented and its performance is compared with the conventional DB control system, see Sec. 6.4. Finally, a summary of this chapter is given in Sec. 6.5.

6.1 Introduction

Deadbeat (DB) predictive control, which relies on the generator model and the reference currents to calculate the reference voltage, presents excellent dynamic performance with constant switching frequency and a lower computational burden than CCS-MPC and FCS-MPC [43]–[45], [47]. Furthermore, the ripples in the current/torque waveforms using DB control is significantly lower that the ripples in case of FCS-MPC. Problems with deadbeat control scheme are delays in the digital control system, and sensitivity to parameter variations of the model. Model-based delay compensation (a Smith predictor) was presented in [44] and this method is the most common method applied today [99]–[101]. However, the Smith predictor relies also on the generator model, and consequently, is sensitive to parameters variations of the machine as well [102]. In [87], a Luenberger observer is proposed for delay compensation (i.e. predict-

ing the current in the next sampling instant), which is a robust observer. However, a phase lag between the estimated current and the actual one due to the post-filtering exists. A sliding-mode observer is employed to predict the currents in the future sampling interval in [103], and, accordingly, compensates the one-step delay of the DB control system. However, undesirable deteriorations occur within the predicted currents due to chattering.

Generally, for implementing/achieving the maximum power point tracking (MPPT) control algorithm for variable-speed WECSs, it is necessary/crucial to detect rotor speed and position of the generator, which can be measured by mechanical sensors, such as position encoders or speed transducers. However, additional mechanical sensors do not only increase the cost/complexity of the system, but also reduce the reliability [53], [104], [105]. Therefore, sensorless operation (i.e. estimation of the rotor speed/position instead of measuring them) is desirable and essential for the further development of variable-speed WECSs.

Recently, several sensorless control techniques have been introduced for PMSGs/DFIGs. Those techniques can be classified into two categories [53]: 1) open-loop techniques and 2) closed-loop observers. The open-loop techniques are not preferred because its performance is dependent on the accuracy of the PMSG/DFIG parameters and measurements [53]. The closed-loop techniques are: Disturbance observers, sliding-mode observers (SMOs), model reference adaptive system (MRAS) observers, and extended Kalman filters (EKFs). Disturbance and MRAS observers are sensitive to variations of the PMSG/DFIG parameters [59], [95], [97]. SMO is an attractive/promising technique for estimating rotor speed and position of the machine due to its robustness against parameters variations [52]. However, a well-tuned low-pass filter is essential for mitigating the oscillating position errors due to the noise caused by switching actions. The EKF is a promising and robust non-linear state observer for estimating the rotor speed and position of AC machines [105]–[107].

The EKF has been used for estimating the rotor speed and position of the PMSG/DFIG in [50], [108]–[110]. However, these papers neglected the mechanical system dynamics as the authors only consider steady-state on the machine side (i.e. $\frac{d\omega}{dt} = 0$) or provided only simulation results. Neglecting the mechanical system dynamics worsens the estimation performance of the EKF and will not represent the real physical system dynamics. In [46], FCS-MPC is used and the dynamics of the mechanical system have been considered. Furthermore, the EKF is employed to additionally estimate the stator inductance of the PMSG to enhance the robustness of the control scheme. However, only simulation results have been presented.

In this work, a robust EKF is proposed for estimating stator (and rotor) currents, rotor speed, rotor position, and the mechanical torque of the PMSG/DFIG. The proposed EKF is insensitive to measurement noise and parameters variations of the generator. *At the same time*, this EKF is used to compensate for the on-step delay in the digital controller. Furthermore, feeding the estimated (filtered) currents to the prediction algorithm instead of the measured (and, hence, noisy) currents reduces the total harmonic distortion (THD) of the output of the control system. Consequently, the current and torque ripples are reduced. Moreover, a disturbance observer, based on a time delay control approach [111], is implemented to enhance the robustness of the deadbeat algorithm against parameter variations of the generator. The performance of the proposed robust sensorless predictive control system is experimentally evaluated. Its control performance is compared with that of the conventional DB control technique for all operation conditions and under parameters variations of the PMSG/DFIG.

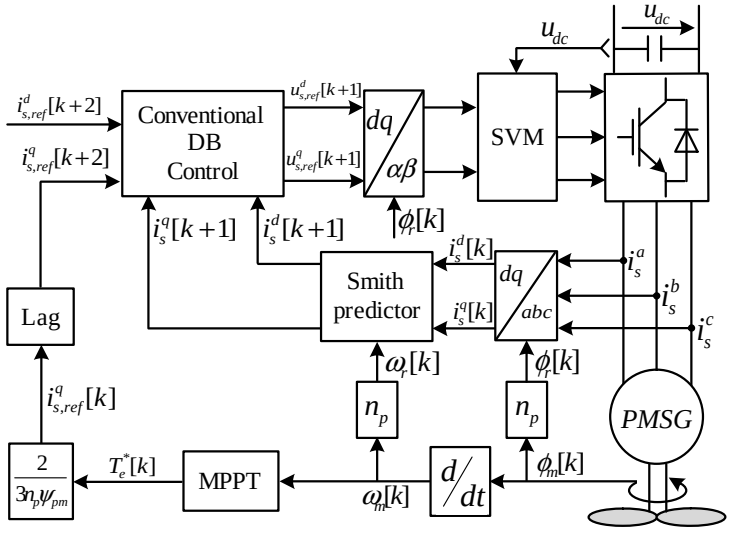

Figure 6.1: Schematic diagram of the conventional DB control with Smith predictor for PMSG based variable-speed wind turbines.

6.2 Deadbeat control schemes for PMSG

In the section, the conventional and proposed DB predictive control for PMSGs are detailed. Considering the perturbations caused by parameter variations of the PMSG or by any un-modeled dynamics, the discrte-time model of the PMSG can be rewritten as

$$\left.\begin{aligned} u^d_s[k] &= R_{so} i^d_s[k] + L_{so}\tfrac{i^d_s[k+1]-i^d_s[k]}{T_s} - \omega_r[k] L_{so} i^q_s[k] + f^d[k], \\ u^q_s[k] &= R_{so} i^q_s[k] + L_{so}\tfrac{i^q_s[k+1]-i^q_s[k]}{T_s} + \omega_r[k] L_{so} i^d_s[k] + \omega_r[k]\psi_{pmo} + f^q[k], \end{aligned}\right\} \tag{6.1}$$

where k is the current sampling instant, T_s is the sampling time, the subscript o denotes the nominal value of the parameters. The terms $f^d[k]$ and $f^q[k]$ represent the summation of the effects of parameter uncertainties and un-modeled dynamics, and can be written as

$$\left.\begin{aligned} f^d[k] &= \Delta R_s i^d_s[k] + \Delta L_s\tfrac{i^d_s[k+1]-i^d_s[k]}{T_s} - \omega_r[k]\Delta L_s i^q_s[k] + \varepsilon^d[k], \\ f^q[k] &= \Delta R_s i^q_s[k] + \Delta L_s\tfrac{i^q_s[k+1]-i^q_s[k]}{T_s} + \omega_r[k]\Delta L_s i^d_s[k] + \omega_r[k]\Delta\psi_{pm} + \varepsilon^q[k], \end{aligned}\right\} \tag{6.2}$$

where $R_s = R_{so} + \Delta R_s$, $L_s = L_{so} + \Delta L_s$, $\psi_{pm} = \psi_{pmo} + \Delta\psi_{pm}$, and $\varepsilon^d[k]$, $\varepsilon^q[k]$ represent the un-modeled uncertainties for the d- and q-axis, respectively.

6.2.1 Conventional DB control for PMSG

Usually, the conventional DB control is designed by considering the nominal system parameters only (i.e. neglecting $f^d[k]$ and $f^q[k]$). Considering the one-sample delay due to the digital controller, the reference voltage vector $\boldsymbol{u}^{dq}_{s,ref}[k+1]$ can by calculated as follows

$$\left.\begin{aligned} u^d_{s,ref}[k+1] &= R_{so} i^d_s[k+1] + L_{so}\tfrac{i^d_{s,ref}[k+2]-i^d_s[k+1]}{T_s} - \omega_r[k+1] L_{so} i^q_s[k+1], \\ u^q_{s,ref}[k+1] &= R_{so} i^q_s[k+1] + L_{so}\tfrac{i^q_{s,ref}[k+2]-i^q_s[k+1]}{T_s} + \omega_r[k+1]\big(L_{so} i^d_s[k+1] + \psi_{pmo}\big). \end{aligned}\right\} \tag{6.3}$$

Using a Smith predictor [44], the currents $i_s^d[k+1]$ and $i_s^q[k+1]$ can be predicted from (6.1) as follows

$$\left.\begin{aligned} i_s^d[k+1] &= (1-\tfrac{T_sR_{so}}{L_{so}})i_s^d[k] + T_s\omega_r[k]i_s^q[k] + \tfrac{T_s}{L_{so}}u_s^d[k], \\ i_s^q[k+1] &= (1-\tfrac{T_sR_{so}}{L_{so}})i_s^q[k] - T_s\omega_r[k]i_s^q[k] - T_s\omega_r[k]\psi_{pmo} + \tfrac{T_s}{L_{so}}u_s^q[k]. \end{aligned}\right\} \tag{6.4}$$

In view of (6.3) and (6.4), calculation of the reference voltages $\boldsymbol{u}_{s,ref}^{dq}[k+1]$ and prediction of the currents $\boldsymbol{i}_s^{dq}[k+1]$ highly depends on the parameters of the machine. Therefore, the conventional DB control is sensitive to parameter uncertainties. The schematic diagram of the conventional DB control with Smith predictor is shown in Fig. 6.1, where an encoder is employed to measure the rotor position of the PMSG. The measured mechanical rotor speed $\omega_m[k]$ is feeding the maximum power point tracking (MPPT) algorithm in order to calculate the optimal torque $T_e^\star[k] = -k_p^\star\omega_m^2[k]$ [32, Chap. 12], where $k_p^\star$ is a known positive constant. This optimal torque is used to calculate the q-axis reference current of the stator as $i_{s,ref}^q[k] = \frac{2}{3n_p\psi_{pm}}T_e^\star[k]$. Then, the reference current

$$i_{s,ref}^q[k+2] = 3i_{s,ref}^q[k] - 3i_{s,ref}^q[k-1] + i_{s,ref}^q[k-2] \tag{6.5}$$

is calculated using Lagrange extrapolation. The d-axis reference current is set to zero, i.e. $i_{s,ref}^d[k] = i_{s,ref}^d[k+1] = i_{s,ref}^d[k+2]$, to reduce copper losses [112].

6.2.2 Proposed Deadbeat Control with EKF for PMSG

The proposed sensorless deadbeat control scheme for PMSG is illustrated in Fig. 6.2. In this work [47], an EKF is utilized to predict/estimate the stator currents $\hat{i}_s^{dq}[k+1]$ at the next sampling instant instead of using the conventional Smith predictor. Moreover, the EKF is designed to estimate rotor speed and position, and the mechanical torque of the PMSG. Hence, the PMSG control will be achieved without mechanical sensors. Furthermore, the perturbations due to parameter variations and un-modeled dynamics are taken into account during the design of the proposed DB control. Therefore, the reference voltages incorporate the disturbance expressions and are computed as follows

$$\left.\begin{aligned} u_{s,ref}^d[k+1] &= R_{so}\hat{i}_s^d[k+1] + L_{so}\tfrac{i_{s,ref}^d[k+2]-\hat{i}_s^d[k+1]}{T_s} - \hat{\omega}_r[k+1]L_{so}\hat{i}_s^q[k+1] + \hat{f}^d[k+1], \\ u_{s,ref}^q[k+1] &= R_{so}\hat{i}_s^q[k+1] + L_{so}\tfrac{i_{s,ref}^q[k+2]-\hat{i}_s^q[k+1]}{T_s} + \hat{\omega}_r[k+1]\big(L_{so}\hat{i}_s^d[k+1] + \psi_{pmo}\big) \\ &+ \hat{f}^q[k+1]. \end{aligned}\right\} \tag{6.6}$$

In (6.6), $\hat{}$ indicates estimated quantities.

The magnitude

$$u_s[k+1] = \|\boldsymbol{u}_{s,ref}^{dq}[k+1]\| = \sqrt{u_{s,ref}^d[k+1]^2 + u_{s,ref}^q[k+1]^2}$$

of the next reference voltage vector $\boldsymbol{u}_{s,ref}^{dq}[k+1]$ is calculated and compared with the maximally available output voltage magnitude $u_{s,max}$ of the voltage source converter which depends on the

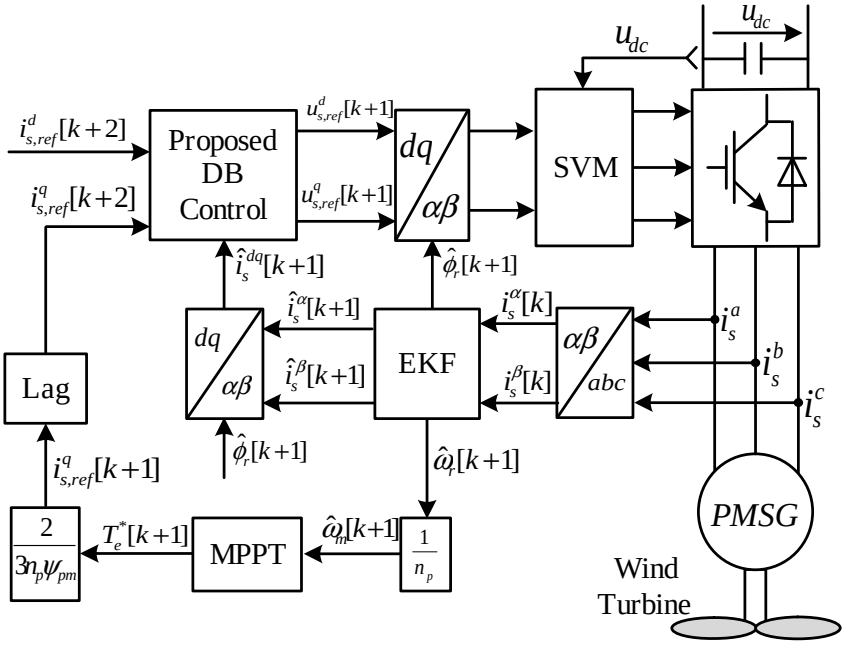

Figure 6.2: Proposed sensorless DB control for PMSG based variable-speed wind turbines.

dc-link voltage u_{dc}. If the magnitude is greater than this value, the reference voltages should be adjusted as follows

$$\boldsymbol{u}^{dq}_{s,ref}[k+1] = \begin{cases} \boldsymbol{u}^{dq}_{s,ref}[k+1], & u_s[k+1] \leq u_{s,max} \\ \frac{u_{s,max}}{u_s[k+1]} \boldsymbol{u}^{dq}_{s,ref}[k+1], & u_s[k+1] > u_{s,max}. \end{cases} \tag{6.7}$$

For implementing the proposed EKF, a state-space model of the PMSG of the form

$$\frac{d}{dt}\boldsymbol{x} = \boldsymbol{g}(\boldsymbol{x}, \boldsymbol{u}), \quad \text{and} \quad \boldsymbol{y} = \boldsymbol{h}(\boldsymbol{x}) \tag{6.8}$$

is necessary. Accordingly, the state vector $\boldsymbol{x}$, the output (measurement) vector $\boldsymbol{y}$ and the input vector $\boldsymbol{u}$ are defined in the stationary reference frame $\alpha\beta$ as follows

$$\left.\begin{aligned} \boldsymbol{x} &= \left(i^{\alpha}_s, \quad i^{\beta}_s, \quad \omega_r, \quad \phi_r, \quad T_m\right)^{\top} \\ \boldsymbol{y} &= \left(i^{\alpha}_s, \quad i^{\beta}_s\right)^{\top} \\ \boldsymbol{u} &= \left(u^{\alpha}_s, \quad u^{\beta}_s\right)^{\top}. \end{aligned}\right\} \tag{6.9}$$

The function $\boldsymbol{g}(\boldsymbol{x}, \boldsymbol{u})$ and $\boldsymbol{h}(\boldsymbol{x})$ can be derived from the model of the PMSG [46] and are given by

$$\boldsymbol{g}(\boldsymbol{x}, \boldsymbol{u}) = \begin{bmatrix} -\frac{R_s}{L_s} i^{\alpha}_s + \frac{\omega_r \psi_{pm}}{L_s} \sin(\phi_r) + \frac{1}{L_s} u^{\alpha}_s) \\ -\frac{R_s}{L_s} i^{\beta}_s - \frac{\omega_r \psi_{pm}}{L_s} \cos(\phi_r) + \frac{1}{L_s} u^{\beta}_s) \\ \frac{n_p}{\Theta}\left(\frac{3}{2} n_p \psi_{pm}\big(- i^{\alpha}_s \sin(\phi_r) + i^{\beta}_s \cos(\phi_r)\big) - T_m - \frac{\nu}{n_p}\omega_r\right) \\ \omega_r \\ 0 \end{bmatrix} \tag{6.10}$$

and

$$\boldsymbol{h}(\boldsymbol{x}) = \underbrace{\begin{bmatrix} 1 & 0 & 0 & 0 & 0 \\ 0 & 1 & 0 & 0 & 0 \end{bmatrix}}_{=:\boldsymbol{C}} \boldsymbol{x}. \tag{6.11}$$

Hence, the nonlinear discrete-time model of the PMSG can be written as

$$\left.\begin{aligned} \boldsymbol{x}[k+1] &= \overbrace{\boldsymbol{x}[k] + T_s \boldsymbol{g}(\boldsymbol{x}[k], \boldsymbol{u}[k])}^{=:\boldsymbol{f}(\boldsymbol{x}[k],\boldsymbol{u}[k])} + \boldsymbol{w}[k], \\ \boldsymbol{y}[k] &= \boldsymbol{h}(\boldsymbol{x}[k]) + \boldsymbol{v}[k], \end{aligned}\right\} \tag{6.12}$$

where the random variables $\boldsymbol{w}[k] := (w_1[k], \ldots, w_5[k])^\top$ and $\boldsymbol{v}[k] := (v_1[k], v_2[k])^\top$ are added to model system uncertainties and measurement noise, respectively. Therefore, the proposed EKF is robust against variations of the PMSG parameters and is capable to withstand and filter out (very) noisy current measurements. For simplicity, constant covariance matrices are considered, i.e., for all k the following holds

$$\boldsymbol{Q} = E\{\boldsymbol{w}[k]\boldsymbol{w}[k]^\top\}, \, \boldsymbol{R} = E\{\boldsymbol{v}[k]\boldsymbol{v}[k]^\top\}. \tag{6.13}$$

Note that $\boldsymbol{Q}$ and $\boldsymbol{R}$ must be positive semi-definite and positive definite, resp. Finally, the EKF is implemented as follows

$$\left.\begin{aligned} \hat{\boldsymbol{x}}[k+1] &= \boldsymbol{f}(\hat{\boldsymbol{x}}[k], \boldsymbol{u}[k]) + \boldsymbol{K}[k]\big(\boldsymbol{y}[k] - \hat{\boldsymbol{y}}[k]\big), \\ \hat{\boldsymbol{y}}[k] &= \boldsymbol{h}(\hat{\boldsymbol{x}}[k]) = \boldsymbol{C}\hat{\boldsymbol{x}}[k]. \end{aligned}\right\} \tag{6.14}$$

where $\boldsymbol{K}[k]$ is the Kalman gain (as defined in **Algorithm 3**) and $\hat{\boldsymbol{x}}$ and $\hat{\boldsymbol{y}}$ are the estimated state and output vector, respectively. The recursive estimation algorithm of the EKF implementation is listed in **Algorithm 3** [46], [47]. An optimal state estimation is realized by minimizing the covariance of the estimation error for each time instant $k \geq 1$.

An important step during the design of the EKF is the choice of the matrices $\boldsymbol{P}_0$, $\boldsymbol{Q}$ and $\boldsymbol{R}$, which influence the response and the convergence of the EKF. The initial error covariance matrix $\boldsymbol{P}_0$ represents the covariances (or mean-squared errors) based on the initial conditions (often $\boldsymbol{P}_0$ is selected to be a diagonal matrix) and controls the initial amplitude of the dynamic behavior of the estimation process, while no impact on the transient and steady-state performance can be observed [113].

The matrix $\boldsymbol{Q}$ characterizes the confidence with the system model. Large values of $\boldsymbol{Q}$ indicate a low confidence with the system model, i.e. large parameter uncertainties are to be expected. Hence, the Kalman gain will increase, and accordingly, a faster/better measurement update is produced. However, excessively large elements of $\boldsymbol{Q}$ may cause oscillations or even instability of the state estimation. On the other hand, low values in $\boldsymbol{Q}$ indicate a high confidence in the system model and may therefore result in slow (weak) measurement corrections [113].

The matrix $\boldsymbol{R}$ is related to the measurement noise characteristics. Increasing the values of $\boldsymbol{R}$ indicates that the measured signals are heavily affected by noise and, therefore, are of little confidence. Accordingly, the Kalman gain will decrease yielding a slower (poorer) dynamic response. Furthermore, extremely high noise in the measured signals may cause the EKF to loose its stability [114], [115].

Algorithm 3 : Extended Kalman filter

Step 1: A priori prediction

(a) State prediction

$$\hat{\boldsymbol{x}}^{-}[k+1] = \boldsymbol{f}(\hat{\boldsymbol{x}}[k], \boldsymbol{u}[k])$$

(b) Error covariance matrix prediction

$$\boldsymbol{P}^{-}[k] = \boldsymbol{A}[k]\boldsymbol{P}[k-1]\boldsymbol{A}[k]^{\top} + \boldsymbol{Q}$$

where

$$\boldsymbol{A}[k] = \left.\frac{\partial \boldsymbol{f}(\boldsymbol{x},\boldsymbol{u})}{\partial \boldsymbol{x}}\right|_{\hat{\boldsymbol{x}}^{-}[k+1]}$$

Step 2: Computation of Kalman gain

$$\boldsymbol{K}[k] = \boldsymbol{P}^{-}[k]\boldsymbol{C}^{\top}\left(\boldsymbol{C}\boldsymbol{P}^{-}[k]\boldsymbol{C}^{\top} + \boldsymbol{R}\right)^{-1}$$

Step 3: Verification of (local) observability

$$n_o[k] := \operatorname{rank}\left(\boldsymbol{S}_o[k]\right) \text{ with } \boldsymbol{S}_o[k] \text{ as in (6.15)}$$

Step 4: Measurement update ("correction")

(a) Estimation update with measurement

$$\hat{\boldsymbol{x}}[k+1] = \hat{\boldsymbol{x}}^{-}[k+1] + \boldsymbol{K}[k](\boldsymbol{y}[k] - \boldsymbol{h}(\hat{\boldsymbol{x}}[k]))$$

(b) Error covariance matrix update

$$\boldsymbol{P}[k] = \boldsymbol{P}^{-}[k] - \boldsymbol{K}[k]\boldsymbol{C}\boldsymbol{P}^{-}[k]$$

Step 5: Go back to Step 1.

In order to ensure that the EKF is capable of estimating all the states correctly, the observability of the system has been checked online in this work. The observability of a linear system can be investigated by computing the observability matrix and its rank. For nonlinear systems, it is possible to check for observability *locally* by analyzing the linearized model around an operating point [116]. The observability matrix of the linearized model of the considered PMSG as in (6.14) can be expressed as

$$\boldsymbol{S}_o[k] := \begin{bmatrix} \boldsymbol{C} \\ \boldsymbol{C}\boldsymbol{A}[k] \\ \boldsymbol{C}\boldsymbol{A}[k]^2 \\ \boldsymbol{C}\boldsymbol{A}[k]^3 \\ \boldsymbol{C}\boldsymbol{A}[k]^4 \end{bmatrix}, \tag{6.15}$$

where $\boldsymbol{A}[k]$ is calculated on-line for each sampling period k (see **Algorithm 3**). The linearized model of the PMSG $\{\boldsymbol{A}[k], \boldsymbol{C}\}$ is locally observable if and only if the observability matrix $\boldsymbol{S}_o[k]$ has full rank, i.e., $\operatorname{rank}\left(\boldsymbol{S}_o[k]\right) = 5$. To verify *local* observability, the rank of the observability matrix $\boldsymbol{S}_o[k]$ is calculated numerically for each sampling period k in Step 3 of **Algorithm 3**.

The estimated stator currents $\hat{\boldsymbol{i}}_s^{dq}[k+1]$ and rotor speed $\hat{\omega}_r[k+1]$ are fed back to the proposed DB control scheme (6.6) as shown in Fig. 6.2. The optimal torque is calculated based on the estimated speed by $T_e^{\star}[k+1] = -k_p^{\star}\,\hat{\omega}_m^2[k+1]$. The q-axis reference current of the stator is found by $i_{s,ref}^{q}[k+1] = \frac{2}{3n_p\psi_{pm}} T_e^{\star}[k+1]$. Then, the reference current $i_{s,ref}^{q}[k+2]$ is calculated using Lagrange extrapolation as explained before.

6.2.2.1 Disturbance observer for PMSGs

The nominal values R_{so}, L_{so}, and ψ_{pmo} are assumed constant and known, whereas the values ΔR_s, ΔL_s, and $\Delta\psi_{pm}$ are not known and vary due to changes in temperature, load, and frequency. Therefore, it is difficult to measure/estimate the real values of the PMSG parameters exactly. Furthermore, the values $\varepsilon^d[k]$ and $\varepsilon^q[k]$ of the un-modeled dynamics are also difficult to obtain. Therefore, a direct calculation of $f^d[k]$ and $f^q[k]$ from (6.2) is difficult (or even impossible), and accordingly, $f^d[k]$ and $f^q[k]$ should be estimated from (6.1) by a simple observer. The proposed observer is based on the time delay control approach [111]. In order to estimate the vale of $f^d[k]$ and $f^q[k]$ in (6.1), it is considered that the values of $f^d[k]$ and $f^q[k]$ at the present sampling instant k are very close to those at a previous sampling instant $k-l$ as follows

$$f^d[k] \approx f^d[k-l] \quad \text{and} \quad f^q[k] \approx f^q[k-l] \tag{6.16}$$

where l is a positive integer. Using this assumption and invoking (6.1), $f^d[k]$ and $f^q[k]$ can be estimated by

$$\left.\begin{aligned}
\hat{f}^d[k] &\approx \hat{f}^d[k-l] = u_s^d[k-l] - \left(R_{so} i_s^d[k-l] + L_{so} \tfrac{i_s^d[k-l+1]-i_s^d[k-l]}{T_s} - \hat{\omega}_r[k-l] L_{so} i_s^q[k-l] \right) \\
\hat{f}^q[k] &\approx \hat{f}^q[k-l] = u_s^q[k-l] - \Big(R_{so} i_s^q[k-l] + L_{so} \tfrac{i_s^q[k-l+1]-i_s^q[k-l]}{T_s} + \hat{\omega}_r[k-l] L_{so} i_s^d[k-l] \\
&+ \hat{\omega}_r[k-l]\psi_{pmo} \Big)
\end{aligned}\right\} \tag{6.17}$$

The main drawback of this method is the numerical differentiation of the measured currents which is necessary in order to estimate the values of $f^d[k]$ and $f^q[k]$. Thus, high frequency noise in the stator current measurements will be amplified. Therefore, a low pass filter (LPF) is utilized to filter out the high frequency noise present in the estimated disturbance signals. However, the LPF will reduce the speed of the proposed observer. Fortunately, in real-world application, the parameter variations (of R_s, L_s, and ψ_{pm}) are slow and the proposed observer can be used effectively; in particular in slow but large-scale direct-driven PMSG based variable-speed WTSs. Furthermore, it is reasonable to assume that $\hat{\boldsymbol{f}}^{dq}[k+1] \approx \hat{\boldsymbol{f}}^{dq}[k]$.

The flow chart of the proposed encoderless DB predictive control scheme of PMSGs is illustrated in Fig. 6.3. The algorithm starts by sampling the current vector $\boldsymbol{i}_s^{\alpha\beta}[k]$ and voltage $\boldsymbol{u}_s^{\alpha\beta}[k]$. Then, the stator current vector $\hat{\boldsymbol{i}}_s^{\alpha\beta}[k+1]$, rotor speed $\hat{\omega}_r[k+1]$, and rotor position $\hat{\phi}_r[k+1]$ will be estimated using the proposed EKF. Subsequently, the disturbance vector $\hat{\boldsymbol{f}}^{dq}[k+1]$ is estimated using the proposed disturbance observer as explained above. Then, the reference voltage vector $\boldsymbol{u}_{s,ref}^{dq}[k+1]$ will be calculated from (6.6). Finally, this reference voltage will be applied to the machine using the SVPWM block.

The computational burden of the proposed DB predictive control with EKF and disturbance observer is rather high, which is a limitation of the proposed control scheme. However, due to the continuous development of faster and more powerful digital signal processors (DSPs), the execution times of more complex algorithms will not be the bottleneck in the future.

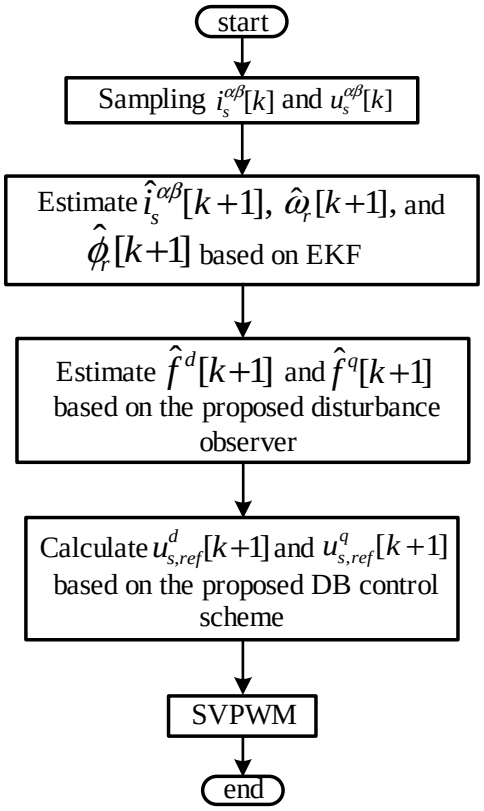

Figure 6.3: Flow chart of the proposed sensorless DB control scheme for PMSG.

6.3 Deadbeat control schemes for DFIGs

In the section, the conventional and proposed DB predictive control for DFIGs are detailed. Considering the perturbations caused by parameter variations of the DFIG or by any un-modeled dynamics, the discrte-time model of the DFIG can be rewritten as

$$\left.\begin{aligned} u_r^d[k] &= R_{ro} i_r^d[k] + \sigma_o L_{ro} \tfrac{i_r^d[k+1]-i_r^d[k]}{T_s} - \omega_{sl}[k] L_{ro} i_r^q[k] + \omega_s \tfrac{L_{mo}^2}{L_{so}} i_r^q[k] - R_{so} \tfrac{L_{mo}}{L_{so}} i_s^d[k] \\ &\quad + \omega_r[k] L_{mo} i_s^q[k] + \tfrac{L_{mo}}{L_{so}} u_s^d[k] + \chi_r^d[k], \\ u_r^q[k] &= R_{ro} i_r^q[k] + \sigma_o L_{ro} \tfrac{i_r^q[k+1]-i_r^q[k]}{T_s} + \omega_{sl}[k] L_{ro} i_r^d[k] - \omega_s \tfrac{L_{mo}^2}{L_{so}} i_r^d[k] - R_{so} \tfrac{L_{mo}}{L_{so}} i_s^q[k] \\ &\quad - \omega_r[k] L_{mo} i_s^d[k] + \tfrac{L_{mo}}{L_{so}} u_s^q[k] + \chi_r^q[k]. \end{aligned}\right\} \tag{6.18}$$

The terms $\chi_r^d[k]$ and $\chi_r^q[k]$ represent the summation of the effects of parameter uncertainties and un-modeled dynamics, and can be written as

$$\left.\begin{aligned} \chi_r^d[k] &= \Delta R_r i_r^d[k] + \Delta\sigma\Delta L_r \tfrac{i_r^d[k+1]-i_r^d[k]}{T_s} - \omega_{sl}[k]\Delta L_r i_r^q[k] + \omega_s \tfrac{\Delta L_m^2}{\Delta L_s} i_r^q[k] - \Delta R_s \tfrac{\Delta L_m}{\Delta L_s} i_s^d[k] \\ &\quad + \omega_r[k]\Delta L_m i_s^q[k] + \tfrac{\Delta L_m}{\Delta L_s} u_s^d[k] + \upsilon^d[k], \\ \chi_r^q[k] &= \Delta R_r i_r^q[k] + \Delta\sigma\Delta L_r \tfrac{i_r^q[k+1]-i_r^q[k]}{T_s} + \omega_{sl}[k]\Delta L_r i_r^d[k] - \omega_s \tfrac{\Delta L_m^2}{\Delta L_s} i_r^d[k] - \Delta R_s \tfrac{\Delta L_m}{\Delta L_s} i_s^q[k] \\ &\quad - \omega_r[k]\Delta L_m i_s^d[k] + \tfrac{\Delta L_m}{\Delta L_s} u_s^q[k] + \upsilon^q[k]. \end{aligned}\right\} \tag{6.19}$$

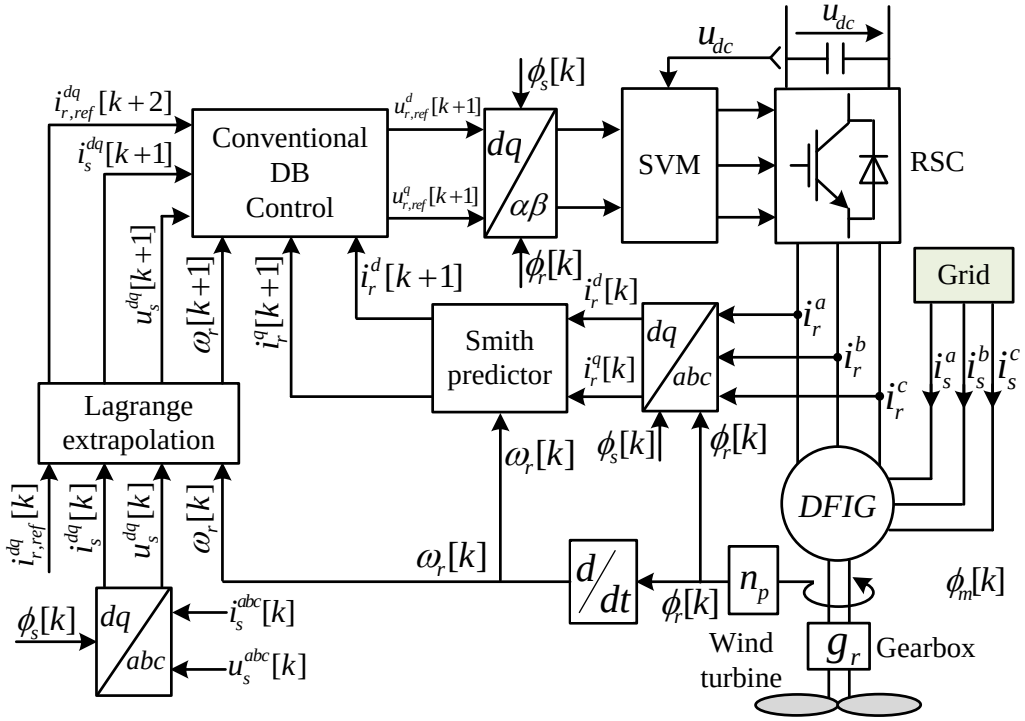

Figure 6.4: Schematic diagram of the conventional DB control with Smith predictor for DFIG based variable-speed wind turbines.

where $R_s = R_{so} + \Delta R_s$, $R_r = R_{ro} + \Delta R_r$, $L_s = L_{so} + \Delta L_s$, $L_r = L_{ro} + \Delta L_r$, $L_m = L_{mo} + \Delta L_m$, and $\upsilon^d[k]$, $\upsilon^q[k]$ represent the un-modeled uncertainties for the d- and q-axis of the DFIG, respectively.

6.3.1 Conventional DB control for DFIG

Considering the nominal system parameters only (i.e. neglecting $\chi_r^d[k]$ and $\chi_r^q[k]$), the one-sample delay due to the digital controller, the reference voltage vector $\boldsymbol{u}_{r,ref}^{dq}[k+1]$ can by calculated as follows

$$\left.\begin{aligned} u_{r,ref}^d[k+1] &= R_{ro} i_r^d[k+1] + \sigma_o L_{ro} \tfrac{i_{r,ref}^d[k+2] - i_r^d[k+1]}{T_s} - \omega_{sl}[k+1] L_{ro} i_r^q[k+1] + \omega_s \tfrac{L_{mo}^2}{L_{so}} i_r^q[k+1] \\ &\quad - R_{so} \tfrac{L_{mo}}{L_{so}} i_s^d[k+1] + \omega_r[k+1] L_{mo} i_s^q[k+1] + \tfrac{L_{mo}}{L_{so}} u_s^d[k+1], \\ u_{r,ref}^q[k+1] &= R_{ro} i_r^q[k+1] + \sigma_o L_{ro} \tfrac{i_{r,ref}^q[k+2] - i_r^q[k+1]}{T_s} + \omega_{sl}[k+1] L_{ro} i_r^d[k+1] - \omega_s \tfrac{L_{mo}^2}{L_{so}} i_r^d[k+1] \\ &\quad - R_{so} \tfrac{L_{mo}}{L_{so}} i_s^q[k+1] - \omega_r[k+1] L_{mo} i_s^d[k+1] + \tfrac{L_{mo}}{L_{so}} u_s^q[k+1]. \end{aligned}\right\} \tag{6.20}$$

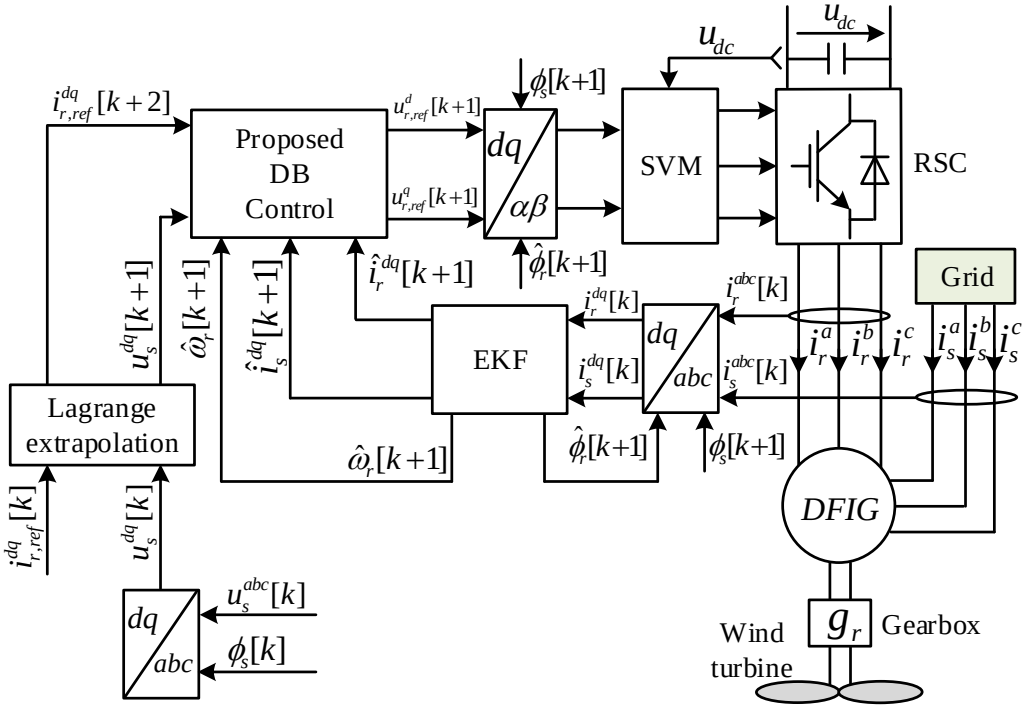

Figure 6.5: Schematic diagram of the proposed DB control with EKF for DFIGs based variable-speed wind turbines.

Similarly to the PMSG, the currents $i_r^d[k+1]$ and $i_r^q[k+1]$ can be predicted from (6.18) using Smith predictor as follows

$$\left.\begin{aligned} i_r^d[k+1] &= i_r^d[k] + \tfrac{T_s}{\sigma_o L_{so} L_{ro}}\Big(- R_{ro}L_{so}i_r^d[k] + (\omega_{sl}[k]L_{ro}L_{so} - \omega_s[k]L_{mo}^2)i_r^q[k] + R_sL_{mo}i_s^d[k] \\ &\quad -\omega_r[k]L_{mo}L_{so}i_s^q[k] + L_{so}u_r^d[k] - L_{mo}u_s^d[k]\Big) \\ i_r^q[k+1] &= i_r^q[k] + \tfrac{T_s}{\sigma_o L_{so} L_{ro}}\Big(- R_{ro}L_{so}i_r^q[k] - (\omega_{sl}[k]L_{ro}L_{so} - \omega_s[k]L_{mo}^2)i_r^d[k] + R_sL_{mo}i_s^q[k] \\ &\quad +\omega_r[k]L_{mo}L_{so}i_s^d[k] + L_{so}u_r^q[k] - L_{mo}u_s^q[k]\Big). \end{aligned}\right\} \tag{6.21}$$

6.3.2 Proposed Deadbeat control with EKF for DFIGs

The proposed sensorless deadbeat control technique for DFIGs is shown in Fig. 6.5. The EKF is employed to predict/estimate the rotor and stator currents $\hat{i}_r^{dq}[k+1]$ & $\hat{i}_s^{dq}[k+1]$ at the next sampling instant. Furthermore, the EKF is designed to estimate rotor speed and position, and the mechanical torque of the DFIG. Hence, the DFIG control will be achieved without mechanical sensors. Furthermore, the perturbations due to parameter variations and un-modeled dynamics are taken into account during the design of the proposed DB control. Therefore, the reference

voltages incorporate the disturbance expressions and are computed as follows

$$\left.\begin{aligned} u^d_{r,ref}[k+1] &= R_{ro}\hat{i}^d_r[k+1] + \sigma_o L_{ro}\frac{i^d_{r,ref}[k+2]-\hat{i}^d_r[k+1]}{T_s} - \hat{\omega}_{sl}[k+1]L_{ro}\hat{i}^q_r[k+1] + \omega_s\frac{L^2_{mo}}{L_{so}}\hat{i}^q_r[k+1] \\ &\quad -R_{so}\frac{L_{mo}}{L_{so}}\hat{i}^d_s[k+1] + \hat{\omega}_r[k+1]L_{mo}\hat{i}^q_s[k+1] + \frac{L_{mo}}{L_{so}}u^d_s[k+1] + \hat{\chi}^d_r[k], \\ u^q_{r,ref}[k+1] &= R_{ro}\hat{i}^q_r[k+1] + \sigma_o L_{ro}\frac{i^q_{r,ref}[k+2]-\hat{i}^q_r[k+1]}{T_s} + \hat{\omega}_{sl}[k+1]L_{ro}\hat{i}^d_r[k+1] - \omega_s\frac{L^2_{mo}}{L_{so}}\hat{i}^d_r[k+1] \\ &\quad -R_{so}\frac{L_{mo}}{L_{so}}\hat{i}^q_s[k+1] - \hat{\omega}_r[k+1]L_{mo}\hat{i}^d_s[k+1] + \frac{L_{mo}}{L_{so}}u^q_s[k+1] + \hat{\chi}^q_r[k]. \end{aligned}\right\} \tag{6.22}$$

The magnitude

$$u_r[k+1] = \|\boldsymbol{u}^{dq}_{r,ref}[k+1]\| = \sqrt{u^d_{r,ref}[k+1]^2 + u^q_{r,ref}[k+1]^2}$$

of the next reference voltage vector $\boldsymbol{u}^{dq}_{r,ref}[k+1]$ is calculated and compared with the maximally available output voltage magnitude $u_{r,max}$ of the voltage source converter which depends on the dc-link voltage u_{dc}. If the magnitude is greater than this value, the reference voltages should be adjusted as follows

$$\boldsymbol{u}^{dq}_{r,ref}[k+1] = \begin{cases} \boldsymbol{u}^{dq}_{r,ref}[k+1], & u_r[k+1] \le u_{r,max} \\ \frac{u_{r,max}}{u_r[k+1]}\boldsymbol{u}^{dq}_{r,ref}[k+1], & u_r[k+1] > u_{r,max}. \end{cases} \tag{6.23}$$

The state-space model, which is essential to design the EKF, of the DFIG can be defined as in (6.8). The state vector $\boldsymbol{x}$, the output (measurement) vector $\boldsymbol{y}$ and the input vector $\boldsymbol{u}$ are defined for the DFIG as follows

$$\left.\begin{aligned} \boldsymbol{x} &= \begin{pmatrix} i^d_s, & i^q_s, & i^d_r, & i^q_r, & \omega_r, & \phi_r, & T_m \end{pmatrix}^\top \\ \boldsymbol{y} &= \begin{pmatrix} i^d_s, & i^q_s, & i^d_r, & i^q_r \end{pmatrix}^\top \\ \boldsymbol{u} &= \begin{pmatrix} u^d_s, & u^q_s, & u^d_r, & u^q_r \end{pmatrix}^\top. \end{aligned}\right\} \tag{6.24}$$

The function $\boldsymbol{g}(\boldsymbol{x},\boldsymbol{u})$ and $\boldsymbol{h}(\boldsymbol{x})$ can be derived from the model of the DFIG [59] and are given by

$$\boldsymbol{g}(\boldsymbol{x},\boldsymbol{u}) = \begin{bmatrix} \frac{1}{\sigma L_s L_r}(-R_s L_r i^d_s + (\omega_r L^2_m + \omega_s \sigma L_s L_r) i^q_s + R_r L_m i^d_r + \omega_r L_m L_r i^q_r + L_r u^d_s - L_m u^d_r) \\ \frac{1}{\sigma L_s L_r}((-\omega_r L^2_m - \omega_s \sigma L_s L_r) i_{sd} - R_s L_r i^q_s - \omega_r L_m L_r i^d_r + R_r L_m i^q_r + L_r u^q_s - L_m u^q_r) \\ \frac{1}{\sigma L_s L_r}(R_s L_m i^d_s - \omega_r L_s L_m i^q_s - R_r L_s i^d_r + (-\omega_r L_r L_s + \omega_s \sigma L_s L_r) i^q_r - L_m u^d_s + L_s u^d_r) \\ \frac{1}{\sigma L_s L_r}(\omega_r L_s L_m i^d_s + R_s L_m i^q_s + (\omega_r L_r L_s - \omega_s \sigma L_s L_r) i^d_r - R_r L_s i^q_r - L_m u^q_s + L_s u^q_r) \\ \frac{n_p}{\Theta}\left[\frac{3}{2} n_p L_m (i^q_s i^d_r - i^d_s i^q_r) - T_m\right] \\ \omega_r \\ 0 \end{bmatrix} \tag{6.25}$$

and

$$\boldsymbol{h}(\boldsymbol{x}) = \begin{bmatrix} 1 & 0 & 0 & 0 & 0 & 0 & 0 \\ 0 & 1 & 0 & 0 & 0 & 0 & 0 \\ 0 & 0 & 1 & 0 & 0 & 0 & 0 \\ 0 & 0 & 0 & 1 & 0 & 0 & 0 \end{bmatrix} \boldsymbol{x}. \tag{6.26}$$

Then, the nonlinear discrete-time model of the DFIG can be expressed as in (6.12). Finally. the EKF is design as explained in **Algorithm 3**.

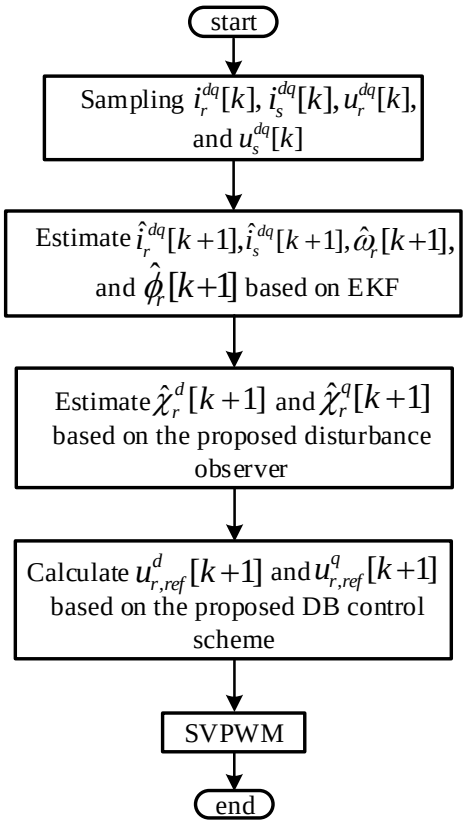

Figure 6.6: Flow chart of the proposed sensorless DB control scheme for DFIG.

6.3.2.1 Disturbance observer for DFIGs

Similarly to the PMSG, it can be assumed that

$$\chi_r^d[k] \approx \chi_r^d[k-l] \quad \text{and} \quad \chi_r^q[k] \approx \chi_r^q[k-l] \tag{6.27}$$

Using this presumption and invoking (6.18), $\chi_r^d[k]$ and $\chi_r^q[k]$ can be computed as follows

$$\left.\begin{aligned}
\hat{\chi}_r^d[k] &= u_r^d[k-l] - \Big(R_{ro} i_r^d[k-l] + \sigma_o L_{ro} \tfrac{i_r^d[k-l+1]-i_r^d[k-l]}{T_s} - \omega_{sl}[k-l] L_{ro} i_r^q[k-l] \\
&+ \omega_s \tfrac{L_{mo}^2}{L_{so}} i_r^q[k-l] - R_{so} \tfrac{L_{mo}}{L_{so}} i_s^d[k-l] + \omega_r[k-l] L_{mo} i_s^q[k-l] + \tfrac{L_{mo}}{L_{so}} u_s^d[k-l]\Big), \\
\hat{\chi}_r^q[k] &= u_r^q[k-l] - \Big(R_{ro} i_r^q[k-l] + \sigma_o L_{ro} \tfrac{i_r^q[k-l+1]-i_r^q[k-l]}{T_s} + \omega_{sl}[k-l] L_{ro} i_r^d[k-l] \\
&- \omega_s \tfrac{L_{mo}^2}{L_{so}} i_r^d[k-l] - R_{so} \tfrac{L_{mo}}{L_{so}} i_s^q[k-l] - \omega_r[k-l] L_{mo} i_s^d[k-l] + \tfrac{L_{mo}}{L_{so}} u_s^q[k-l]\Big).
\end{aligned}\right\} \tag{6.28}$$

The flow chart of the proposed robust DB predictive control without mechanical sensors for DFIGS is illustrated in Fig. 6.6.

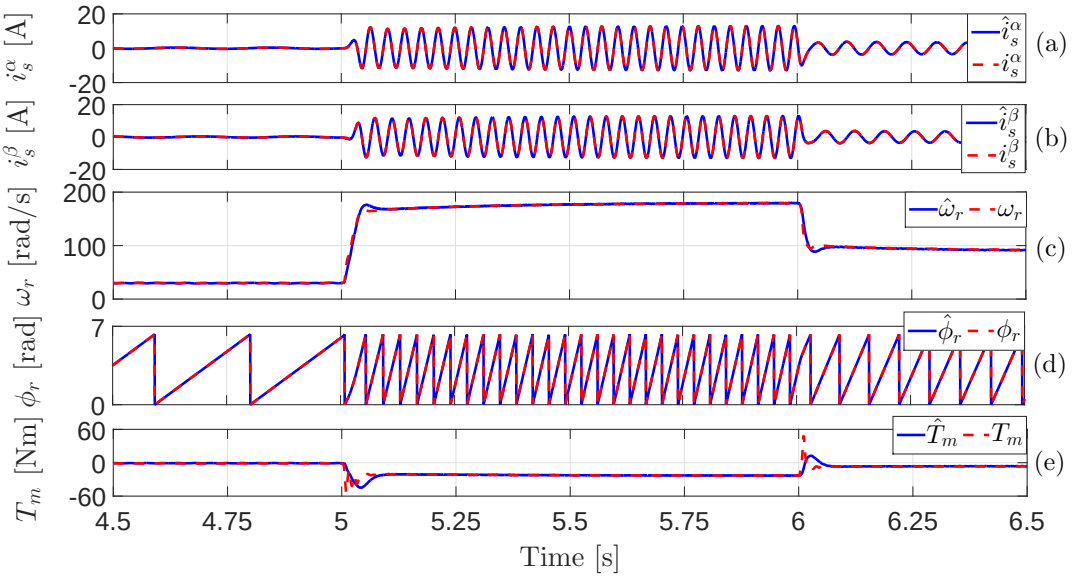

Figure 6.7: Estimation performance of the proposed EKF under step changes in the rotor speed of the PMSG: (a) estimated and measured α-axis current ($\hat{i}_s^\alpha$, i_s^α), (b) estimated and measured β-axis current ($\hat{i}_s^\beta$, i_s^β), (c) estimated and measured rotor speed ($\hat{\omega}_r$, ω_r), (d) estimated and measured rotor position ($\hat{\phi}_r$, ϕ_r), and (e) estimated and measured mechanical torque ($\hat{T}_m$, T_m).

6.4 Experimental results

6.4.1 Experimental results for PMSGs

In order to emulate the real wind turbine, the mechanical speed range is chosen to vary between 4–100 rad/s and the electro-magnetic torque is calculated based on the estimated rotor speed $T_e^\star[k+1] = -0.0061\hat{\omega}_m^2[k+1]$ (i.e. $k_p^\star = 0.0061$) as explained in section 6.2. The selection of the value of $k_p^\star$ is based on the rated torque of the RSM. Therefore, any variation in the rotor speed of the PMSG will be followed with a variation in the generated power.

For the EKF, the initial values of state vector and covariance matrices (following the guide lines in [113]) have been set to

$$\begin{aligned} \boldsymbol{x}_0 &= (0,0,0,0,0)^\top, \\ \boldsymbol{Q} &= \mathrm{diag}\{0.6, 0.6, 0.16, 0.08, 0.45\}, \\ \boldsymbol{R} &= \mathrm{diag}\{0.5, 0.5\}, \quad \text{and} \\ \boldsymbol{P}_0 &= \mathrm{diag}\{0.8, 0.8, 0.03, 0.08, 2\}. \end{aligned}$$

6.4.1.1 Estimation performance of the proposed EKF for PMSGs

Fig. 6.7 shows the estimation performance of the proposed EKF under step changes in the reference mechanical speed of the RSM from 10 rad/s to 60 rad/s at $t = 5$ s and then back to 30 rad/s at $t = 6$ s, respectively. According to Fig. 6.7, the proposed EKF tracks the stator

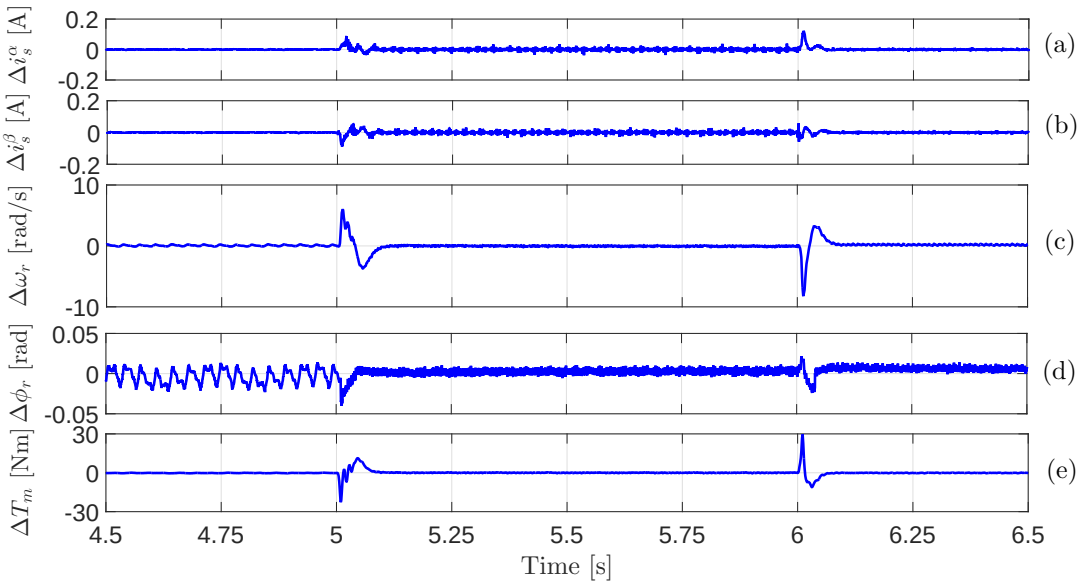

Figure 6.8: Estimation error of the proposed EKF under step changes in the rotor speed of the PMSG: (a) $\Delta i_s^\alpha = i_s^\alpha - \hat{i}_s^\alpha$, (b) $\Delta i_s^\beta = i_s^\beta - \hat{i}_s^\beta$, (c) $\Delta\omega_r = \omega_r - \hat{\omega}_r$, (d) $\Delta\phi_r = \phi_r - \hat{\phi}_r$, and (e) $\Delta T_m = T_m - \hat{T}_m$.

currents, rotor speed, rotor position, and the mechanical torque with a good dynamic and steady-state performance. The steady-state values of the estimation errors are almost zero (see Fig. 6.8) and the transient errors decay quickly to zero. The rank of the observability matrix in this case is 5 (not shown due to the space limitations). This means that the observability matrix has full ranked and the linearized system is locally observable.

In order to check the robustness of the EKF under (unknown) parameter variations of the PMSG, the value of the stator resistance R_s is decreased/increased by 50% in the software model at the time instants $t = 4.4\,\mathrm{s}$ and $t = 4.8\,\mathrm{s}$, respectively. For this scenario, Fig. 6.9 shows the estimation performances of the proposed EKF. The mechanical speed of the rotor is set to $40\,\mathrm{rad/s}$ by the RSM control system. The proposed EKF is robust against parameter uncertainties in stator resistance. Only, small deviations in the estimated speed appeared due to variations in R_s. However, no impact on the estimated stator currents, rotor position, and mechanical torque is visible. Also for this scenario, the rank of the observability matrix is 5.

Furthermore, the robustness with respect to changes (due to magnetic saturation) in the stator inductance L_s is investigated. Therefore, L_s is decreased/increased by 50% in the software model at the time instants $t = 4.4\,\mathrm{s}$ and $t = 4.8\,\mathrm{s}$, respectively. The mechanical speed of the rotor is set to $50\,\mathrm{rad/s}$ by the RSM control system. Fig. 6.10 illustrates the experimental results of the proposed EKF for this scenario. Again, the EKF shows an accurate estimation performance and is robust against parameter uncertainties in L_s. Only, small deviations in the estimated speed occurs due to the inductance variation. However, it has no effect on the estimated stator currents, rotor position, and mechanical torque. Also in this case, the rank of the observability matrix is 5.

Finally, the capability of the proposed EKF in filtering the harmonics of the measured currents (particularly for low values of the stator currents) is investigated. Fig. 6.11 shows the waveforms of the estimated and measured α-axis stator current of the PMSG at $\omega_m = 15\,\mathrm{rad/s}$

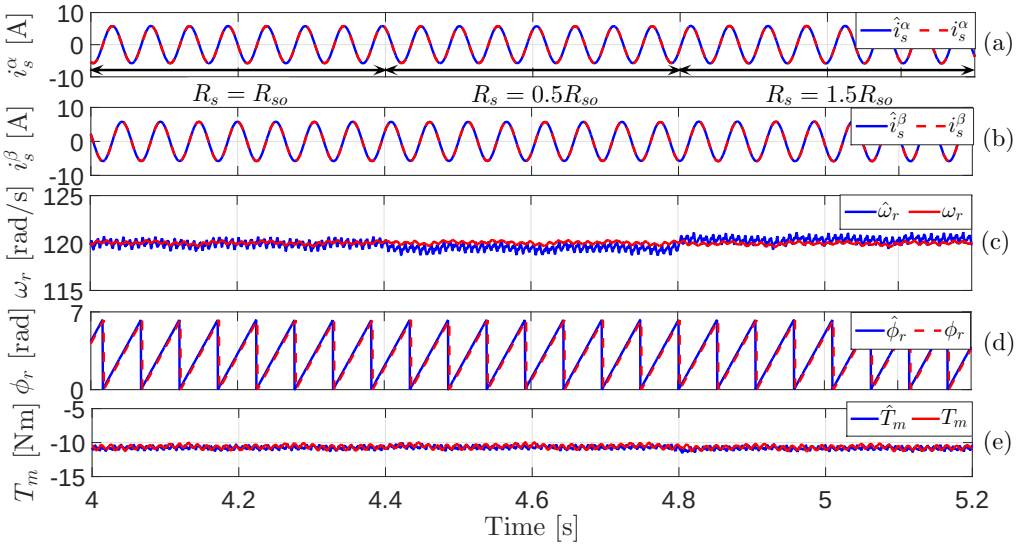

Figure 6.9: Estimation performance of the proposed EKF at step changes in the stator resistance R_s of the PMSG: (a) estimated and measured α-axis current ($\hat{i}_s^\alpha$, i_s^α), (b) estimated and measured β-axis current ($\hat{i}_s^\beta$, i_s^β), (c) estimated and measured rotor speed ($\hat{\omega}_r$, ω_r), (d) estimated and measured rotor position ($\hat{\phi}_r$, ϕ_r), and (e) estimated and measured mechanical torque ($\hat{T}_m$, T_m).

and $60\,\mathrm{rad/s}$, respectively. The THDs of the measured current are 10.86% and 1.56%, while the THDs of the estimated currents are 6.12% and 0.65%, respectively. Obviously, the THDs are significantly reduced by the EKF. The current THDs were computed with 10 cycles of the respective stator currents up to 250 times of its fundamental frequency using MATLAB Power-GUI.

6.4.1.2 Control performance of the proposed DB control for PMSGs

Fig. 6.12 illustrates the transient performance of the conventional and proposed DB control schemes during step changes in the rotor mechanical speed ω_m from $20\,\mathrm{rad/s}$ to $80\,\mathrm{rad/s}$, and then back to $40\,\mathrm{rad/s}$ at $t = 4\,\mathrm{s}$ and $t = 5\,\mathrm{s}$, respectively. It can be seen from this figure that the dynamic performance of both schemes is similar. However, the steady-state response of the proposed DB control scheme is better than that of the conventional DB control system. Using the conventional DB control scheme, the d- and q-axis currents deviate from their reference values. The reason for that is the nominal values of the PMSG parameters R_{so}, L_{so}, ψ_{pmo} are used in the model (6.3) to calculate the reference voltage vector without considering the parameters variations and the un-modeled dynamics. In comparison with the conventional DB control scheme, no steady-state error (SSE) remains for the proposed DB current control system. The estimated values $\hat{f}^d$ and $\hat{f}^q$ of the perturbations are also illustrated in Fig. 6.12. It can be observed that the estimated perturbation values $\hat{f}^d$ and $\hat{f}^q$ are not zero although the nominal parameters R_{so}, L_{so}, ψ_{pmo} of the PMSG have been used in this scenario. Those estimated values $\hat{f}^d$ and $\hat{f}^q$ are considered during the calculation of the reference voltages in (6.6) in order to make the d- and q-axis currents track their reference values.

The robustness of the conventional and proposed DB predictive control systems against parameter variations of the PMSG is investigated. Fig. 6.13 shows the performance of the con-

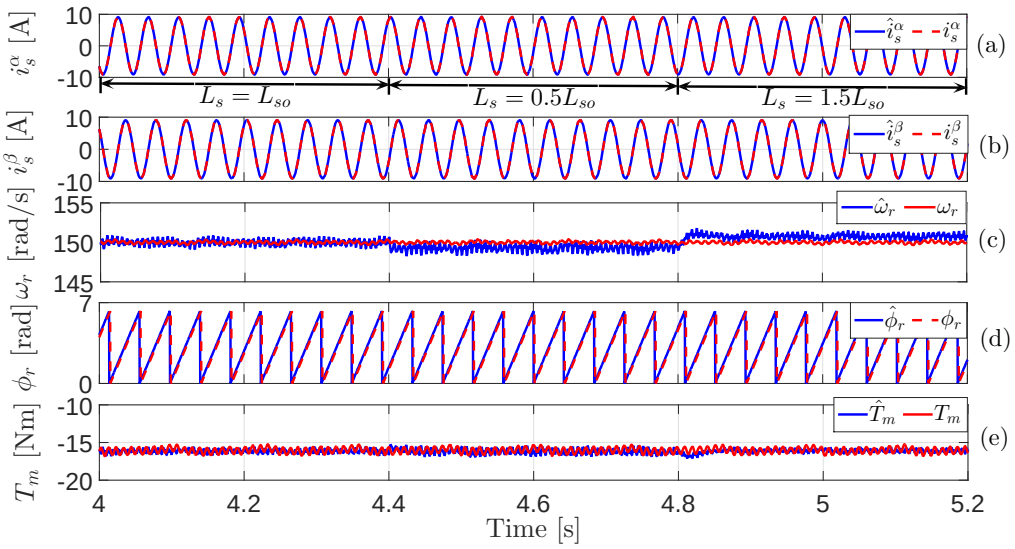

Figure 6.10: Estimation performance of the proposed EKF at step changes in the stator inductance L_s of the PMSG: (a) estimated and measured α-axis current ($\hat{i}_s^\alpha$, i_s^α), (b) estimated and measured β-axis current ($\hat{i}_s^\beta$, i_s^β), (c) estimated and measured rotor speed ($\hat{\omega}_r$, ω_r), (d) estimated and measured rotor position ($\hat{\phi}_r$, ϕ_r), and (e) estimated and measured mechanical torque ($\hat{T}_m$, T_m).

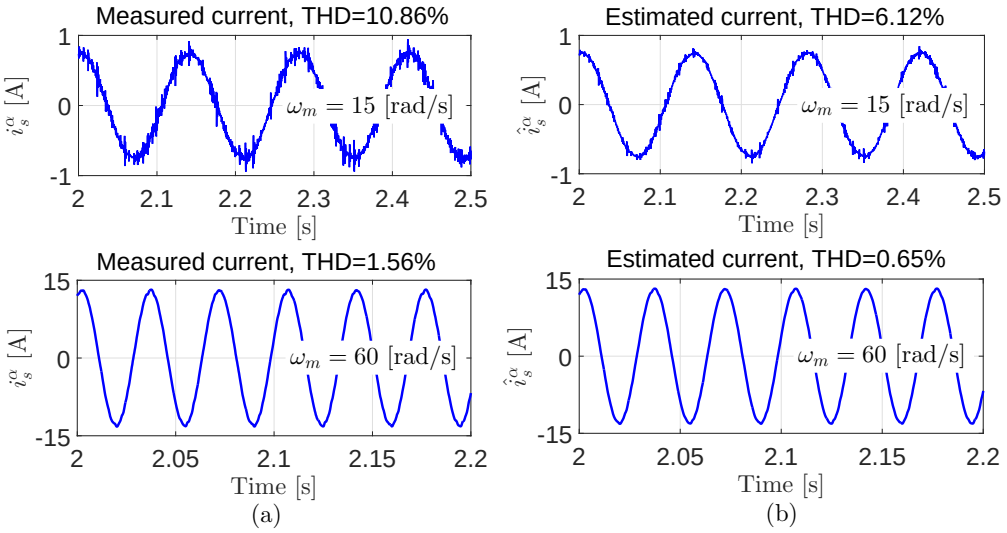

Figure 6.11: Steady-state waveforms of α-axis current i_s^α of the PMSG: (a) Measured α-axis current i_s^α, and (b) estimated α-axis current $\hat{i}_s^\alpha$ using the proposed EKF.

ventional and proposed DB predictive control scheme under $\mp 50\%$ software step changes in the stator resistance R_s of the PMSG. The mechanical speed of the rotor is set to $60\,\mathrm{rad/s}$ by the RSM control system. The influence of resistance variations of the PMSG is effectively suppressed by the proposed control scheme, whereas the performance of the conventional DB control strategy is deteriorated by the uncertainty in R_s. The estimated values $\hat{f}^d$ and $\hat{f}^q$ are also illustrated in Fig. 6.13.

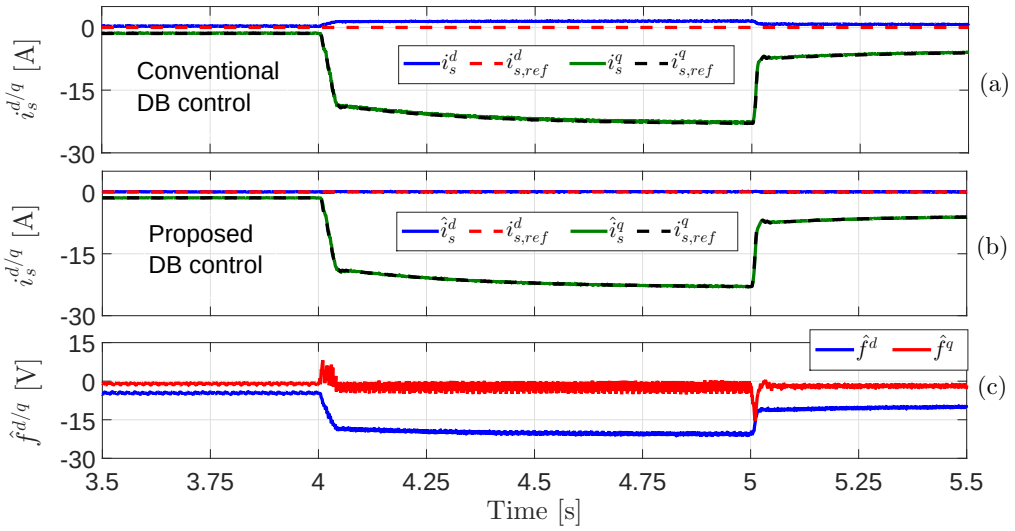

Figure 6.12: Dynamic performance of the conventional and proposed predictive DB control systems for PMSGs: (a) Measured and reference d- and q-axis currents (i_s^{dq}, $i_{s,ref}^{dq}$), (b) Estimated and reference d- and q-axis currents ($\hat{i}_s^{dq}$, $i_{s,ref}^{dq}$), and (c) estimated disturbance ($\hat{f}^d$, $\hat{f}^q$).

Fig. 6.14 illustrates the performance of the conventional and proposed DB control techniques under $\mp 50\%$ software step changes in the stator inductance L_s of the PMSG. The mechanical speed of the rotor is set to $50\,\mathrm{rad/s}$ by the RSM control system. In contrast to the conventional DB control scheme, the proposed control strategy is robust to uncertainties in the stator inductance L_s of the PMSG. The estimated values $\hat{f}^d$ and $\hat{f}^q$ are also shown in Fig. 6.14.

Furthermore, the performances of the conventional and proposed DB control schemes under $\mp 25\%$ software step changes in the permanent-magnet flux linkage ψ_{pm} are illustrated in Fig. 6.15. The mechanical speed of the rotor is set to $70\,\mathrm{rad/s}$ by the RSM control system. It can be observed from this figure that the conventional DB control technique is sensitive to uncertainties in the permanent-magnet flux linkage ψ_{pm}. The q-axis current deviates from its references and a large SSE remains. In contrast to the conventional DB control system, the proposed control technique demonstrates good robustness against variations of the permanent-magnet flux linkage ψ_{pm}. The d- and q-axis currents track their references with good dynamic and steady-state performance and the SSE is zero. $\hat{f}^d$ and $\hat{f}^q$ are also illustrated in Fig. 6.15.

Finally, the steady-state waveforms of the electro-magnetic torque T_e of the PMSG using the conventional and proposed control technique are illustrated in Fig. 6.16 for different mechanical rotor speeds. It is worth noting that the torque ripples are significantly smaller for the proposed DB controller than for the conventional DB scheme.

6.4.2 Experimental results for DFIGs

The estimation performance of the EKF and control response of the proposed DB control technique have been extensively investigated for PMSGs. Accordingly, it is not required to repeat all the scenarios again for DFIGs. Only, one scenario for each category will be investigated.

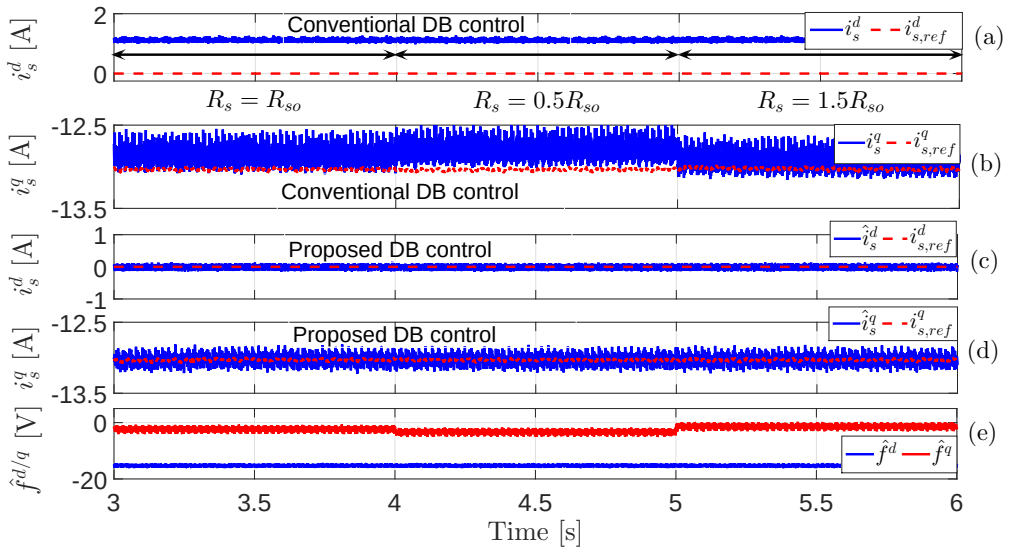

Figure 6.13: Performance of the conventional and proposed DB control strategies at step changes in the stator resistance R_s of the PMSG: (a) Measured and reference d-axis currents (i_s^d, $i_{s,ref}^d$), (b) Measured and reference q-axis currents (i_s^q, $i_{s,ref}^q$), (c) Estimated and reference d-axis currents ($\hat{i}_s^d$, $i_{s,ref}^d$), (d) Estimated and reference q-axis currents ($\hat{i}_s^q$, $i_{s,ref}^q$), and (e) estimated disturbance ($\hat{f}^d$, $\hat{f}^q$).

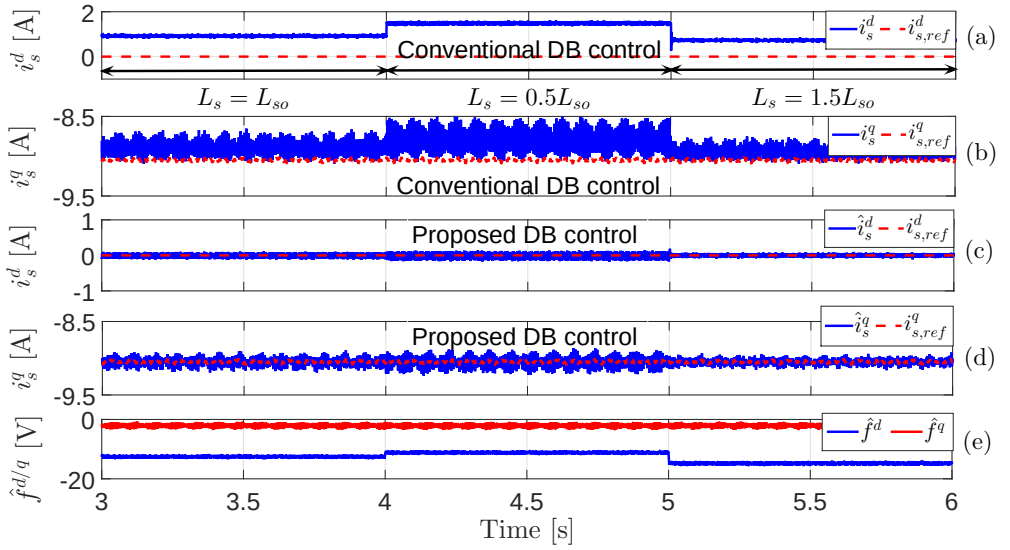

Figure 6.14: Performance of the conventional and proposed DB control strategies at step changes in the stator inductance L_s of the PMSG: (a) Measured and reference d-axis currents (i_s^d, $i_{s,ref}^d$), (b) Measured and reference q-axis currents (i_s^q, $i_{s,ref}^q$), (c) Estimated and reference d-axis currents ($\hat{i}_s^d$, $i_{s,ref}^d$), (d) Estimated and reference q-axis currents ($\hat{i}_s^q$, $i_{s,ref}^q$), and (e) estimated disturbance ($\hat{f}^d$, $\hat{f}^q$).

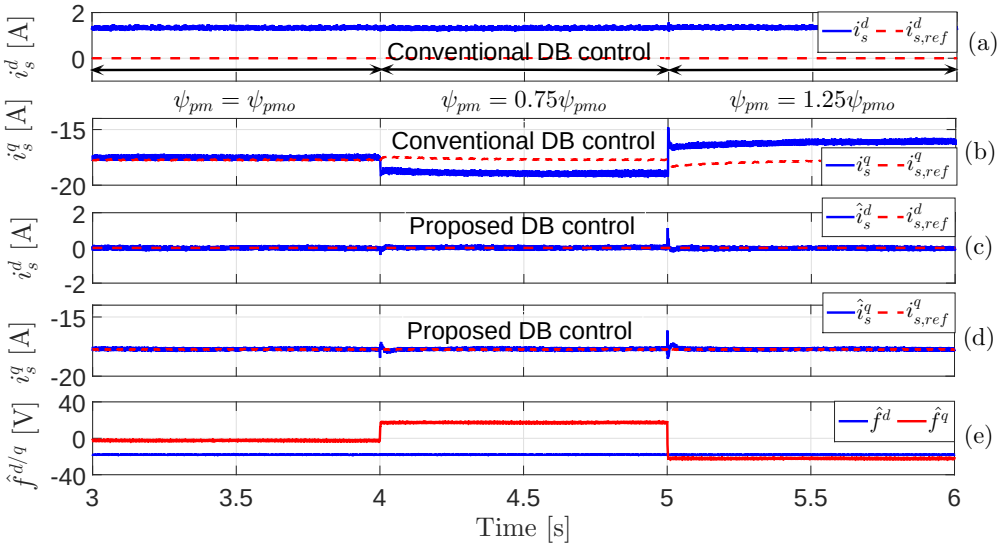

Figure 6.15: Performance of the conventional and proposed DB control strategies at step changes in the permanent-magnet flux linkage ψ_{pm}: (a) Measured and reference d-axis currents (i_s^d, $i_{s,ref}^d$), (b) Measured and reference q-axis currents (i_s^q, $i_{s,ref}^q$), (c) Estimated and reference d-axis currents ($\hat{i}_s^d$, $i_{s,ref}^d$), (d) Estimated and reference q-axis currents ($\hat{i}_s^q$, $i_{s,ref}^q$), and (e) estimated disturbance ($\hat{f}^d$, $\hat{f}^q$).

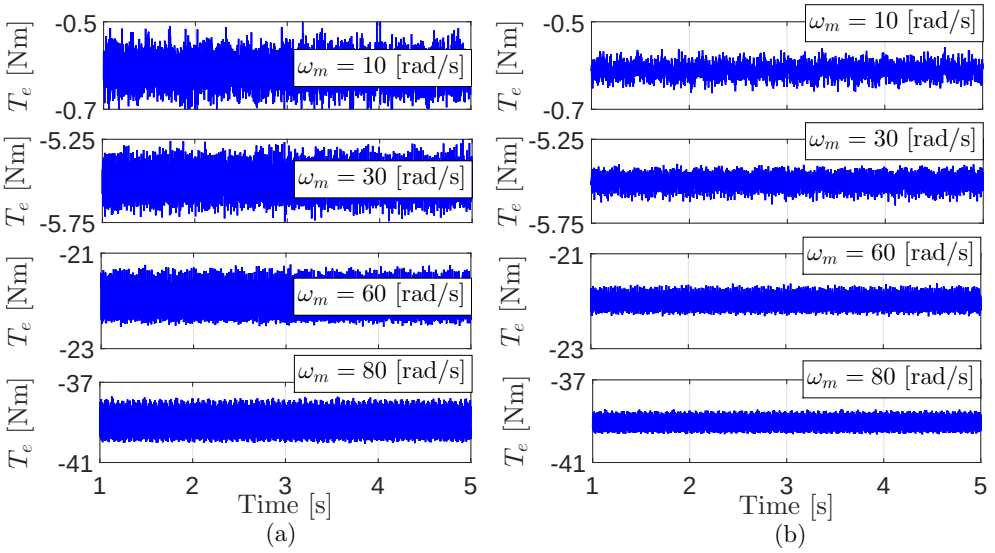

Figure 6.16: Steady-state waveforms of the electro-magnetic torque T_e of the PMSG: (a) Conventional DB control strategy, and (b) proposed DB control scheme.

6.4.2.1 Estimation performance of the proposed EKF for DFIGs

For the estimation performance of the proposed EKF for DFIGs, the capability in filtering the harmonics of the measured currents is investigated. Fig. 6.17 illustrates the waveforms of the estimated and measured phase a rotor current of the DFIG at $\omega_m = 120\,\mathrm{rad/s}$, $130\,\mathrm{rad/s}$, $140\,\mathrm{rad/s}$, $150\,\mathrm{rad/s}$, and $160\,\mathrm{rad/s}$, respectively. The reference d-axis current $i_{r,ref}^d$ is set

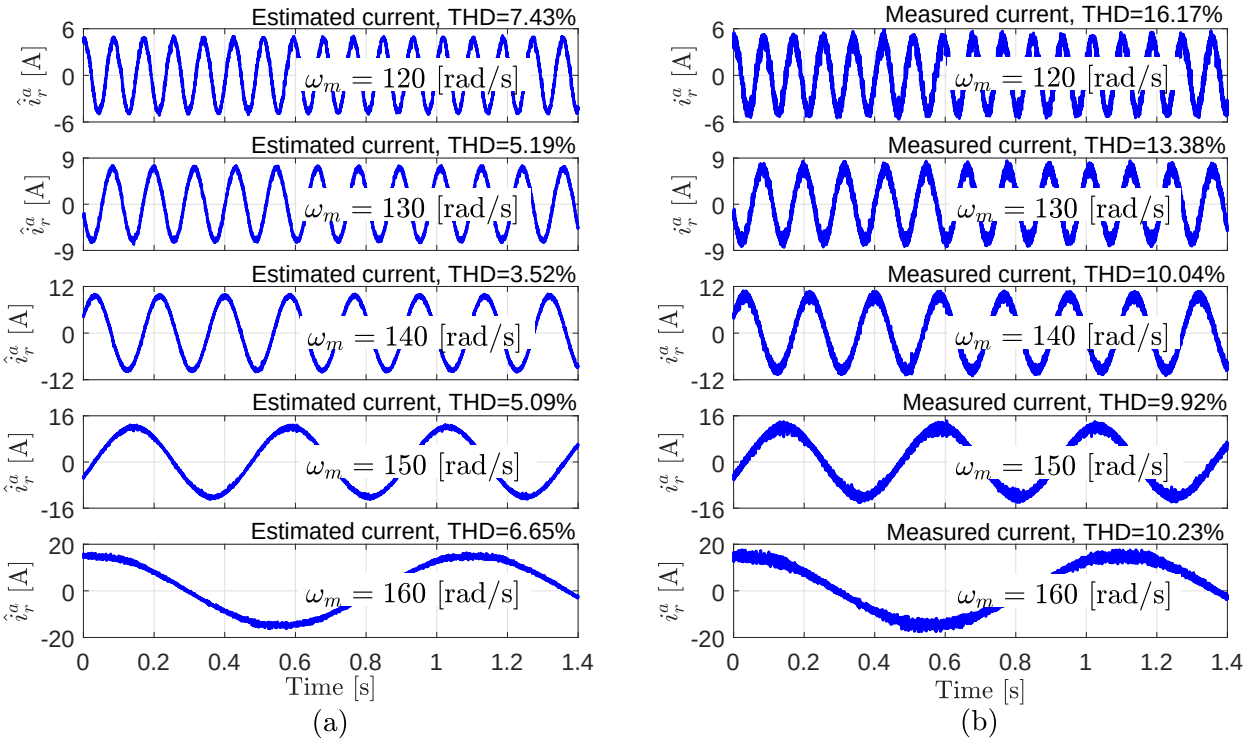

Figure 6.17: Steady-state waveforms of phase a current i_r^a of the DFIG rotor: (a) Estimated phase a current $\hat{i}_r^a$ using the proposed EKF, and (b) measured phase a current i_r^a.

to 5 A, 7.5 A, 10 A, 12.5 A, and 15 A, respectively. The THDs of the measured current are 16.17%, 13.38%, 10.04%, 9.92%, and 10.23%, while the THDs of the estimated currents are 7.43%, 5.19%, 3.52%, 5.09%, and 6.65%, respectively. Obviously, the THDs are significantly reduced by the EKF.

6.4.2.2 Control performance of the proposed DB control for DFIGs

Fig. 6.18 illustrate the performance of the classical DB control scheme and proposed DB control technique at variations of the mutual inductance L_m, which reduced to $0.5L_{mo}$ and increased gradually to $2.5L_{mo}$. The mechanical speed of the rotor is set to $145\,\mathrm{rad/s}$ by the EESM control system. It can be observed that the proposed DB algorithm demonstrated good robustness to variation of the mutual inductance L_m in comparison with the conventional DB technique. The estimated sum of disturbances $\hat{\chi}_r^{d/q}$ is also showed in Fig. 6.18.

6.5 Summary

In this chapter, a robust and sensorless deadbeat predictive control scheme for PMSGs/DFIGs in variable-speed wind turbines is presented. The proposed control system used an EKF to estimate the stator (and rotor) currents, rotor speed and position, and mechanical torque of the PMSG/DFIG. The one-step-delay in the digital control system was compensated by feeding back the estimated stator (and rotor) currents to the prediction algorithm. Furthermore, a simple

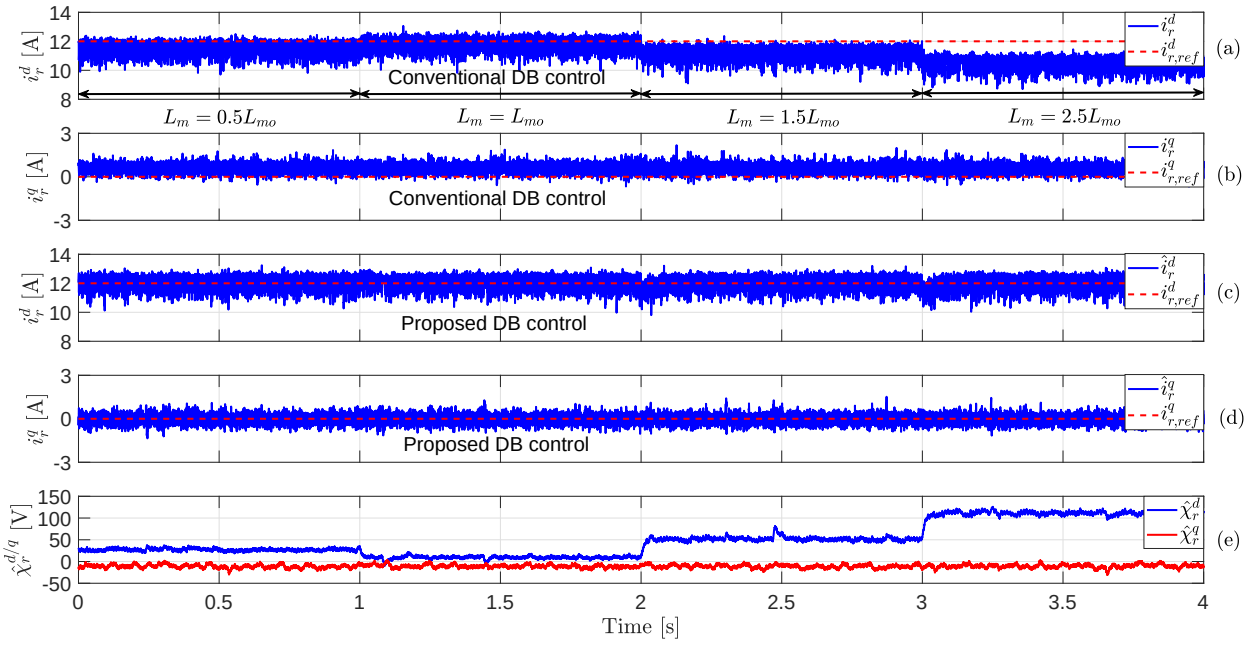

Figure 6.18: Performance of the conventional and proposed DB control strategies for DFIGs at step changes in the mutual inductance L_m: (a) Measured and reference d-axis currents (i_r^d, $i_{r,ref}^d$), (b) Measured and reference q-axis currents (i_r^q, $i_{r,ref}^q$), (c) Estimated and reference d-axis currents ($\hat{i}_r^d$, $i_{r,ref}^d$), (d) Estimated and reference q-axis currents ($\hat{i}_r^q$, $i_{r,ref}^q$), and (e) estimated disturbance ($\hat{\chi}_r^d, \hat{\chi}_r^q$).

disturbance observer was presented in order to increase the robustness of the proposed DB algorithm against parameters uncertainties of the PMSG/DFIG. The proposed control system was implemented and experimentally validated in the laboratory. The experimental results showed that the EKF estimates stator (and rotor) currents, rotor speed, rotor position, and mechanical torque with high accuracy and is robust to variations in the PMSG/DFIG parameters. Furthermore, the proposed disturbance observer improves the robustness of the DB control scheme against parameter variations and achieves zero steady-state estimation errors. Moreover, the THD of the stator (and rotor) currents and the electro-magnetic torque ripples are significantly reduced by the filtering capability of the EKF. Concluding, the overall proposed encoderless predictive control system achieves a fast, accurate and robust control performance even under parameter variations.

CHAPTER 7

Simple and robust FCS-MPC for PMSGs and DFIGs

This chapter presents a simple and robust FCS-MPC for PMSGs (Sec. 7.3) and DFIGs (Sec. 7.5) in variable-speed wind energy conversion systems (WECS). The proposed FCS-MPC strategy significantly reduces the calculation burden of the conventional FCS-MPC. Accordingly, it can be implemented in the current DSPs available in the industrial platforms. Furthermore, the perturbations due to parameters variations or un-modeled dynamics for PMSGs and DFIGs have been considered in the proposed control technique, see Sec. 7.3.1 and Sec. 7.5.1, respectively. The proposed control system has been experimentally implemented and validated for PMSGs and DFIGs (Sec. 7.6). Finally, a summary of this chapter is given in Sec. 7.7.

7.1 Introduction

DMPC schemes have been successfully applied for various applications such as 2-level power converters, multi-level power converters, induction motors (IMs), permanent-magnet synchronous machines (PMSMs), and others due to their intuitive concept, straightforward implementation, and ability to handle constraints and non-linearities [20]–[24], [117]–[119]. However, DMPC relays on the system model to predict its future performance. This model is based on the parameters of the system, which may not match with their actual values because of measurement errors or they may vary during the operation of the system (i.e variation of the operation frequency, temperature, aging, etc.). Variations of the model parameter cause inaccurate prediction of system behavior and deteriorates the performance of the DMPC, i.e., large steady-state error and large ripples in the current/torque waveforms. The effect of parameter variations on the performance of FCS-MPC has been studied in [120]. Furthermore, due to the lack of an integral term in the MPC schemes, a non-zero steady-state error is always exist, which is a well-known drawback of the DMPC techniques.

To overcome the parameter-dependent problem in MPC schemes, several approaches have been presented in the literature [121]–[145]. Model free predictive control (MFPC) has been presented in [121] and [122]. This method utilizes the sampled current differences, instead of the system model, to predict the current gradient under each switching state, thus the sensitivity to parameter variations is avoided. However, MFPC technique is strongly dependent on the accuracy of the current measurement, and accordingly, any noise or measuring error can lead to instability of the system. Similar idea of storing modeling error information in each switching state has been presented in [123] and [124], in which the previous error of the same switching state is multiplied by a gain and added to the current prediction of the current sampling instant.

Estimation of the model/machine parameters is another solution to deal with the parameter-dependent problem in MPC techniques. In [125], an on-line estimation technique of the model parameters based on least-square method (LSM) is presented. The extended Kalman filter (EKF), which is a powerful observer for non-linear systems, has been employed for parameters estimation in [46], [126]–[128]. Model reference adaptive system (MRAS) observer [128], [129], neural-networks [130], and others [131]–[133] have been proposed in the literature for parameters estimation of the model/machine. However, the main disadvantage of those on-line parameter estimation techniques is the significantly high computational burden. Therefore, the current real-time systems available in the industry platforms may not be capable to implement the DMPC with the on-line parameter estimation technique. Consequently, a powerful digital signal processor (DSP) is required, which means higher cost.

A more familiar approach is estimation of the total disturbance caused by parameter mismatch and compensate the lumped mismatch in a feed-forward way. Luenberger observer [134], [135], time delay control approach (TDCA) [47], [136], [137], model reference adaptive control (MRAC) [138], internal model based observer [139], sliding-mode observer [103], [140], generalized proportional integral observers [141], disturbnace observers [142], [143], and others [144], [145] have been presented to enhance the robustness of MPC strategies to variations of the model parameters. However, the main disadvantage of those observers is the relatively high calculation load.

In this work, an efficient DMPC (EDMPC) with discrete-time integral action (DTIA) for PMSGs/DFIGs is proposed. In order to reduce the calculation burden of the conventional DMPC, the reference voltage vector (VV) is directly computed from the reference currents. Then, in order to enhance the robustness of the proposed EDMPC and achieve a zero steady-state error, a weighted DTIA is added to this reference VV calculation. This DTIA is simple and easy to implement, i.e., its calculation burden is low in comparison with that of the other observers (Luenberger observer, TDCA, internal model based observer, etc.). Then, according to the location of this reference VV, the quality function is evaluated for only two times to get the optimal VV. Experimental results are given in this chapter to validate the effectiveness of the proposed EDMPC with DTIA in comparison with those of: i) EDMPC with TDCA [137], and ii) conventional DMPC. These experimental results illustrated that the proposed EDMPC with DTIA is robust to variations of the model parameters and gives a zero steady-state error. Moreover, the calculation burden of the proposed EDMPC with DTIA is significantly lower than that of the conventional one, which means that the proposed EDMPC with DTIA can be implemented using the current real-time systems available in the industry platforms without additional cost.

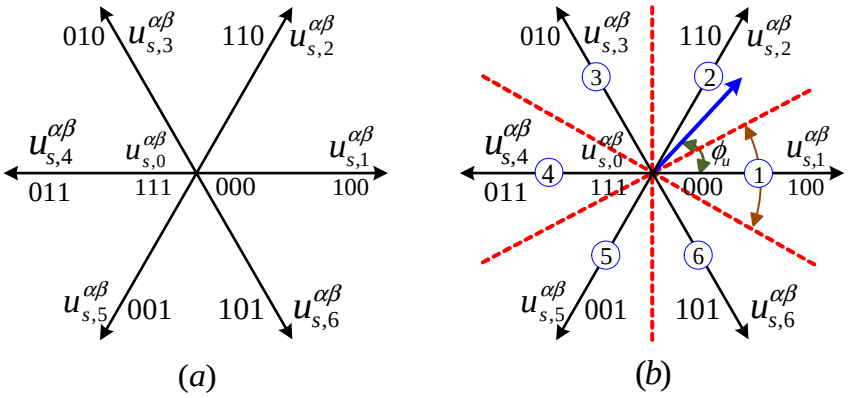

Figure 7.1: (a) All the candidates VVs for 2-level power converter, and (b) proposed sector distribution.

7.2 Conventional DMPC for PMSGs

The discrete-time model of the PMSG considering the perturbations caused by parameter variations of the PMSG or by any un- modeled dynamics is given in (6.1). Generally, in the conventional DMPC, the nominal parameters of the system/machine are considered (i.e. neglecting $f^d[k]$ and $f^q[k]$) to predict its future performance [137], [146]. Hence, considering the one-sample delay due to the digital controller, the prediction model can be expressed as follows

$$\left.\begin{aligned} i_s^d[k+2] &= (1-\tfrac{T_s R_{so}}{L_{so}})i_s^d[k+1] + \omega_r[k+1]T_s i_s^q[k+1] + \tfrac{T_s}{L_{so}}u_s^d[k+1], \\ i_s^q[k+2] &= (1-\tfrac{T_s R_{so}}{L_{so}})i_s^q[k+1] - \omega_r[k+1]T_s i_s^d[k+1] - \tfrac{T_s}{L_{so}}\omega_r[k+1]\psi_{pmo} + \tfrac{T_s}{L_{so}}u_s^d[k+1]. \end{aligned}\right\} \tag{7.1}$$

The currents $i_s^d[k+1]$ and $i_s^q[k+1]$ can be computed as illustrated in (6.4). The rotor speed $\omega_r[k+1]$ can be calculated using Lagrange extrapolation [23] as follows

$$\omega_r[k+1] = 2\omega_r[k] - \omega_r[k-1]. \tag{7.2}$$

Finally, the quality function is defined as

$$\begin{aligned} g_c &= \left|i_{s,ref}^d[k+2] - i_s^d[k+2]\right| + \left|i_{s,ref}^q[k+2] - i_s^q[k+2]\right| \\ &+ \begin{cases} 0 & \text{if} \sqrt{i_s^d[k+2]^2 + i_s^q[k+2]^2} \leq i_{s,max} \\ \infty & \text{if} \sqrt{i_s^d[k+2]^2 + i_s^q[k+2]^2} > i_{s,max}, \end{cases} \end{aligned} \tag{7.3}$$

where $i_{s,max}$ is the maximum allowable current of the stator of the PMSG.

Using the seven different voltage vectors (VVs) shown in Fig. 7.1a ($u_{s0}^{\alpha\beta}$–$u_{s6}^{\alpha\beta}$) of the two-level power converter and the prediction model in (7.1), seven different values of the currents can be predicted. Then, the quality function is evaluated for each VV and the VV, which its prediction minimizes the quality function (7.3), will be applied at the next sampling period. The schematic diagram of the conventional DMPC is illustrated in Fig. 7.2.

According to (7.1), the conventional DMPC is highly depended on the model parameters. Therefore, variations of the machine parameters will deteriorate the control performance, i.e., high ripples will exist in the currents waveforms and non-zero steady-state error will result. Furthermore, the high calculation burden is another drawback of the conventional DMPC.

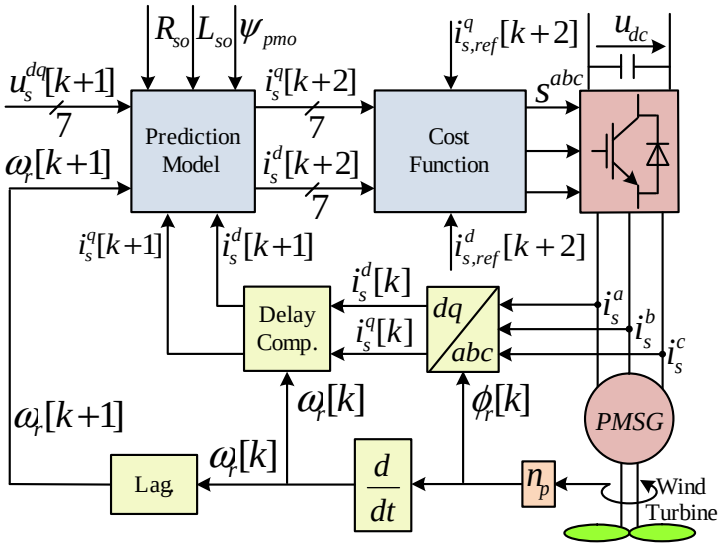

Figure 7.2: Conventional DMPC for PMSGs in variable speed wind turbines.

7.3 Proposed DMPC for PMSGs

The proposed Efficient DMPC (EDMPC) takes into consideration the perturbations due to parameter variations and un-modeled dynamics [146]. Furthermore, the calculation burden of the proposed EDMPC is significantly lower than that of the conventional DMPC.

The idea of the conventional DMPC is to choose a VV $u^{dq}_s[k+1]$ which makes the predicted current $i^{dq}_s[k+2]$ close or equal to its reference $i^{dq}_{s,ref}[k+2]$ in the next sampling instant. In the proposed EDMPC, the reference VV $u^{dq}_{s,ref}[k+1]$ can be directly computed by replacing the current $i^{dq}_s[k+2]$ with the reference value $i^{dq}_{s,ref}[k+2]$ as follows

$$\left.\begin{aligned} u^d_{s,ref}[k+1] &= R_{so} i^d_s[k+1] + L_{so}\frac{i^d_{s,ref}[k+2]-i^d_s[k+1]}{T_s} - \omega_r[k+1]L_{so} i^q_s[k+1] + \hat{f}^d[k+1], \\ u^q_{s,ref}[k+1] &= R_{so} i^q_s[k+1] + L_{so}\frac{i^q_{s,ref}[k+2]-i^q_s[k+1]}{T_s} + \omega_r[k+1]L_{so} i^d_s[k+1] + \omega_r[k+1]\psi_{pmo} \\ &\quad + \hat{f}^q[k+1], \end{aligned}\right\} \tag{7.4}$$

where $\hat{f}^d[k+1]$ and $\hat{f}^q[k+1]$ are the estimated values of the summation of disturbances due to parameter mismatch and un-modeled dynamics.

The magnitude of the reference VV $\boldsymbol{u}^{dq}_{s,ref}[k+1]$ is computed and compared with the maximally available output voltage magnitude $u_{s,max}$ of the power converter and if the magnitude is higher than this value, the reference voltages is adjusted as illustrated in (6.7).

Then, this reference VV $\boldsymbol{u}^{dq}_{s,ref}[k+1]$ is transformed to the stationary reference frame $\alpha\beta$ using the Park transformation. Accordingly, its location can be determined as illustrated in Fig. 7.1b. Its angle is given by

$$\phi_u[k] = \text{atan2}(u^{\beta}_{s,ref}[k+1], u^{\alpha}_{s,ref}[k+1]). \tag{7.5}$$

The new quality function can now be written as

$$g_n = \left|u^{\alpha}_{s,ref}[k+1] - u^{\alpha}_s[k+1]\right| + \left|u^{\beta}_{s,ref}[k+1] - u^{\beta}_s[k+1]\right|. \tag{7.6}$$

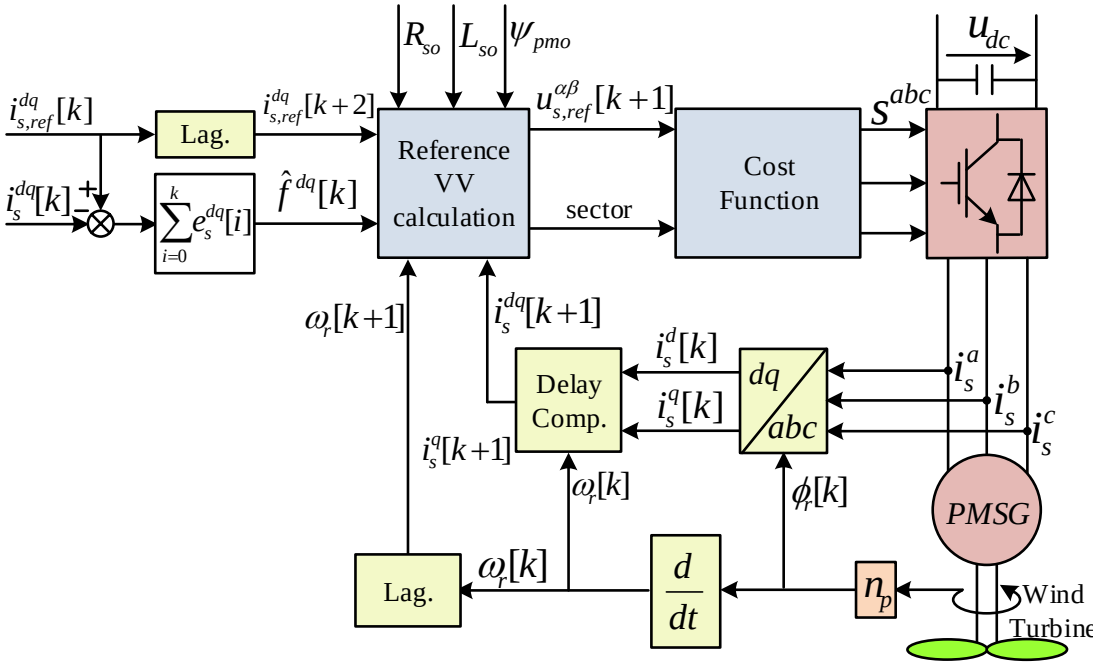

Figure 7.3: Proposed EDMPC with DTIA for PMSGs in variable speed wind turbines.

Based on the location of the reference VV $u_{s,ref}^{\alpha\beta}[k+1]$, the six sectors are defined, which are shown in in Fig. 7.1b. For clarification, when $\phi_u[k] \in [\frac{\pi}{6}, \frac{\pi}{2}]$, then the reference VV is located in sector 2 and the only reasonable candidate VVs are $u_{s,0}^{\alpha\beta}$ and $u_{s,2}^{\alpha\beta}$. Hence, (7.6) is evaluated for only two times to obtain the optimal VV. The schematic diagram of the proposed EDMPC with DTIA is illustrated in Fig. 7.3.

7.3.1 Estimation of the Disturbances

The main reason of the sensitivity of DMPC schemes to variations of the model/machine parameters is the lack of integral term in the controller. In the PI controller, the integral term integrates the error until the controlled state fellow its reference value even under variations of the model/machine parameters [146]. Furthermore, this integral term enhances the steady-state performance of the controller, i.e., steady-state error of zero can be realized. Accordingly, $\boldsymbol{f}^{dq}[k]$ can be estimated as follows

$$\hat{f}^d[k] = k_I \sum_{i=0}^{k} e_s^d[i] \qquad \text{and} \qquad \hat{f}^q[k] = k_I \sum_{i=0}^{k} e_s^q[i]. \tag{7.7}$$

In (7.7), $k_I > 0$ is an integral gain of the discrete-time integral action (DTIA) and, $e_s^d[i] = i_{s,ref}^d[i] - i_s^d[i]$ and $e_s^q[i] = i_{s,ref}^q[i] - i_s^q[i]$ are discrete-time current errors. In one hand, if the value of the DTIA gain k_I is selected very small, i.e., close to zero, the compensation of the parameter uncertainties and un-modeled dynamics will be very slow. In the other hand, if the value of the DTIA gain k_I is selected very high, the compensation speed will be high. However, the magnitude of the reference voltage vector may exceed the maximum limit. Therefore, k_I

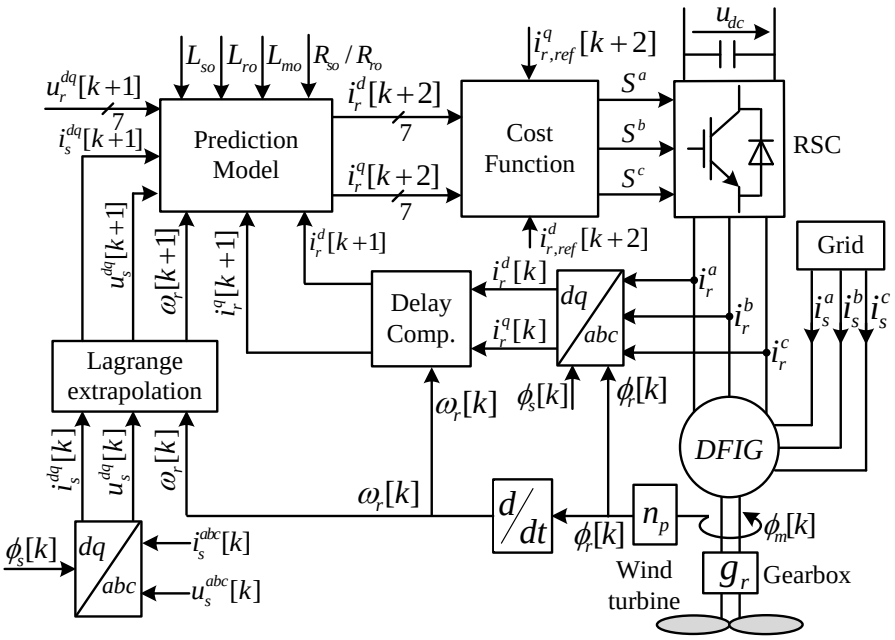

Figure 7.4: Conventional DMPC for DFIGs in variable speed wind turbines.

should be selected higher than zero and smaller/equal than one (i.e. $0 < k_I \leq 1$). Furthermore, it is reasonable to assume that

$$\hat{f}^d[k+1] = \hat{f}^d[k] \qquad \text{and} \qquad \hat{f}^q[k+1] = \hat{f}^q[k]. \tag{7.8}$$

7.4 Conventional DMPC for DFIGs

Similarly to the PMSG (i.e. neglecting $\chi_r^d[k]$ and $\chi_r^q[k]$), invoking (6.18) and considering the one-sample delay, the prediction model can be expressed as follows

$$\left.\begin{aligned} i_r^d[k+2] &= i_r^d[k+1] + \tfrac{T_s}{\sigma_o L_{so} L_{ro}}\Big(- R_{ro}L_{so}i_r^d[k+1] + (\omega_{sl}[k+1]L_{ro}L_{so} - \omega_s[k+1]L_{mo}^2)i_r^q[k+1] \\ &+ R_s L_{mo} i_s^d[k+1] - \omega_r[k+1]L_{mo}L_{so}i_s^q[k+1] + L_{so}u_r^d[k+1] - L_{mo}u_s^d[k+1]\Big), \\ i_r^q[k+2] &= i_r^q[k+1] + \tfrac{T_s}{\sigma_o L_{so} L_{ro}}\Big(- R_{ro}L_{so}i_r^q[k+1] - (\omega_{sl}[k+1]L_{ro}L_{so} - \omega_s[k+1]L_{mo}^2)i_r^d[k+1] \\ &+ R_s L_{mo} i_s^q[k+1] + \omega_r[k+1]L_{mo}L_{so}i_s^d[k+1] + L_{so}u_r^q[k+1] - L_{mo}u_s^q[k+1]\Big). \end{aligned}\right\} \tag{7.9}$$

The currents $i_r^d[k+1]$ and $i_r^q[k+1]$ can be computed as illustrated in (6.21). Finally, the

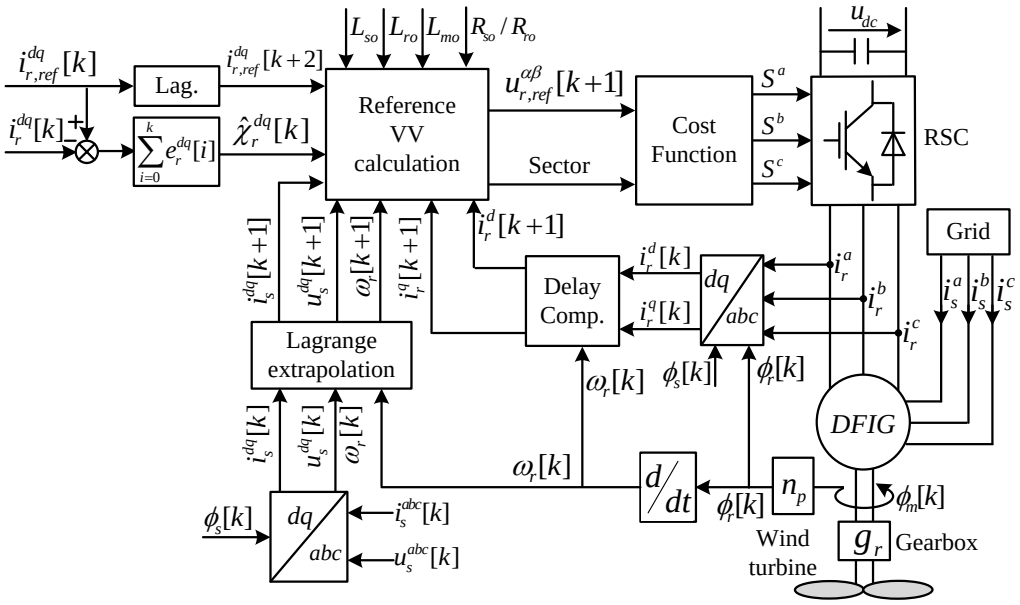

Figure 7.5: Proposed EDMPC with DTIA for DFIGs in variable speed wind turbines.

quality function is defined as

$$
\begin{aligned}
g_c &= \left|i^d_{r,ref}[k+2] - i^d_r[k+2]\right| + \left|i^q_{r,ref}[k+2] - i^q_r[k+2]\right| \\
&+ \begin{cases} 0 & \text{if} \sqrt{i^d_r[k+2]^2 + i^q_r[k+2]^2} \leq i_{r,max} \\ \infty & \text{if} \sqrt{i^d_r[k+2]^2 + i^q_r[k+2]^2} > i_{r,max}, \end{cases}
\end{aligned} \tag{7.10}
$$

where $i_{r,max}$ is the maximum allowable current of the rotor of the DFIG. The schematic diagram of the conventional DMPC for DFIGs is illustrated in Fig. 7.4.

7.5 Proposed DMPC for DFIGs

Considering the perturbations due to parameter variations and un-modeled dynamics, the reference VV $\boldsymbol{u}^{dq}_{r,ref}[k+1]$ can be directly computed by replacing the current $\boldsymbol{i}^{dq}_r[k+2]$ in (7.9) with the reference value $\boldsymbol{i}^{dq}_{r,ref}[k+2]$ as follows

$$
\left.
\begin{aligned}
u^d_{r,ref}[k+1] &= R_{ro} i^d_r[k+1] + \sigma_o L_{ro} \tfrac{i^d_{r,ref}[k+2] - i^d_r[k+1]}{T_s} - \omega_{sl}[k+1] L_{ro} i^q_r[k+1] + \omega_s \tfrac{L^2_{mo}}{L_{so}} i^q_r[k+1] \\
&\quad - R_{so} \tfrac{L_{mo}}{L_{so}} i^d_s[k+1] + \omega_r[k+1] L_{mo} i^q_s[k+1] + \tfrac{L_{mo}}{L_{so}} u^d_s[k+1] + \hat{\chi}^d_r[k+1], \\
u^q_{r,ref}[k+1] &= R_{ro} i^q_r[k+1] + \sigma_o L_{ro} \tfrac{i^q_{r,ref}[k+2] - i^q_r[k+1]}{T_s} + \omega_{sl}[k+1] L_{ro} i^d_r[k+1] - \omega_s \tfrac{L^2_{mo}}{L_{so}} i^d_r[k+1] \\
&\quad - R_{so} \tfrac{L_{mo}}{L_{so}} i^q_s[k+1] - \omega_r[k+1] L_{mo} i^d_s[k+1] + \tfrac{L_{mo}}{L_{so}} u^q_s[k+1] + \hat{\chi}^q_r[k+1].
\end{aligned}
\right\} \tag{7.11}
$$

The magnitude of this reference VV $\boldsymbol{u}^{dq}_{r,ref}[k+1]$ is calculated and compared with the maximally available output voltage magnitude $u_{r,max}$ of the power converter and if the magnitude is higher than this value, the reference voltages is adjusted as illustrated in (6.23). Then the reference VV $\boldsymbol{u}^{dq}_{r,ref}[k+1]$ is transformed to the stationary reference frame $\alpha\beta$ using the Park

Table 7.1: Steady-state performance for PMSG at the nominal parameters of the PMSG.

	EDMPC with DTIA	EDMPC with TDCA	CDMPC
SSE^d[A]	0	-0.23	-1.38
SSE^q[A]	0	-0.15	1.56
$f_{sw,avg}$[kHz]	3.91	4.03	4.12
THD_i%	11.79	12.51	13.14

transformation. Accordingly, its location can be determined as illustrated in Fig. 7.1b. Its angle is given by

$$\phi_u[k] = \text{atan2}(u^{\beta}_{r,ref}[k+1], u^{\alpha}_{r,ref}[k+1]). \tag{7.12}$$

The new quality function can now be written as

$$g_n = \left|u^{\alpha}_{r,ref}[k+1] - u^{\alpha}_{r}[k+1]\right| + \left|u^{\beta}_{r,ref}[k+1] - u^{\beta}_{r}[k+1]\right|. \tag{7.13}$$

Based on the location of the reference VV $u^{\alpha\beta}_{r,ref}[k+1]$, the cost function (7.13) is evaluated for only two times to obtain the optimal VV. The schematic diagram of the proposed EDMPC with DTIA for DFIGs is illustrated in Fig. 7.5.

7.5.1 Estimation of the Disturbances

Similary to the PMSG, $\boldsymbol{\chi}^{dq}_r[k]$ can be estimated as follows

$$\hat{\chi}^d_r[k] = k_I \sum_{i=0}^{k} e^d_r[i] \qquad \text{and} \qquad \hat{\chi}^q_r[k] = k_I \sum_{i=0}^{k} e^q_r[i]. \tag{7.14}$$

In (7.14), $e^d_r[i] = i^d_{r,ref}[i] - i^d_r[i]$ and $e^q_r[i] = i^q_{r,ref}[i] - i^q_r[i]$ are discrete-time current errors. Furthermore, it is reasonable to assume that

$$\hat{\chi}^d_r[k+1] = \hat{\chi}^d[k] \qquad \text{and} \qquad \hat{\chi}^q_r[k+1] = \hat{\chi}^q_r[k]. \tag{7.15}$$

7.6 Experimental results

7.6.1 Experimental results for PMSGs

In this section, the performance of the proposed EDMPC with DTIA is compared to that of EDMPC with TDCA [47], [137] and to the performance of the conventional one. In this work, the value of the DTIA gain k_I is set to 0.6.

7.6.1.1 Dynamic and steady-state performance at the nominal parameters of the machine

Fig. 7.6 illustrates the dynamic performance of the proposed EDMPC with DTIA, EDMPC with TDCA, and the conventional DMPC. From top to bottom, the plotted signals are reference

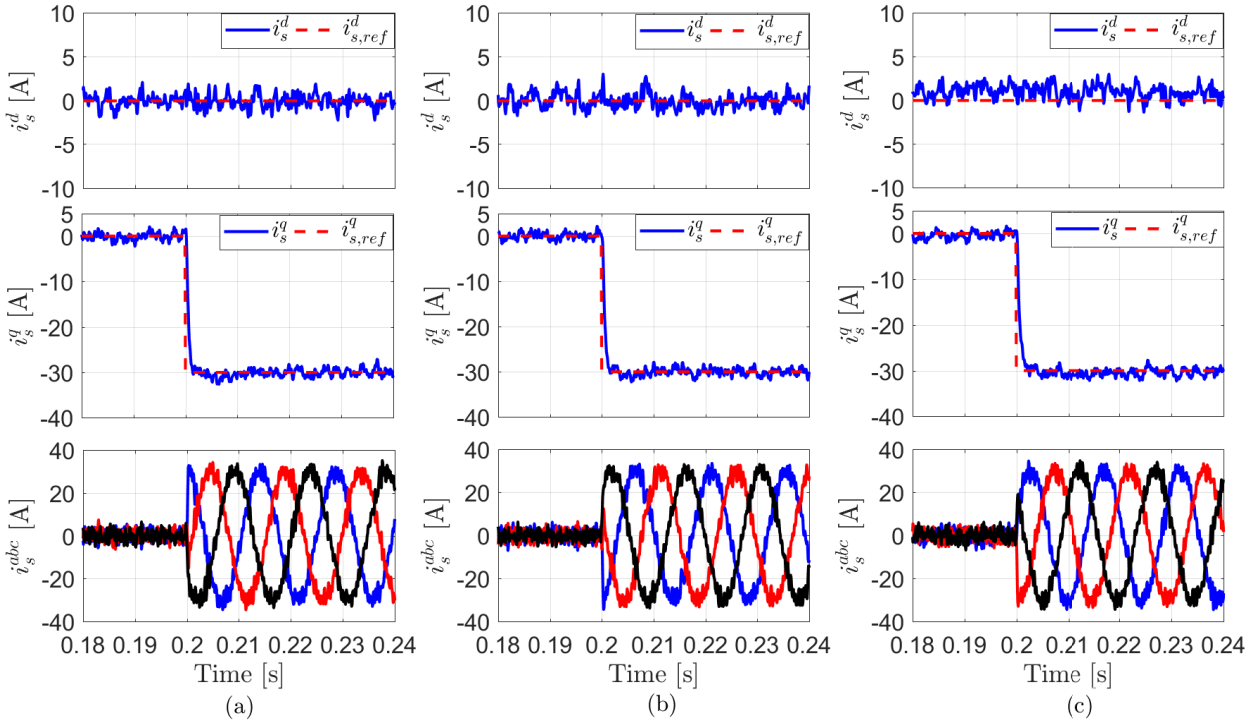

Figure 7.6: Experimental results for PMSG under a step change in the q-axis current at the nominal parameters of the machine: (a) Proposed EDMPC with DTIA, (b) EDMPC with TDCA, and (c) conventional DMPC.

and measured d-axis current ($i_{s,ref}^d$, i_s^d), reference and measured q-axis current ($i_{s,ref}^q$, i_s^q), and stator currents i_s^{abc} in the abc reference frame, respectively. The mechanical speed ω_m is kept constant at the rated value (i.e. $157\,\mathrm{rad/s}$) by the RSM control scheme. At the time instant $t = 0.2\,\mathrm{s}$, a step change in the reference q-axis current $i_{s,ref}^q$ from $0\,\mathrm{A}$ to $-30\,\mathrm{A}$ is applied to the PMSG control technique. This current (i.e. $i_{s,ref}^q = -30$) caused generation of the full-load torque of the RSM because its nominal power is lower than that of the PMSG. This test is performed at the nominal values of the machine parameters (i.e. $R_s = R_{so}$, $L_s = L_{so}$, and $\psi_{pm} = \psi_{pmo}$). It can be seen that the dynamic performance of the proposed EDMPC with DTIA (Fig. 7.6a) and EDMPC with TDCA (Fig. 7.6b) are similar to that of the conventional DMPC (Fig. 7.6c). However, the proposed EDMPC with DTIA calls for approximately $15\,\mu\mathrm{s}$ execution time, while, the EDMPC with TDCA and conventional DMPC require approximately $18\,\mu\mathrm{s}$ and $41\,\mu\mathrm{s}$ execution time, respectively. Hence, the computational burden is reduced to $\frac{15}{41} \times 100\% \approx 36\%$ (i.e., a reduction by 64%!) in comparison with the conventional DMPC. Furthermore, the steady-state performance of the proposed EDMPC with DTIA and EDMPC with TDCA are better than that of the conventional one as illustrated in Table 7.1. The average value of the steady-state error (SSE) using the proposed EDMPC with DTIA is zero, while, a non-zero average value of the SSE is observed using the conventional DMPC and EDMPC with TDCA. The reasons for this non-zero SSE in the conventional DMPC are: (I) Parameter mismatches, (II) un-modeled dynamics, and (III) the lack of integral control action. For the EDMPC with TDCA, the non-zero SSE is due to the use of a low-pass filter (LPF) to filter the

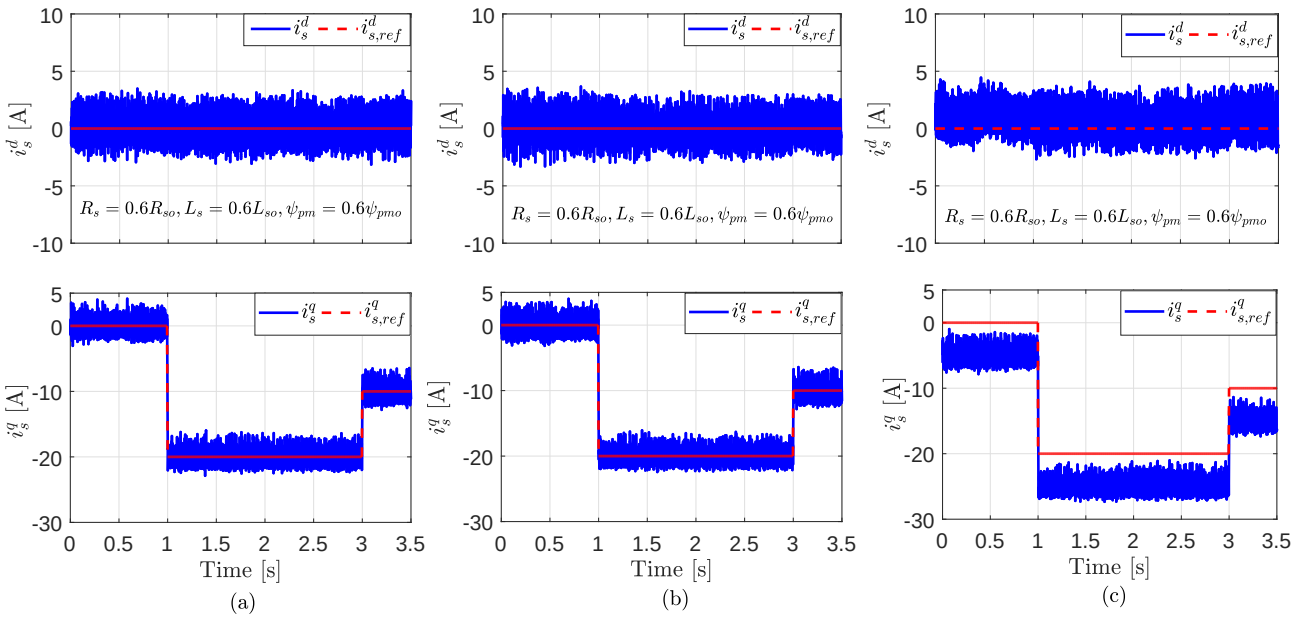

Figure 7.7: Experimental results for PMSG under step changes in the q-axis current at parameter mismatches of the machine: (a) Proposed EDMPC with DTIA, (b) EDMPC with TDCA, and (c) conventional DMPC.

Table 7.2: Steady-state performance for PMSG at variations of the PMSG parameters

	EDMPC with DTIA	EDMPC with TDCA	CDMPC
SSE^d[A]	0	-0.34	-2.47
SSE^q[A]	0	-0.27	5.73
$f_{sw,avg}$[kHz]	4.28	4.39	4.53
THD$_i$%	12.17	12.83	14.89

estimated disturbance due to parameter variations, which causes change in the magnitude and phase. However, the SSE is significantly lower than that of the conventional DMPC as shown in Table 7.1.

Furthermore, the average switching frequency $f_{sw,avg}$ and total harmonic distortion of the stator current THD$_i$ of the different control schemes has been computed and given in Table 7.1. It can be observed from this table that the proposed EDMPC with DTIA gives the lowest average switching frequency and THD$_i$ in comparison with the EDMPC with TDCA and conventional DMPC. The THD$_i$ were computed with 10 cycles of the respective stator currents up to 150 times of its fundamental frequency using MATLAB PowerGUI.

7.6.1.2 Dynamic and steady-state performance at variations of the machine parameters

In order to investigate the effect of mismatches in the machine parameters on the dynamic/steady state performance of the controller, step changes in the q-axis current is applied to the PMSG control system at 40% reduction in the values of the machine parameters, i.e. $R_s = 0.6R_{so}$,

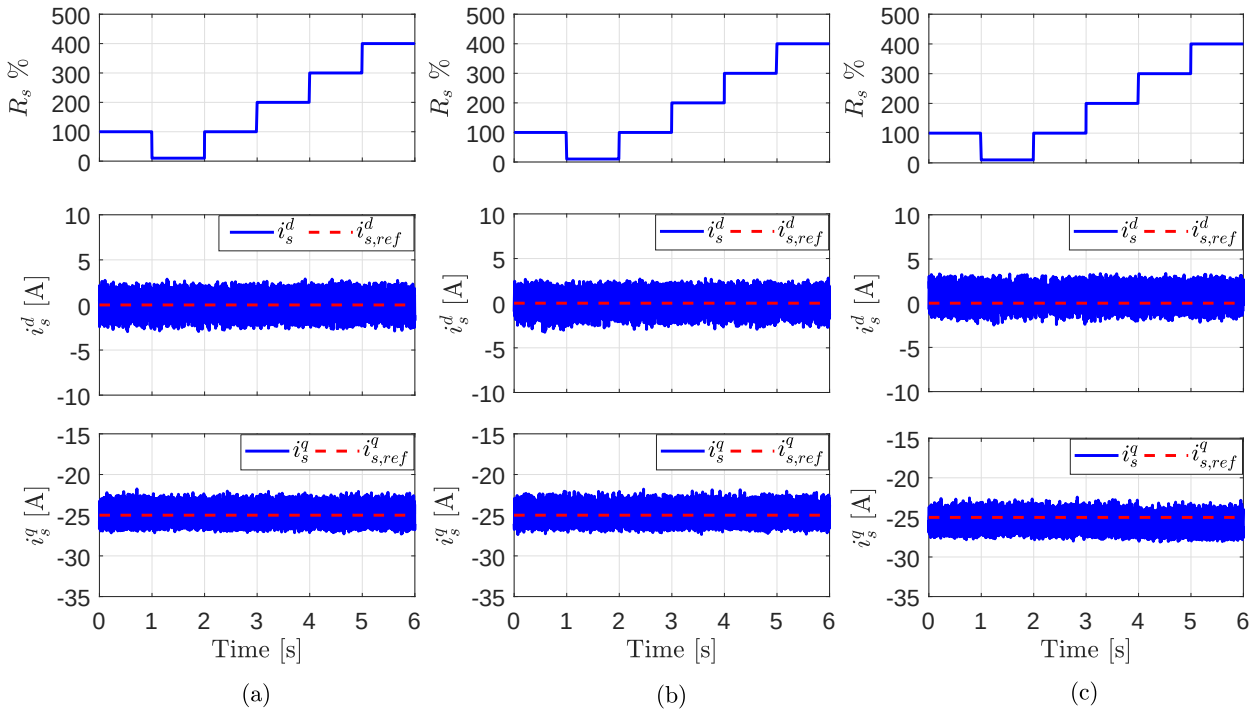

Figure 7.8: Experimental results for PMSG at step changes in the stator resistance R_s of the PMSG: (a) Proposed EDMPC with DTIA, (b) EDMPC with TDCA, and (c) conventional DMPC.

$L_s = 0.6L_{so}$, and $\psi_{pm} = 0.6\psi_{pmo}$. At the time instants $t = 1\,\text{s}$ and $t = 3\,\text{s}$, step changes in the reference q-axis current from $0\,\text{A}$ to $-20\,\text{A}$ and then to $-10\,\text{A}$, respectively, have been applied to the PMSG control strategy. The mechanical speed ω_m is kept constant at $100\,\text{rad/s}$ by the RSM control system. It can be observed from Fig. 7.7 that the dynamic/steady state performance of the proposed EDMPC with DTIA and EDMPC with TDCA is better than that of the conventional one. Using the proposed EDMPC with DTIA and EDMPC with TDCA, only very small ripples appear in the current waveforms, however, the average value of the steady-state error is still zero (close to zero for EDMPC with TDCA). In contrast, a large steady-state error is exist using the conventional DMPC, in paralytically, in the q-axis current as illustrated in Table 7.2. The steady-state performance in this table is performed for the waveforms in the time period from $t = 1.5\,\text{s}$ and $t = 2.5\,\text{s}$. Again, the proposed EDMPC with DTIA gives the lowest average switching frequency and THD_i in comparison with the EDMPC with TDCA and conventional DMPC.

7.6.1.3 Performance at variations of the stator resistance

The robustness of the proposed EDMPC with DTIA to variations of each parameter of the PMSG is also investigated and compared with that of the EDMPC with TDCA and that of the conventional one. Fig. 7.8 shows the performance of the proposed EDMPC with DTIA, EDMPC with TDCA, and conventional one at variations of the stator resistance R_s of the PMSG. The stator resistance R_s is reduced to 10% of its nominal value (i.e. $R_s = 0.1R_{so}$) and

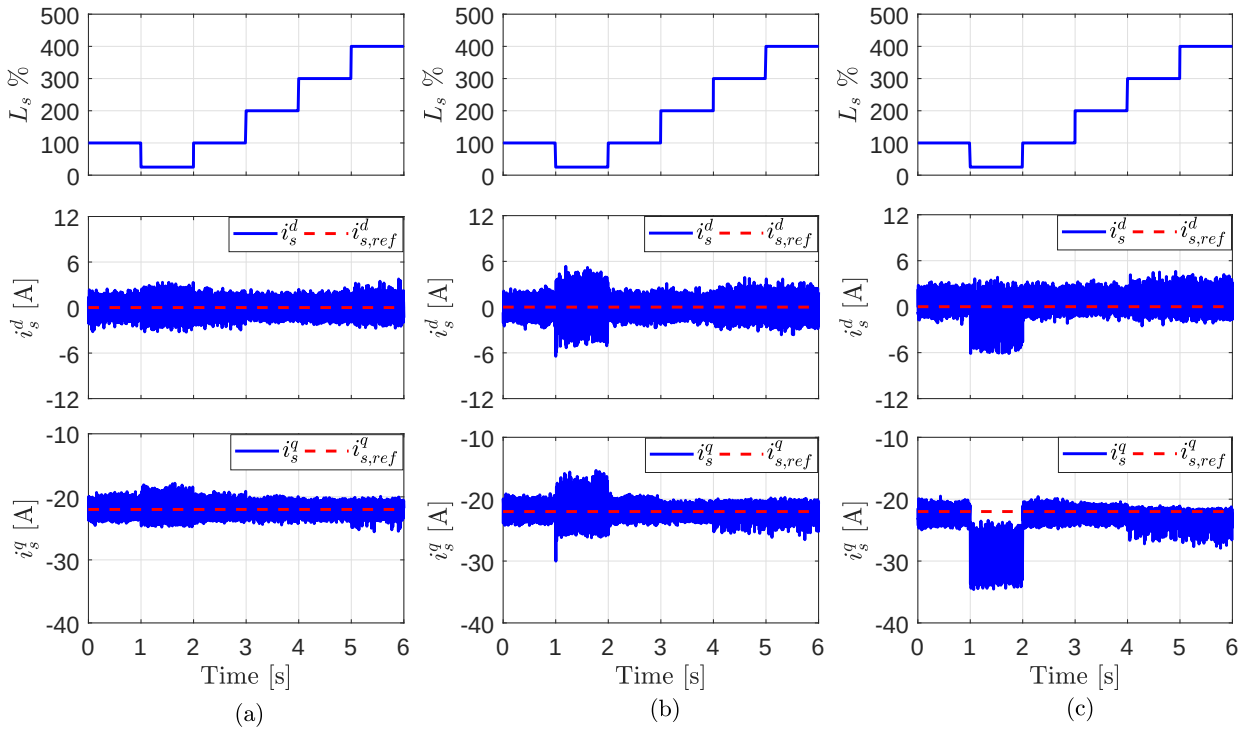

Figure 7.9: Experimental results for PMSG at step changes in the stator inductance L_s of the PMSG: (a) Proposed EDMPC with DTIA, (b) EDMPC with TDCA, and (c) conventional DMPC.

then gradually increased to 400% of its nominal value (i.e. $R_s = 4R_{so}$) as shown in Fig. 7.8. The values of the stator inductance and permanent-magnet flux linkage are set to the nominal ones (i.e. $L_s = L_{so}$ and $\psi_{pm} = \psi_{pmo}$). The mechanical speed of the rotor ω_m is set to $110\,\mathrm{rad/s}$ by the RSM control technique and the reference q-axis current $i_{s,ref}^q$ of the PMSG is set to $-25\,\mathrm{A}$. It can be observed from this figure that the proposed EDMPC with DTIA and EDMPC with TDCA give better performance than that of the conventional one. Again, the average value of the SSE utilizing the proposed EDMPC with DTIA and EDMPC with TDCA is zero (close to zero for EDMPC with TDCA), whereas, a non-zero average value of the SSE is seen using the conventional DMPC.

7.6.1.4 Performance at variations of the stator inductance

Furthermore, the performance of the proposed EDMPC with DTIA is investigated under variations of the stator inductance L_s of the PMSG. At the time instant $t = 1\,\mathrm{s}$, a -75% software decrease in the stator inductance L_s of the PMSG have been applied. Then, the stator inductance is gradually increased to 400% of its nominal value (i.e. $L_s = 4L_{so}$). The values of the stator resistance and permanent-magnet flux linkage are set to the nominal ones (i.e. $R_s = R_{so}$ and $\psi_{pm} = \psi_{pmo}$). The mechanical speed of the rotor ω_m is set to $120\,\mathrm{rad/s}$ by the RSM control scheme and the reference q-axis current $i_{s,ref}^q$ of the PMSG is set to $-22\,\mathrm{A}$. According to Fig. 7.9, the performance of the proposed EDMPC with DTIA is better than that of the EDMPC with TDCA and that of the conventional DMPC. In contrast to the conventional one, only very

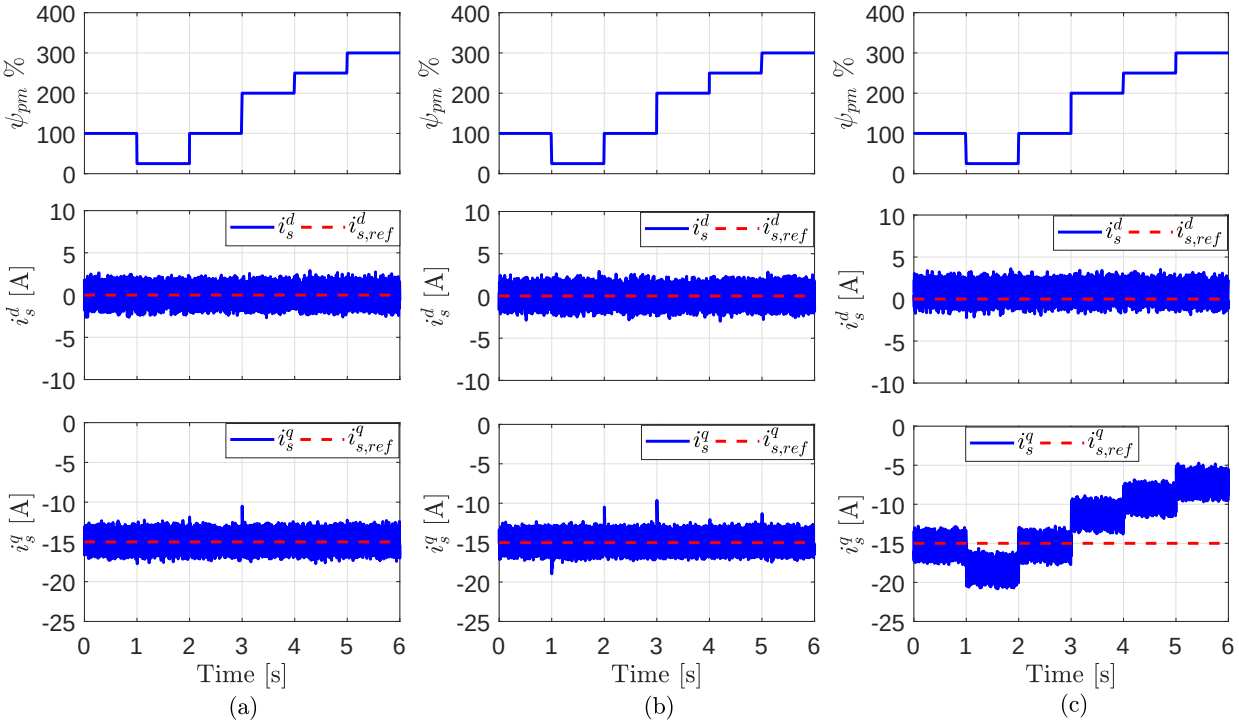

Figure 7.10: Experimental results for PMSG at step changes in the permanent-magnet flux linkage ψ_{pm} of the PMSG: (a) Proposed EDMPC with DTIA, (b) EDMPC with TDCA, and (c) conventional DMPC.

small ripples appear in the currents i_s^d and i_s^q due to inductance variations, however, the average value of the SSE is still zero. In case of the conventional DMPC, the q-axis current i_s^q significantly deviates from its reference value $i_{s,ref}^q$ due to the variations of the stator inductance L_s, in particularly, during the decrease of the stator inductance L_s. Furthermore, higher ripples appear in the currents i_s^d and i_s^q. The SSE using the EDMPC with TDCA is close to zero and significantly lower than that of the conventional DMPC. However, higher ripples in the current waveforms than that of the EDMPC with DTIA can be observed.

7.6.1.5 Performance at variations of the permanent-magnet flux linkage

Finally, the performance of proposed EDMPC with DTIA is investigated under mismatches in the permanent-magnet flux linkage ψ_{pm}. Fig. 7.10 shows the performance of the proposed EDMPC with DTIA, EDMPC with TDCA, and the conventional one for step changes in the permanent-magnet flux linkage ψ_{pm}, where ψ_{pm} is reduced to 25% of its nominal value (i.e. $\psi_{pm} = 0.25\psi_{pm0}$) and then gradually increased to 300% of its nominal value (i.e. $\psi_{pm} = 3\psi_{pm0}$). The values of the stator resistance and inductance of the PMSG are set to the nominal ones (i.e. $R_s = R_{so}$ and $L_s = L_{so}$). The mechanical speed of the rotor ω_m is set to $130\,\mathrm{rad/s}$ by the RSM control technique and the reference q-axis current $i_{s,ref}^q$ of the PMSG is set to $-15\,\mathrm{A}$. It can be seen that the proposed EDMPC with DTIA is robust to variations of the permanent-magnet flux linkage ψ_{pm}. Thanks to the proposed DTIA, negligible ripples/impact appear in the currents i_s^d and i_s^q (see Fig. 7.10a). The EDMPC with TDCA also demonstrates good robustness

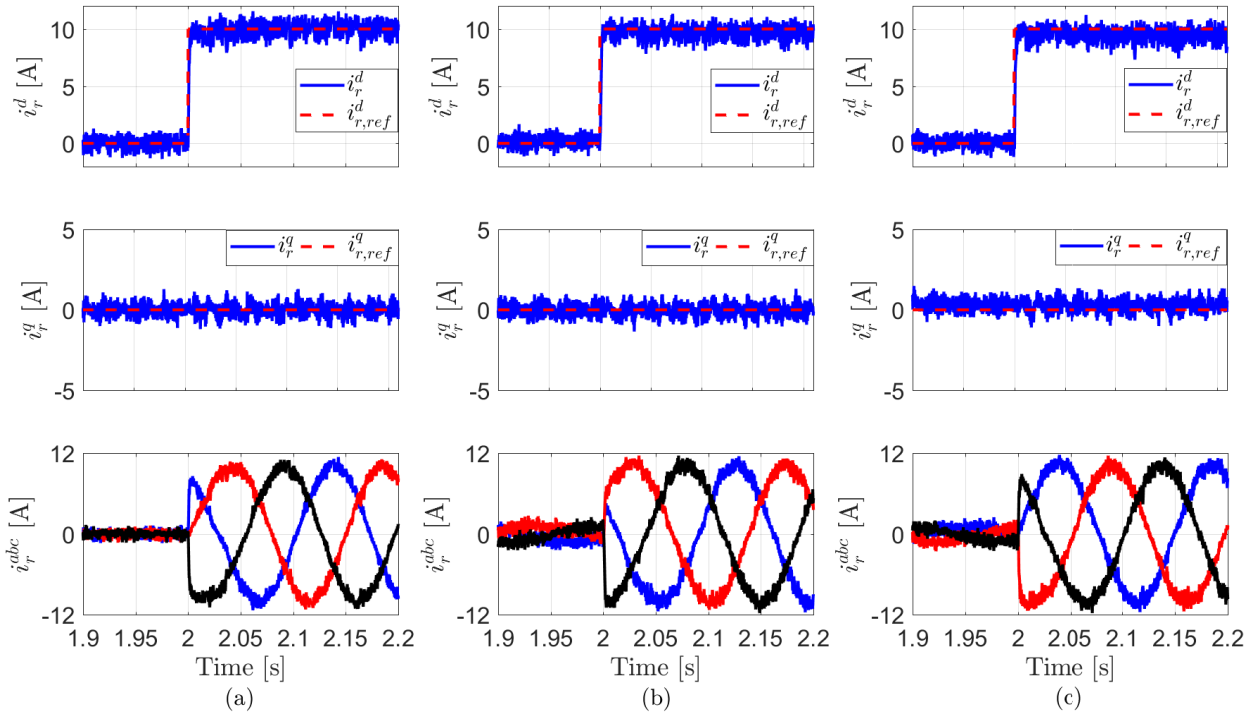

Figure 7.11: Experimental results for DFIGs under a step change in the d-axis current $i^d_{r,ref}$ of the DFIG at the nominal parameters of the machine: (a) Proposed EDMPC with DTIA, (b) EDMPC with TDCA, and (c) conventional DMPC.

to variations of ψ_{pm} as shown in Fig. 7.10b. However, its response is a little bit worse than that of the proposed EDMPC with DTIA. In contrast to the proposed EDMPC with DTIA and EDMPC with TDCA, the performance of the conventional one is significantly deteriorated (see Fig. 7.10c). The q-axis current i^q_s is significantly deviates from its reference value $i^q_{s,ref}$ as illustrated in Fig. 7.10c.

7.6.2 Experimental results for DFIGs

In this section, the performance of the proposed EDMPC with DTIA for DFIGs is experimentally validated. The q-axis reference current is set to zero, i.e. $i^q_{r,ref} = 0$.

7.6.2.1 Dynamic and steady-state performance at the nominal parameters of the DFIG

Fig. 7.11 shows the dynamic performance of the proposed EDMPC with DTIA, EDMPC with TDCA, and the conventional DMPC. From top to bottom, the plotted signals are reference and measured d-axis current ($i^d_{r,ref}$, i^d_r), reference and measured q-axis current ($i^q_{r,ref}$, i^q_r), and rotor currents of the DFIG i^{abc}_r in the abc reference frame, respectively. The mechanical speed ω_m is kept constant at $140\,\mathrm{rad/s}$ by the EESM control system. At the time instant $t = 2\,\mathrm{s}$, a step change in the reference d-axis current $i^d_{r,ref}$ from $0\,\mathrm{A}$ to $10\,\mathrm{A}$ is applied to the DFIG control algorithm. This test is performed at the nominal values of the machine parameters (i.e. $R_s = R_{so}$, $R_r = R_{ro}$, $L_s = L_{so}$, $L_r = L_{ro}$, and $L_m = L_{mo}$). Similarly to the PMSG, It can

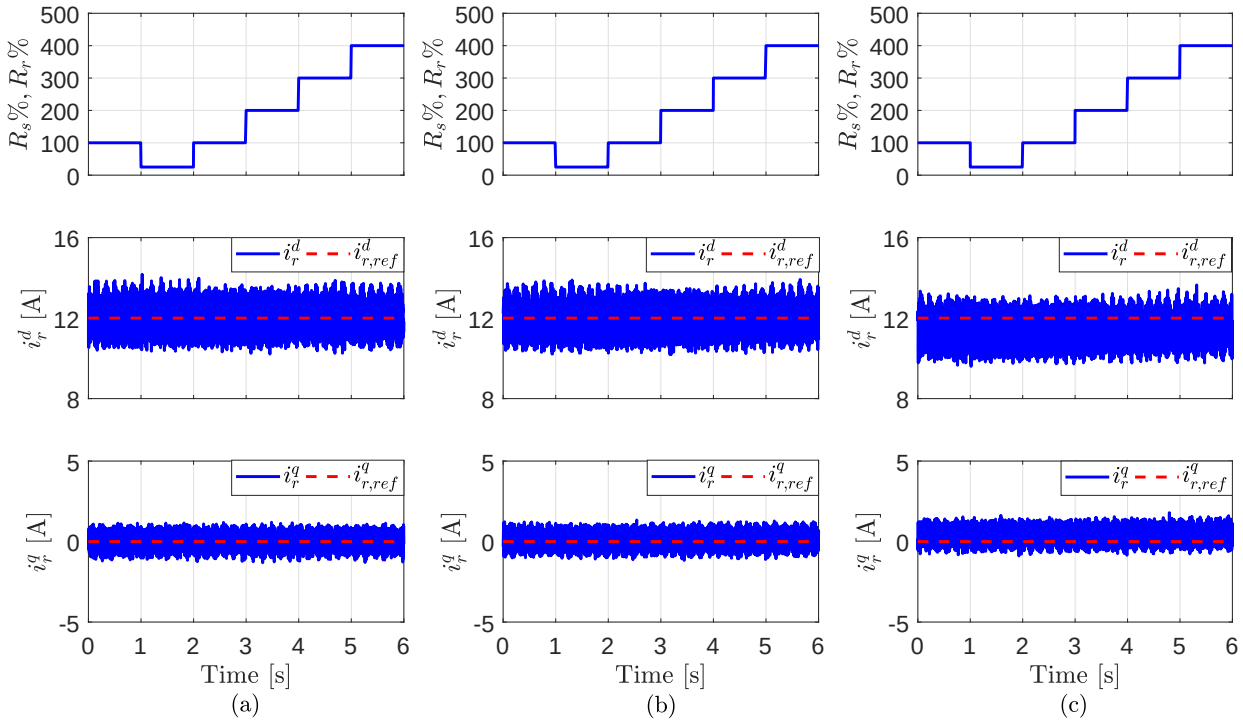

Figure 7.12: Experimental results for DFIGs at step changes in the stator/rotor resistances R_s and R_r of the DFIG: (a) Proposed EDMPC with DTIA, (b) EDMPC with TDCA, and (c) conventional DMPC.

be seen that the dynamic performance of the proposed EDMPC with DTIA (Fig. 7.11a) and EDMPC with TDCA (Fig. 7.11b) are similar to that of the conventional DMPC (Fig. 7.11c). However, the steady-state performance of the proposed EDMPC with DTIA and EDMPC with TDCA are better than that of the conventional one. The average value of the steady-state error (SSE) using the proposed EDMPC with DTIA is zero, while, a non-zero average value of the SSE is observed using the conventional DMPC and EDMPC with TDCA.

7.6.2.2 Performance at variations of the stator and rotor resistances

The robustness of the proposed EDMPC with DTIA to variations of each parameter of the DFIG is also investigated and compared with that of the EDMPC with TDCA and that of the conventional one. Fig. 7.12 illustrates the response of the proposed EDMPC with DTIA, EDMPC with TDCA, and conventional one at variations of the stator R_s and rotor R_r resistances of the DFIG. The stator R_s and rotor R_r resistances are reduced to 25% of its nominal value (i.e. $R_s = 0.25R_{so}$ and $R_r = 0.25R_{ro}$) and then gradually increased to 400% of its nominal value (i.e. $R_s = 4R_{so}$ and $R_r = 4R_{ro}$) as shown in Fig. 7.12. The values of the stator, rotor, and mutual inductances are set to the nominal ones (i.e. $L_s = L_{so}$, $L_r = L_{ro}$, and $L_m = L_{mo}$). The mechanical speed of the rotor ω_m is set to $160\,\mathrm{rad/s}$ by the EESM control technique and the reference d-axis current $i_{r,ref}^d$ of the DFIG rotor is set to $12\,\mathrm{A}$. It can be observed from this figure that the proposed EDMPC with DTIA and EDMPC with TDCA give better performance than that of the conventional one. Again, the average value of the SSE utilizing the proposed

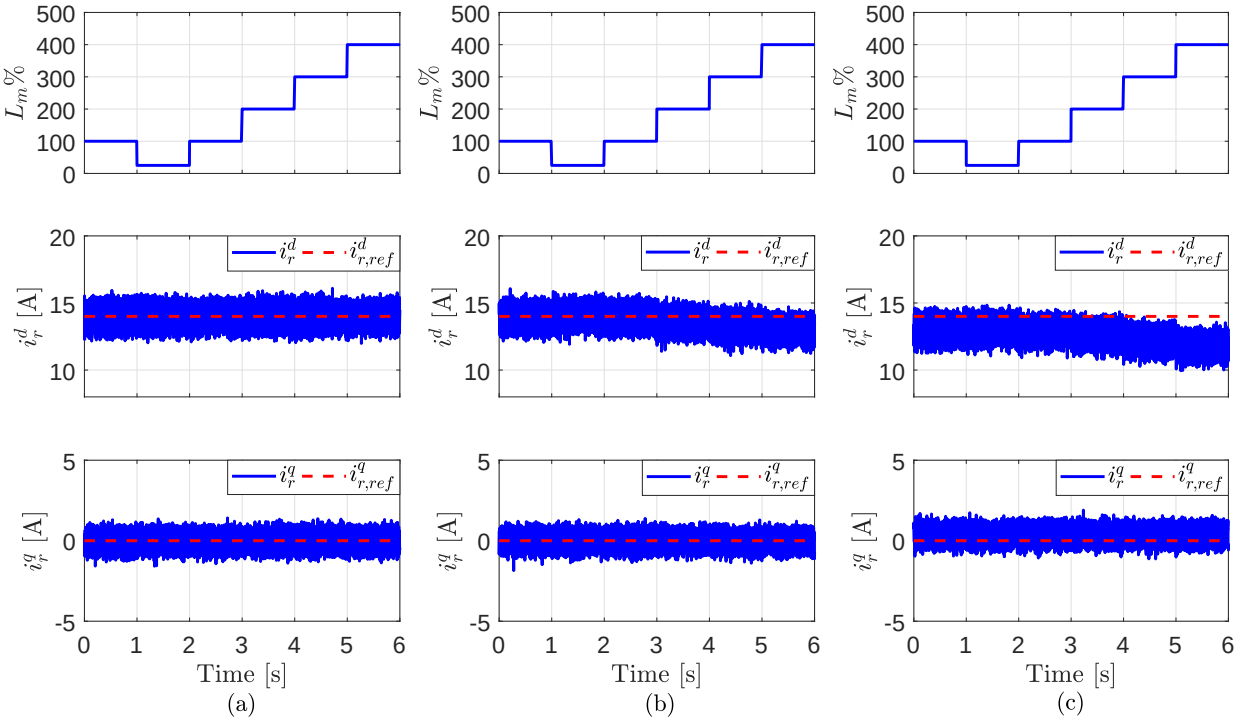

Figure 7.13: Experimental results for DFIGs at step changes in the mutual inductance L_m of the DFIG: (a) Proposed EDMPC with DTIA, (b) EDMPC with TDCA, and (c) conventional DMPC.

EDMPC with DTIA and EDMPC with TDCA is zero (close to zero for EDMPC with TDCA), whereas, a non-zero average value of the SSE is seen using the conventional DMPC.

7.6.2.3 Performance at variations of the mutual inductance

Finally, the performance of the proposed EDMPC with DTIA is investigated under variations of the mutual inductance L_m of the DFIG. Note that variation of the mutual inductance L_m results in variation of the stator inductance $L_s = L_m + L_{s\sigma}$ and rotor inductance $L_r = L_m + L_{r\sigma}$. At the time instant $t = 1\,\mathrm{s}$, a -75% software decrease in the mutual inductance L_m of the DFIG have been applied. Then, the mutual inductance is gradually increased to 400% of its nominal value (i.e. $L_m = 4L_{mo}$). The values of the stator and rotor resistances are set to the nominal ones (i.e. $R_s = R_{so}$ and $R_r = R_{ro}$). The mechanical speed of the rotor ω_m is set to $145\,\mathrm{rad/s}$ by the EESM control technique and the reference d-axis current $i_{r,ref}^d$ of the DFIG is set to $14\,\mathrm{A}$. According to Fig. 7.13 and similarly to the PMSG, the performance of the proposed EDMPC with DTIA is better than that of the EDMPC with TDCA and that of the conventional DMPC. In contrast to the conventional DMPC and EDMPC with TDCA, the average value of the SSE is zero. In case of the conventional DMPC, the d-axis current i_r^d significantly deviates from its reference value $i_{r,ref}^d$ due to the variations of the mutual inductance L_m. The SSE using the EDMPC with TDCA is close to zero and significantly lower than that of the conventional DMPC.

7.7 Summary

In this chapter, an efficient direct model predictive control (EDMPC) with a discrete-time integral action (DTIA) for PMSGs/DFIGs is proposed. The proposed EDMPC directly computes the reference voltage vector from the required reference current vector to overcome the high computational burden of the conventional direct model predictive control (DMPC). Furthermore, the DTIA is added to the calculation of the reference voltage vector to enhance the robustness of the proposed algorithm and realize a good steady-state response. Finally, by knowing the location of this reference voltage vector, only two evaluations of the quality function are requested to find the optimal switching state. The performance of the proposed EDMPC with DTIA is validated experimentally and compared with that of: I) EDMPC with time-delay control approach (TDCA), and II) conventional DMPC. The results have shown that: 1) The proposed EDMPC with DTIA reduces the computational load significantly in comparison with the conventional DMPC, 2) the performance of the proposed EDMPC with DTIA is robust to variations of the machine parameters, while the performance of the conventional DMPC is deteriorated, 3) the steady-state performance of the proposed EDMPC with DTIA is significantly better than that of the conventional one (i.e. zero steady-state error has been realized during all the operation conditions), and 4) the response of the proposed EDMPC with DTIA is better than that of EDMPC with TDCA.

CHAPTER 8

Efficient PDTC without weighting factors

In this chapter, the predictive direct torque control (PDTC) and its advantages/disadvantages are highlighted in Sec. 8.1. Furthermore, in this section, review of the literature that related to tuning/eliminating of the weighting factors in the cost function is given and the contribution of this work is detailed. In Sec. 8.2 and Sec. 8.3, the traditional and proposed PDTC techniques for PMSGs and DFIGs, respectively, are explained. Then, the experimental results to validate the proposed PDTC without weighting factors for PMSGs/DFIGs are illustrated and discussed in Sec. 8.4. Finally, a summary of this chapter is given in Sec. 8.5.

8.1 Introduction

Direct torque control (DTC) [147]–[149], which is based on formulating a switching table to control the torque and stator flux of the machine, is a powerful and widely adopted control scheme for electrical machines due to its fast transient torque response, easy implementation, and absence of modulators and PI controllers. Furthermore, DTC demonstrates good robustness at variations of the machine parameters [150]. However, DTC has several disadvantages such as high torque ripple and variable switching frequency. Furthermore, to get a good control response, a high sampling frequency (HSF) is essential in the digital implementation of the controller.

Accordingly, in the last years, several researchers addressed the challenges of the conventional DTC with a switching table and presented solutions of those challenges. In [151]–[154], a DTC with SVM (DTC-SVM) is presented to reduce the torque ripples and achieve constant switching frequency. Unlike the conventional switching-table-based DTC, which uses one voltage vector with constant magnitude and position in each sampling period, DTC-SVM can synthesize an arbitrary reference voltage vector within its linear range with multiple vectors in each control period. However, a modulator is essential to generates the switching signals of the power converter. Furthermore, a modification in the conventional DTC algorithm to generate

the continuous output is essential, which adds complexity to the conventional DTC scheme. Hence, a powerful real-time system is required to implement this DTC-SVM technique.

Recently, the DMPC has been integrated with the conventional DTC scheme to enhance its performance [23], [155]–[158], which called predictive DTC (PDTC). Generally, in PDTC schemes, the control variables are the torque and stator flux. However, prediction of the stator flux in the next sampling instant and calculation of the reference stator flux according to the maximum torque per ampere (MTPA) trajectory increase the complexity of the control system. Furthermore, a weighting factor is employed to penalize the stator flux magnitude error. This weighting factor has a significant impact on the control response, particularly on the harmonic current distortions. Furthermore, tuning of this weighting factor is normally realized by trail-and-error method, which is a time consuming technique.

Several solutions have been proposed for the flux weighting factor design in the PDTC algorithm [159]–[166]. An empirical procedure to calculate the suitable weighting factors is proposed in [159]. However, this procedure lacks sufficient theoretical support. In [160], the principle of torque ripple minimization is used to compute the required weighting factor online. A fuzzy decision making strategy, a multi-objective ranking based method, and VIKOR method are presented in [161]–[163], respectively, to simplify the selection of this weighting factor. However, the main drawback of those methods is the required high calculation burden. To reduce the calculation load, the computation of the weighting factor is realized by a simple look up table technique in [164]. However, this method requires substantial offline calculation. In [165], a new cost function based on the torque and reactive torque, which is used to indirectly control the stator flux, is presented to eliminate the weighting factor. However, the control performance of the stator flux is slightly poor in comparison with the conventional PDTC. A very simple PDTC technique for AC machines is presented in [166]. This method is based on using one cost function for the torque and a separate cost function for the flux, which eliminates the weighting factor. The evaluation of the two cost functions is realized in a sequential way. The performance of this method is good, however, no comparison with the traditional PDTC is given in this work.

This work proposes a computationally efficient PDTC technique for PMSGs and DFIGs without weighting factors [167]. The proposed control strategy is based on computing the q-axis reference current of the PMSG and d-axis reference current of the DFIG from the demanded torque. Furthermore, the d-axis reference current of the PMSG and q-axis reference current of the DFIG are used to be the second control variable instead of the stator flux, which slightly simplifies the control algorithm. Then, the reference voltage vector (VV) is directly computed from the reference current vector using the deadbeat principle. Finally, according to the location of this reference VV, only three evaluations of the cost function are required. The cost function includes only the error between the reference VV and the candidates ones, which eliminates the need of weighting factors. Therefore, the proposed control scheme overcomes the following drawbacks of the classical PTC: 1) High calculation burden, and 2) tuning of the weighting factors.

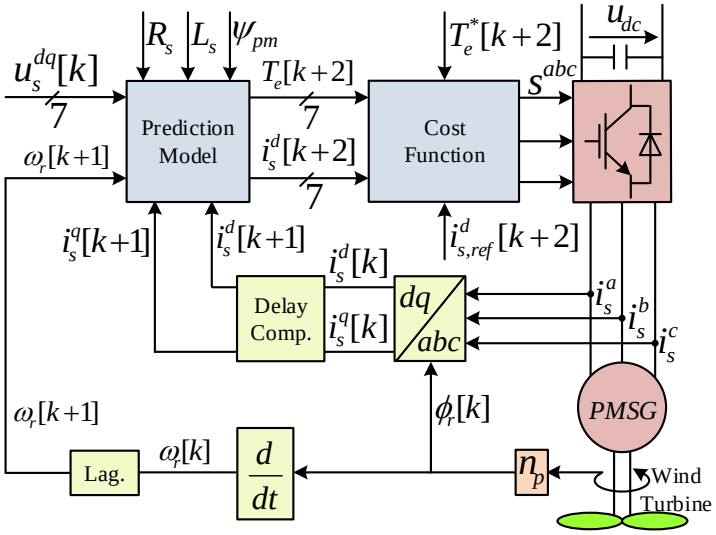

Figure 8.1: Traditional PDTC strategy for surface-mounted PMSGs.

8.2 Predictive direct torque control for PMSGs

The MTPA for surface-mounted PMSGs can be achieved by regulating the d-axis component of the stator current to be zero [39], [157]. Accordingly, the control variables are selected to be the torque and the d-axis current of the PMSG. Hence, prediction of the stator flux in the next sampling interval and computation of the reference stator flux are eliminated, which simplifies the control algorithm.

8.2.1 Traditional PDTC technique for PMSGs

The discrete-time model for predicting the currents in the next sampling interval is given in (3.32) and the electro-magnetic torque can be predicted as follows

$$\begin{aligned} T_e[k+2] &= \tfrac{3}{2} n_p \psi_{pm} i_s^q[k+2] \\ &= \tfrac{3}{2} n_p \psi_{pm} \Big((1 - \tfrac{T_s R_s}{L_s}) i_s^q[k+1] - \omega_r[k+1] T_s i_s^d[k+1] \\ &- \tfrac{T_s}{L_s} \omega_r[k+1] \psi_{pm} + \tfrac{T_s}{L_s} u_s^d[k+1] \Big). \end{aligned} \tag{8.1}$$

According to the PDTC algorithm [157], seven predictions of the electro-magnetic torque $T_e[k+2]$ and d-axis current $i_s^d[k+2]$ can be obtained by using the seven VVs of the power converter. Then, the following cost function

$$\begin{aligned} g_t = & \left| T_e^*[k+2] - T_e[k+2] \right| + \gamma \left| i_{s,ref}^d[k+2] - i_s^d[k+2] \right| \\ & + \begin{cases} 0 & \text{if} \quad T_e[k+2] \le T_{e,max}, \\ \infty & \text{if} \quad T_e[k+2] > T_{e,max}, \end{cases} \\ & + \begin{cases} 0 & \text{if} \quad \sqrt{i_s^d[k+2]^2 + i_s^q[k+2]^2} \le i_{s,max}, \\ \infty & \text{if} \quad \sqrt{i_s^d[k+2]^2 + i_s^d[k+2]^2} > i_{s,max}, \end{cases} \end{aligned} \tag{8.2}$$

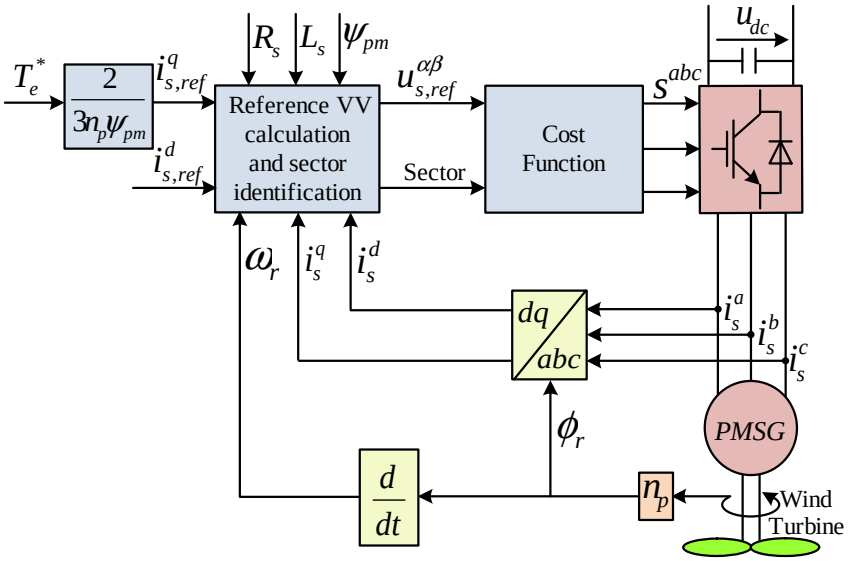

Figure 8.2: Proposed PDTC strategy without weighting factors for surface-mounted PMSGs.

with soft constraints is employed to select the optimal switching state vector which minimizes the cost function. This optimal switching vector is then applied at the next sampling instant. In (8.2), γ is a weighting factor, $T_{e,max}$ is the maximum allowable torque of the PMSG, and $i_{s,max}$ is the maximum current of the stator. The structure of the traditional PTC scheme is illustrated in Fig. 8.1.

The traditional PTC strategy suffers from the following disadvantages: 1) Tuning of the weighting factor γ, which is normally tuned by trial-and-error method, and 2) high calculation load.

8.2.2 Proposed PDTC technique for PMSGs

Fig. 8.2 shows the proposed PDTC [167]. Firstly, the q-axis reference current $i_{s,ref}^q[k+2]$ can by computed directly from the reference electro-magnetic torque $T_e^*[k+2]$ as follows

$$i_{s,ref}^q[k+2] = \frac{2T_e^*[k+2]}{3n_p\psi_{pm}}. \tag{8.3}$$

Secondly, using the reference current $\boldsymbol{i}_{s,ref}^{dq}[k+2]$, the reference VV $\boldsymbol{u}_{s,ref}^{dq}[k+1]$ can be directly calculated using the deadbeat principle as follows

$$\left.\begin{aligned} u_{s,ref}^d[k+1] &= R_s i_s^d[k+1] + L_s \tfrac{i_{s,ref}^d[k+2]-i_s^d[k+1]}{T_s} - \omega_r[k+1]L_s i_s^q[k+1], \\ u_{s,ref}^q[k+1] &= R_s i_s^q[k+1] + L_s \tfrac{i_{s,ref}^q[k+2]-i_s^q[k+1]}{T_s} + \omega_r[k+1]L_s i_s^d[k+1] + \omega_r[k+1]\psi_{pm}. \end{aligned}\right\} \tag{8.4}$$

The magnitude of the reference voltage vector $\boldsymbol{u}_{s,ref}^{dq}[k+1]$ is calculated and compared with the maximally available output voltage magnitude $u_{s,max}$ of the voltage source converter and if the magnitude is greater than this value, the reference voltages should be adjusted as illustrated in (6.7).

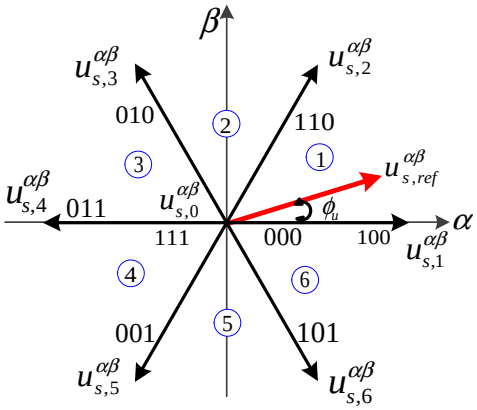

Figure 8.3: Proposed sectors for 2-level power converter.

This reference VV $\boldsymbol{u}^{dq}_{s,ref}[k+1]$ is transformed to the stationary reference frame $\alpha\beta$ using the Park transformation. Therefore, its location can be identified as shown in Fig. 8.3 using its angle $\phi_u[k+1] = \text{atan2}(u^{\beta}_{s,ref}[k+1], u^{\alpha}_{s,ref}[k+1])$. The new cost function has the form

$$g_{new} = \left|u^{\alpha}_{s,ref}[k+1] - u^{\alpha}_{s}[k+1]\right| + \left|u^{\beta}_{s,ref}[k+1] - u^{\beta}_{s}[k+1]\right|. \tag{8.5}$$

Based on the location of the reference VV $u^{\alpha\beta}_{s,ref}[k+1]$, the six sectors are defined, which are illustrated in Fig. 8.3. For clarification, when $\phi_u[k+1] \in [0, \frac{\pi}{3}]$, then the reference VV is located in sector 1 and the only reasonable candidate VVs are $u^{\alpha\beta}_{s,0}$, $u^{\alpha\beta}_{s,1}$, and $u^{\alpha\beta}_{s,2}$. Hence, (8.5) is evaluated for only three times to obtain the optimal VV. Moreover, there is no need to use a weighting factor in the cost function. Accordingly, the proposed PTC overcomes the disadvantages of the traditional one.

8.3 Predictive direct torque control for DFIGs

The reactive power of the DFIG stator can be controlled by regulating the q-axis component of the rotor current [27]. Accordingly, the control variables are selected to be the torque and the q-axis rotor current of the DFIG.

8.3.1 Traditional PDTC system for DFIGs

The discrete-time model for predicting the currents in the next sampling interval is given in (3.51) and the electro-magnetic torque can be predicted as follows

$$\begin{aligned} T_e[k+2] &= -\tfrac{3}{2} n_p \tfrac{L_m}{\omega_s L_s} i^d_r[k+2] u^d_s[k+2] \\ &= -\tfrac{3}{2} n_p \tfrac{L_m}{\omega_s L_s} u^d_s[k+2] \Big[i^d_r[k+1] + \tfrac{T_s}{\sigma L_s L_r} \Big(- R_r L_s i^d_r[k+1] \\ &+ (\omega_{sl}[k+1] L_r L_s - \omega_s[k+1] L^2_m) i^q_r[k+1] + R_s L_m i^d_s[k+1] \\ &- \omega_r[k+1] L_m L_s i^q_s[k+1] + L_s u^d_r[k+1] - L_m u^d_s[k+1] \Big) \Big] \end{aligned} \tag{8.6}$$

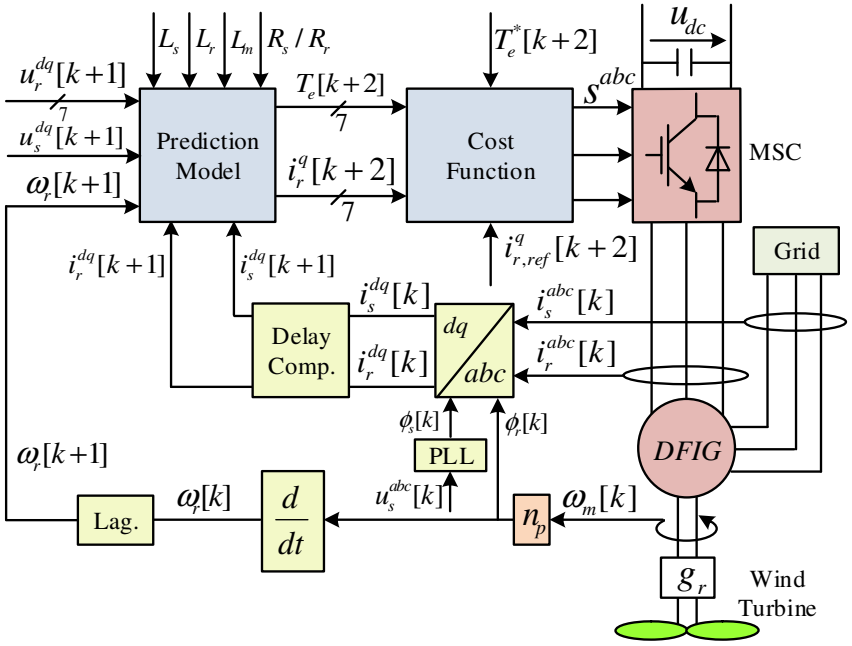

Figure 8.4: Traditional PDTC strategy for DFIGs.

Again, seven predictions of the electro-magnetic torque $T_e[k+2]$ and q-axis current $i_r^q[k+2]$ can be obtained by using the seven VVs of the power converter. Then, the following cost function

$$\begin{aligned} g_t = &\left|T_e^*[k+2] - T_e[k+2]\right| + \gamma_1 \left|i_{r,ref}^q[k+2] - i_r^q[k+2]\right| \\ &+ \begin{cases} 0 & \text{if} \quad T_e[k+2] \le T_{e,max}, \\ \infty & \text{if} \quad T_e[k+2] > T_{e,max}, \end{cases} \\ &+ \begin{cases} 0 & \text{if} \quad \sqrt{i_r^d[k+2]^2 + i_r^q[k+2]^2} \le i_{r,max}, \\ \infty & \text{if} \quad \sqrt{i_r^d[k+2]^2 + i_r^d[k+2]^2} > i_{r,max}, \end{cases} \end{aligned} \tag{8.7}$$

with soft constraints is employed to select the optimal switching state vector which minimizes the cost function. This optimal switching vector is then applied at the next sampling instant. In (8.7), γ_1 is a weighting factor, $T_{e,max}$ is the maximum allowable torque of the DFIG, and $i_{r,max}$ is the maximum current of the rotor. The structure of the traditional PTC scheme is illustrated in Fig. 8.4.

8.3.2 Proposed PDTC system for DFIGs

Fig. 8.5 shows the proposed PDTC without weighting factors for DFIGs. Similarly to the PMSG, the d-axis reference current of the rotor $i_{r,ref}^d[k+2]$ is calculated directly from the optimal electro-magnetic torque $T_e^*[k+2]$ as follows

$$i_{r,ref}^d[k+2] = -\frac{2}{3}\frac{\omega_s L_s}{n_p L_m}\frac{T_e^*[k+2]}{u_s^d[k+1]}. \tag{8.8}$$

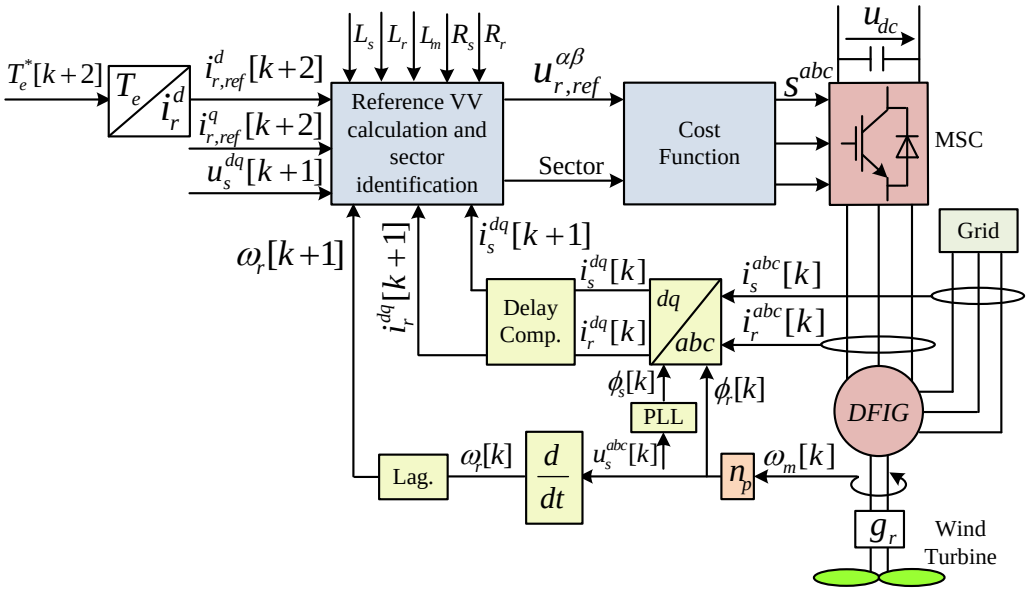

Figure 8.5: Proposed PDTC technique without weighting factors for DFIGs.

Then, using the reference current $\boldsymbol{i}_{r,ref}^{dq}[k+2]$, the reference VV $\boldsymbol{u}_{r,ref}^{dq}[k+1]$ can be directly calculated using the deadbeat principle as follows

$$\left.\begin{aligned} u_{r,ref}^{d}[k+1] &= R_r i_r^d[k+1] + \sigma L_r \frac{i_{r,\mathrm{ref}}^{d}[k+2]-i_r^d[k+1]}{T_s} - \omega_{sl}[k+1] L_r i_r^q[k+1] + \omega_s \frac{L_m^2}{L_s} i_r^q[k+1] \\ &\quad -R_s \frac{L_m}{L_s} i_s^d[k+1] + \omega_r[k+1] L_m i_s^q[k+1] + \frac{L_m}{L_s} u_s^d[k+1], \\ u_{r,ref}^{q}[k+1] &= R_r i_r^q[k+1] + \sigma L_r \frac{i_{r,\mathrm{ref}}^{q}[k+2]-i_r^q[k+1]}{T_s} + \omega_{sl}[k+1] L_r i_r^d[k+1] - \omega_s \frac{L_m^2}{L_s} i_r^d[k+1] \\ &\quad -R_s \frac{L_m}{L_s} i_s^q[k+1] - \omega_r[k+1] L_m i_s^d[k+1] + \frac{L_m}{L_s} u_s^q[k+1]. \end{aligned}\right\} \tag{8.9}$$

The magnitude of this reference VV $\boldsymbol{u}_{r,ref}^{dq}[k+1]$ is calculated and compared with the maximally available output voltage magnitude $u_{r,max}$ of the power converter and if the magnitude is higher than this value, the reference voltages is adjusted as illustrated in (6.23).

This reference VV $\boldsymbol{u}_{r,ref}^{dq}[k+1]$ is transformed to the stationary reference frame $\alpha\beta$ using the Park transformation. Therefore, its location can be identified as shown in Fig. 8.3 using its angle $\phi_u[k+1] = \mathrm{atan2}(u_{r,ref}^{\beta}[k+1], u_{r,ref}^{\alpha}[k+1])$. The new cost function has the form

$$g_{new} = \left|u_{r,ref}^{\alpha}[k+1] - u_r^{\alpha}[k+1]\right| + \left|u_{r,ref}^{\beta}[k+1] - u_r^{\beta}[k+1]\right|. \tag{8.10}$$

Similarly to the PMSG, (8.10) is evaluated for only three times to obtain the optimal VV. Moreover, there is no need to use a weighting factor in the cost function. Accordingly, the proposed PDTC overcomes the disadvantages of the traditional one.

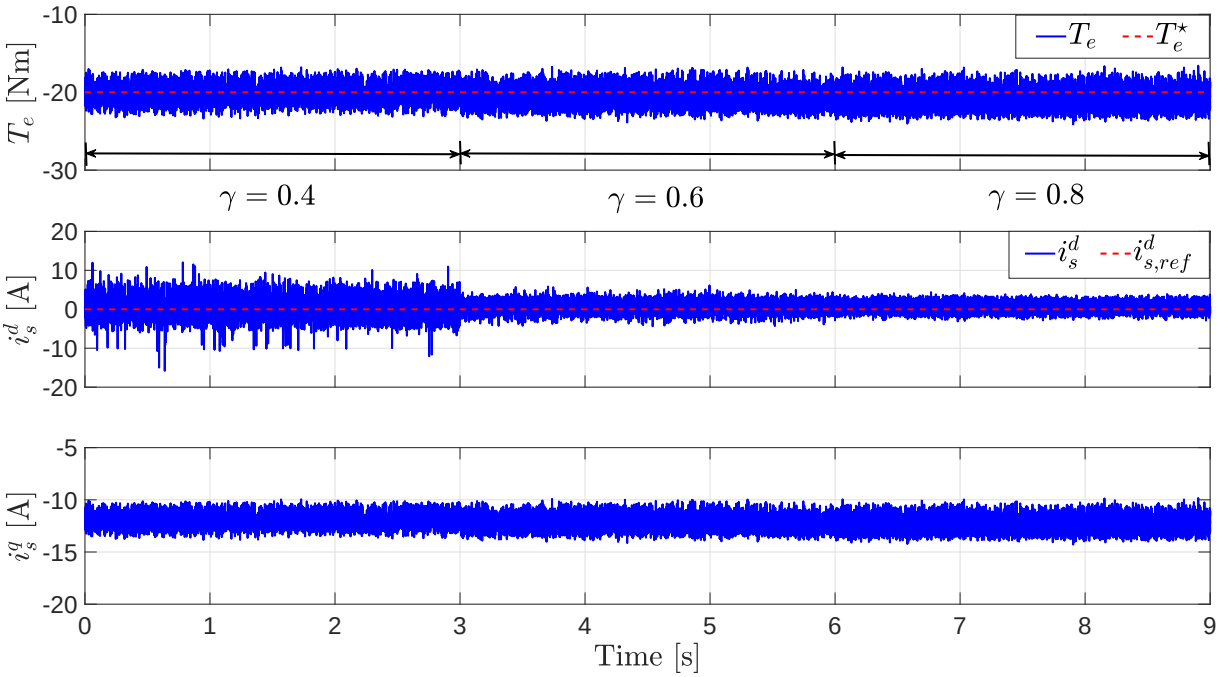

Figure 8.6: Performance of the traditional PDTC for PMSGs at different values of the weighting factor γ.

8.4 Experimental results and discussion

8.4.1 Experimental results for PMSGs

The reference value of the electro-magnetic torque $T_e^\star$ is selected to be lower than the rated value of the RSM (i.e. $T_{RSM}^{rated} = 61\,\mathrm{N\,m}$) and the reference value of the d-axis current $i_{s,ref}^d$ is set to zero to achieve the MTPA condition.

Fig. 8.6 illustrates the performance of the traditional PDTC at different values of the weighting factor γ. The electro-magnetic torque is set to $-20\,\mathrm{N\,m}$ by the PMSG control system and the mechanical speed of the shaft is kept constant at $100\,\mathrm{rad/s}$ by the RSM control technique. It is clear from this figure that the weighting factor γ is playing an important role in the ripples that appeared in the current waveform. Accordingly, the weighting factor $\gamma = 0.8$ is selected in the work.

The dynamic performance of the proposed PDTC and traditional one for PMSGs is shown in Fig. 8.7. At the time instants $t = 1.0\,\mathrm{s}$ and $t = 3.0\,\mathrm{s}$, step changes in the reference electro-magnetic torque $T_e^\star$ from $0\,\mathrm{N\,m}$ to $-40\,\mathrm{N\,m}$ and then to $-20\,\mathrm{N\,m}$, respectively, have been applied to the PMSG control strategy. The mechanical speed of the shaft ω_m is kept constant at $80\,\mathrm{rad/s}$. It can been seen from Fig. 8.7 that the dynamic performance of the proposed PTC is similar to that of the traditional one. However, the proposed PDTC requires approximately $15\,\mu\mathrm{s}$ execution time, while the traditional PDTC requires approximately $35\,\mu\mathrm{s}$. Hence, the computational load is reduced to $\frac{15}{35} \times 100\% = 42\%$ (i.e., a reduction by 58%). Furthermore, in the proposed PDTC, no effort is required for tuning of the weighting factor.

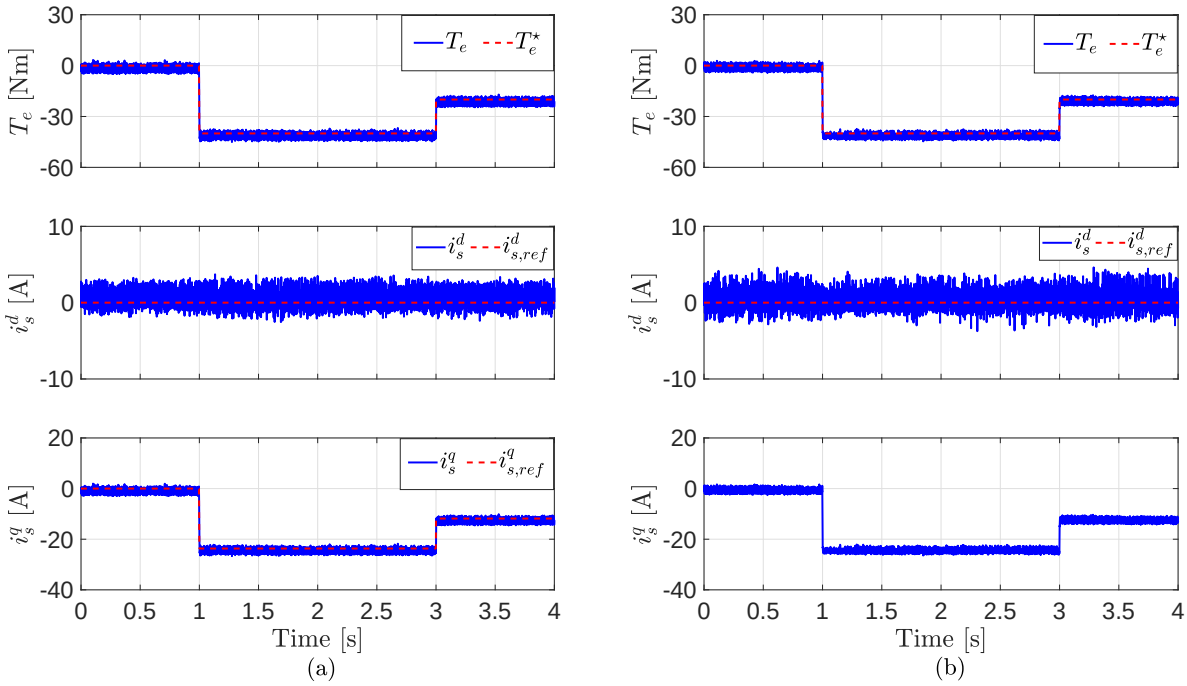

Figure 8.7: Experimental results for step changes in the electro-magnetic torque T_e of the PMSG: (a) Proposed PDTC, and (b) traditional PDTC.

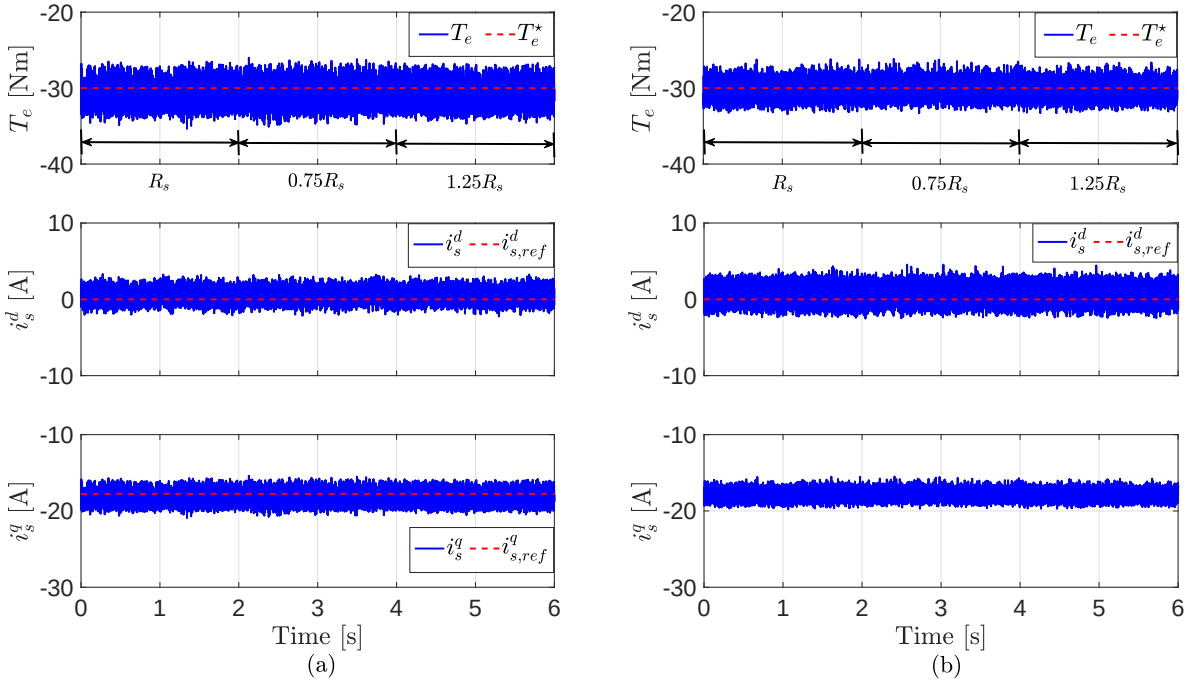

Figure 8.8: Experimental results for step changes in the stator resistance R_s of the PMSG: (a) Proposed PDTC, and (b) traditional PDTC.

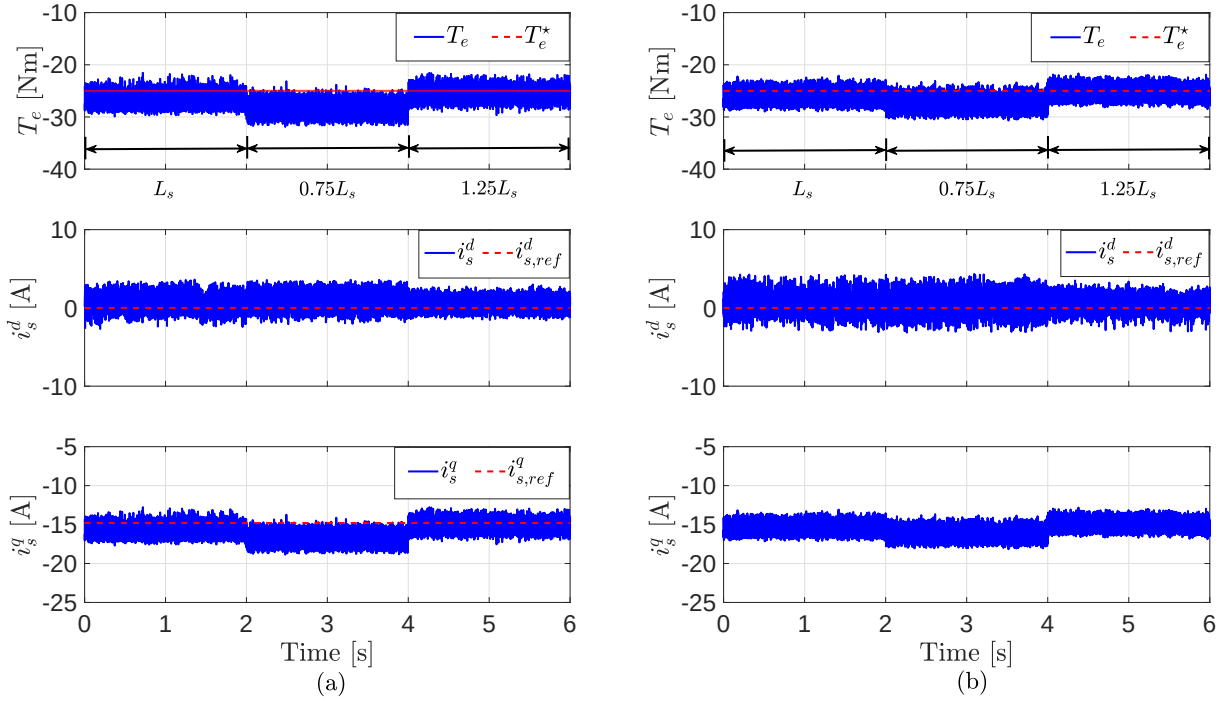

Figure 8.9: Experimental results for step changes in the stator inductance L_s of the PMSG: (a) Proposed PDTC, and (b) traditional PDTC.

The robustness of the proposed PDTC is also investigated and compared with the traditional one. In Fig. 8.8, the performance of the proposed PDTC and traditional one for $\mp 25\%$ software step changes in the stator resistance R_s of the PMSG is illustrated. The electro-magnetic torque T_e is set to $-30\,\mathrm{N\,m}$ and the mechanical speed of the shaft ω_m is kept constant at $120\,\mathrm{rad/s}$. According to that figure, both control schemes (i.e. proposed and traditional PTC) show good robustness to variations of the stator resistance R_s of the PMSG.

Finally, the performance of the proposed PDTC and traditional one under variations of the stator inductance L_s of the PMSG is given in Fig. 8.9. The electro-magnetic torque T_e is set to $-25\,\mathrm{N\,m}$ and the mechanical speed of the shaft ω_m is kept constant at $90\,\mathrm{rad/s}$. It can be observed that both control techniques (i.e. proposed and traditional PDTC) are sensitive to mismatches in the stator inductance L_s of the PMSG. This is because predicting the torque/d-axis current and computing the reference voltage vector are highly dependent on the parameters of the machine. However, both control systems are still stable.

8.4.2 Experimental results for DFIGs

The transient response of the classical and proposed PDTC schemes for DFIGs is illustrated in Fig. 8.10. At the time instants $t = 1.0\,\mathrm{s}$ and $t = 3.0\,\mathrm{s}$, step changes in the reference electro-magnetic torque $T_e^\star$ from $0\,\mathrm{N\,m}$ to $-35\,\mathrm{N\,m}$ and then to $-15\,\mathrm{N\,m}$, respectively, have been applied to the DFIG control strategy. The mechanical speed of the shaft ω_m is kept constant at $150\,\mathrm{rad/s}$ by the EESM control scheme. According to Fig. 8.10, the transient response of the electro-magnetic torque for both control techniques (i.e. classical and proposed PDTC)

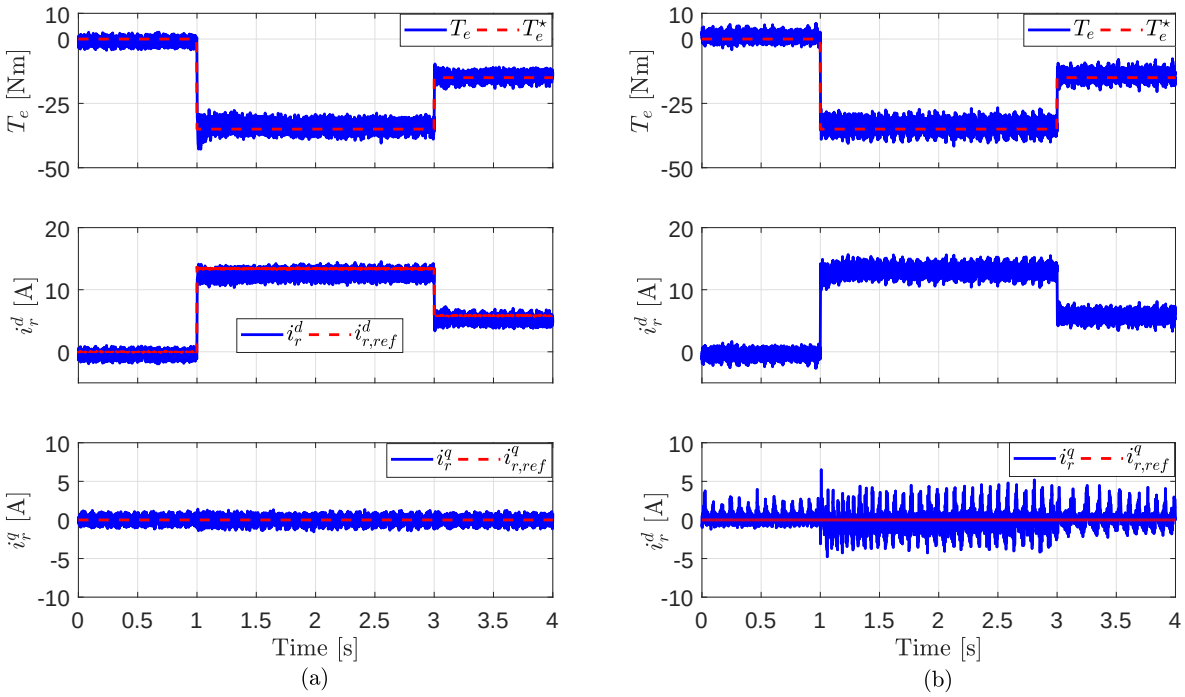

Figure 8.10: Experimental results for step changes in the electro-magnetic torque T_e of the DFIG: (a) Proposed PDTC, and (b) traditional PDTC.

is almost similar. However, the q-axis current is not well regulated using the traditional PDTC, while it is well controlled using the proposed PDTC without weighting factors.

To further compare the performance of the proposed PDTC without weighting factors with the response of the traditional one, a step change in the reference electro-magnetic torque $T_e^\star$ form $0\,\mathrm{N\,m}$ to $-20\,\mathrm{N\,m}$ at the synchronous speed (i.e. $157\,\mathrm{rad/s}$) has been applied. It can be observed from Fig. 8.11 that the performance of the proposed PDTC is better than that of the traditional one. Using the proposed PDTC, no oscillation, high ripples, and deviation from the reference signal are observed like the traditional method.

8.5 Summary

In this chapter, a computationally efficient predictive direct torque control (PDTC) technique without weighting factors for PMSGs/DFIGs has been proposed. The proposed PDTC strategy is based on using the d/q-axis current of the PMSG/DFIG to be the second control variable beside the torque, which reduces (slightly) the calculation burden. Furthermore, in order to overcome the weighting factors tuning problem in the cost function, the reference current of the q/d-axis for the PMSG/DFIG is computed according to the reference torque. Then, the reference VV is directly computed from the reference d- and q-axis currents using a deadbeat function. Finally, in order to reduce the computational effort, the sector where the reference VV is located is determined. Therefore, three evaluations of the cost function are only required to find the optimal VV. The performance of the proposed PDTC technique is experimentally investigated

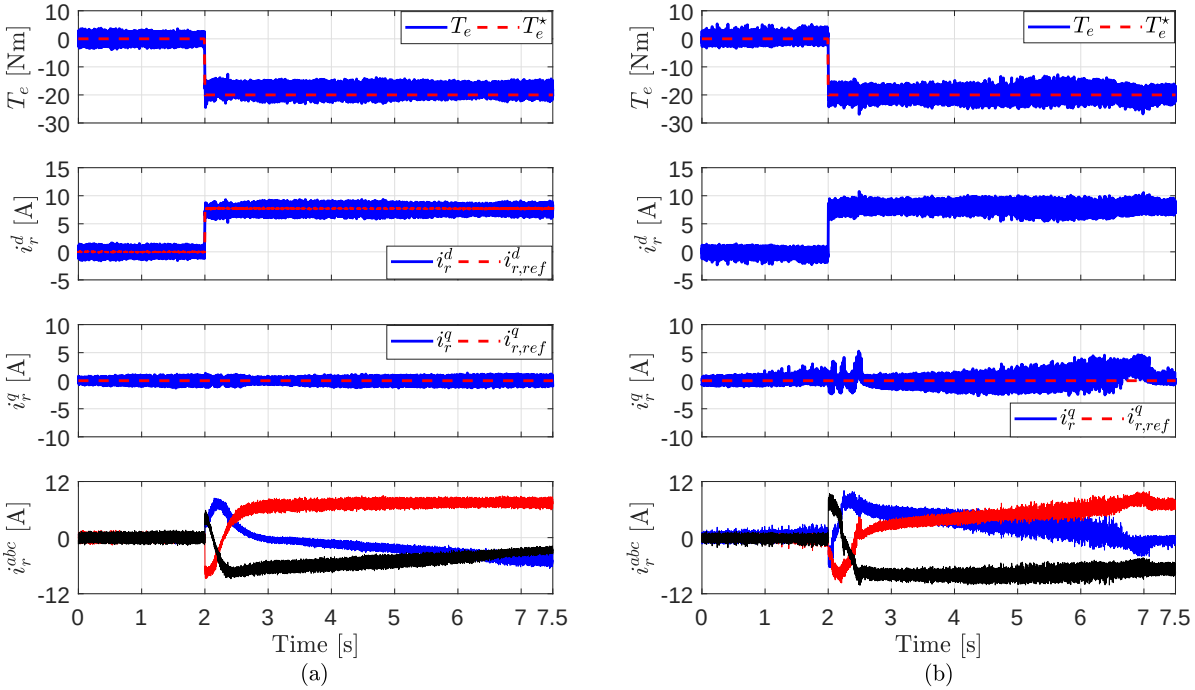

Figure 8.11: Experimental results for a step change in the electro-magnetic torque T_e of the DFIG at the synchronous speed: (a) Proposed PDTC, and (b) traditional PDTC.

and compared with that of the conventional one. The results have shown that: 1) The calculation burden of the proposed PDTC strategy is significantly lower that of the traditional one, 2) the dynamic performance of the proposed PDTC technique for PMSGs/DFIGs is similar to that of the traditional PDTC, 3) the steady-state response of the proposed PDTC for DFIGs is better than that of the classical one, and 4) both the proposed and traditional PDTC techniques are sensitive to variations of the machine parameters, in particular, the inductance of the stator.

CHAPTER 9

Predictive speed control

In this chapter, the predictive speed control (PSC) and its advantages/disadvantages are highlighted in Sec. 9.1. Furthermore, in this section, review of the literature and the contribution of this work is detailed. In Sec. 9.2 and Sec. 9.3, the traditional speed control and proposed PSC techniques for PMSGs are explained. Then, the conventional speed control and PSC schemes for DFIGs are presented in Sec. 9.4 and Sec. 9.5, respectively. Then, the experimental results to validate the proposed PSC for PMSGs/DFIGs are illustrated and discussed in Sec. 9.6. Finally, a summary of this chapter is given in Sec. 9.7.

9.1 Introduction

Generally, the control systems for PMSGs/DFIGs use decoupled current controllers implemented in a synchronously rotating dq-reference frame using proportional-integral (PI) regulators [27], [35]. The control of the PMSGs/DFIGs consists of two cascaded loops, inner current/torque control loop and outer speed control loop. This cascaded structure gives good steady-state response and is robust to variations of the machine parameters. However, the dynamic performance is relatively slow due to the limited bandwidth of the outer loop. Therefore, predictive current control (PCC) and predictive torque control are widely utilized in the literature to replace the PI controllers in the inner current/torque control loop, which slightly enhanced the dynamic response of the control system [23], [168]. However, the dynamic performance of the outer loop is still slow due to the use of PI controller.

In order to enhance the dynamic performance of the outer speed control loop, a full cascaded predictive control technique for induction motors has been presented in [169]. The inner control loop is based on FCS-MPC, while the outer control loop uses deadbeat predictive control. Therefore, the dynamic response of the outer speed control loop is better than that of the PI controller. However, the sampling time used for the outer loop is 10 times higher than the sampling time of the inner current control loop , which is slightly difficult to implement. In [170], a gen-

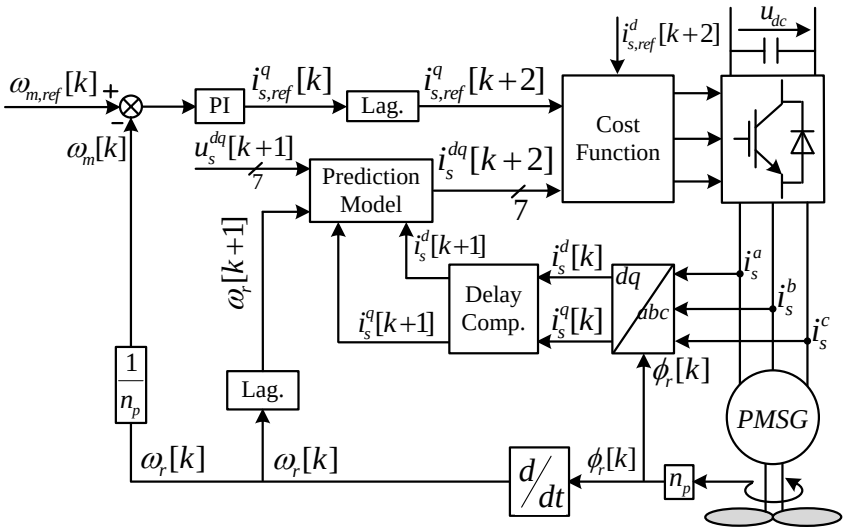

Figure 9.1: Classical speed control of the PMSG in variable-speed wind turbines.

eralized predictive control (GPC) for regulating the speed and position of a PMSM is proposed. The proposed GPC demonstrated good dynamic response, however, its computational load is high.

Newly, DMPC principles have been extended to control both the speed and current/torque in a single control law. Thus, the slow outer loop is eliminated and the dynamic response is improved. In [171], due to the large difference between the mechanical and electrical time constants, a long prediction horizon for the predictive speed control (PSC) is implemented. However, the high computational load is the main drawback. A short prediction horizon MPC for speed control of PMSM is presented in [172]. However, the calculation load is still relatively high. In [173]–[175], a prediction horizon of one is used in the proposed PSC strategy, which significantly reduces the calculation burden. However, several weighting factors are used in the cost function to achieve the control of the speed/current in one control law. Tuning of those weighting factors has been realized by trial-and-error, which is a time consuming technique. A multi-constrained quality function with dynamically adjustable weighting factors to realize the speed/current tracking is presented in [176], [177]. Due to the use of dynamically adjustable weighting factors, the control performance is good in the different operating conditions. However, the rules of computing those adjustable weighting factors are complicated and significantly increase the calculation load. In [178], A sliding-manifold term is combined with the cost function to realize the control of variables with different time constants (i.e speed and current), where a good transient/steady-state performance has been achieved. However, this sliding-manifold term added more weighting factors to the cost function (i.e more effort is required in the tuning of those weighting factors).

In this chapter, a predictive speed control (PSC) strategy with a prediction horizon of one for PMSGs/DFIGs in variable speed wind turbines without mechanical sensors is proposed. The mechanical and electrical variables (i.e. speed and current/torque) are included together in one control law to find the optimum switching state of the power converter. The proposed control law is simple and contains only two weighting factors. Furthermore, guidelines are provided to ease tuning of those two factors. An extended Kalman filter (EKF) is presented to estimate

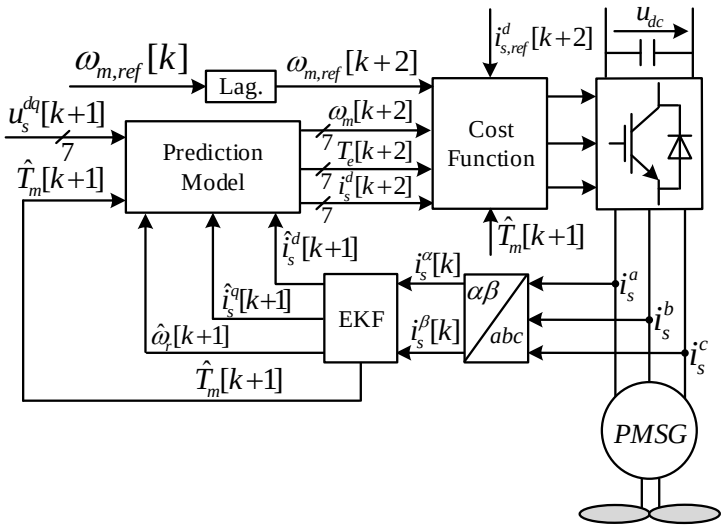

Figure 9.2: Proposed predictive speed control of the PMSG in variable-speed wind turbines.

the speed/position of the rotor and the load torque. The performance of the proposed PSC is experimentally validated and compared with that of the conventional one (i.e. PCC in the inner-loop and outer speed control loop with a PI regulator).

9.2 Classical speed control for PMSGs

The conventional control technique of the PMSG is illustrated in Fig. 9.1, which consists of an outer speed control loop with PI controller and an inner predictive current control (PCC) loop. The design of the traditional speed control with an inner predictive current control is explained in Sec 3.2.1 and 3.2.3. Therefore, it will not be repeated here again.

9.3 Proposed sensorless predictive speed control for PMSGs

The proposed PSC of the PMSG is illustrated in Fig. 9.2, where all the mechanical and electrical variables are included in one control law, and accordingly, the cascaded control structure is eliminated [179]. The discrete-time model for predicting the currents in the next sampling interval is given in (3.32) and the prediction model of the electro-magnetic torque and speed can be expressed as

$$T_e[k+2] = \frac{3}{2} n_p \psi_{pm} i^q_s[k+2]. \tag{9.1}$$

Accordingly, the rotor speed can be predicted as

$$\omega_m[k+2] = \omega_m[k+1] + \frac{T_s}{\Theta}(T_e[k+2] - T_m[k+1] - \nu\omega_m[k+1]). \tag{9.2}$$

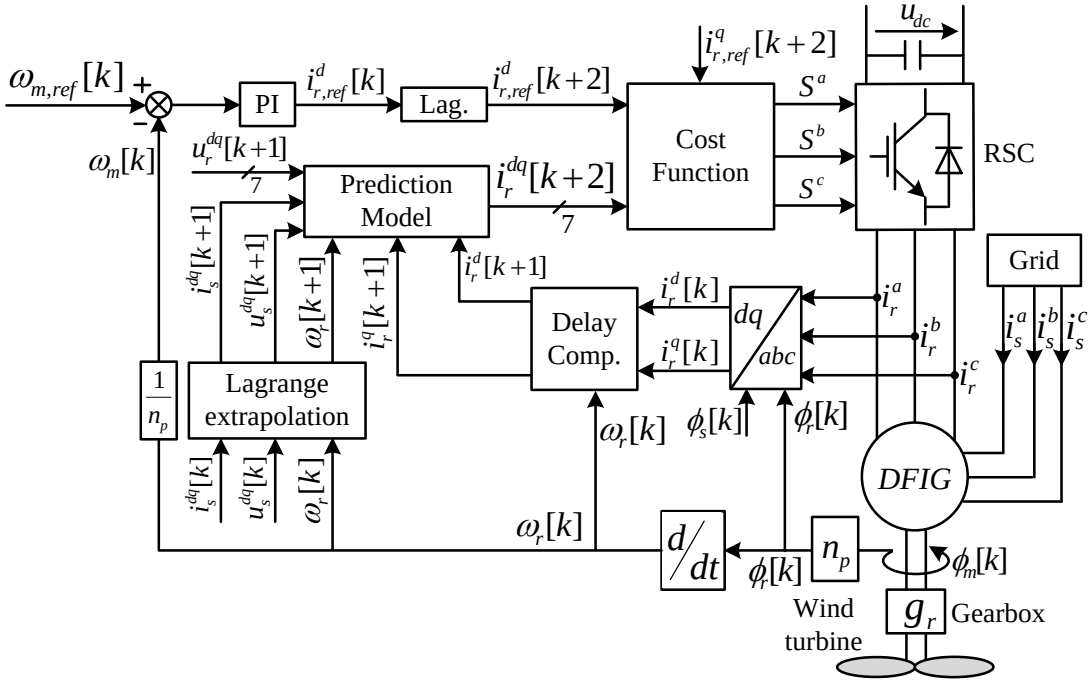

Figure 9.3: Classical speed control of the DFIG in variable-speed wind turbines.

The new cost function is expressed as

$$\begin{aligned} g_{new} &= \lambda_1 \left| \omega_{m,ref}[k+2] - \omega_m[k+2] \right| \\ &+ \left| i^d_{s,ref}[k+2] - i^d_s[k+2] \right| \\ &+ \lambda_2 \left| T_e[k+2] - T_m[k+1] \right|, \end{aligned} \tag{9.3}$$

where λ_1 and λ_2 are weighting factors. The first term of the cost function weights the speed error, which have higher priority. Accordingly, λ_1 must have a high value (i.e. $\lambda_1 >> 1$). The second term of the cost function controls the d-axis current of the PMSG to achieve the maximum torque per ampere (MTPA) operation conditions (i.e. $i^d_{s,ref} = 0$). The last term is added to penalizes the voltage vectors that generate high frequency components in the electromagnetic torque, and accordingly, a smooth q-axis current will be obtained. Therefore, λ_2 should be a small value (i.e. $\lambda_2 < 1$).

In order to implement the proposed PSC technique, the mechanical torque T_m is required. Furthermore, to enhance the control system reliability and reduce the cost, estimation of the speed/position of the rotor is essential. Therefore, an extended Kalman filter (EKF) is employed to estimate those signals. The design of the EKF is given in Sec 6.2.2. Therefore, it will not be repeated here again.

9.4 Classical speed control for DFIGs

The classical control scheme of the DFIG is depicted in Fig. 9.3, which consists of an outer speed control loop with PI controller and an inner predictive current control (PCC) loop. The

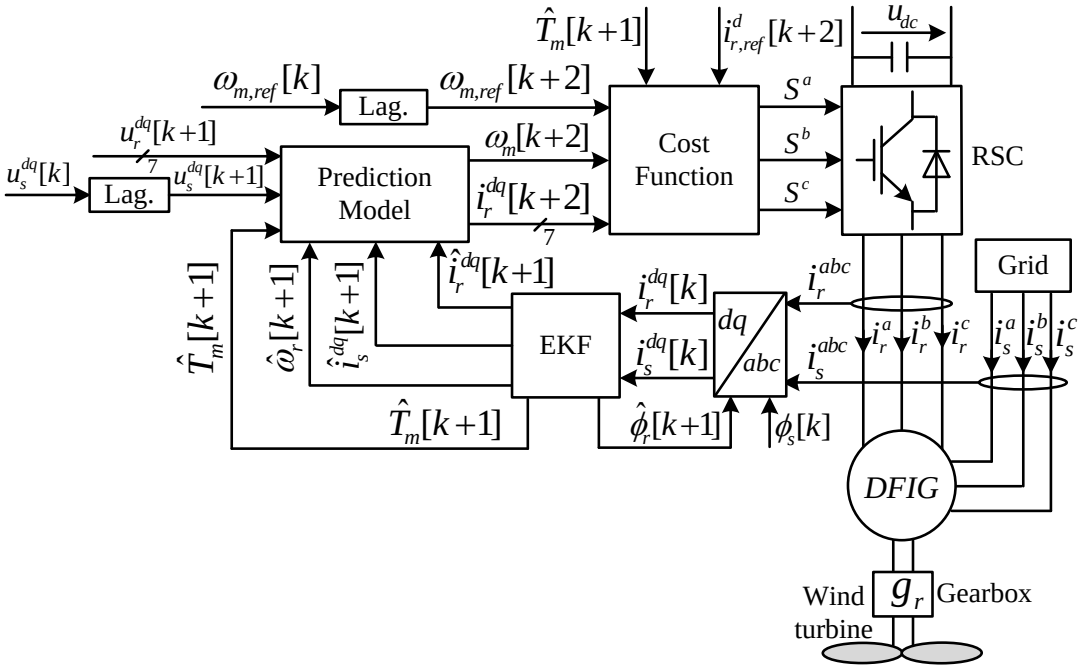

Figure 9.4: Proposed predictive speed control of the DFIG in variable-speed wind turbines.

design of the conventional speed control with an inner predictive current control is explained in Sec 3.3.1 and 3.3.3. Therefore, it will not be repeated here again.

9.5 Proposed sensorless predictive speed control for DFIGs

The proposed PSC for the DFIG is illustrated in Fig. 9.4, where all the mechanical/electrical variables are incorporated in one control law, and accordingly, the cascaded control structure is eliminated. The discrete-time model for predicting the currents in the next sampling interval is given in (3.51) and the prediction model of the electro-magnetic torque and speed can be expressed as

$$T_e[k+2] = -\frac{3}{2} n_p \frac{L_m}{\omega_s L_s} i_r^d[k+2] u_s^d[k+2]. \tag{9.4}$$

Accordingly, the rotor speed can be predicted as

$$\omega_m[k+2] = \omega_m[k+1] + \frac{T_s}{\Theta}(T_e[k+2] - T_m[k+1] - \nu\omega_m[k+1]). \tag{9.5}$$

The new cost function is expressed as

$$\begin{aligned} g_{new} &= \lambda_I \left|\omega_{m,ref}[k+2] - \omega_m[k+2]\right| \\ &+ \left|i^q_{r,ref}[k+2] - i^q_r[k+2]\right| \\ &+ \lambda_{II} \left|T_e[k+2] - T_m[k+1]\right|, \end{aligned} \tag{9.6}$$

where λ_I and λ_{II} are weighting factors. The first term of the cost function weights the speed error, which have higher priority. Accordingly, λ_1 must have a high value (i.e. $\lambda_I >> 1$). The

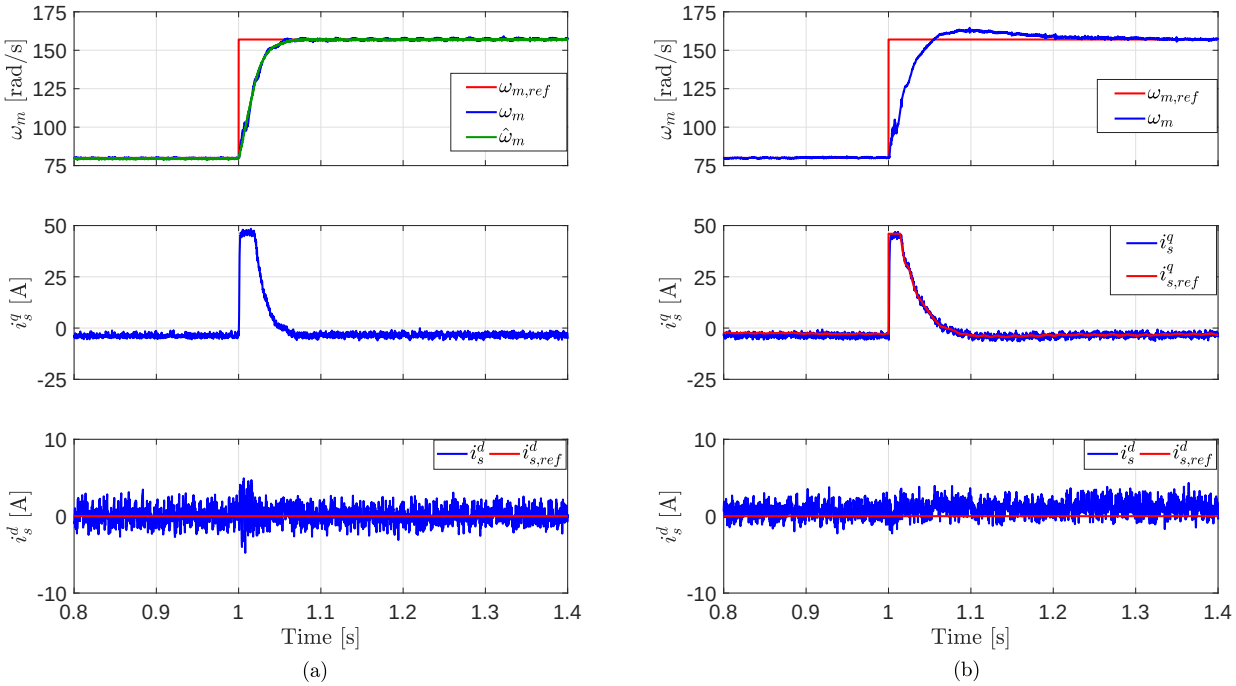

Figure 9.5: Experimental results for the PMSG at step change in the rotor speed ω_m: (a) Proposed PSC method, and (b) classical speed control technique.

second term of the cost function controls the q-axis rotor current of the DFIG for regulating the reactive power exchange between the stator of the DFIG and grid. The last term is added to penalizes the voltage vectors that generate high frequency components in the electro-magnetic torque, and accordingly, a smooth d-axis current will be obtained. Therefore, λ_{II} should be a small value (i.e. $\lambda_{II} < 1$).

In order to implement the proposed PSC technique, the mechanical torque T_m is required. Furthermore, to enhance the control system reliability and reduce the cost, estimation of the speed/position of the rotor is essential. Therefore, an extended Kalman filter (EKF) is employed to estimate those signals. The design of the EKF is given in Sec 6.3.2. Therefore, it will not be repeated here again.

9.6 Experimental results

9.6.1 Experimental results of PMSGs

Figure 9.5 shows the dynamic performance of the proposed PSC technique and classical one for PMSG at step change in the reference mechanical speed of the rotor $\omega_{m,ref}$. At the time instant $t = 1\,\mathrm{s}$, a step change in $\omega_{m,ref}$ from $80\,\mathrm{rad/s}$ to $157\,\mathrm{rad/s}$ has been applied. The load torque is kept constant at $T_m = 10\,\mathrm{N\,m}$ by the RSM control system. It can be seen from this figure that the dynamic performance of the proposed PSC is significantly better than that of the classical method. Using the proposed PSC technique, the settling time is $60\,\mathrm{ms}$, while a settling time of $110\,\mathrm{ms}$ is requested using the conventional control method. The settling times were computed

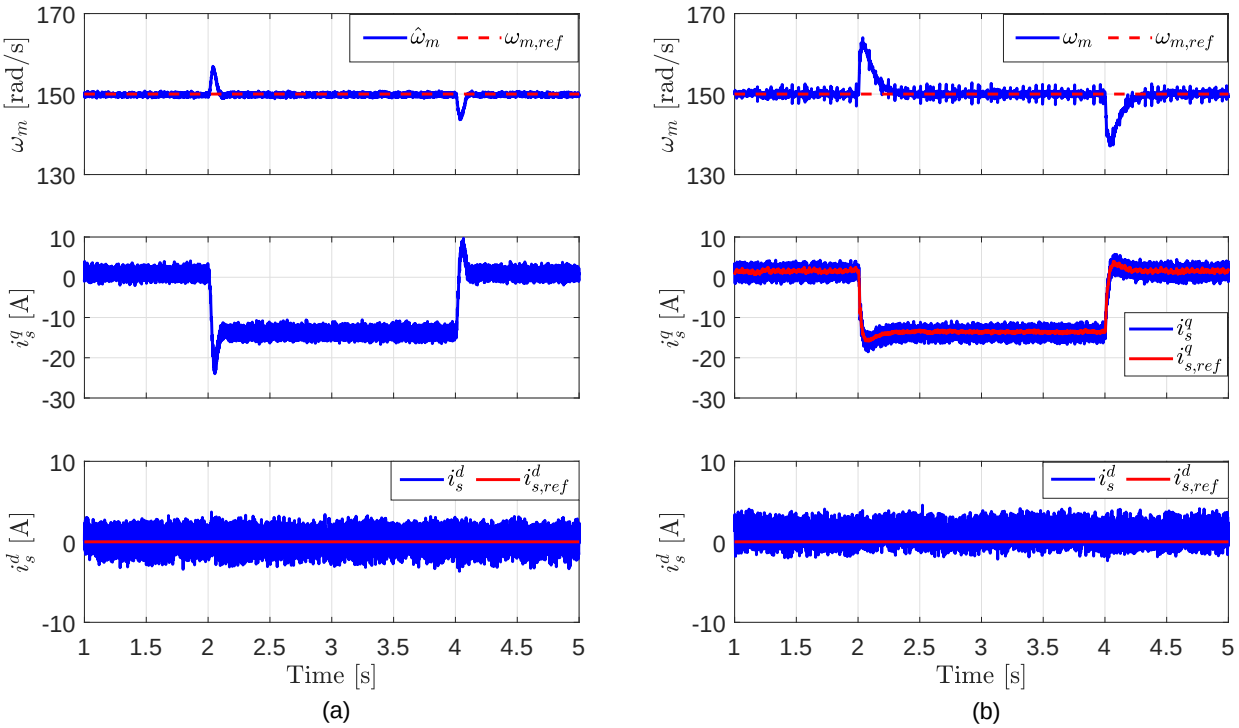

Figure 9.6: Experimental results for the PMSG at step changes in the load torque T_m: (a) Proposed PSC method, and (b) classical speed control technique.

for a band of $\pm 2.5\%$. In addition, no overshoot in the rotor speed is observed using the proposed PSC in comparison with the traditional speed control technique. Furthermore, due to the use of EKF, the noise in the speed signal $\hat{\omega}_m$ is eliminated in comparison with the actual measured one ω_m. Finally, the dynamic response of the d-axis current i_s^d using the proposed PSC is slightly poor in comparison with the conventional speed control technique. However, the steady-state performance of the d-axis current i_s^d using the proposed PSC is significantly better than that of the traditional one.

In order to further compare the transient/steady-state performance of the proposed PSC with that of the classical one, step changes in the load torque have been applied and illustrated in Fig. 9.6. At the time instants $t = 2\,\mathrm{s}$ and $t = 4\,\mathrm{s}$, step changes in the load torque from $0\,\mathrm{N\,m}$ to $30\,\mathrm{N\,m}$ and then back to $0\,\mathrm{N\,m}$, respectively, have been applied to the RSM control system. The mechanical speed of the rotor is remained constant at $150\,\mathrm{rad/s}$ by the PMSG control technique. According to Fig. 9.6, the dynamic performance of the proposed PSC method is obviously better than that of the traditional speed control technique. The recovery time and overshoot of the proposed technique are significantly lower than that of the conventional speed control method. Furthermore, it is quite clear that the estimated speed signal $\hat{\omega}_m$ contains much less noise in comparison with the actual measured signal ω_m, thanks for the EKF.

Finally, the robustness of both control schemes to variations of the machine parameters has been investigated. The stator inductance L_s has been decreased/increased by 50% in the software model at the time instants $t = 1\,\mathrm{s}$ and $t = 3\,\mathrm{s}$, respectively. The mechanical speed of the rotor and the load torque are kept constant at $120\,\mathrm{rad/s}$ and $20\,\mathrm{N\,m}$, respectively. It can be observed from Fig. 9.7 that, the proposed PSC is slightly sensitive to variations of the stator

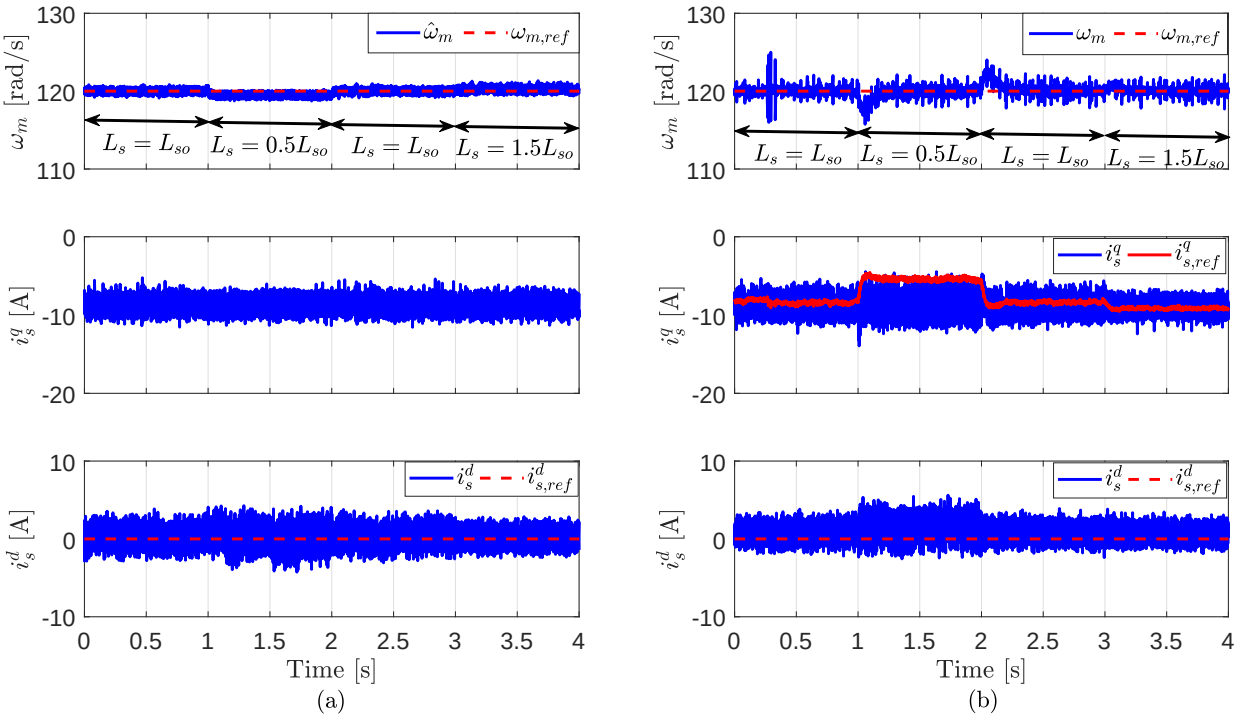

Figure 9.7: Experimental results for the PMSG at step changes in the stator inductance L_s: (a) Proposed PSC method, and (b) classical speed control technique.

inductance L_s. However, the speed tracking is still satisfactory. The traditional speed control technique demonstrates better robustness to variation of stator inductance L_s due to the exist of an integral part in the PI controller. However, the current tracking is not good.

9.6.2 Experimental results of DFIGs

Figure 9.8 shows the dynamic performance of the proposed PSC technique and classical one for DFIG at step change in the reference mechanical speed of the rotor $\omega_{m,ref}$. At the time instant $t = 2\,\mathrm{s}$, a step change in $\omega_{m,ref}$ from $140\,\mathrm{rad/s}$ to $155\,\mathrm{rad/s}$ has been applied. The load torque is kept constant at $T_m = 10\,\mathrm{N\,m}$ by the EESM control technique. Similarly to the PMSG, it can be observed that the transient response of the proposed PSC is significantly better than that of the traditional method. Using the proposed PSC technique, the settling time is $95\,\mathrm{ms}$, while a settling time of $165\,\mathrm{ms}$ is requested using the conventional control method. The settling times were computed for a band of $\pm 2.5\%$. In addition, no overshoot in the rotor speed is observed using the proposed PSC in comparison with the traditional speed control technique. Finally, the dynamic response of the q-axis current i_r^q using the proposed PSC is slightly poor in comparison with the conventional speed control technique.

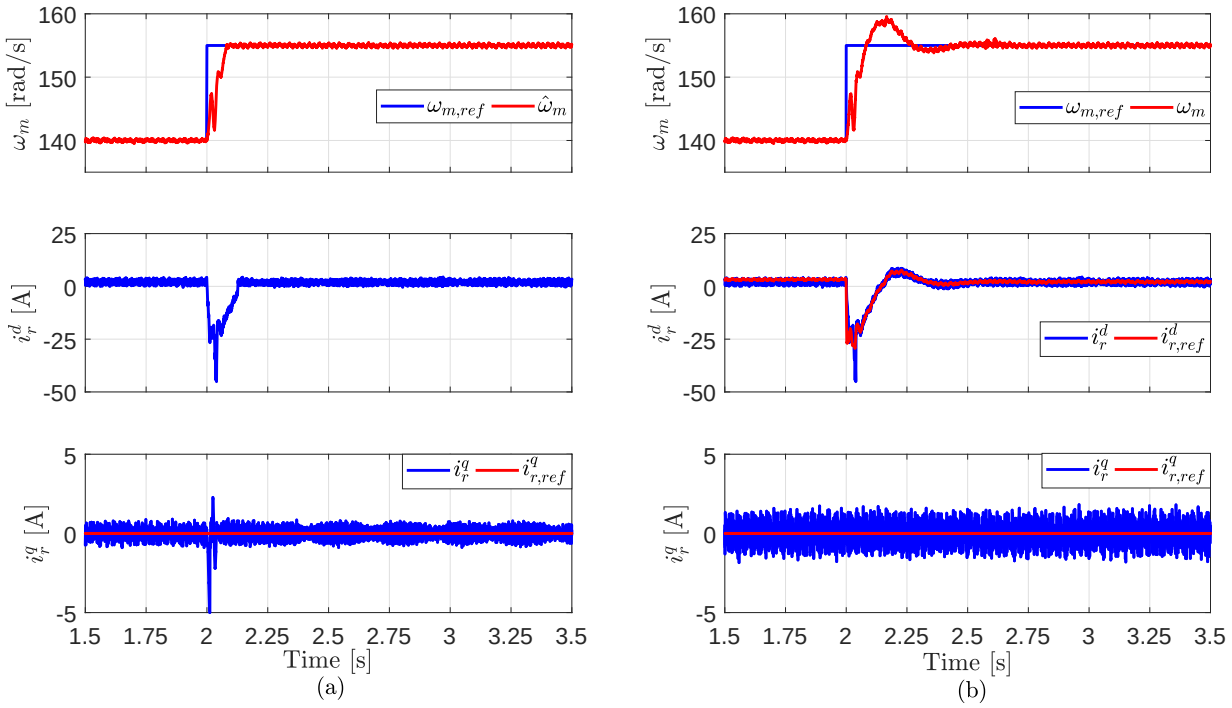

Figure 9.8: Experimental results for the DFIG at step change in the rotor speed ω_m: (a) Proposed PSC method, and (b) classical speed control technique.

9.7 Summary

In this chapter, an encoderless predictive speed control (PSC) technique for PMSGs/DFIGs in variable-speed wind turbine systems is proposed. The mechanical speed, d-axis current (q-axis current in case of DFIGs), and torque are included together in one optimization based objective function, which eliminates the cascaded control structure that normally used in control of AC drive. Furthermore, an extended Kalman filter (EKF) is presented to estimate the mechanical variables, i.e. load torque and speed/position of the rotor. The proposed PSC strategy is experimentally validated and its response is compared with that of the conventional method (i.e. predictive current control (PCC) with an outer (PI) speed control loop). The results have illustrated that the dynamic response of the proposed PSC method is significantly better than that of the conventional technique. Furthermore, the noise in the speed signal is filtered by the EKF, which further improves the performance of the control system, enhance the whole system reliability, and reduces the cost. Finally, the proposed PSC showed satisfactory performance under variations of the machine parameters.

CHAPTER 10

Multiple-vector DMPC with novel inductance estimation technique

In this chapter, review of the literature and the contribution of this work is detailed in Sec. 10.1. The standard VOC and traditional DMPC for grid-connected power converters are briefly explained in Sec. 10.2 and Sec. 10.3, respectively. The proposed multiple-vector FCS-MPC for grid connected voltage-source converters (VSCs) is detailed in Sec. 10.4. Then, the proposed (novel) inductance estimation technique with finite-set is explained in Sec. 10.4.1. The simulation results to validate the proposed multiple-vector FCS-MPC and inductance estimation technique are illustrated and discussed in Sec. 10.5. Finally, a summary of this chapter is given in Sec. 10.6.

10.1 Introduction

FCS-MPC has been recently applied to several converter topologies due to its advantages of fast dynamics, multi-target control capability, and relatively easy implementation on digital control platforms. However, characterized by its one-voltage vector (VV) per control period, higher ripples are seen in the waveforms of current/torque/power than the conventional FOC/VOC with a modulator. One solution for this problem is increasing the sampling frequency, which will enhance the steady state control response (i.e. reduces the ripples in the waveforms of current/torque/power). However, this technique needs a powerful DSP which increases the cost. Accordingly, enhancing the steady state control performance without increasing the sampling frequency of the DMPC algorithm is desired and essential.

Several solutions have been presented in the literature to overcome this problem [180]-[201]. A combination between the DMPC and optimized pulse patterns (OPPs) to enhance the steady-state performance of the DMPC is presented in [180]. However, the computational load increases due to this combination. In [181], pre-computed offline switching patterns have been employed in the online optimization criteria to reduce the number of online calculations and

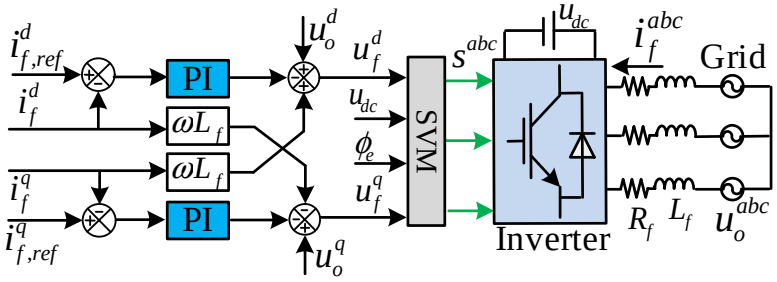

Figure 10.1: Standard VOC for grid connected power converters.

give constant switching frequency DMPC. However, implementing part of the controller offline is not preferred. In [182], by nullifying the derivative of the cost function, a synthesized vector with a minimized cost function can be obtained. Furthermore, a closed-loop space vector modulator is included in the controller. However, this technique abandoned the FCS-MPC superiority of multi-variable control.

In [183], the so called modulated MPC (M^2PC) has been proposed for active-front end rectifiers to reduce the ripples in the waveforms of the output current/power. The M^2PC computes the switching instants by considering an inverse SVM technique. By knowing a priori the required active vectors to apply, the duty cycles can be computed for any possible state and utilized to evaluate the cost function to select the optimal one. The M^2PC gives good dynamic/steady-state performance in comparison with the standard FCS-MPC and has been extended to different converter topologies [184]–[188]. However, the direct application of the switching voltage vector, which is one advantage of the FCS-MPC, is lost by using M^2PC technique.

Another alternative to improve the steady-state performance of the FCS-MPC is increasing the prediction horizon [189]–[194]. The main drawback of this solution is that the increased numbers of switching states result in a larger calculation load, i.e. special real-time system is essential. To overcome this problem, several techniques to reduce the computational burden of the long prediction horizon FCS-MPC such as sphere decoding method have been proposed in the literature [190]–[194].

Applying two or three voltage vectors instead of one in each sampling interval is another solution to enhance the steady-state performance of the standard FCS-MPC [195]–[200]. However, the high complexity of this solution is the main drawback. In [201], the real voltage vectors (8 VVs for two level converter) is employed together with virtual VVs to enhance the steady-state performance of the DMPC. However, the computational load is very high due to the high number of virtual VVs that has been utilized (30 VVs or more). For example, if 30 virtual VVs are used in addition to the 8 real ones, the proposed algorithm in [201] calls for 38 iterations for current predication and 38 evaluations of the cost function, which required powerful digital signal processor (DSP), e.g. high cost. Furthermore, a modulator is employed to generate the switching signals of the power converter.

In this work, a multiple-vector DMPC with low computational load is proposed. In order to reduce the calculation load, the reference voltage vector is directly computed based on the reference currents. Then, according to the location of this reference VV, the number of candidates real VVs in addition to virtual VVs is significantly reduced. The best VV is selected via a cost function to be applied in the next sampling interval. Furthermore, a novel inductance

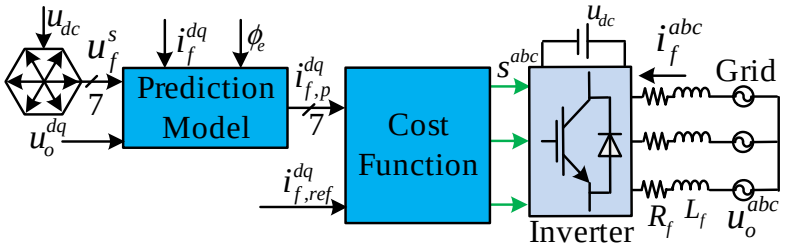

Figure 10.2: Traditional FCS-MPC for grid connected power converters.

estimation method that based on the principles of the FCS-MPC is proposed to enhance the robustness of the proposed efficient multiple-vector DMPC. The performance of the proposed control scheme is validated by simulation results and compared with the classical DMPC and with the well-known voltage oriented control (VOC) with PI regulators.

10.2 Standard VOC for grid connected inverter

The standard VOC for grid connected power converters is explained in Sec. 3.2.1. The main difference here is that the outer DC controller loop is eliminated and the DC-link voltage is assumed to be constant, see Fig. 10.1. The control system regulates the active/reactive power that injected to the grid. The active/reactive power can be expressed in rotating reference frame as:

$$P = \frac{3}{2}(u_o^d i_f^d + u_o^q i_f^q) \quad \& \quad Q = \frac{3}{2}(u_o^q i_f^q - u_o^d i_f^q) \tag{10.1}$$

By aligning the d-axis of the rotating reference frame with the grid voltage vector $u_o^s(t)$ so that $u_o^d(t) = u_o^s(t)$ and $u_o^q(t) = 0$. With this arrangement, the active and reactive power components are decoupled and (10.1) can be expressed as follows:

$$P = \frac{3}{2}u_o^d i_f^d \quad \& \quad Q = -\frac{3}{2}u_o^d i_f^q \tag{10.2}$$

Based on (10.2), independent control of the active and reactive power by the d- and q-axis currents can be achieved through:

$$i_{f,ref}^d = \frac{2}{3}\frac{P_{ref}}{u_o^d} \quad \& \quad i_{f,ref}^q = -\frac{2}{3}\frac{Q_{ref}}{u_o^d}, \tag{10.3}$$

where P_{ref} and Q_{ref} are the reference values of the active and reactive power, respectively.

10.3 Traditional DMPC for grid connected inverter

The traditional FCS-MPC for grid connected power converters is explained in Sec. 3.2.3 and illustrated in Fig. 10.2. The prediction model of the currents in the next sampling interval is given in (3.35) and the cost function is expressed as in (3.36). The main drawback is that only one voltage vector is applied for the whole sampling period, which causes high ripples in the waveforms of the output current/power.

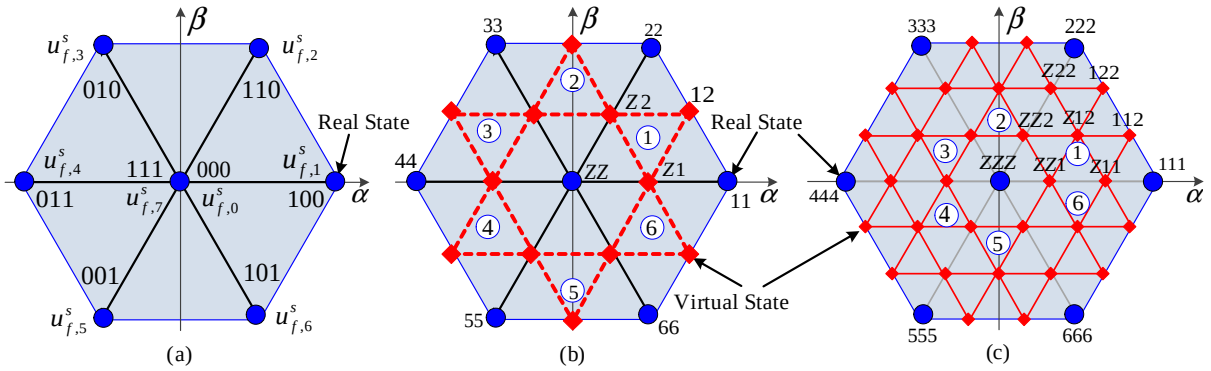

Figure 10.3: (a) All the possible switching vectors of a 2-level converter, (b) three additional virtual VVs/sector, and (c) seven additional virtual VVs/sector.

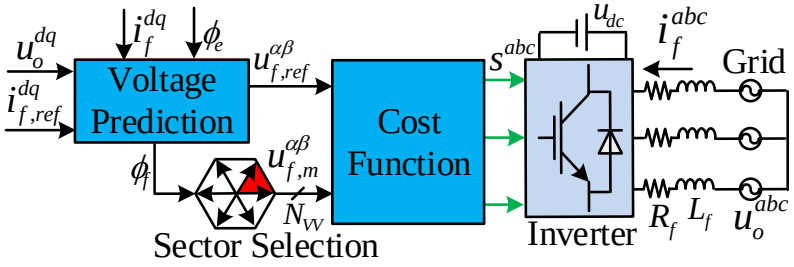

Figure 10.4: Proposed multiple-vector DMPC for grid connected power converters.

10.4 Proposed multiple-vector DMPC for grid connected inverter

In order to improve the steady-state response of the traditional DMPC [202], virtual voltage vectors are added to each sector as shown in Fig. 10.3(b) and (c). In Fig. 10.3(b), 3 additional voltage vectors are added to each sector. Therefore, two VVs will be applied in each sampling interval (2VV-DMPC) instead of one VV for the whole sampling period. For example, $Z1$ means that the zero VV will be applied for the first half of the switching period (i.e $\frac{T_s}{2}$) and $u^s_{f,1}$ will be applied for the second half of the period. Furthermore, for more and more improvement in the steady-state response, three VVs (3VV-DMPC) can be applied in each sampling period as shown in Fig. 10.3(c). The schematic diagram of the proposed DMPC technique is illustrated in Fig. 10.4.

In order to reduce the computational load, the reference voltage $\boldsymbol{u}^k_{f,ref}[k+1] = (u^d_{f,ref}[k+1],\, u^q_{f,ref}[k+1])^\top$ is computed directly by replacing $\boldsymbol{i}^k_f[k+2]$ with $\boldsymbol{i}^k_{f,ref}[k+2]$ in (3.35) as

$$\left.\begin{aligned} u^d_{f,ref}[k+1] &= -R_f i^d_f[k+1] - L_f \tfrac{i^d_{f,ref}[k+2]-i^d_f[k+1]}{T_s} + \omega_e L_f i^q_f[k+1] + u^d_o[k+1], \\ u^q_{f,ref}[k+1] &= -R_f i^q_f[k+1] - L_f \tfrac{i^q_{f,ref}[k+2]-i^q_f[k+1]}{T_s} - \omega_e L_f i^d_f[k+1] + u^q_o[k+1]. \end{aligned}\right\} \tag{10.4}$$

Subsequently, the reference VV $\boldsymbol{u}^k_{f,ref}[k+1]$ based on the rotating reference frame dq in (10.4) is transformed to the stationary reference frame $\alpha\beta$ using the Park transformation. The angle of

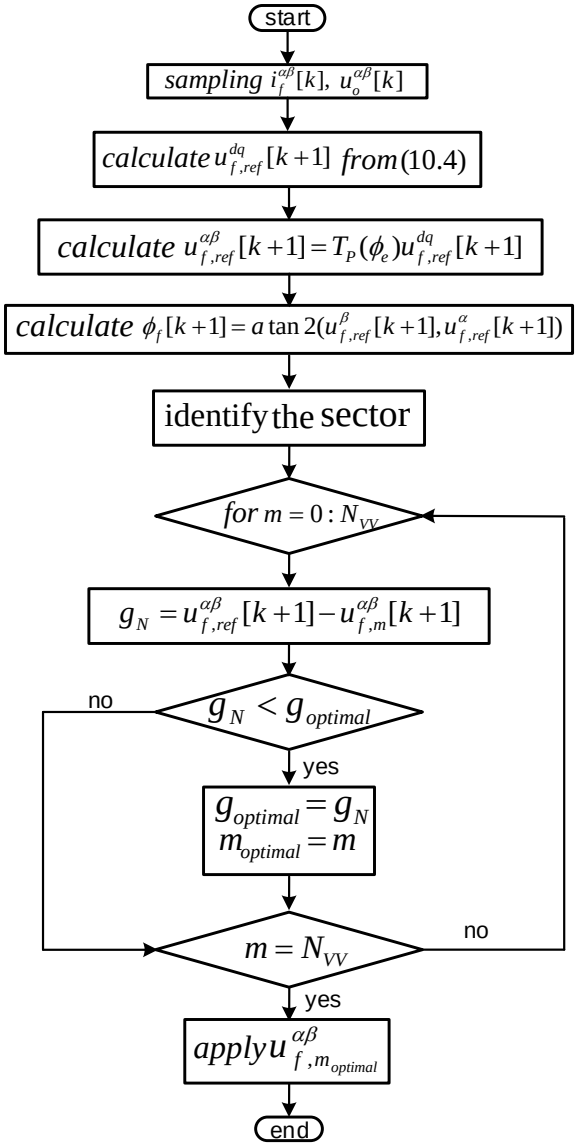

Figure 10.5: Flowchart for the proposed multiple-vector FCS-MPC with improved steady-state performance for grid-connected power converters.

this voltage vector $\boldsymbol{u}_{f,ref}^{k}[k+1] = (u_{f,ref}^{\alpha}[k+1],\ u_{f,ref}^{\beta}[k+1])^{\top}$ is determined by

$$\phi_f[k+1] = \text{atan2}(u_{f,ref}^{\beta}[k+1], u_{f,ref}^{\alpha}[k+1]). \tag{10.5}$$

According to the location of the reference voltage vector, one sector is selected as illustrated in Fig. 10.3(b) and (c). Hence, the cost function is modified to

$$g_N = \left|u_{f,ref}^{\alpha}[k+1] - u_{f,m}^{\alpha}[k+1]\right| + \left|u_{f,ref}^{\beta}[k+1] - u_{f,m}^{\beta}[k+1]\right|, \tag{10.6}$$

For 2VV-DMPC and 3VV-DMPC, the cost function (10.6) is evaluated for 6 and 10 times, respectively, which means that the computational load of the proposed MV-DMPC is significantly lower than that of the method proposed in [201].

The flow chart of the proposed computationally efficient FCS-MPC with enhanced steady-state response is given in Fig. 10.5, where N_{VV} is the number of voltage vectors in each sector (i.e. number of real VVs in addition to virtual VVs).

10.4.1 Novel inductance estimation technique

As discussed in Chapter 6 and 7, the model based predictive control schemes (i.e. DB and FCS-MPC) are sensitive to variations of the model parameters. Therefore, in these chapters, the sum of perturbations caused by parameters variations or by any un-modeled dynamics is estimated. In this section, another alternative to enhance the robustness of the proposed multiple-vector FCS-MPC is proposed. The proposed solution is based on on-line estimating of the model inductance.

Several methods have been proposed in the literature for the estimation of the model inductance (or impedance) [203]–[209]. In [203], a virtual flux-based predictive direct power control (DPC) with on-line inductance estimation for AC/DC converters is proposed. An analytic method for the estimation of the coupling inductance of AFE converters is proposed in [204]. The authors in [205] proposed a fuzzy logic controller based method to compensate for the unknown coupling inductance used in an AFE converter control strategy. A grid impedance estimation method based on variations of active and reactive power was proposed in [206]. A grid parameter estimation method based on the assumption that the grid voltage magnitude is equal at two consecutive sampling instants was proposed in [207]. A predictive DPC with an adaptive on-line parameter identification technique for AFE converters was proposed in [125]. The proposed parameter identification technique is based on a least squares method to estimate the filter inductance and resistance for the grid-connected AFE converter. In [208], model reference adaptive system (MRAS) is employed to estimate the model inductance is presented. Extended Kalman filter (EKF) is a powerful tools to estimate the model inductance and resistance, see [126], [209], [210].

In this work, a finite inductance set (FIS) observer is proposed, which based on using the idea of the FCS-MPC scheme [211]. The flow chart of the proposed inductance observer is illustrated in Fig. 10.6. The algorithm starts by reading the current i_f^{dq} and voltages u_o^{dq} and u_f^{dq}. Then, a certain displacement for the inductance ΔL is selected, which controls the accuracy of the proposed observer. To produce a finite set of inductances, a **for** loop is defined, see Fig. 10.6. Similar to the seven voltage vector of the two-level VSC, this loop gives seven discrete values of the inductance as fellow:

$$\hat{L}_{fi}[k] = \hat{L}_f[k] + (i-3)\Delta L. \tag{10.7}$$

By using these seven values of the inductance, seven values of the current $\hat{i}_f^{dq}$ can be computed as:

$$\left.\begin{array}{rcl} \hat{i}_f^d[k] & = & (1-\frac{T_s R_f}{\hat{L}_{fi}[k]})i_f^d[k-1] + \omega_e[k-1]T_s i_f^q[k-1] + \frac{T_s}{\hat{L}_{fi}[k]}(u_o^d[k-1] - u_f^d[k-1]), \\ \hat{i}_f^q[k] & = & (1-\frac{T_s R_f}{\hat{L}_{fi}[k]})i_f^q[k-1] - \omega_e[k-1]T_s i_f^d[k-1] + \frac{T_s}{\hat{L}_{fi}[k]}(u_o^q[k-1] - u_f^q[k-1]). \end{array}\right\} \tag{10.8}$$

Then, a cost function in the form,

$$g_{Li} = \left|i_f^d[k] - \hat{i}_f^d[k]\right| + \left|i_f^q[k] - \hat{i}_f^q[k]\right|, \tag{10.9}$$

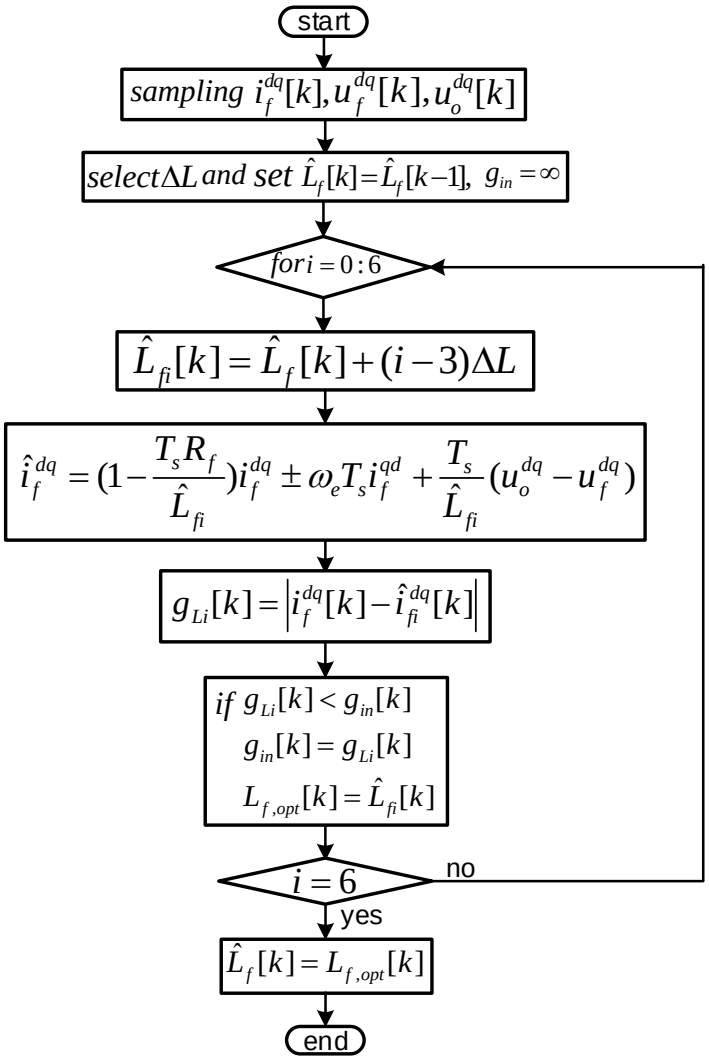

Figure 10.6: Flowchart for the proposed finite inductance set observer for grid-tied power converters.

is employed to selected the optimal value of the inductance. Note that, the proposed observer always searches around the inductance of the last sampling instant as illustrated in Fig. 10.6, i.e. $\hat{L}_f[k] = \hat{L}_f[k-1]$ in (10.7).

10.5 Simulation results

For the validation of the proposed computationally efficient FCS-MPC with improved steady-state performance, a 20 kW grid connected PV inverter is implemented in Matlab/Simulink, where the parameters of the system is the same like the parameters of the GSC in PMSG wind turbine systems, see Appedix B.

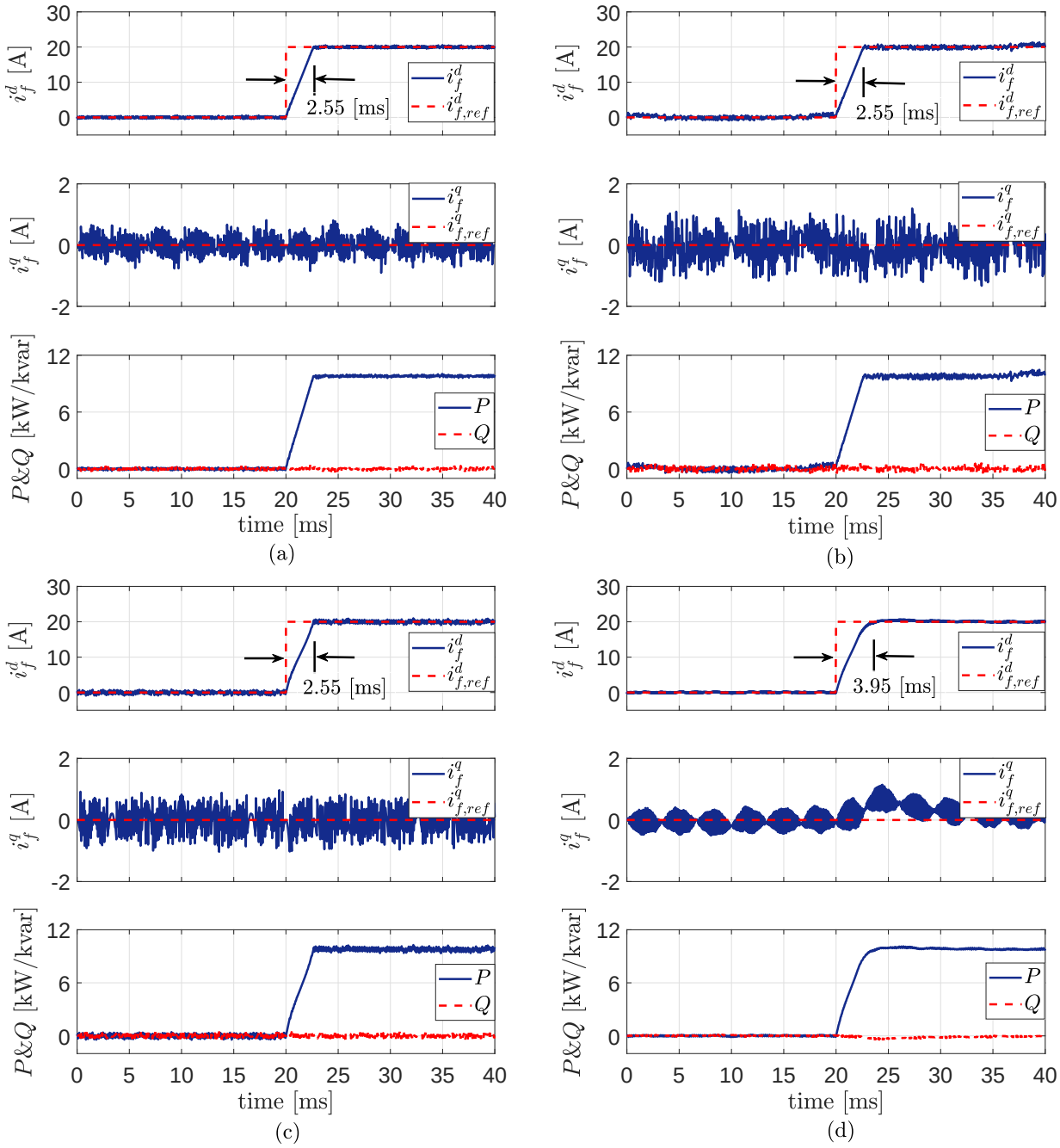

Figure 10.7: Performance of the various control schemes at step change in the d-axis current i_f^d: (a) Proposed 3VV-FCS-MPC, (b) proposed 2VV-FCS-MPC, (c) traditional FCS-MPC, and (d) VOC.

10.5.1 Performance of the proposed multiple-vector DMPC

Figure 10.7 shows the dynamic response of the different control schemes (3VV-FCS-MPC, 2VV-FCS-MPC, traditional FCS-MPC, and VOC) at step change in the d-axis current i_f^d. At the time instant $t = 20$ ms, a step change in the reference d-axis current $i_{f,ref}^d$ from 0 A to 20 A is applied to each control scheme. According to Fig. 10.7, the proposed 3VV-FCS-MPC and 2VV-

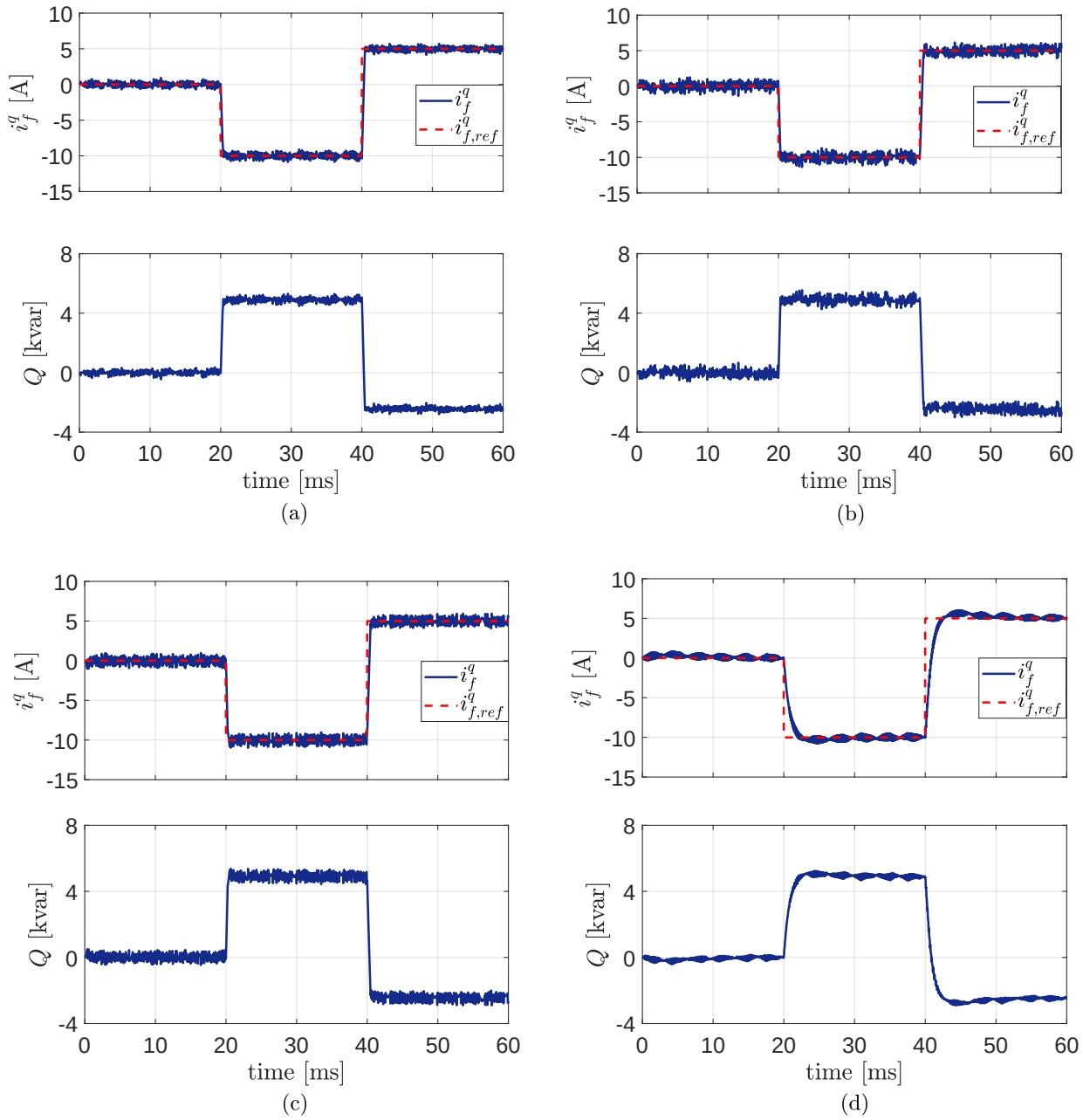

Figure 10.8: Performance of the various control schemes at step change in the q-axis current i_f^q: (a) Proposed 3VV-FCS-MPC, (b) Proposed 2VV-FCS-MPC, (c) traditional FCS-MPC, and (d) VOC.

FCS-MPC have a similar transient response like the traditional FCS-MPC. The three control techniques (i.e. 3VV-FCS-MPC, 2VV-FCS-MPC, and traditional FCS-MPC) need 2.55 ms to reach the steady-state operation, while VOC scheme needs longer time (3.95 ms). Furthermore, the ripples in the current/power waveforms in case of using the proposed 3VV-FCS-MPC are significantly lower than the ripples in case of the traditional FCS-MPC. The execution time of each control system (i.e. 3VV-FCS-MPC, 2VV-FCS-MPC, traditional FCS-MPC, and VOC) in intel CORE i7 CPU 2.7 GHz is 12 µs, 9 µs, 18 µs, and 5 µs, respectively.

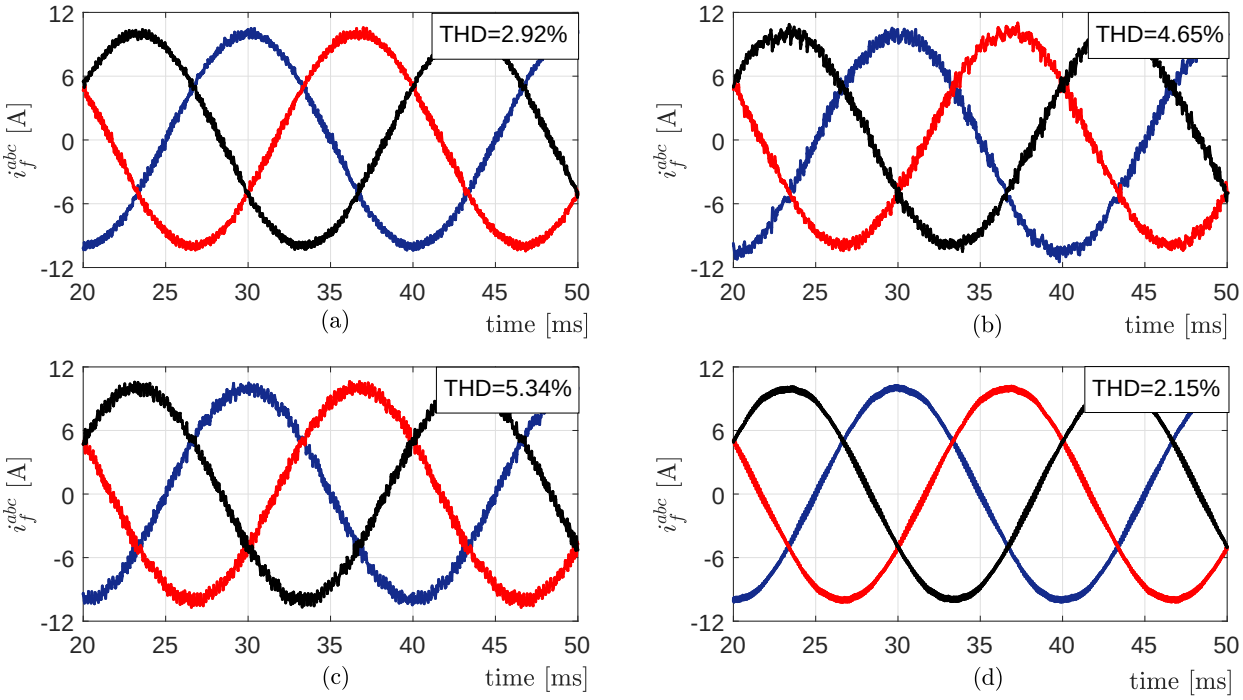

Figure 10.9: Steady-state waveforms of the three-phase currents i_f^{abc}: (a) Proposed 3VV-FCS-MPC, (b) Proposed 2VV-FCS-MPC, (c) traditional FCS-MPC, and (d) VOC.

Generally, grid-connected power converter must have the ability to inject/absorb reactive power to/from the grid. Therefore, the performance of the different control schemes (i.e. 3VV-FCS-MPC, 2VV-FCS-MPC, traditional FCS-MPC, and VOC) is investigated for this scenario. At the time instants $t = 20$ ms and $t = 40$ ms, step changes in the reference q-axis current $i_{f,ref}^q$ form 0 A to -10 A and then to 5 A, respectively, have been applied. It can be seen from Fig. 10.8 that the proposed 3VV-FCS-MPC, 2VV-FCS-MPC, and traditional FCS-MPC give better dynamic performance than the well-known VOC with PI controllers. Again, the ripples in the current/power waveforms in case of using the proposed 3VV-FCS-MPC are significantly lower than the ripples in case of the traditional FCS-MPC.

Finally, the waveforms of the three-phase currents using the different control schemes are illustrated in Fig. 10.9. It can be observed that the ripples in the three phase currents i_f^{abc} using the proposed 3VV-FCS-MPC is significantly lower than the traditional FCS-MPC and almost similar to the waveforms of the three phase currents i_f^{abc} using the well-known VOC. The total harmonic distortion (THD) of the current using 3VV-FCS-MPC, 2VV-FCS-MPC, traditional FCS-MPC, and VOC schemes is 2.92%, 4.65%, 5.34%, and 2.15%, respectively, which matches the IEEE standard specifications [212].

10.5.2 Performance of the proposed finite-set inductance observer

The response of the proposed finite-set inductance observer is illustrated in Fig. 10.10. Firstly, the effect of selecting the displacement ΔL is investigated by testing three different values $\Delta L = 0.0001\,\text{mH}$, $\Delta L = 0.0005\,\text{mH}$, and $\Delta L = 0.001\,\text{mH}$, respectively. For this test, the

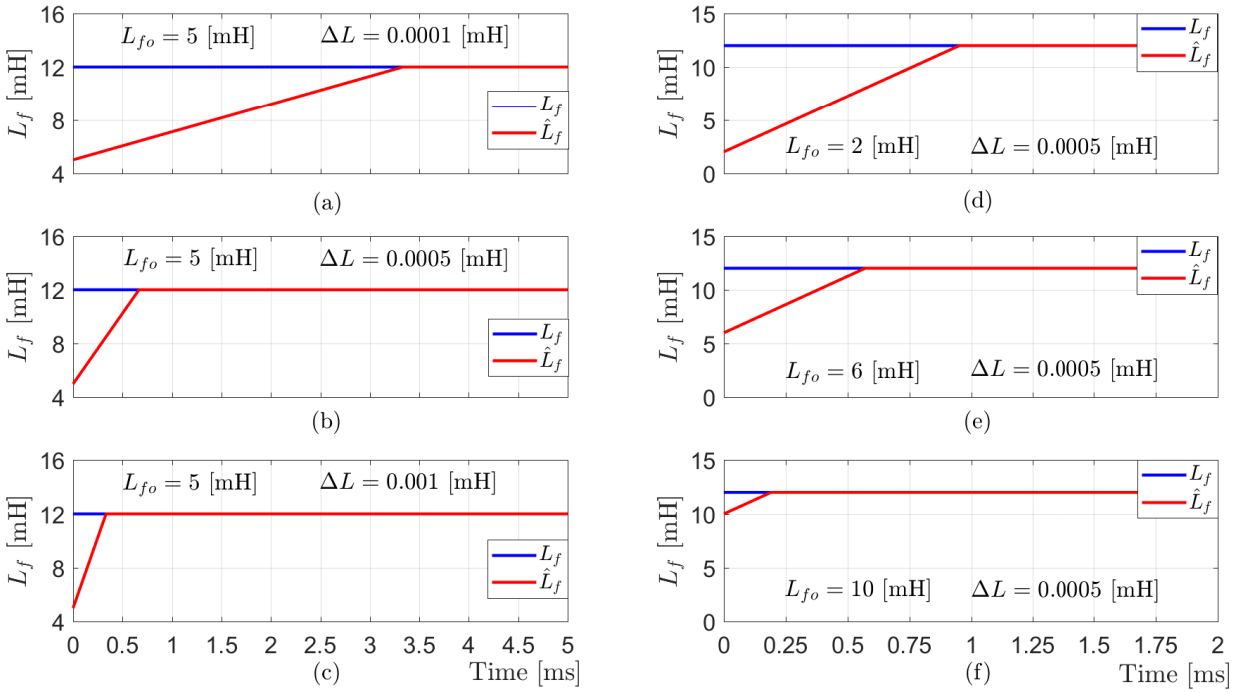

Figure 10.10: Estimation performance of the proposed finite-set inductance observer at different values of ΔL (a–c) and L_{fo} (d–f).

initial value of the inductance L_{fo} is set to $5\,\mathrm{mH}$. According to Fig. 10.10a–c, the dynamic performance of the proposed finite-set inductance observer is enhanced by increasing the value of the displacement ΔL. The proposed observer takes $0.3\,\mathrm{ms}$ to track the actual inductance at $\Delta L = 0.001\,\mathrm{mH}$, while $3.25\,\mathrm{ms}$ is required at $\Delta L = 0.0001\,\mathrm{mH}$. However, the ripples in the estimated inductance in case of $\Delta L = 0.001\,\mathrm{mH}$ is higher than the ripples in case of $\Delta L = 0.0001\,\mathrm{mH}$.

Secondly, the response of the proposed finite-set inductance observer at different values of the initial inductance L_{fo} is investigated, see Fig. 10.10d–f. Three different values of L_{fo} are selected. i.e $2\,\mathrm{mH}$, $6\,\mathrm{mH}$, and $10\,\mathrm{mH}$. It can be seen that at $L_{fo} = 10\,\mathrm{mH}$, the proposed observer converge faster than in case of $L_{fo} = 6\,\mathrm{mH}$ and $L_{fo} = 2\,\mathrm{mH}$.

10.6 Summary

In this chapter, a multiple-vector DMPC for grid connected power converters to enhance the steady-state performance of the traditional DMPC is proposed. The proposed control technique is based on using virtual voltage vectors (VVs) in addition to the real ones to reduce the ripples in the current/power waveforms, which improves the steady-state response. Moreover, in order to enhance the robustness of the proposed multiple-vector DMPC to variations of the model parameters, a novel inductance estimation technique, which is based on the principles of the FCS-MPC, is presented. The effectiveness of the proposed control technique is validated by simulation results and its performance is compared with the classical DMPC and VOC with

PI controllers. The results have shown that the proposed 3VV-FCS-MPC and 2VV-FCS-MPC schemes have similar dynamic response to that of the traditional FCS-MPC, but with reduced calculation burden. The steady-state performance of the proposed 3VV-FCS-MPC is much better than that of the traditional FCS-MPC, i.e. lower ripples in the current/power waveforms and lower total harmonic distortion (THD). Furthermore, the steady-state response of the proposed 3VV-FCS-MPC is almost similar to that of the VOC with PI controllers, but its dynamic performance is much better.

CHAPTER 11

Fault-ride through strategy for PMSGs and DFIGs

In this chapter, an overview of the modern grid code requirements for large wind turbine farms is explained in Sec. 11.1. Furthermore, in this section, the low voltage-ride through (LVRT) profile and reactive current support requirements of the German grid code is detailed. Then, a review of the LVRT techniques for PMSGs/DFIGs is given. The proposed LVRT technique for PMSGS and DFIGs is described in Sec. 11.2 and Sec. 11.3, respectively. Afterward, the simulation results for PMSGs/DFIGs are illustrated in Sec. 11.4. Finally, the chapter is summarized in Sec. 11.5.

11.1 Introduction

Currently, wind energy has been distinguished as the major power generation source among all renewable energy resources, which causes a strong increase of the wind power penetration into the electrical network [5]–[13]. Therefore, various countries have revised their grid codes (GCs) to add specific requirements for wind power generation systems [213]–[216]. The main elements in grid codes include active/reactive power regulation, frequency/voltage control, power factor control, power quality, fault-ride through (FRT) capability [also called low voltage-ride through (LVRT)], and system protection.

Faults, such as three-phase short-circuit faults, cause severe voltage dips which lead to disconnection of large-scale wind farms from the grid. This sudden disconnection of large generation units might lead to instability of the utility network. The modern grid codes have added some special requirements such as LVRT operation to avoid the aforementioned scenario. Accordingly, LVRT/FRT capability is one of the most challenging requirements for the wind turbine manufacturers. According to the LVRT requirements, wind energy conversion systems (WECSs) must remain tied to the grid during voltage dips/faults and deliver active and reactive power to the grid [213]–[216].

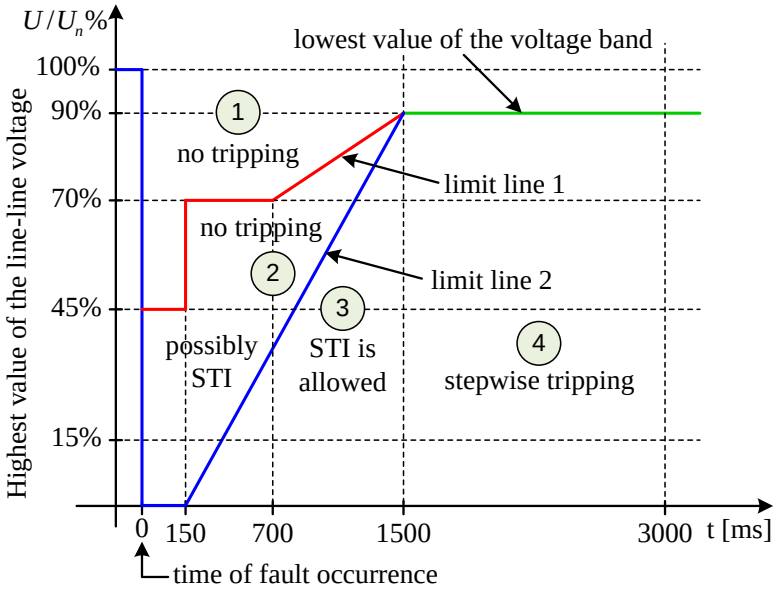

Figure 11.1: LVRT profile of Germany and operation regions of wind power units during faults/voltage dips.

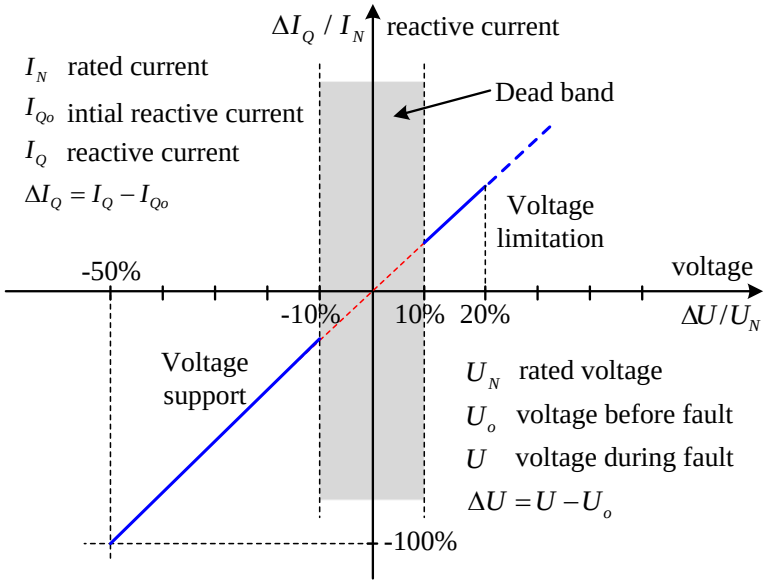

Figure 11.2: Reactive current (power) profile to support the grid during faults/voltage dips according to the E. ON code [216].

The transmission and distribution system operators (TSOs and DSOs) of diverse countries issued different LVRT profiles [213]. Despite the different shapes of those LVRT profiles, they share a common goals such as keeping the electric power system stable and secure during faults and voltage dips. Among various LVRT profiles, the German Transmission and Distribution Utility (E.ON) regulation is likely to set the standard [214]–[216]. Fig. 11.1 illustrates the LVRT profile of Germany, which is divided to four regions. In region 1 (above limit line 1)

and 2 (between limit line 1 and 2), the wind generation unit must stay connected to the grid and support with active/reactive power. However, a short term interruption (STI) with a re-synchronization in the next $2\,\mathrm{s}$ is allowed in region 2 if the wind generation unit faces stability or other kind of technical problems. Note that, in region 2, the wind generation unit have to stay connected to the grid for $150\,\mathrm{ms}$ when the voltage drop to 0% of the nominal value, which is a real challenge. In region 3, faults and voltage dips are effecting considerably the wind generation unit. Therefore, STI is allowed in this area. However, within the next $2\,\mathrm{s}$, re-synchronization is always requested. Finally, if the fault/voltage dip remains for longer than $1.5\,\mathrm{s}$ (i.e region 4), tripping of wind generation unit by system protection is reasonable.

In order to support/limit the grid voltage during abnormal/normal operation, a specific amount of reactive current (power) must be injected/absorbed to/from the grid. The quantity of reactive current (power) to be exchanged with the grid depends on the percentage of grid voltage reduction/increase during faults/voltage dips, the system rated current, and the reactive current exchanged with the grid before the fault occurrences. Fig. 11.2 shows the reactive current (power) profile of Germany [216]. The voltage/reactive current (power) control must be activated once a voltage deviation (increase/decrease) of more than $\pm 10\%$ of the nominal value is detected.

11.1.1 Survey of FRTs techniques for PMSGs

Faults/voltage dips in the grid side cause a reduction of the delivered active power from the DC-link to the grid by the GSC. Consequently, the generated active power accumulates in the DC-link capacitor, which increases the DC-link voltage. Thus, the DC-link capacitor might damage. Therefore, in order to improve the FRT capability of the PMSG, various solutions have been proposed in the last years [217]-[235]. Most of the presented solutions use external devices to improve the FRT capability of the PMSG. The external devices include braking chopper (BC) [218]-[220], energy storage devices [221]-[223], FACTS devices [224]-[226], series dynamic breaking resistor (SDBR) [227]-[229], auxiliary parallel grid-side converter [230], and electronic power transformer [231]. The drawbacks of these external devices include high cost and complexity. During grid faults, the power extracted from the WT can be reduced using blade pitch angle control [232]. However, the response of the mechanical system is very slow in comparison with the electrical system.

FRT can be achieved by storing the surplus active power in the inertia of the wind turbine and PMSG mechanical system. In [233], a new control structure is presented. According to this structure, the DC-link voltage is regulated by the machine side converter (MSC), q-axis current of the PMSG, and the maximum power point tracking (MPPT) is realized by grid side converter (GSC), d-axis current of the GSC. Consequently, when faults/voltage dips occur in the grid, the generated power from the PMSG will be reduced, result in reduced input power to the DC-link. Thus, the DC-link voltage remains constant [233]. However, this control structure is deviated from the conventional control system (DC-link voltage is controlled by the GSC (d-axis current of the GSC) and MPPT is achieved by MSC (q-axis current of the PMSG)) and the control performance in steady-state (normal operation conditions) is not accurate due to inaccurate estimation of the losses (neglecting of iron losses and resistive losses of the DC-link). Therefore, this control structure was modified in [234]. During the normal operation conditions, the DC-link voltage is regulated by the GSC and the MPPT is achieved by the MSC

and during the faults/voltage dips, the DC-link voltage control is achieved by the MSC control system. According to the design procedure of the cascaded control loops, the PI controller of the outer loop (DC-link voltage control loop) is tuned according to the time constant of the inner loop (current control loop). The time constant of the inner control loop of the GSC is different than the time constant of the inner control loop of the MSC. Consequently, exchanging the DC-link voltage control between the GSC and MSC is deteriorating the control performance and endangering the stability. In [235], a model predictive control (MPC) is presented for the inner control loop to improve the FRT capability of PMSGs using the same idea in [234]. The proposed MPC gives good transient response, however, the proposed control suffers from the same disadvantages that explained before.

11.1.2 Survey of FRTs techniques for DFIGs

In order to improve the FRT ability of the DFIG-based variable-speed wind turbine systems (WTSs), different strategies have been presented in the literature. A crowbar circuit (CB) has been applied for the FRT in [236]. So far, the CB solution is the most adopted strategy by wind turbines manufacturers. However, when the CB is activated, the DFIG becomes a grid-connected induction motor (IM) absorbing reactive current/power from the grid and loses its controllability. Therefore, some approaches installed dynamic voltage compensators (DVCs) or dynamic resistors (DRs) between the stator and grid to support the stator/grid voltage during voltage dips/faults [237]-[239]. DVCs and DRs improved the ability of the DFIG to ride-through the different faults and inject reactive power to the grid. However, those solutions (i.e. DVCs and DRs) call for additional hardware with its control, consequently, the hardware cost will be increased and the reliability of the WECS will be reduced. Furthermore, the control complexity will be increased. Other solutions presented special control systems to improve the use of the existing hardware. In [240], a FRT strategy based on injecting demagnetizing currents from the RSC is presented. Full DFIG control is kept, however a large rotor current capacity is required (i.e. higher RSC rating is essential). A robust controller in the $\alpha - \beta$ stationary frame is proposed in [241], claiming full control in all voltage dip/fault cases. However, the results have been obtained with an oversized voltage source converter. In [242], the FRT requirements has been realized by storing the surplus active power in the inertia of the DFIG-rotor. However, the classical field oriented control (FOC) and voltage oriented control (VOC) have been used to control the RSC and GSC, respectively. Those control schemes (i.e. FOC and VOC) suffer from poor dynamic response due to the limited bandwidth of the PI controllers.

11.2 Proposed FRT strategy for PMSGs

In this work, a new idea for storing the surplus active power in the rotor inertia of the WECS during faults/voltage dips without exchanging the rules of the MSC and GSC is proposed [243]–[245]. The proposed method based on reducing the generated active power from the PMSG by multiplying the reference q-axis current of the PMSG by a factor $k_F \leq 1$. This factor is depending on the depth of the fault/voltage dip. Moreover, a direct model predictive control

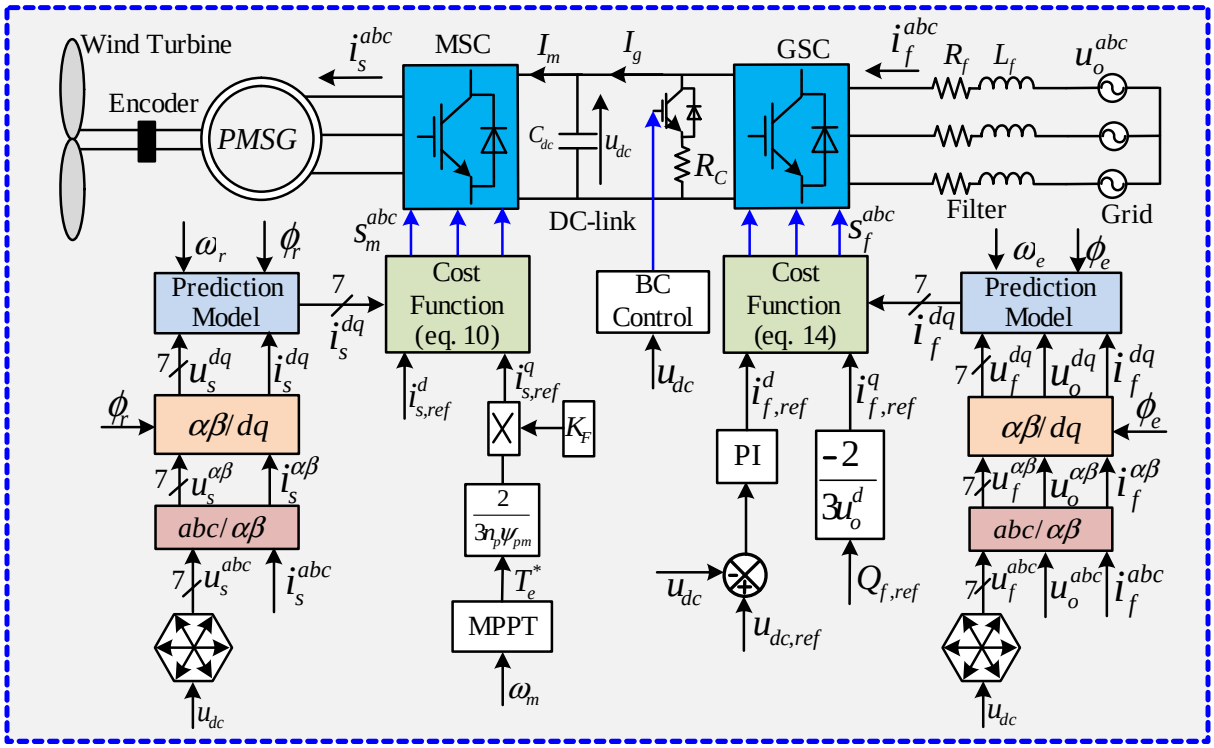

Figure 11.3: Proposed FRT strategy for PMSG based wind turbines.

(DMPC) is presented for enhancing the dynamic response of the WECS. Simulation results are presented to validate the proposed FRT strategy. The results are compared with the conventional braking chopper (BC) solution.

During faults or voltage dips in the grid side, the grid voltage $\|u_o\| = \sqrt{(u_o^d)^2 + (u_o^q)^2}$ will be lower than the rated value 1 [pu], therefore, the delivered active power to the grid will be reduced. However, without FRT control strategy, the PMSG will continue supplying active power to the DC-link. Consequently, the difference between the generated power from the PMSG and the delivered power to the grid will be accumulated in the DC-link capacitor. Accordingly, The DC-link voltage u_{dc} increases to a value that can cause damage of the DC-link capacitor. The traditional solution for this problem is utilizing a braking chopper (BC) in the DC-link. When the DC-link voltage reaches the threshold value (i.e. $1.1u_{dc}$), the BC will turn on. Consequently, the surplus power dissipates in the BC resistance R_c as shown in Fig.11.3. However, BC solution can only dissipate the surplus power and cannot deliver reactive power to the grid. Accordingly, this solution failed in achieving the new grid code requirements.

The proposed FRT strategy is illustrated in Fig. 11.3. The q-axis reference current $i_{s,ref}^q$ of the PMSG is multiplied by a factor K_F, which can be expressed as

$$K_F = \begin{cases} 1 & \text{if} \|u_o\| \geq 0.9 \text{[pu]} \\ \frac{u_o}{u_{o,rated}} & \text{if} \|u_o\| < 0.9 \text{[pu]}, \end{cases} \tag{11.1}$$

where $u_{o,rated} = 1$ [pu] is the rated value of the grid voltage and u_o is the magnitude of the grid voltage during the fault/voltage dip. Therefore, during the normal operation conditions $\|u_o\| \geq 0.9$, the DMPC of the MSC will track the maximum power point of the wind turbine (i.e.

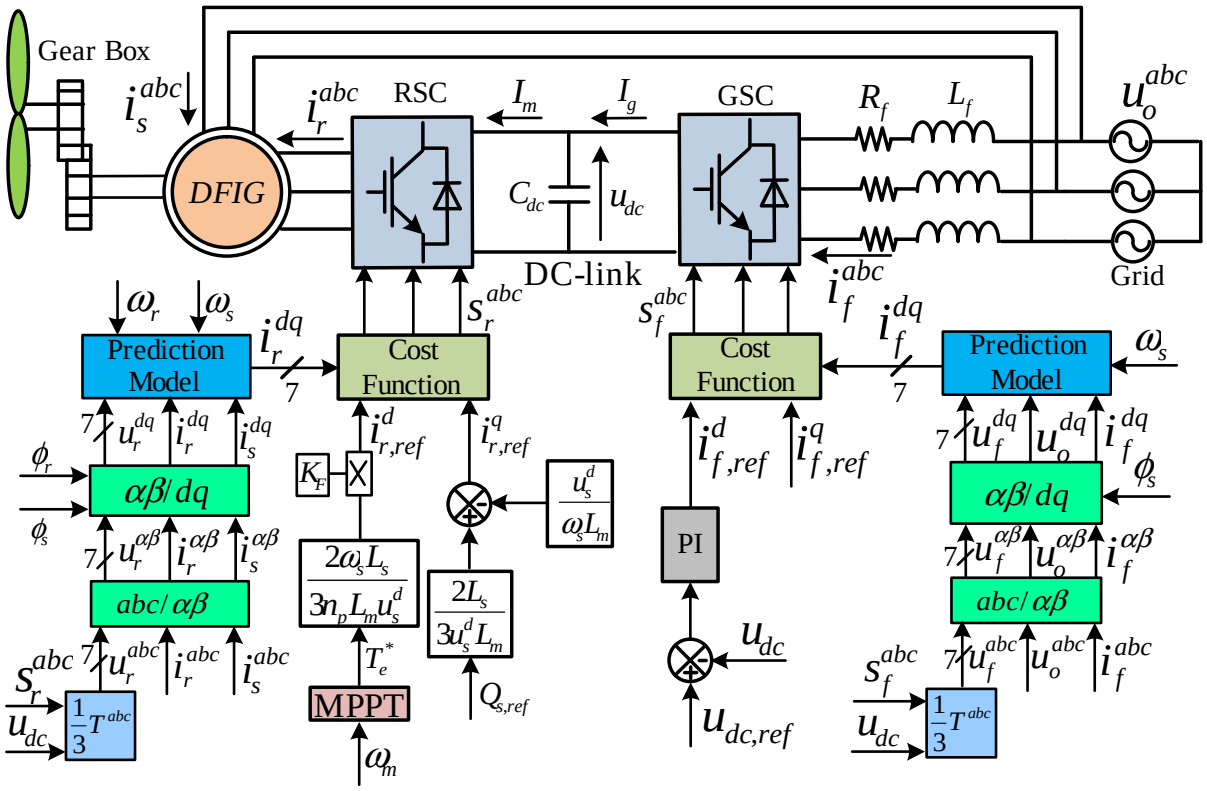

Figure 11.4: Proposed DMPC for FRT capability improvement of DFIGs in variable-speed wind turbines

$K_F = 1$). During faults/voltage dips in the grid side, the generated power from the PMSG will be decreased according to the depth of the voltage dip/fault (i.e. $K_F < 1$). Consequently, the surplus active power will be stored in the inertia of the rotor of the WECS, thus, the mechanical speed of the shaft increases. After fault clearness, this stored active power will be injected back to the grid.
In order to fulfill the new grid code requirements, the maximum allowable reactive current will be injected to the grid during the fault, which can be expressed as

$$i^q_{f,ref} = \sqrt{(i_{f,max})^2 - (i^d_{f,ref})^2}. \tag{11.2}$$

11.3 Proposed FRT strategy for DFIGs

Similarly to the PMSG, during faults/voltage dips, the generated active power from the DFIG can be reduced by multiplying the d-axis reference current $i^d_{r,ref}$ by the factor K_F (see [246], [247]) as illustrated in Fig. 11.4. In reality, the inertia of the WECS with DFIG is higher than that of the WECS with PMSG due to the exist of the large gear-box.

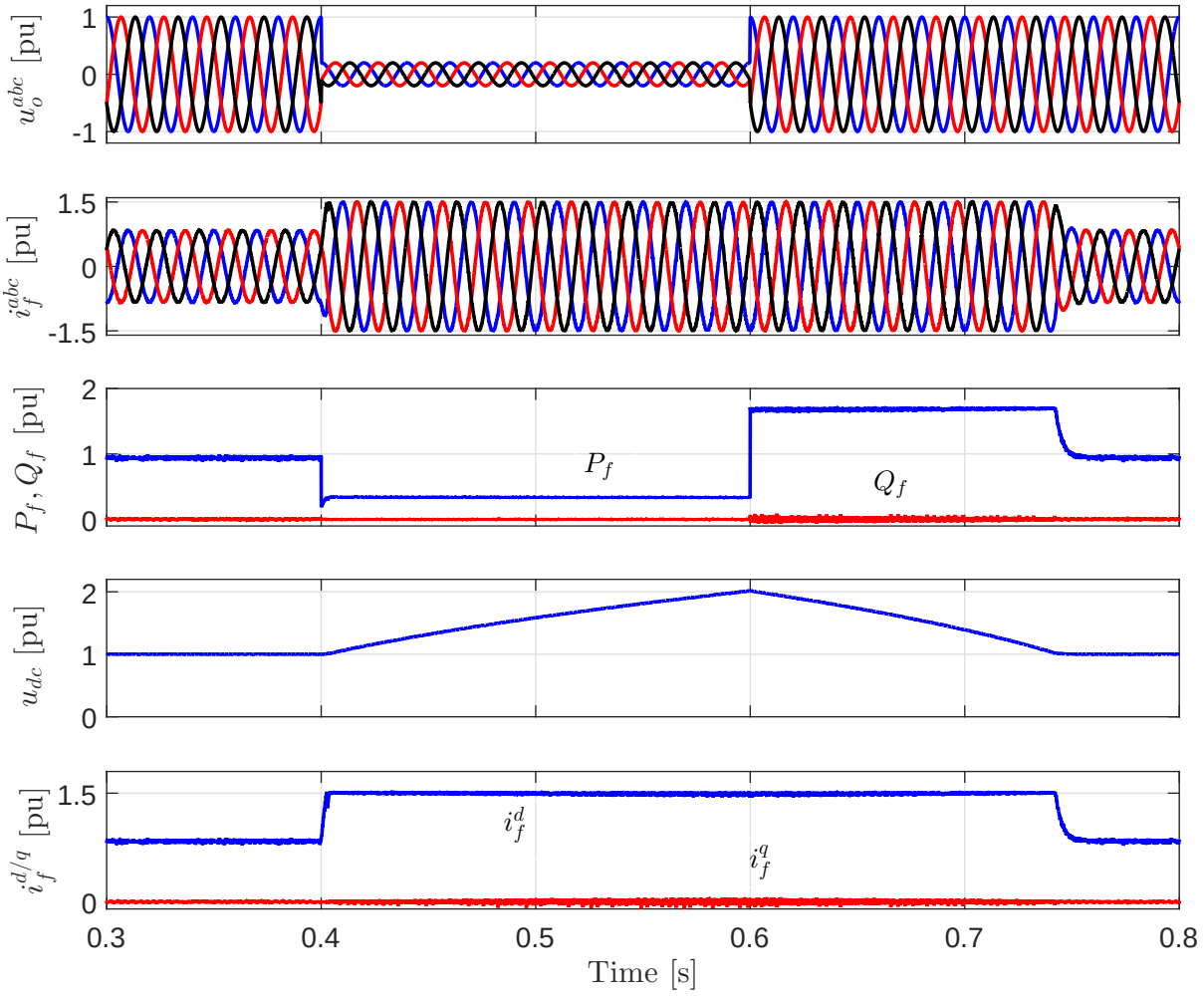

Figure 11.5: Performance of the GSC and DC-link during a three-phase fault without FRT strategy for PMSGs (from **top**): grid voltages $u_o^{abc} = (u_o^a, u_o^b, u_o^c)^\top$, GSC output currents $i_f^{abc} = (i_f^a, i_f^b, i_f^c)^\top$, active and reactive power injected to the grid (P_f, Q_f), DC-link voltage u_{dc}, and d- and q-axis currents of the GSC (i_f^d, i_f^q).

11.4 Simulation results

The parameters of the simulation models and base values for the pu system are listed in Appendix B.

11.4.1 Simulation results of PMSGS

Figure 11.5 shows the performance of the GSC and DC-link during a three-phase fault in the grid side without FRT strategy at the rated wind speed 20 m/s. At the time instant $t = 0.4$ s, an 85% voltage dip in the grid voltage occurred for a period 200 [ms]. As explained above, dur-

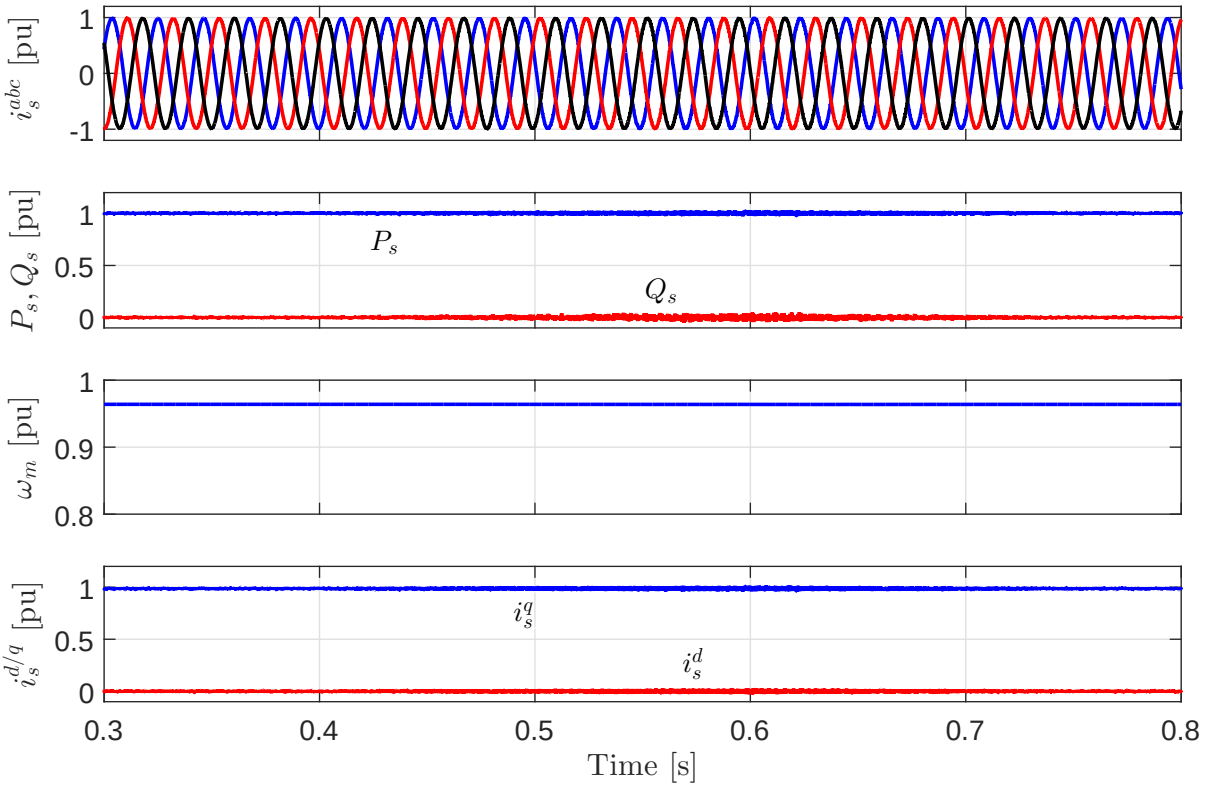

Figure 11.6: Performance of the MSC and PMSG during a three-phase fault without FRT strategy (from **top**): PMSG output currents $i_s^{abc} = (i_s^a, i_s^b, i_s^c)^\top$, PMSG active and reactive power (P_s, Q_s), mechanical speed of the PMSG rotor ω_m, and d- and q-axis currents of PMSG (i_s^d, i_s^q).

ing the faults/voltage dips, the active power P_f injected to the grid decreases (see Figure 11.5) while the generated active power P_s from the PMSG is constant (see Figure 11.6). Therefore, the output currents of the GSC i_f^{abc} increase in order to regulate the DC-link voltage. However, the output currents reach the maximum allowable value 1.5 pu, as shown in Figure 11.5. Accordingly, the surplus active power accumulates in the DC-link capacitor causing an increase of the DC-link voltage u_{dc} to a very high value 2 pu. This voltage is enough to destroy the DC-link capacitor. After the fault clearance at the instant $t = 0.6$ s, the DC-link voltage recovers by injecting more active power to the grid than that generated. Consequently, the d-axis current i_f^d of the GSC is still constant at the maximum allowable value even after the fault clearance.

Figure 11.6 illustrates the performance of the MSC and PMSG during the same three-phase fault as in Figure 11.5 without FRT strategy. There are no changes in the PMSG currents, generated active and reactive power, and mechanical speed of the rotor due to the full decoupling between the grid and the generator.

In order to protect the DC-link capacitor, the traditional solution is connecting a braking chopper in parallel with the DC-link capacitor. In order to investigate the effectiveness of this BC solution, the simulation is re-performed under the same wind speed (i.e., 20 m/s) and the same three-phase fault as in Figure 11.5. Figure 11.7 illustrates the performance of the GSC and grid with the BC-FRT solution. After the fault occurrences, the DC-link voltage increases.

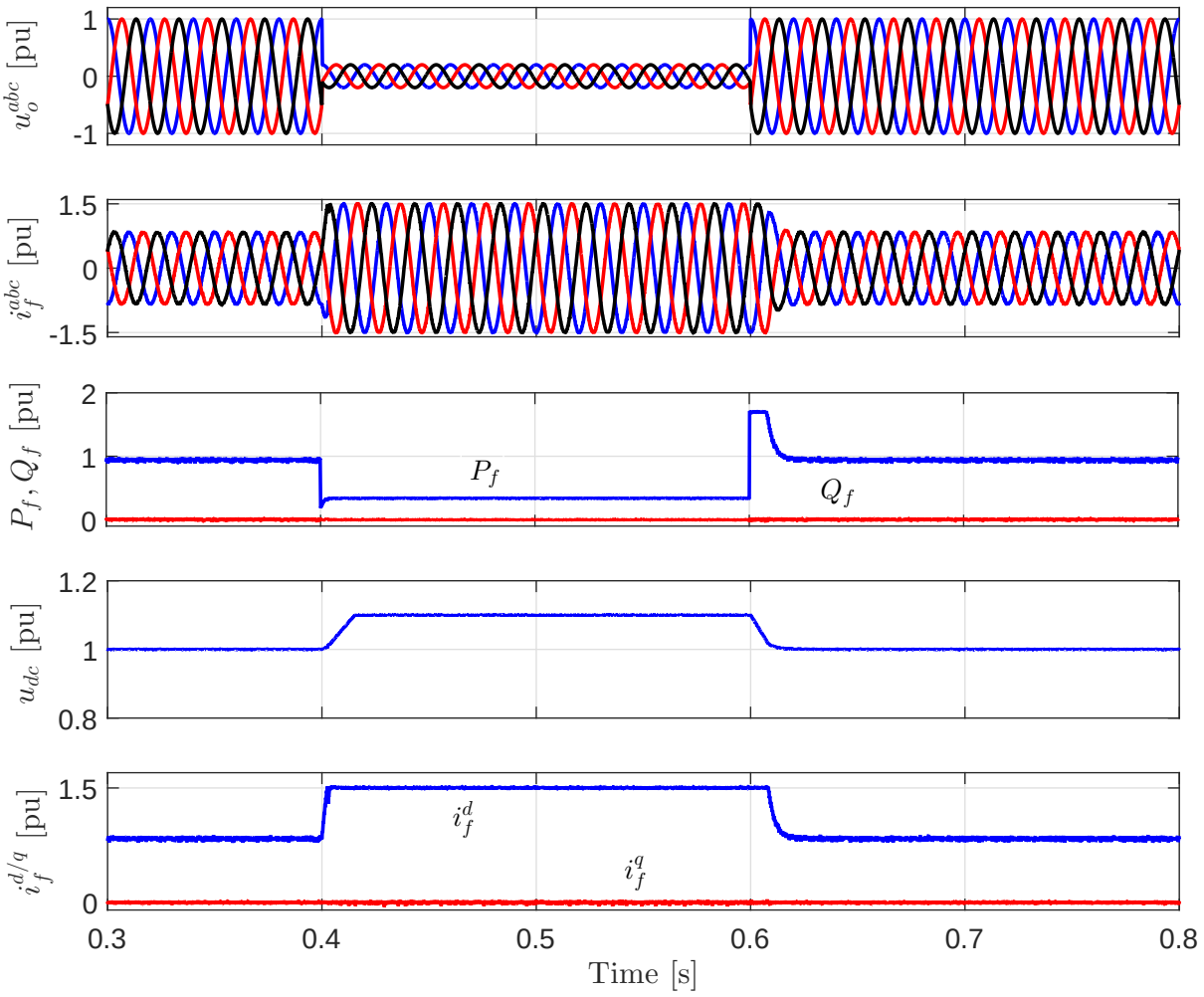

Figure 11.7: Performance of the GSC and DC-link during a three-phase fault with BC-FRT strategy for PMSGs (from **top**): grid voltages $u_o^{abc} = (u_o^a, u_o^b, u_o^c)^\top$, GSC output currents $i_f^{abc} = (i_f^a, i_f^b, i_f^c)^\top$, active and reactive power injected to the grid (P_f, Q_f), DC-link voltage u_{dc}, and d- and q-axis currents of the GSC (i_f^d, i_f^q).

However, when the DC-link voltage reaches the threshold value (i.e., $u_{dc} = 1.1$ pu), the BC is activated and the surplus active power dissipates in the BC resistance. Accordingly, the DC-link voltage is kept constant at the threshold value. According to Figure 11.7, the BC solution has the capability to protect the DC-link capacitor. However, according to the new grid code requirements, the WECS must inject reactive power to the grid during the faults/voltage dips. This requirements can not be achieved using the BC solution.

Figure 11.8 shows the performance of the MSC and PMSG during the same three-phase fault as in Figure 11.5 with the BC-FRT strategy. Again, there are no changes in the generator currents, active and reactive power, and mechanical speed of the rotor, thanks to the full decoupling between the grid and the generator.

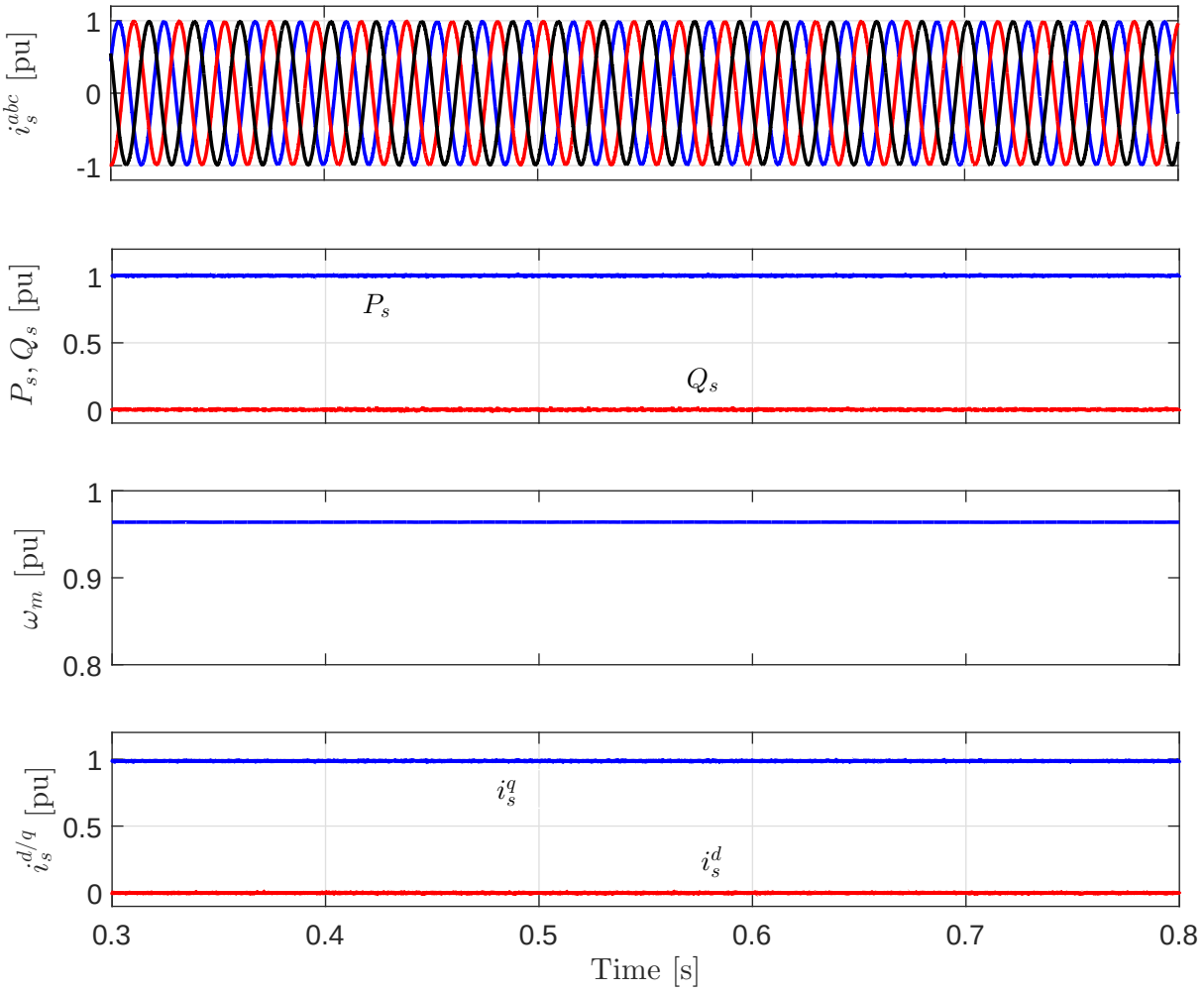

Figure 11.8: Performance of the MSC and PMSG during a three-phase fault with BC-FRT strategy (from **top**): PMSG output currents $i_s^{abc} = (i_s^a, i_s^b, i_s^c)^\top$, PMSG active and reactive power (P_s, Q_s), mechanical speed of the PMSG rotor ω_m, and d- and q-axis currents of PMSG (i_s^d, i_s^q).

The performance of the GSC and DC-link during the same three-phase fault with the proposed FRT strategy is illustrated in Figure 11.9. According to equation (11.1), when the fault/voltage dip is detected, the q-axis reference current $i_{s,ref}^q$ of the PMSG is multiplied by the factor K_F. Accordingly, the generated active power P_s from the PMSG decreases as shown in Figure 11.10. Therefore, a mismatch between the output mechanical power from the wind turbine and generated power from the PMSG is produced. As a consequence, the rotor mechanical speed ω_m of the PMSG increases and the surplus power will be stored in the inertia of the rotor of the WECS (see Figure 11.10). Therefore, the DC-link voltage is kept almost constant at its reference value 1 pu. Moreover, during the fault, a reactive power Q_f is injected to the grid. The q-axis reference current $i_{f,ref}^q$ of the GSC is calculated according to (11.2). Thus, more than 1 pu reactive current is injected into the grid. Accordingly, the proposed FRT strategy suc-

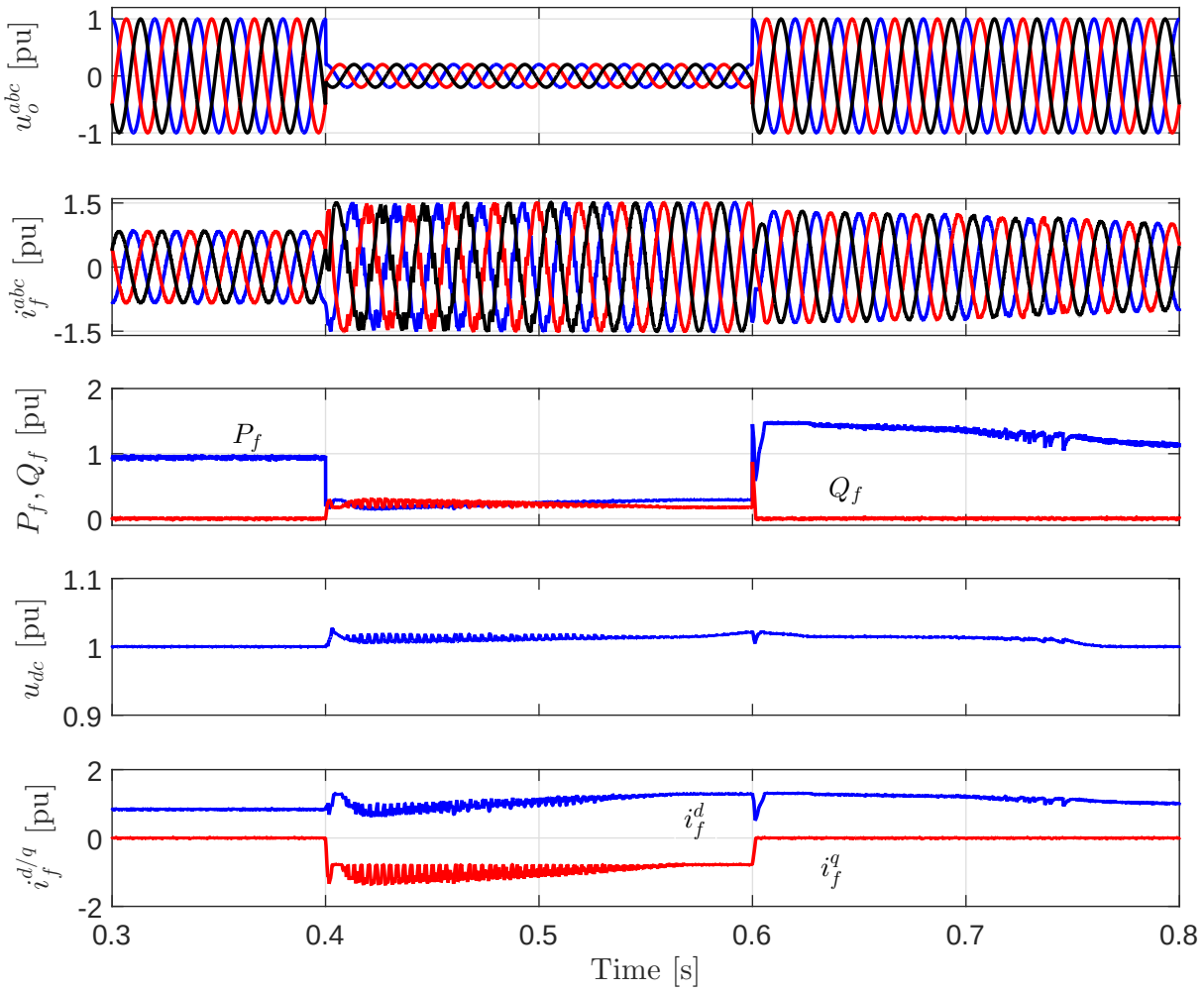

Figure 11.9: Performance of the GSC and DC-link during a three-phase fault with the proposed FRT strategy for PMSGs (from **top**): grid voltages $u_o^{abc} = (u_o^a, u_o^b, u_o^c)^\top$, GSC output currents $i_f^{abc} = (i_f^a, i_f^b, i_f^c)^\top$, active and reactive power injected to the grid (P_f, Q_f), DC-link voltage u_{dc}, and d- and q-axis currents of the GSC (i_f^d, i_f^q).

ceeded in protecting the DC-link capacitor and achieving the grid code requirements without any extra hardware components.

After the fault clearance, the stored energy in the rotating mechanical system of the WECS is injected back into the grid via the DC-link. The injected power after the fault is equal to the sum of the output mechanical power from the wind turbine and the stored power during the fault. Therefore, the q-axis current of the PMSG i_s^q and the d-axis current of the GSC i_f^d reach the limit 1.5 pu. Consequently, the speed of the rotor of the PMSG decreases and reaches the pre-fault value after delivering all the stored power to the grid.

Comparing the performance of the proposed FRT strategy (Figures 11.9 and 11.10) with the performance of BC solution (Figures 11.7 and 11.8) shows that the proposed FRT strategy

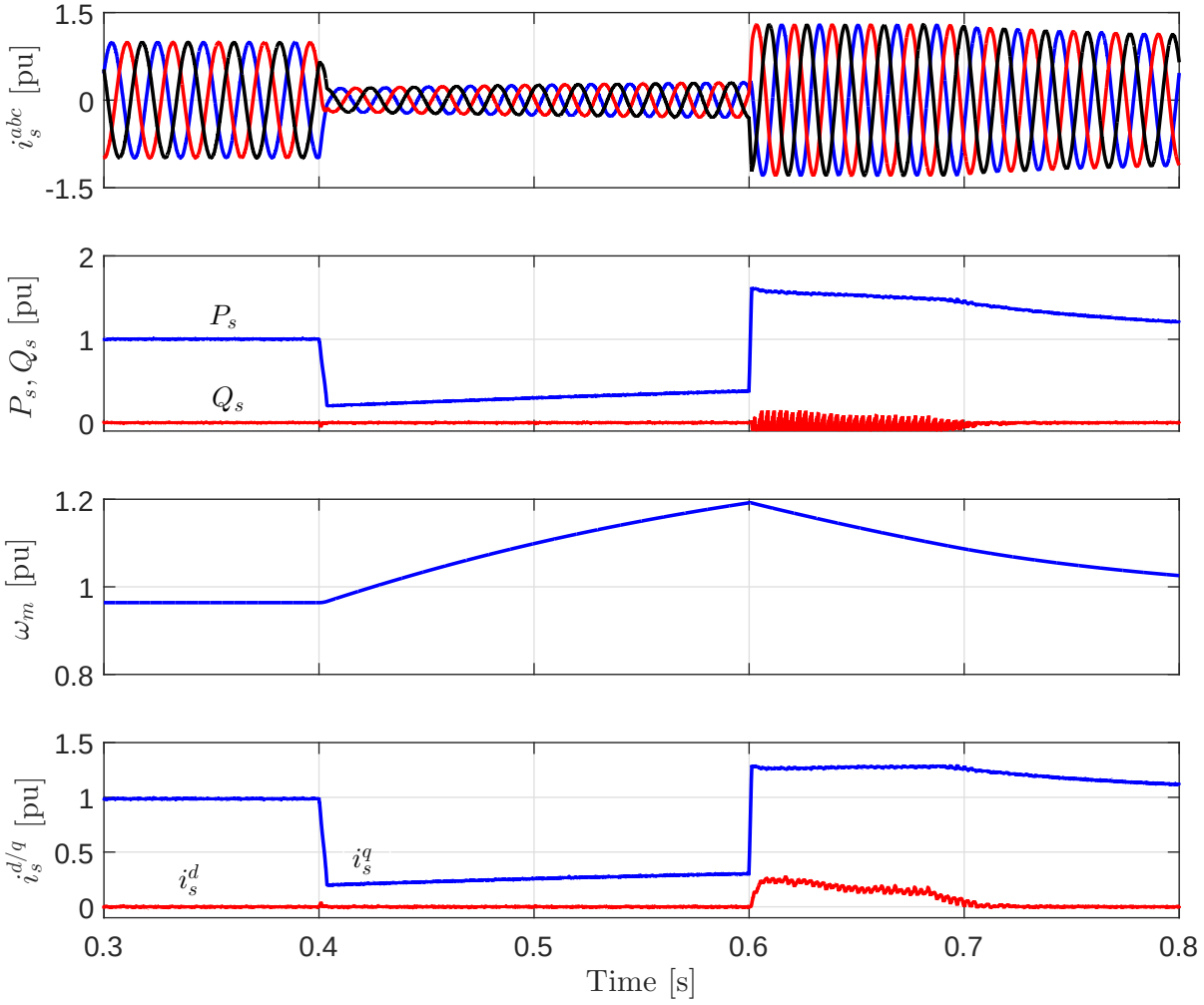

Figure 11.10: Performance of the MSC and PMSG during a three-phase fault with the proposed FRT strategy (from **top**): PMSG output currents $i_s^{abc} = (i_s^a, i_s^b, i_s^c)^\top$, PMSG active and reactive power (P_s, Q_s), mechanical speed of the PMSG rotor ω_m, and d- and q-axis currents of PMSG (i_s^d, i_s^q).

gives superior performance. The main drawback of the proposed FRT strategy is the stress in the mechanical components of the wind turbine and PMSG during the fault. However, as shown in Figure 11.10, the mechanical speed of the PMSG is still within the safe limit 1.2 pu, although the wind turbine operates at the rated wind speed 20 m/s.

In order to investigate the performance of the proposed FRT strategy during unbalanced faults, a single phase to ground fault has been applied in the grid side. At the time instant $t = 0.5$ s, a 50% voltage dip in phase a of the grid is applied for a period of 300 ms. The simulation is re-performed under a wind speed 15 m/s. Figure 11.11 shows the performance of the GSC and DC-link under the single phase to ground fault with the proposed FRT strategy. Again, the proposed FRT strategy succeeded in protecting the DC-link capacitor. The DC-link voltage

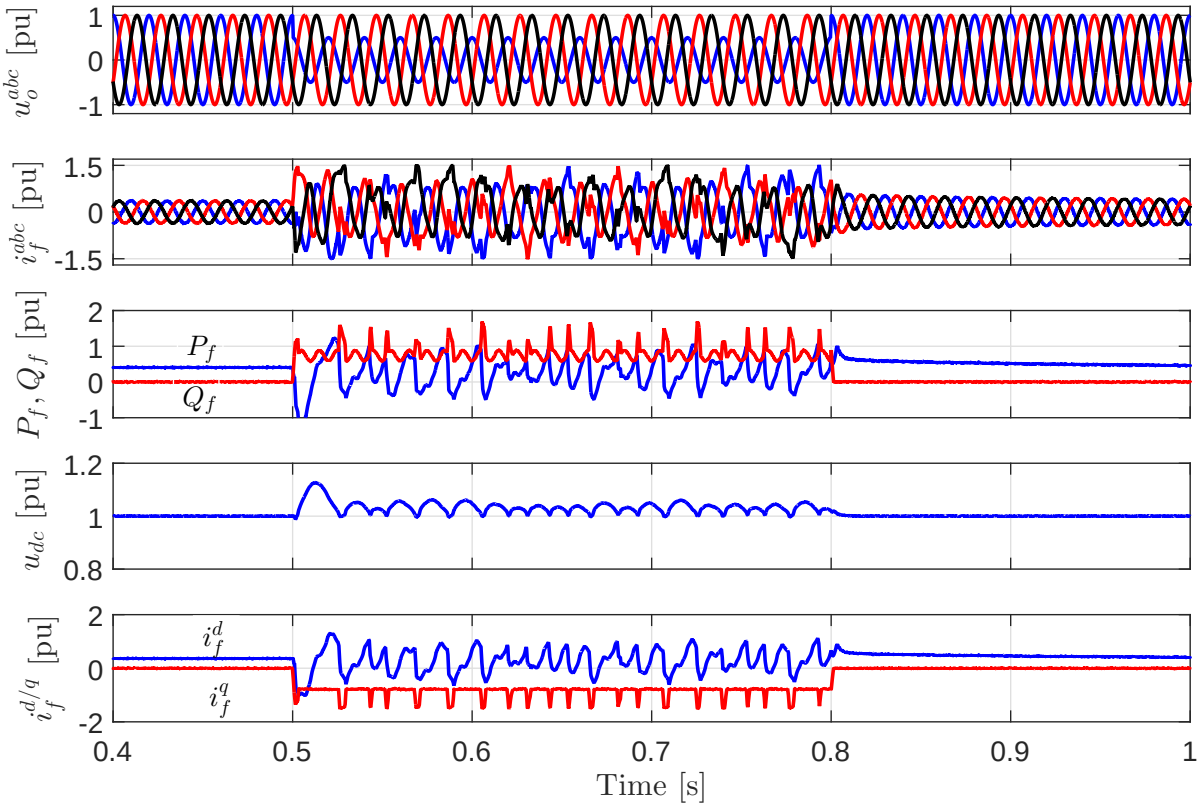

Figure 11.11: Performance of the GSC and DC-link during a single phase to ground fault with the proposed FRT strategy for PMSGs (from **top**): grid voltages $u_o^{abc} = (u_o^a, u_o^b, u_o^c)^\top$, GSC output currents $i_f^{abc} = (i_f^a, i_f^b, i_f^c)^\top$, active and reactive power injected to the grid (P_f, Q_f), DC-link voltage u_{dc}, and d- and q-axis currents of the GSC (i_f^d, i_f^q).

is almost constant at 1 pu. Moreover, approximately 1 pu reactive power/current is injected into the grid. Thus, the proposed FRT fulfills the new grid code requirements.

The performance of the MSC and PMSG under the single phase to ground fault is illustrated in Figure 11.12. As explained above, during the fault, the generated active power from the PMSG reduces and the surplus active power is stored in the inertia of the WECS. Therefore, the mechanical speed of the PMSG increases. However, the mechanical speed did not reach the rated value 1 pu. Accordingly, there is no stress on the mechanical components of the wind turbine and PMSG in this case.

11.4.2 Simulation results of DFIGs

Fig. 11.13 illustrates the response of the WECS based on DFIG during a three-phase fault with the proposed FRT solution under the rated wind speed of the wind turbine (i.e. $v_w = 14$ [m/s]), which represents the worst case because the wind turbine operates in the super-synchronous mode (i.e. $\omega_m > \omega_{syn}$, where $\omega_{syn} = 157$ [rad/s] is the synchronous speed of the generator). At the time instant $t = 0.2$ [s] a 60% voltage dip in the grid voltage u_o^{abc}

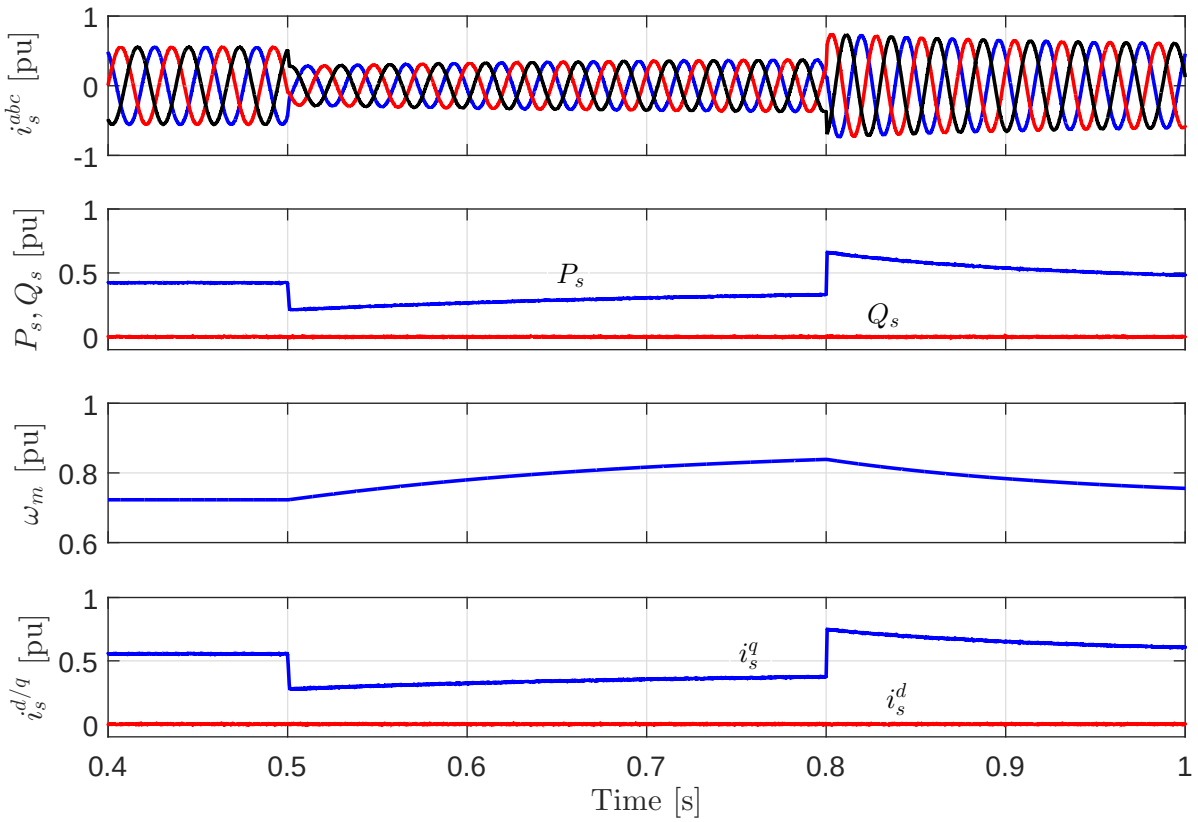

Figure 11.12: Performance of the MSC and PMSG during a single phase to ground fault with the proposed FRT strategy (from **top**): PMSG output currents $i_s^{abc} = (i_s^a, i_s^b, i_s^c)^\top$, PMSG active and reactive power (P_s, Q_s), mechanical speed of the PMSG rotor ω_m, and d- and q-axis currents of PMSG (i_s^d, i_s^q).

for 200 [ms] has been occurred, see Fig. 11.13 (top). The proposed FRT solution forces the generator to reduce the total generated active power $P_t = P_s + P_f$ during the fault (P_s, P_f are the active powers generated by the stator of the DFIG and the GSC, respectively). As a consequence, there is a torque mismatch in the mechanical system between the wind turbine and the DFIG, which causes the mechanical speed ω_m of the DFIG to increase, see Fig. 11.13. However, the mechanical speed ω_m of the DFIG is still lower than the maximum allowable speed (i.e. 1.3 [pu]). Therefore, no stress on the mechanical system is produced even when the wind turbine operates at the rated wind speed. After the fault clearness, the stored active power in the DFIG-rotor inertia is released back to the grid. Therefore, the mechanical speed ω_m of the DFIG decreases. The injected power to the grid after the fault is equal to the sum of the output mechanical power from the wind turbine and the stored power during the fault. Therefore, more than 1 [pu] active power is delivered to the grid after the fault clearness. The DC-link voltage u_{dc} is kept almost constant at its reference value. However, a very small oscillation in the DC-link voltage appeared during the fault. The rotor current of the DFIG $\boldsymbol{i}_r = \sqrt{(i_r^d)^2 + (i_r^q)^2}$ and the output filter current $\boldsymbol{i}_f = \sqrt{(i_f^d)^2 + (i_f^q)^2}$ are lower than the maximum allowable values (i.e.

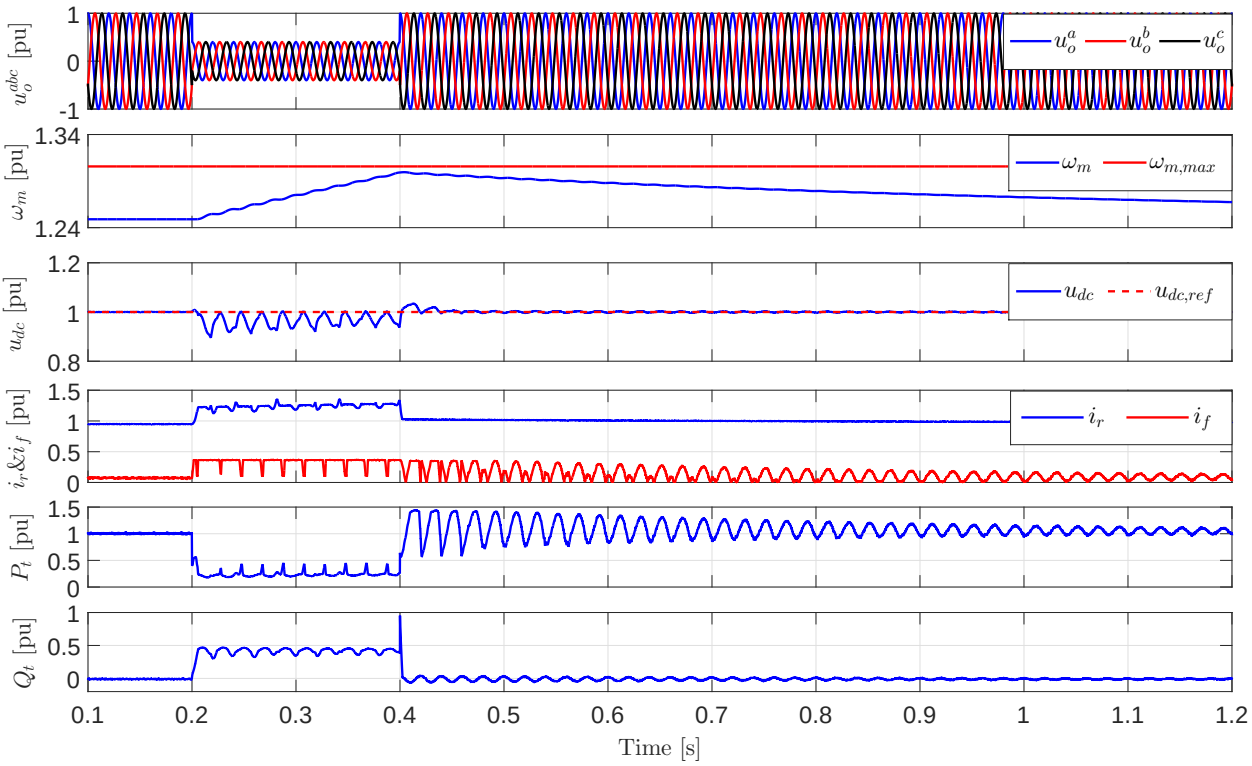

Figure 11.13: Performance of the WECS based on DFIG during a 60% voltage dip in u_o^{abc} (deep three-phase fault) with the proposed FRT solution (from top): grid/stator voltages $\boldsymbol{u}_o^{abc}$, mechanical speed ω_m of the DFIG rotor, DC-link voltage (u_{dc}, $u_{dc,ref}$), current of the rotor and output filter (i_r, i_f), total active power P_t injected to the grid, total reactive power Q_t injected to the grid.

1.5 & 0.5 [pu] of the rated value, respectively). Furthermore, using the proposed FRT strategy, the DFIG has the ability to inject active and reactive power to the grid during the fault, see Fig. 11.13 (bottom). A reactive power $Q_t \approx 0.5$ [pu] is injected to the grid during the fault ($Q_t = Q_s + Q_f$ where Q_s and Q_f are the reactive powers generated by the stator of the DFIG and GSC, respectively). Thus, the proposed FRT fulfill the grid codes requirements.

In order to further investigate the performance of the proposed FRT strategy, Fig. 11.14 shows the simulation results of the proposed FRT solution during light (i.e 25%) voltage dip/fault that applied for a long period of time (500 [ms]). Again, the wind speed is set to $v_w = 14$ [m/s] to represent the worst case. According to Fig. 11.14, the proposed FRT gives excellent performance for this scenario. The mechanical speed ω_m is lower than the maximum allowable value $\omega_{m,max}$ and the DC-link voltage u_{dc} is almost constant with very small oscillations around the reference value $u_{dc,ref}$. Moreover, active P_t and reactive Q_t power are delivered to the grid during the voltage dip/fault.

Fig. 11.15 illustrates the response of the proposed FRT method under asymmetrical fault (single-phase to ground fault). At the time instant $t = 0.2$ [s] a 50% voltage dip in phase c (u_o^c) of the grid for 200 [ms] has been applied. The simulation is also performed under wind speed of $v_w = 14$ [m/s]. It is clear that the mechanical speed ω_m of the DFIG rotor is lower than

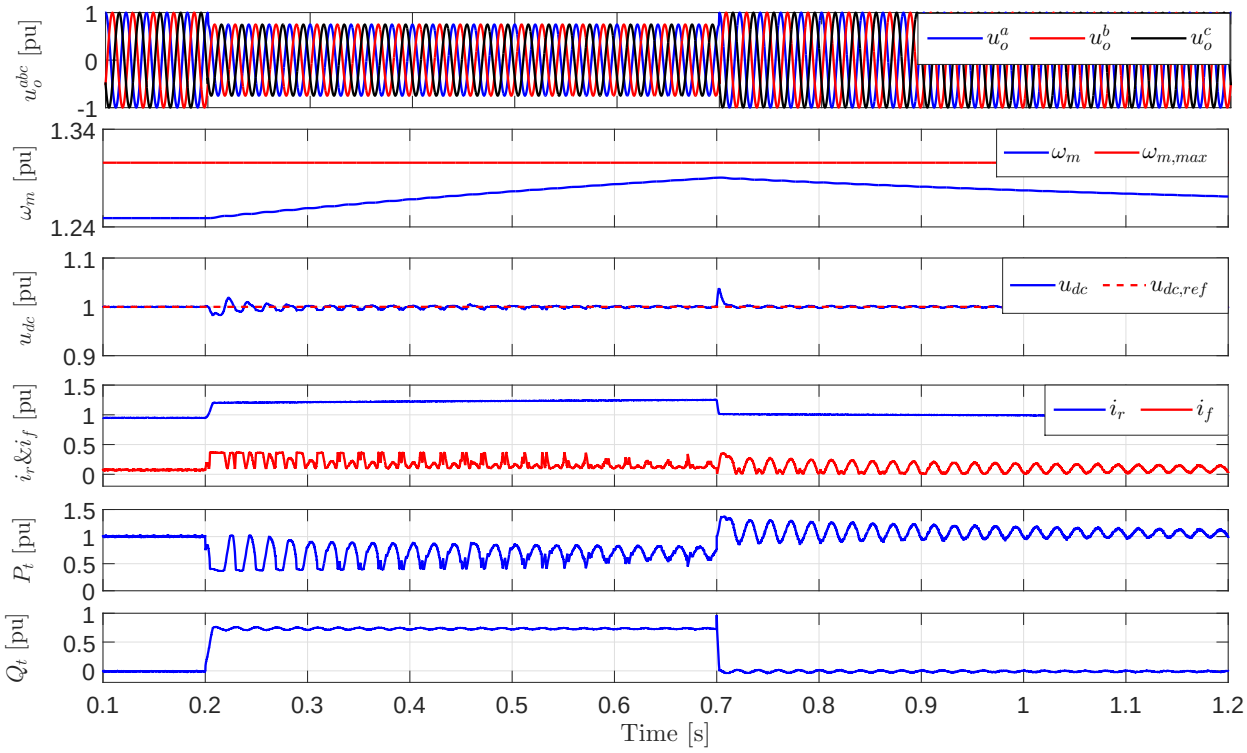

Figure 11.14: Performance of the WECS based on DFIG during a 25% voltage dip in u_o^{abc} (light three-phase fault) with the proposed FRT solution (from top): grid/stator voltages $\boldsymbol{u}_o^{abc}$, mechanical speed ω_m of the DFIG rotor, DC-link voltage (u_{dc}, $u_{dc,ref}$), current of the rotor and output filter (i_r, i_f), total active power P_t injected to the grid, total reactive power Q_t injected to the grid.

the maximum value $\omega_{m,max}$ and the DC-link voltage u_{dc} is almost constant. However, slightly high oscillations in the DC-link voltage u_{dc} around its reference value $u_{dc,ref}$ is observed due to the negative sequence component of the grid voltage. Again, the rotor current $\boldsymbol{i}_r$ and the output filter current $\boldsymbol{i}_f$ are lower than the maximum allowable value. Furthermore, active P_t and reactive Q_t power are delivered to the grid during the voltage dip/fault. Hence, the grid code requirements (i.e. full DFIG control and injection of active and reactive power to the grid during various voltage dips/faults) have been realized using the proposed FRT strategy.

11.5 Summary

In this chapter, an FRT strategy for PMSGs and DFIGs in variable-speed wind turbines is proposed. Voltage dips/faults in the grid cause a transient active power surplus in the WECS. The proposed FRT strategy uses the rotor inertia of the WECS (inertia of the wind turbine and PMSG/DFIG) to store the surplus power during faults/voltage dips in the grid side. The performance of the proposed FRT strategy has been verified and compared with the traditional BC solution (for PMSGs) by simulation results under symmetrical and asymmetrical faults/voltage dips. The results illustrated that the proposed FRT strategy guarantees keeping the DC-link

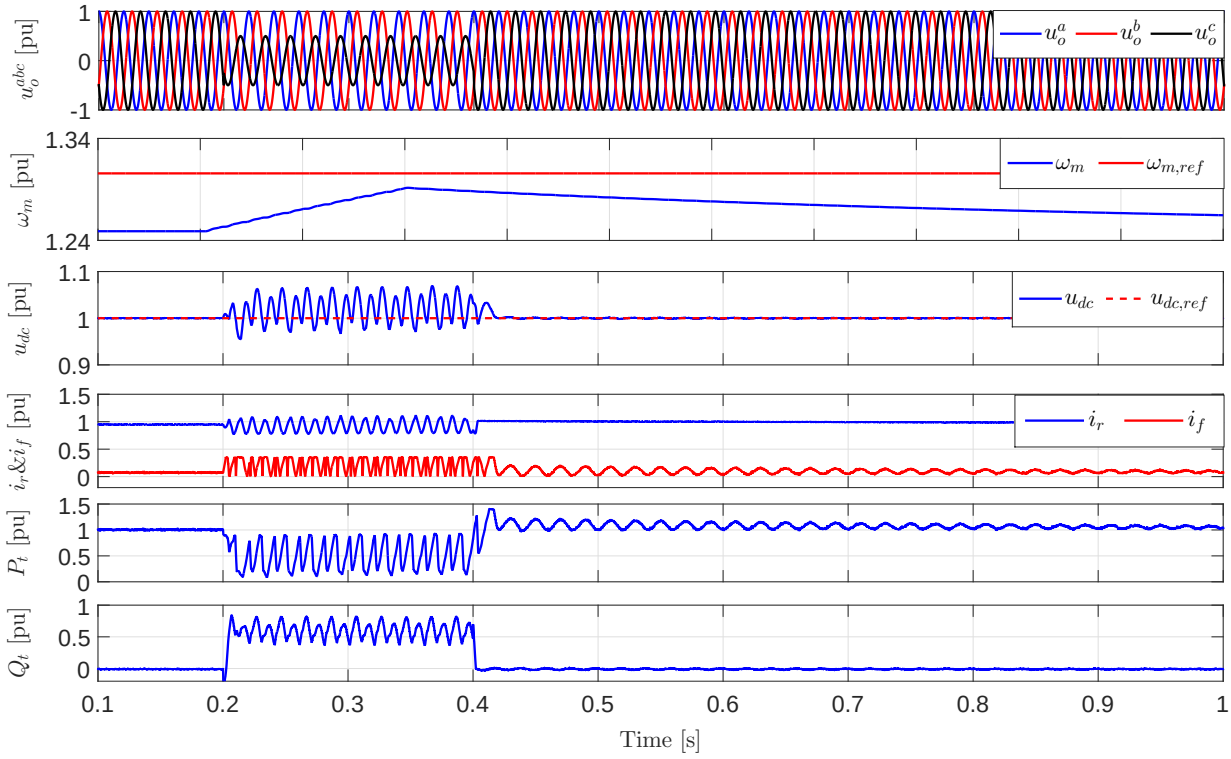

Figure 11.15: Performance of the WECS based on DFIG during a 50% voltage dip in u_o^c (single-phase to ground fault) with the proposed FRT solution (from top): grid/stator voltages $\boldsymbol{u}_o^{abc}$, mechanical speed ω_m of the DFIG rotor, DC-link voltage (u_{dc}, $u_{dc,ref}$), current of the rotor and output filter (i_r, i_f), total active power P_t injected to the grid, total reactive power Q_t injected to the grid.

voltage almost constant at its reference value (i.e., 1 pu) and injecting active and reactive power into the grid during faults/voltage dips. Furthermore, Being a simple control method without extra hardware components, the proposed FRT strategy gives superior performance in comparison with the traditional BC solution for PMSGs and the classical crowbar protection for DFIGs . Accordingly, the proposed FRT strategy fulfills the new grid code requirements without any additional hardware components.

CHAPTER 12

Conclusion and Future Outlook

In this work, both classical and modern model based predictive control techniques for permanent-magnet synchronous generators (PMSGs) and doubly-fed induction generators (DFIGs) have been closely investigated. The investigated schemes in this dissertation for PMSGs/DFIGs include field and voltage oriented control (FOC/VOC), deadbeat predictive control (DBPC), finite-control-set model predictive control (FCS-MPC), predictive direct torque control (PDTC), predictive speed control (PSC), multiple-vector FCS-MPC, and low-voltage ride through (LVRT). Furthermore, novel finite position set (FPS) observers for sensorless FOC/VOC of PMSGs/DFIGs have been proposed to enhance the reliability and reduce the complexity/cost of the controller. A new finite inductance set observer is presented for estimating the model inductance, i.e improve the controller robustness to variations of the inductance. More specifically, the work achieved in his dissertation can be briefly summarized as fellows:

- In Chapter 2, the mathematical symbols used in this dissertation are summarized. Furthermore, the mathematical basics of the system modeling are explained, which incorporates coordinate transformations, and continuous and discrete time system descriptions. The mathematical models for both the PMSG and DFIG in variable-speed wind turbine systems are developed in details. Finally, the constructed test-benches of the PMSG and DFIG for validation of the proposed speed/position observers and control algorithms are described. Additionally , the simulink models for PMSG and DFIG are are briefly presented as well.

- In chapter 3, the classical control techniques for PMSGs and DFIGs have been described. These control techniques include: vector control (FOC/VOC for PMSGs/DFIGs), DBPC, and FCS-MPC. Their physical/mathematical fundamentals, control principles and realization steps have been clearly discussed and explicitly presented. The performances of those different control techniques have been validated and compared by experimental and simulation results. The results illustrated that: I) Vector control gives a satisfactory dynamic performance, very good steady-state response, and is robust to parameters variations, II)

DBPC enhances the dynamic performance of the system and gives good steady-state response; however, its sensitivity to parameters variations and the one-sample delay due to the digital controller are the main drawbacks, III) FCS-MPC gives excellent dynamic response; however the high ripples in the current/torque and sensitivity to parameters variations are the main disadvantages.

- In chapter 4, a novel search-based algorithm for extending the principles of the FCS-MPC to be applied for speed/position observers is proposed. The search-based algorithm produces 64 positions of the rotor and with the help of a cost function, only one position is selected to be the optimal rotor position. The proposed algorithm is firstly applied to the well-known phase locked loop (PLL) based observer for sensorless control of PMSGs, which called finite-position-set PLL (FPS-PLL). Then, it is extended to MRAS observer for PMSGs/DFIGs. The proposed finite-position-set (FPS) observers have been experimentally implemented and their performances have been compared with that of the traditional ones. The results illustrated that the FPS observers have the following advantages:

  1. The dynamic performance and robustness of the proposed FPS-PLL/FPS-MRAS observers are better than that of the conventional ones.
  2. The required effort to tune the PI controllers in the conventional PLL/MRAS observers is eliminated.
  3. The concept of the proposed search-based algorithm is simple and easy to understand.

  However, the proposed FPS-PLL/FPS-MRAS observers have the following drawbacks:

  1. The computational burden of the proposed FPS-PLL/FPS-MRAS observers is significantly higher than that of the conventional ones, where 64 iterations are required to find the optimal rotor position.
  2. The accuracy of the proposed search-based algorithm is high due to the fact that it produces a limited number of rotor position angles. Accordingly, the ripples in the estimated speed/position using the proposed FPS-PLL/FPS-MRAS observers are higher than that of the traditional PLL/MRAS observers.

- In Chapter 5, two computationally-efficient finite-position-set phase looked loops (CE-FPS-PLLs1&2) are proposed to reduce the computational effort of the FPS-PLL presented in Chapter 4. The proposed CE-FPS-PLL2 and CE-FPS-PLL1 highly reduced the number of iterations requested to find the optimal rotor position, where 24 and 36 iterations, respectively, are required in comparison with 64 iterations for the FPS-PLL. Furthermore, the accuracy of the proposed CE-FPS-PLL2 is significantly better than that of CE-FPS-PLL1 and FPS-PLL. The proposed CE-FPS-PLL2, CE-FPS-PLL1, FPS-PLL, and traditional PLL were experimentally implemented and compared. The results illustrated that the dynamic response and robustness of the CE-FPS-PLL2, CE-FPS-PLL1, FPS-PLL are better than that of the traditional one. Furthermore, the steady-state response of the proposed CE-FPS-PLL2 is similar to the traditional PLL, i.e. the ripples in the estimated speed/position are almost comparable.

- In chapter 6, a robust and sensorless DBPC technique for PMSGs/DFIGs in variable-speed wind turbines is presented. The proposed control system used an EKF to estimate the stator (and rotor) currents, rotor speed and position, and mechanical torque of the PMSG/DFIG. The one-step-delay in the digital control system was compensated by feeding back the estimated stator (and rotor) currents to the prediction algorithm. Furthermore, a simple disturbance observer was presented in order to increase the robustness of the proposed DBPC against parameters uncertainties of the PMSG/DFIG. The proposed control system was implemented and experimentally validated in the laboratory. The experimental results showed that the EKF estimates stator (and rotor) currents, rotor speed, rotor position, and mechanical torque with high accuracy and is robust to variations of the PMSG/DFIG parameters. Furthermore, the proposed disturbance observer improves the robustness of the DBPC scheme against parameter variations and achieves zero steady-state estimation errors. Moreover, the THD of the stator (and rotor) currents and the electro-magnetic torque ripples are significantly reduced by the filtering capability of the EKF. Concluding, the overall proposed encoderless predictive control system achieves a fast, accurate and robust control performance even under parameter variations.

- In chapter 7, an efficient direct model predictive control (EDMPC) with a discrete-time integral action (DTIA) for PMSGs/DFIGs is proposed. The proposed EDMPC directly computes the reference voltage vector from the required reference current vector to overcome the high computational burden of the conventional FCS-MPC. Furthermore, the DTIA is added to the calculation of the reference voltage vector to enhance the robustness of the proposed algorithm and to realize a good steady-state response. Finally, by knowing the location of this reference voltage vector, only two evaluations of the quality function are requested to find the optimal switching state. The performance of the proposed EDMPC with DTIA is validated experimentally and compared with that of: I) EDMPC with time-delay control approach (TDCA), and II) conventional DMPC. The results have shown that: 1) The proposed EDMPC with DTIA reduces the computational load significantly in comparison with the conventional DMPC, 2) the performance of the proposed EDMPC with DTIA is robust to variations of the machine parameters, while the performance of the conventional DMPC is deteriorated, 3) the steady-state performance of the proposed EDMPC with DTIA is significantly better than that of the conventional one (i.e. zero steady-state error has been realized during all the operation conditions), and 4) the response of the proposed EDMPC with DTIA is better than that of EDMPC with TDCA.

- In chapter 8, a computationally efficient predictive direct torque control (PDTC) technique without weighting factors for PMSGs/DFIGs has been proposed. The proposed PDTC strategy is based on using the d/q-axis current of the PMSG/DFIG to be the second control variable beside the torque, which reduces (slightly) the calculation burden. Furthermore, in order to overcome the weighting factors tuning problem in the cost function, the reference current of the q/d-axis for the PMSG/DFIG is computed according to the reference torque. Then, the reference VV is directly computed from the reference d- and q-axis currents using a deadbeat function. Finally, in order to reduce the computational effort, the sector where the reference VV is located is determined. Therefore, three evaluations of the cost function are only required to find the optimal VV. The performance

of the proposed PDTC technique is experimentally investigated and compared with that of the conventional one. The results have shown that: 1) The calculation burden of the proposed PDTC strategy is significantly lower that of the traditional one, 2) the dynamic performance of the proposed PDTC technique for PMSGs/DFIGs is similar to that of the traditional PDTC, 4) the steady-state response of the proposed PDTC for DFIGs is better than that of the classical one, and 4) both the proposed and traditional PDTC techniques are slightly sensitive to variations of the machine parameters, in particular, the inductance.

- In Chapter 9, an encoderless predictive speed control (PSC) technique for PMSGs/DFIGs in variable-speed wind turbine systems is proposed. The mechanical speed, d-axis current (q-axis current in case of DFIGs), and torque are included together in one optimization based objective function, which eliminates the cascaded control structure that normally used in control of AC drive. Furthermore, an extended Kalman filter (EKF) is presented for estimating the mechanical variables, i.e. load torque and speed/position of the rotor. The proposed PSC strategy is experimentally validated and its response is compared with that of the conventional method (i.e. predictive current control (PCC) with an outer (PI) speed control loop). The results have illustrated that the dynamic response of the proposed PSC method is significantly better than that of the conventional technique. Furthermore, the noise in the speed signal is filtered by the EKF, which further improves the performance of the control system, enhance the whole system reliability, and reduces the cost. Finally, the proposed PSC showed satisfactory performance under variations of the machine parameters.

- In Chapter 10, a multiple-vector DMPC for grid connected power converters to enhance the steady-state performance of the traditional DMPC is proposed. The proposed control technique is based on using virtual voltage vectors (VVs) in addition to the real ones to reduce the ripples in the current/power waveforms, which improves the steady-state response. Moreover, in order to enhance the robustness of the proposed multiple-vector DMPC to variations of the model parameters, a novel inductance estimation technique, which is based on the principles of the FCS-MPC, is presented. The effectiveness of the proposed control technique is validated by simulation results and its performance is compared with the classical DMPC and VOC with PI controllers. The results have shown that the proposed three voltage vectors (3VV)-FCS-MPC and two voltage vectors (2VV)-FCS-MPC schemes have similar dynamic response to that of the traditional FCS-MPC, but with reduced calculation burden. The steady-state performance of the proposed 3VV-FCS-MPC is much better than that of the traditional FCS-MPC, i.e. lower ripples in the current/power waveforms and lower total harmonic distortion (THD). Furthermore, the steady-state response of the proposed 3VV-FCS-MPC is almost similar to that of the VOC with PI controllers, but its dynamic performance is much better.

- In Chapter 11, a fault-ride through (FRT) strategy for PMSGs and DFIGs in variable-speed wind turbines is proposed. Voltage dips/faults in the grid cause a transient active power surplus in the WECS. The proposed FRT strategy uses the rotor inertia of the WECS (inertia of the wind turbine and PMSG/DFIG) to store the surplus power during faults/voltage dips in the grid side. The performance of the proposed FRT strategy has been verified and compared with the traditional BC solution (for PMSGs) by simulation

results under symmetrical and asymmetrical faults/voltage dips. The results illustrated that the proposed FRT strategy guarantees keeping the DC-link voltage almost constant at its reference value (i.e., 1 pu) and injecting active and reactive power into the grid during faults/voltage dips. Furthermore, Being a simple control method without extra hardware components, the proposed FRT strategy gives superior performance in comparison with the traditional BC solution for PMSGs and the classical crowbar protection for DFIGs . Accordingly, the proposed FRT strategy fulfills the new grid code requirements without any additional hardware components.

Apart from the afore-summarized techniques, the following investigation outputs, which are not presented in this thesis due to the limited scopes, have been also achieved during my Ph.D. research period:

1. Direct predictive speed control with a novel sliding manifold term for permanent-magnet synchronous motor (PMSM) drives.
2. Direct power control (DPC) strategy for for three level neutral-point-clamped (3L-NPC) rectifier under unbalanced grid volt- age.
3. Voltage sensorless direct model predictive control with fast dynamics for 3L-NPC Back-to-Back power converter PMSG in wind turbine systems.
4. Computationally efficient predictive control of three-level NPC converters with DC-link voltage balancing.
5. Efficient FCS-MPC for grid-connected photovoltaic (PV) inverters with on-line parameters estimations.
6. Control of cascaded H-Bridge (CHB) multilevel converter for battery energy storage systems and design of the output filter.
7. Position estimation for linear electromagnetic actuators.
8. Modeling and Control of dual three phase machines.
9. Control of quasi-/semi-Z-source inverters for PV applications.
10. Sensorless control of squirrel-cage induction machines (IM) and reluctance synchronous motor (RSM).

For future work, the following research directions will be considered:

- Reducing the calculation burden and enhancing the accuracy of the proposed finite-position-set observers are highly required to be competitive to the conventional observers, and accordingly, further investigation will be carried out in these directions.
- Predictive speed control (PSC) schemes require high effort to tune the weighting factors of the cost function. Furthermore, enhancing the robustness of those control schemes to variations of the model parameters are extremely required. Therefore, these two problems will be investigated in the future.

- Long-horizon predictive control techniques for PMSGs/DFIGs to enhance the control performance will be investigated. Furthermore, new methods to reduce the computational burden of those long-horizon predictive control methods will be considered.
- Theoretical proof of the stability of the FCS-MPC schemes for power electronics and electrical drive is one of the interesting research points for the future work.
- Many other interesting control techniques, including continuous model predictive control, constant switching frequency FCS-MPC, full speed range sensorless DMPC, Artificial control, etc., will be some of the research focuses in the near future.

APPENDIX A

List of publications

A.1 Journal papers

1. **M. Abdelrahem**, C. Hackl, R. Kennel, "Finite Position Set-Phase Locked Loop for Sensorless Control of Direct-Driven Permanent-Magnet Synchronous Generators", *IEEE Transactions on Power Electronics*, vol. 33, no. 4, pp. 3097–3105, April 2018.

2. **M. Abdelrahem**, C. Hackl, Z. Zhang, R. Kennel, "Robust Predictive Control for Direct-Driven Surface-Mounted Permanent-Magnet Synchronous Generators Without Mechanical Sensors", *IEEE Transactions on Energy Conversion*, vol. 33, no. 1, pp. 179–189, March 2018.

3. **M. Abdelrahem**, C. Hackl, R. Kennel and J. Rodriguez, "Efficient Direct-Model Predictive Control with Discrete-Time Integral Action for PMSGs", *IEEE Transactions on Energy Conversion*, vol. 34, no. 2, pp. 1063–1072, June 2019.

4. X. Gao, **M. Abdelrahem**, C. Hackl, Z. Zhang, and R. Kennel, "Direct Predictive Speed Control with a Sliding Manifold Term for PMSM Drives", *Journal of Emerging and Selected Topics in Power Electronics*, early access, doi: 10.1109/JESTPE.2019.2923285.

5. **M. Abdelrahem**, R. Kennel, "Fault-Ride through Strategy for Permanent-Magnet Synchronous Generators in Variable-Speed Wind Turbines", *Energies*, vol. 9, no. 12, pp. 1–15, 2016.

6. **M. Abdelrahem**, R. Kennel, "Efficient Direct Model Predictive Control for Doubly-Fed Induction Generators", *Electric Power Components and Systems*, vol. 45, no. 5, pp 574–587, 2017.

7. **M. Abdelrahem**, C. Hackl, R. Kennel, "Simplified Model Predictive Current Control without Mechanical Sensors for Variable-Speed Wind Energy Conversion Systems", *Electrical Engineering*, vol. 99, no. 1, pp. 367–377, 2017.

8. **M. Abdelrahem**, C. Hackl, and R. Kennel, "Implementation and experimental investigation of a sensorless field-oriented control scheme for permanent-magnet synchronous generators", *Electrical Engineering*, vol. 100, no. 2, pp. 849–856, June 2018.

9. **M. Abdelrahem**, C. Hackl, R. Kennel, "Finite set model predictive control with on-line parameter estimation for active frond-end converters", *Electrical Engineering*, vol. 100, no. 3, pp. 1497–1507, September 2018.

10. B. Kahia, A. Bouafia, A. Chaoui, Z. Zhang, **M. Abdelrahem**, R. Kennel, "A direct power control strategy for three level neutral-point-clamped rectifier under unbalanced grid voltage", *Electric Power Systems Research*, vol. 161, pp. 103–113, August 2018.

11. M. Abdel-Salam, K. Sayed, A. Ahmed, M. Amery, **M. Swify Abdelrahem**, "Design, implementation and operation of a stand-alone residential photovoltaic system", *International Journal of Power and Energy Conversion*, vol.8, no. 1, pp. 47–67, 2017.

12. **M. Abdelrahem**, F. Hamadto, A. Garikapati, and R. Kennel, "Efficient Direct Model Predictive Control for Grid-Connected Power Converters with Improved Steady-State Performance", *Electrical Engineering*, under second round of review after receiving a decision of "Major Revision", 2019.

13. **M. Abdelrahem**, I. Hammoud, K. Morsy, and R. Kennel, "Simplified FCS-MPC with Online Finite Set Model Inductance Estimation Technique for Grid-Connected Photovoltaic Inverters", *Electrical Engineering*, under second round of review after receiving a decision of "Minor Revision", 2019.

14. Z. Zhang, Z. Cu, Y. Li, **M. Abdelrahem**, F. Gao, M. Kazmierkowski, J. Rodriguez, and R. Kennel, "Advanced Control Strategies for Back-to-Back Power Converter PMSG Wind Turbines: Vector Control, Direct Control, and Predictive Control", *IEEE Transactions on Energy Conversion*, under review, 2019.

15. **M. Abdelrahem**, C. Hackl, R. Kennel and J. Rodriguez, "Computationally Efficient Finite Position Set-Phase Locked Loop for Encoderless Control of PMSGs in Wind Turbine Applications", *IEEE Transactions on Power Electronics*, under preparation, 2019.

16. **M. Abdelrahem**, C. Hackl, R. Kennel, and J. Rodriguez, "MRAS Observers based finite-position-set for sensorless control of PMSGs/DFIGs in wind energy conversion systems", *Energies*, under preparation, 2019.

A.2 Conference papers

1. **M. Abdelrahem**, C. Hackl, and R. Kennel, "Sensorless Control of Doubly-Fed Induction Generators in Variable-Speed Wind Turbine Systems", *in Proceedings of the* 5^{th} *Interna-*

tional Conference on Clean Electrical Power (ICCEP), Taormina, Italy, 16-18 June 2015, pp. 406-413.

2. **M. Abdelrahem**, C. Hackl, and R. Kennel, "Application of Extended Kalman Filter to Parameter Estimation of Doubly-Fed Induction Generators in Variable-Speed Wind Turbine Systems", *in Proceedings of the* 5^{th} *International Conference on Clean Electrical Power (ICCEP)*, Taormina, Italy, 16-18 June 2015, pp. 226–233.

3. **M. Abdelrahem**, C. Hackl, and R. Kennel, "Model Predictive Control of Permanent Magnet Synchronous Generators in Variable-Speed Wind Turbine Systems", *in Proceedings of Power and Energy Student Summit (PESS 2016)*, Aachen, Germany, 19-20 January 2016.

4. **M. Abdelrahem**, C. Hackl, Z. Zhang, and R. Kennel, "Sensorless Control of Permanent Magnet Synchronous Generators in Variable-Speed Wind Turbine Systems", *in Proceedings of Power and Energy Student Summit (PESS 2016)*, Aachen, Germany, 19–20 January 2016, pp. 1-8.

5. Z. Zhang, C. Hackl, **M. Abdelrahem**, and R. Kennel, "Voltage Sensorless Direct Model Predictive Control of 3L-NPC Back-to-Back Power Converter PMSG Wind Turbine Systems with Fast Dynamics", *in Proceedings of Power and Energy Student Summit (PESS 2016)*, Aachen, Germany, 19-20 January 2016.

6. **M. Abdelrahem**, C. Hackl, R. Kennel, "Encoderless Model Predictive Control of Doubly-Fed Induction Generators in Variable-Speed Wind Turbine Systems", *Journal of Physics: Conference Series*, vol. 753, pp. 1-10, 2016.

7. N. Stati, **M. Abdelrahem**, M. H. Mobarak, and R. Kennel, "Finite control set-model predictive control with on-line parameter estimation for variable-speed wind energy conversion systems", *IEEE International Symposium on Industrial Electronics (INDEL)*, Banja Luka, 2016, pp. 1-6.

8. K. A. Islam, **M. Abdelrahem**, and R. Kennel, "Efficient finite control set-model predictive control for grid-connected photovoltaic inverters", *in proceedings of IEEE International Symposium on Industrial Electronics (INDEL)*, Banja Luka, 2016, pp. 1-6.

9. M. H. Mobarak, **M. Abdelrahem**, N. Stati and R. Kennel, "Model predictive control for low-voltage ride-through capability improvement of variable-speed wind energy conversion systems", *in proceedings of IEEE International Symposium on Industrial Electronics (INDEL)*, Banja Luka, 2016, pp. 1-6.

10. **M. Abdelrahem**, M. H. Mobarak, and R. Kennel, "Model Predictive Control for Low-Voltage Ride Through Capability Enhancement of DFIGs in Variable-Speed Wind Turbine Systems", *in proceedings of IEEE* 9^{th} *International Conference on Electrical and Computer Engineering (ICECE 2016)*, 20-22 December 2016, Dhaka, Bangladesh, pp. 70-73.

11. **M. Abdelrahem**, M. H. Mobarak and R. Kennel, "Realization of low-voltage ride through requirements for PMSGs in wind turbines systems using generator-rotor inertia", *in proceedings of IEEE* 9^{th} *International Conference on Electrical and Computer Engineering (ICECE 2016)*, 20-22 December 2016 Dhaka, pp. 54-57.

12. T. Lahlou, **M. Abdelrahem**, S. Valdes, and H. Herzog, "Filter design for grid-connected multilevel CHB inverter for battery energy storage systems", *International Symposium on Power Electronics, Electrical Drives, Automation and Motion (SPEEDAM)*, Anacapri, 2016, pp. 831-836.

13. T. Lahlou, D. Wittmann, **M. Abdelrahem**, and H. Herzog, "Stabilization of the DC-link voltage in a two stage cascaded H-Bridge multilevel converter for battery energy storage systems", *IEEE International Energy Conference (ENERGYCON)*, Leuven, 2016, pp. 1-6.

14. **M. Abdelrahem**, C. Hackl, R. Kennel, "A Robust Encoderless Predictive Current Control Using Novel MRAS Observer for Surface-Mounted Permanent-Magnet Synchronous Generators", *in proceedings of International Conference for Power Electronics, Intelligent Motion, Renewable Energy and Energy Management (PCIM)*, 16-18 May 2017, Nuremberg, Germany, pp. 113-120.

15. **M. Abdelrahem**, C. Hackl, R. Kennel, "Implementation of Extended Kalman Filter for PMSG Considering the Dynamics of the Mechanical System", *in proceedings of International Conference for Power Electronics, Intelligent Motion, Renewable Energy and Energy Management (PCIM)*, 16-18 May 2017, Nuremberg, Germany, pp. 1214-1221.

16. **M. Abdelrahem**, R. Kennel, "Direct-Model Predictive Control for Fault Ride-Through Capability Enhancement of DFIG", *in proceedings of International Conference for Power Electronics, Intelligent Motion, Renewable Energy and Energy Management (PCIM)*, 16-18 May 2017, Nuremberg, Germany, pp. 1917-1924.

17. **M. Abdelrahem**, Z. Zhang, R. Kennel, H. Eldeeb and C. Hackl, "Simple and robust direct-model predictive current control technique for PMSGs in variable-speed wind turbines", *in IEEE International Symposium on Predictive Control of Electrical Drives and Power Electronics (PRECEDE)*, Pilsen, 2017, pp. 1-6.

18. F. Grimm, Z. Zhang, **M. Abdelrahem**, and R. Kennel, "Computationally efficient predictive control of three-level NPC converters with DC-link voltage balancing: A priori state selection approach", *in IEEE International Symposium on Predictive Control of Electrical Drives and Power Electronics (PRECEDE)*, Pilsen, 2017, pp. 72-77.

19. **M. Abdelrahem**, C. Hackl, B. Kahia, and R. Kennel, "Predictive Direct Torque Control Strategy for Surface-Mounted Permanent-Magnet Synchronous Generators", *in Conference on sustainable energy supply and energy storage systems (NEIS)*, Hamburg, Germany, 21-22 September 2017, pp. 1-6.

20. B. Kahia, A. Bouafia, A. Chaoui, **M. Abdelrahem**, and R. Kennel, "A new Look-up Table-Direct Power Control Strategy for Three-Level NPC Rectifier Using Predictive

DPC", *in Conference on sustainable energy supply and energy storage systems (NEIS)*, Hamburg, Germany, 21-22 September 2017, pp. 1-6.

21. **M. Abdelrahem**, A. E. Hafni, R. Kennel and C. M. Hackl, "Predictive phase locked loop for sensorless control of PMSG based variable-speed wind turbines", *IEEE International Symposium on Sensorless Control for Electrical Drives (SLED)*, Catania, 2017, pp. 151-156.

22. A. Hafni, **M. Abdelrahem**, and R. Kennel, "Position estimation for linear electromagnetic actuators", *IEEE International Symposium on Sensorless Control for Electrical Drives (SLED)*, Catania, 2017, pp. 219-224.

23. H. Eldeeb, C. Hackl, **M. Abdelrahem** and A. S. Abdel-Khalik, "A unified SVPWM realization for minimizing circulating currents of dual three phase machines", *in proceedings of IEEE* 12^{th} *International Conference on Power Electronics and Drive Systems (PEDS)*, Honolulu, HI, 2017, pp. 925-931.

24. B. Kahia, A. Bouafia, **M. Abdelrahem**, Z. Zhang, and R. Kennel, "A predictive direct power control strategy for three-level npc rectifier", 5^{th} *International Conference on Electrical Engineering-Boumerdes (ICEE-B)*, Boumerdes, 2017, pp. 1-5.

25. B. Kahia, A. Bouafia, **M. Abdelrahem**, Z. Zhang, and R. Kennel, "Multi level hysteresis direct power control strategy for three-level npc rectifier", 5^{th} *International Conference on Electrical Engineering-Boumerdes (ICEE-B)*, Boumerdes, 2017, pp. 1-6.

26. B. Kahia, A. Bouafia, A. Chaoui, **M. Abdelrahem**, A. Krama, and R. Kennel, "An Improved Look-up Table-Direct Power Control strategy for Three-Level NPC Rectifier", 2^{nd} *International Conference on Applied Automation and Industrial Diagnostics (ICAAID)*, Djelfa, 2017, pp. 1-6.

27. **M. Abdelrahem**, P. Catterfeld, C. Hackl, and R. Kennel, "A Sliding-Mode-Observer for Encoderless Direct Model Predictive Control of PMSGs", *in proceedings of International Exhibition and Conference for Power Electronics, Intelligent Motion, Renewable Energy and Energy Management (PCIM)*, Nuremberg, Germany, 2018, pp. 1-8.

28. **M. Abdelrahem**, H. Eldeeb, C. Hackl, R. Kennel and J. Rodriguez, "Computationally Efficient Predictive Direct Torque Control Strategy for PMSGs without Weighting Factors", *in proceedings of International Exhibition and Conference for Power Electronics, Intelligent Motion, Renewable Energy and Energy Management (PCIM)*, Nuremberg, Germany, 2018, pp. 1-8.

29. H. Eldeeb, **M. Abdelrahem**, C. Hackl, and A. S. Abdel-Khalik, "Enhanced Electromechanical Modeling of Asymmetrical Dual Three-Phase IPMSM Drives", *IEEE* 27^{th} *International Symposium on Industrial Electronics (ISIE)*, Cairns, QLD, 2018, pp. 126-132.

30. **M. Abdelrahem**, C. Hackl, R. Kennel and J. Rodriguez, "Sensorless Predictive Speed Control of Permanent-Magnet Synchronous Generators in Wind Turbine Applications",

in proceedings of International Exhibition and Conference for Power Electronics, Intelligent Motion, Renewable Energy and Energy Management (PCIM 2019), Nuremberg, Germany, 2019, pp. 1-8.

31. **M. Abdelrahem**, M. Ismeil, M. Orabi, and R. Kennel, "Three phase Semi-Z-Source Inverter for PV Applications", *in proceedings of International Exhibition and Conference for Power Electronics, Intelligent Motion, Renewable Energy and Energy Management (PCIM 2019)*, Nuremberg, Germany, 2019, pp. 1-6.

32. M. Begh, E. Liegmann, A. Mahajan, A. Palanisamy, Y. Siwakoti, P. Karamanakos, **M. Abdelrahem**, and R. Kennel, "Design of State-Feedback Controller for a Single-Phase Grid- Connected Siwakoti-H Inverter with LCL filter", *in proceedings of International Exhibition and Conference for Power Electronics, Intelligent Motion, Renewable Energy and Energy Management (PCIM 2019)*, Nuremberg, Germany, 2019, pp. 1-8.

33. **M. Abdelrahem**, C. Hackl, M. Dal, R. Kennel and J. Rodriguez, "Efficient Finite-Position-Set MRAS Observer for Encoder-less Control of DFIGs", *in IEEE International Symposium on Predictive Control of Electrical Drives and Power Electronics (PRECEDE)*, Quanzhou, China., 2019, pp. 1-6.

34. I. Hammoud, K. Morsy, **M. Abdelrahem**, and R. Kennel, "Computationally Efficient Model Predictive Direct Power Control with Online Finite Set Model Inductance Estimation Technique for Grid-Connected Photovoltaic Inverters", *in IEEE International Symposium on Predictive Control of Electrical Drives and Power Electronics (PRECEDE)*, Quanzhou, China., 2019, pp. 1-6.

35. **M. Abdelrahem**, F. Hamadto, A. Garikapati, and R. Kennel, "Multiple-Vector Direct Model Predictive Control for Grid-Connected Power Converters with Reduced Calculation Burden", *in the* 5^{th} *IEEE International Symposium on Predictive Control of Electrical Drives and Power Electronics (PRECEDE)*, Quanzhou, China, 2019, pp. 1-6.

36. A. Farhan, **M. Abdelrahem**, A. Saleh, A. Shaltout, and R. Kennel, "High-Performance Position Sensorless control of Reluctance Synchronous Motor using High-Frequency Injection", *in the* 13^{th} *IEEE International Conference on Power Electronics and Drive Systems (PEDS)*, Toulouse, France, 2019, pp. 1-6.

37. **M. Abdelrahem**, C. Hackl, A. Farhan, and R. Kennel, "Finite-Set MRAS Observer for Encoderless Control of PMSGs in Wind Turbine Applications", *accepted for publications in proceedings of IEEE Conference on Power Electronics and Renewable Energy (CPERE)*, Aswan, Egypt, 23-25 October 2019.

38. P. Das, **M. Abdelrahem**, A. Farhan, and R. Kennel, "Predictive Direct Torque Control of Permanent Magnet Synchronous Generators (PMSGs) without Weighting Factors", *accepted for publications in proceedings of IEEE Conference on Power Electronics and Renewable Energy (CPERE)*, Aswan, Egypt, 23-25 October 2019.

39. A. Soliman, A. Farhan, **M. Abdelrahem**, and R. Kennel, "Enhanced Sensorless Model Predictive Control of Induction Motor Based on Extended Kalman Filter", *accepted for*

publications in proceedings of IEEE Conference on Power Electronics and Renewable Energy (CPERE), Aswan, Egypt, 23-25 October 2019.

40. A. Farhan, **M. Abdelrahem**, A. Saleh, A. Shaltout, and R. Kennel, "High-Precision Sensorless Predictive Control of Salient-Pole Permanent Magnet Synchronous Motor based-on Extended Kalman Filter", *submitted to* 21^{st} *International Middle East Power Systems Conference (MEPCON)*, Cairo, Egypt, December 17-19, 2019.

A.3 Awards

1. **Best paper award**, received from the 5^{th} IEEE International Symposium on Predictive Control of Electrical Drives and Power Electronics (PRECEDE 2019), Quanzhou, China, for the paper entitled "Multiple-Vector Direct Model Predictive Control for Grid-Connected Power Converters with Reduced Calculation Burden".

2. **Best student paper award**, received from the 5^{th} IEEE International Symposium on Predictive Control of Electrical Drives and Power Electronics (PRECEDE 2019), Quanzhou, China, for the paper entitled "Computationally Efficient Model Predictive Direct Power Control with Online Finite Set Model Inductance Estimation Technique for Grid-Connected Photovoltaic Inverters".

3. **Best paper award**, received from Power and Energy Student Summit (PESS 2016), Aachen, Germany, for the paper entitled "Voltage Sensorless Direct Model Predictive Control of 3L-NPC Back-to-Back Power Converter PMSG Wind Turbine Systems with Fast Dynamics".

APPENDIX B

Test benches and simulink models

B.1 Test benches of the PMSG and DFIG

B.1.1 Permanent-magnet synchronous generator (PMSG)

The permanent-magnet synchronous machine (PMSM), which is used as a generator in this work, has been manufactured by SEW-Eurodrive GmbH & Co KG. The parameters of this machine are listed in Table B.1.

Table B.1: Parameters of the PMSG.

Name	Symbol	Value
Rated power	p_{rated}	$14.5\,\mathrm{kW}$
Rated stator line-line voltage	$u_{s,rated}$	$400\,\mathrm{V}$
Rated mechanical angular speed	$\omega_{m,rated}$	$209\,\mathrm{rad/s}$
Stator resistance	R_s	$0.15\,\Omega$
Stator inductance	L_s	$3.4\,\mathrm{mH}$
Permanent-magnet flux linkage	ψ_{pm}	$0.3753\,\mathrm{Wb}$
Pole pairs	n_p	3
Inertia of the machine	Θ_{PMSM}	$0.0163\,\mathrm{kg/m^2}$
Rated torque	T_{rated}	$69\,\mathrm{N\,m}$
Peak torque	T_{peak}	$225\,\mathrm{N\,m}$

B.1.2 Reluctance synchronous machine (RSM)

This machine has been designed and manufactured in the **EMLab** (Stellenbosch University, South Africa) by Prof. M. J. Kamper. The available flux maps were generated during the design

process using the Finite Element Method (FEM) [112]. The parameters of this machine are listed in Table B.2.

Table B.2: Parameters of the RSM.

Name	Symbol	Value
Rated power	p_{rated}	$9.5\,\mathrm{kW}$
Rated stator line-line voltage	$u_{s,rated}$	$400\,\mathrm{V}$
Rated mechanical angular speed	$\omega_{m,rated}$	$157\,\mathrm{rad/s}$
Stator resistance	R_s	$0.4\,\Omega$
Stator inductances	L_s^d, L_s^q	nonlinear (see [112])
Pole pairs	n_p	2
Inertia of the machine	Θ_{PMSM}	$0.0189\,\mathrm{kg/m^2}$
Rated torque	T_{rated}	$61\,\mathrm{N\,m}$

B.1.3 Doubly-fed induction generator (DFIG)

The doubly-fed induction machine (DFIM), which is used as a generator in this work, has been manufactured by Emod Motoren GmbH. The parameters of this machine are listed in Table B.3.

Table B.3: Parameters of the DFIG.

Name	Symbol	Value
Rated power	p_{rated}	$10\,\mathrm{kW}$
Rated stator line-line voltage	$u_{s,rated}$	$400\,\mathrm{V}$
Rated rotor line-line voltage	$u_{r,rated}$	$400\,\mathrm{V}$
Rated mechanical angular speed	$\omega_{m,rated}$	$150.3\,\mathrm{rad/s}$
Synchronous speed	ω_{syn}	$157\,\mathrm{rad/s}$
Stator resistance	R_s	$0.72\,\Omega$
Rotor resistance	R_r	$0.55\,\Omega$
Stator inductance	L_s	$73.5\,\mathrm{mH}$
Rotor inductance	L_r	$86\,\mathrm{mH}$
Mutual inductance	L_m	$60\,\mathrm{mH}$
Pole pairs	n_p	2
Rated torque	T_{rated}	$66.5\,\mathrm{N\,m}$
Inertia of the machine	Θ_{PMSM}	$0.083\,\mathrm{kg/m^2}$

B.1.4 Electrical-excited synchronous machine (EESM)

The EESM has been manufactured by EME Elektromaschinenbau GmbH. The parameters of this machine are listed in Table B.4.

Table B.4: Parameters of the EESM.

Name	Symbol	Value
Rated power	p_{rated}	$10\,\mathrm{kW}$
Rated stator line-line voltage	$u_{s,rated}$	$400\,\mathrm{V}$
Rated rotor DC voltage	$u_{dc,rated}$	$14\,\mathrm{V}$
Maximum rotor DC voltage	$u_{dc,max}$	$100\,\mathrm{V}$
Rated rotor DC current	$I_{dc,rated}$	$19\,\mathrm{A}$
Rated mechanical angular speed	$\omega_{m,rated}$	$157.4\,\mathrm{rad/s}$
Stator resistance	R_s	$0.28\,\Omega$
Stator inductance	L_s	$4.8\,\mathrm{mH}$
Pole pairs	n_p	2
Rated torque	T_{rated}	$64\,\mathrm{N\,m}$
Inertia of the machine	Θ_{PMSM}	$0.273\,\mathrm{kg/m^2}$

B.1.5 Voltage source converters

The stator of the PMSG, RSM, and EESM are powered by three off-the-shelf $22\,\mathrm{kW}$ three-phase voltage source converters (22-VSCs) manufactured by SEW-Eurodrive GmbH & Co KG. The rotor of the DFIG is powered by a $15\,\mathrm{kW}$ (15)-VSC manufactured also by SEW-Eurodrive GmbH & Co KG. The three 22-VSCs are supplied by a three-phase diode rectifier energized by the standard utility grid. Accordingly, The DC-link voltage is approximately $580\,\mathrm{V}$. The 15-VSC is connected to the standard utility grid through a three-phase diode rectifier and an auto transformer to reduce its input DC voltage, and accordingly, the DC-link voltage is adjusted to $360\,\mathrm{V}$. In the DC-link of the four VSCs, a chopper circuit is connected to dissipate the power generated by the PMSG/DFIG. Furthermore, During breaking instants of the drive, the kinetic energy stored in the machine is extracted and fed back to the DC-link, which dissipated also in the chopper circuit. Thus, avoiding overcharging of the DC-link capacitors. The aforementioned VSCs are equipped with current measurements. The switching action of the inverter is governed by a built-in field programmable gate array (FPGA) which translates the switching commands sent by the dSPACE DS5101 PWM card into meaningful switching action applied to the gate signal of the insulated-gate bipolar junction transistors (IGBTs). The switching frequency range of those VSCs is between $2\,\mathrm{kHz}$ and $16\,\mathrm{kHz}$.

B.1.6 Encoders

For each machine (i.e PMSG, RSM, DFIG, and EESM), the measurement of the rotor position/speed is essential. Therefore, four ROD 486 incremental encoders manufactured by DR. JOHANNES HEIDENHAIN GmbH are employed for this purpose. Each encoder with 2048 lines is mounted on every machine.

B.1.7 Current and voltage sensors

The stator currents of the PMSG/RSM and rotor currents of the DFIG are measured by the mounted current measurement circuits in the VSCs. However, for DFIGs, it is essential to

measure the stator currents and voltages. Therefore, a three CMS3050 current sensors, which is a highly dynamic magnetoresistive current sensor, are employed to mesure the stator currents of the DFIG stator. For measuring the voltages of the DFIG stator, three DVL 500 ROHS are utilized.

B.2 Simulink models of the PMSG and DFIG

The parameters of the simulink models for wind energy conversion system with PMSG and DFIG are listed in Table B.5 and Table B.6, respectively. Furthermore, the base values for pu transformation are also given in those tables.

Table B.5: Parameters of the simulation model for PMSG-based WECS.

Name	**Nomenclature**	**Value**
Wind turbine radius	r_t	$1.65\,\mathrm{m}$
Rated wind speed	v_{wrated}	$20\,\mathrm{m/s}$
cut-in wind speed	$v_{w,cut-in}$	$4\,\mathrm{m/s}$
cut-out wind speed	$v_{w,cut-out}$	$25\,\mathrm{m/s}$
Optimal tip speed ratio	$\lambda^{\star}$	8.11
Optimal power coefficient	$c_p^{\star}$	0.48
PMSG rated power	P_{rated}	$20\,\mathrm{kW}$
PMSG rated voltage (line-line)	u_s^{rms}	$400\,\mathrm{V}$
Number of pair poles	n_p	3
Stator resistance	R_s	$0.2\,\Omega$
Stator inductance	L_s	$15\,\mathrm{mH}$
Permanent magnet flux	ψ_{pm}	$0.85\,\mathrm{V\,s}$
PMSG moment of inertia	Θ	$0.9\,\mathrm{kg/m^2}$
DC capacitor	C_{dc}	$3\,\mathrm{mF}$
DC-link voltage	u_{dc}	$700\,\mathrm{V}$
Grid line-line voltage	u_o	$400\,\mathrm{V}$
Grid normal frequency	f_e	$50\,\mathrm{Hz}$
Filter resistance	R_f	$0.16\,\Omega$
Filter inductance	L_f	$12\,\mathrm{mH}$
Sampling time	T_s	$40\,\mu\mathrm{s}$
Simulation step	T_{sim}	$1\,\mu\mathrm{s}$
Base active power	P_{base}	$20\,\mathrm{kW}$
Base reactive power	Q_{base}	20 kvar
Base current of the PMSG (peak)	$i_{s,base}$	$54\,\mathrm{A}$
Base mechanical speed	$\omega_{m,base}$	$102\,\mathrm{rad/s}$
Base DC-link voltage	$u_{dc,base}$	$700\,\mathrm{V}$
Base line–line voltage of the grid	$u_{o,base}$	$400\,\mathrm{V}$
Base current of the GSC (peak)	$i_{f,base}$	$46\,\mathrm{A}$

Table B.6: Parameters of the simulation model DFIG-based WECS.

Name	**Nomenclature**	**Value**
Wind turbine radius	r_t	$4.5\,\mathrm{m}$
Rated wind speed	v_{wrated}	$14\,\mathrm{m/s}$
cut-in wind speed	$v_{w,cut-in}$	$6\,\mathrm{m/s}$
cut-out wind speed	$v_{w,cut-out}$	$20\,\mathrm{m/s}$
Optimal tip speed ratio	$\lambda^{\star}$	8.16
Optimal power coefficient	$c_p^{\star}$	0.48
DFIG rated power	p_{nom}	$50\,\mathrm{kW}$
DFIG stator voltage (line-line)	u_s^{rms}	$400\,\mathrm{V}$
Number of pair poles	n_p	2
Stator resistance	R_s	$0.2448\,\Omega$
Rotor resistance	R_r	$0.4847\,\Omega$
Stator inductance	L_s	$80.76\,\mathrm{mH}$
Rotor inductance	L_r	$82.12\,\mathrm{mH}$
Mutual inductance	L_m	$77.2\,\mathrm{mH}$
DFIG moment of inertia	Θ	$2.8\,\mathrm{kg/m^2}$
DC capacitor	C_{dc}	$3\,\mathrm{mF}$
DC-link voltage	u_{dc}	$700\,\mathrm{V}$
Grid line-line voltage	u_o	$400\,\mathrm{V}$
Grid normal frequency	f_e	$50\,\mathrm{Hz}$
Filter resistance	R_f	$0.16\,\Omega$
Filter inductance	L_f	$12\,\mathrm{mH}$
Sampling time	T_s	$40\,\mu\mathrm{s}$
Simulation step	T_{sim}	$1\,\mu\mathrm{s}$
Base active power	P_{base}	$50\,\mathrm{kW}$
Base reactive power	Q_{base}	50 kvar
Base current of the DFIG (peak)	$i_{s,base}$	$101\,\mathrm{A}$
Base mechanical speed	$\omega_{m,base}$	$157\,\mathrm{rad/s}$
Base DC-link voltage	$u_{dc,base}$	$700\,\mathrm{V}$
Base line–line voltage of the grid	$u_{o,base}$	$400\,\mathrm{V}$
Base current of the GSC (peak)	$i_{f,base}$	$101\,\mathrm{A}$

APPENDIX C

List of symbols and abbreviations

C.1 List of Symbols

$\mathbb{N}, \mathbb{R}, \mathbb{C}$	Sets of natural, real and complex numbers
x	Real or complex scalar
$\boldsymbol{x}$	Real valued (state) vector
$\boldsymbol{u}$	Input vector
$\boldsymbol{y}$	Output vector
$\boldsymbol{X}$	Real valued matrix
$\boldsymbol{A}$	State matrix
$\boldsymbol{B}$	Input matrix
$\boldsymbol{C}$	Output matrix
$\boldsymbol{D}$	Feed-through matrix
t	Time (continuous)
k	Current Sample (discrete)
$\frac{d}{dt}$	Time derivation
T_s	Sampling time
g	Cost function
abc	Natural three-phase reference frame
$\alpha\beta$	Stationary two-phase reference frame
dq	Synchronously rotating two-phase reference frame
$\boldsymbol{T}_C$	Clarke transformation
$\boldsymbol{T}_P(\phi)$	Park transformation
p_t	Mechanical (wind turbine) power
c_p	Power coefficient of the wind turbine
ρ	Air density
r_t	Radius of the wind turbine rotor

v_w	Wind speed
β	Pitch angle
λ	Tip speed ratio
ω_m	Mechanical angular speed of the rotor
ω_r	Electrical angular speed of the rotor
$\omega_{m,ref}$	Reference of the mechanical angular speed
ω_e	Frequency of the grid voltage
ω_{syn}	Synchronous speed
ϕ_m	Mechanical position of the rotor
ϕ_r	Electrical position of the rotor
ϕ_e	Electrical position of the grid voltage
T_m	Mechanical torque
T_e	Electro-magnetic torque
T_e^*	Reference value of the electro-magnetic torque
$T_{e,max}$	Maximum allowable electro-magnetic torque
$\boldsymbol{u}_s$, $\boldsymbol{u}_r$	Stator and rotor voltage
$\boldsymbol{u}_{s,ref}$, $\boldsymbol{u}_{r,ref}$	Stator and rotor reference voltage
$\boldsymbol{u}_{s,max}$, $\boldsymbol{u}_{r,max}$	Maximum allowable value of stator and rotor voltage
$\boldsymbol{i}_s$, $\boldsymbol{i}_r$	Stator and rotor current
$\boldsymbol{i}_{s,ref}$, $\boldsymbol{i}_{r,ref}$	Stator and rotor reference current
$\boldsymbol{i}_{s,max}$, $\boldsymbol{i}_{r,max}$	Maximum allowable value of stator and rotor current
$\boldsymbol{\psi}_s$, $\boldsymbol{\psi}_r$	Stator and rotor flux
R_s, R_r	Stator and rotor resistance
L_s, L_r	Stator and rotor inductance
$L_{s\sigma}$, $L_{r\sigma}$	Stator and rotor self inductance
L_m	Mutual inductance
n_p	Number of pole pairs
ψ_{pm}	Permanent-magnet flux linkage
Θ	Rotor inertia
ν	Viscous friction coefficient
$\boldsymbol{u}_{dc}$	DC-link voltage
$\boldsymbol{u}_{dc,ref}$	Reference value of the DC-link voltage
s^{abc}	Switching state vector
$\boldsymbol{u}_f$, $\boldsymbol{u}_o$	GSC and grid voltage
$\boldsymbol{u}_{f,ref}$	Reference voltage of the GSC
$\boldsymbol{i}_f$	Current flow in the output filter
$\boldsymbol{i}_{f,ref}$	Reference value of the current flow in the output filter
$\boldsymbol{i}_{f,max}$	Maximum allowable value of the current flow in the output filter
R_f, L_f	Resistance and inductance of the output filter
γ, γ_1, λ_1, λ_2,	Weighting factors
P, Q	Active and reactive power
P_{ref}, Q_{ref}	Reference values of the active and reactive power

C.2 List of abbreviations

AC	Alternating current
DC	Direct current
PMSG	Permanent-magnet synchronous generator
DFIG	Doubly-fed induction generator
WTS	Wind turbine system
WECS	Wind energy conversion system
VC	Vector control
DBPC	Deadbeat predictive control
FCS-MPC	Finite-control-set model predictive control
FPS	Finite-position-set
DMPC	Direct Model Predictive Control
EKF	Extended Kalman filter
PDTC	Predictive direct torque control
PSC	Predictive speed control
MV-FCS-MPC	Multiple-vector finite-control-set model predictive control
LVRT	Low-voltage ride through
RES	Renewable energy source
SCIG	Squirrel-cage induction generator
WRIG	Wound rotor induction generator
WRSG	Wound rotor synchronous generator
BTB	Back-to-back
MPPT	Maximum power point tracking
FRT	Fault-ride through
VSC	Voltage source converter
2L-VSC	Two-level voltage source converter
ML-NPC	Three-level neutral point clamped
IGBT	Insulated gate bipolar transistors
TSO	Transmission system operator
DSO	Distribution system operator
PWM	Pulse width modulation
SVM	space vector modulation
FOC	Field-oriented control
VOC	Voltage-oriented control
THD	Total harmonic distortion
PC	Predictive control
MPC	Model predictive control
DSP	Digital signal processing
FPGA	Field programmable gate array
CCS-MPC	Continuous-control-set model predictive control
DTC	Direct torque control
DPC	Direct power control
DSC	Direct speed control

TSR	Tip speed ratio
PSF	Power signal feedback
P&O	Perturb and Observe
OTC	Optimal torque control
PLL	Phase-locked loop
MRAS	Model reference adaptive system
LTI	Linear time-invariant
MSC	Machine side converter
GSC	Grid side converter
RSC	Rotor side converter
RSM	Reluctance synchronous machine
EESM	Electrical-excited synchronous machine
WTE-SC	Wind turbine emulator side converter
VV	Voltage vector
FPS-PLL	Finite-position-set phase-locked loop
EMF	Electromotive force
LPF	Low-pass filter
FPS-MRAS	Finite-position-set model reference adaptive system
SBA	Search-based algorithm
CE-SBA	Computationally efficient search-based algorithm
CE-FPS-PLL	Computationally efficient finite-position-set phase-locked loop
DB	Deadbeat
MFPC	Model free predictive control
LSM	Least-square method
TDCA	Time delay control approach
MRAC	Model reference adaptive control
EDMPC	Efficient direct Model Predictive Control
DTIA	Discrete-time integral action
SSE	Steady-state error
MTPA	Maximum torque per ampere
OPP	Optimized pulse pattern
M^2PC	modulated model predictive control
2VV-DMPC	Two voltage vectors direct model predictive control
3VV-DMPC	Three voltage vectors direct model predictive control
FIS	Finite inductance set
GC	Grid code
STI	Short term interruption
BC	Braking Chopper
CB	Crowbar circuit
SDBR	Series dynamic breaking resistor

List of Figures

List of Tables

Bibliography

[1] United Nations, "What is the Paris Agreement?", available at: https://unfccc.int/process-and-meetings/the-paris-agreement/what-is-the-paris-agreement, viewed at 29 April 2019.

[2] Renewables 2018 Global Status Report, *Renewable Energy Policy Network for the* 21^{st} *Centuray (REN21)*, available at: http://www.ren21.net/gsr-2018/, viewed at 30 April 2019.

[3] Global Wind Energy Council (GWEC), Global Wind Report 2018, available at: https://gwec.net/global-wind-report-2018/, viewed at 03 May 2019.

[4] Egyptian Electricity Holding Company, annual report 2016/2017, available at: http://www.moee.gov.eg/english_new/report.aspx, viewed at 03 May 2019.

[5] H. Polinder, F. van der Pijl, G. de Vilder, and P. Tavner, "Comparison of direct-drive and geared generator concepts for wind turbines", *IEEE Transactions on Energy Conversion*, vol. 21, no. 3, pp. 725–733, Sept. 2006.

[6] H. Li and Z. Chen, "Overview of different wind generator systems and their comparisons", *IET Renewable Power Generation*, vol. 2, no. 2, pp. 123–138, June 2008.

[7] M. Liserre, R. Cardenas, M. Molinas, and J. Rodriguez, "Overview of Multi-MW Wind Turbines and Wind Parks", *IEEE Transactions on Industrial Electronics*, vol. 58, no. 4, pp. 1081–1095, April 2011.

[8] H. Polinder, et. al., "Trends in Wind Turbine Generator Systems", *IEEE Journal of Emerging and Selected Topics in Power Electronics*, vol. 1, no. 3, pp. 174–185, Sept. 2013.

[9] V. Yaramasu, B. Wu, P. C. Sen, S. Kouro, and M. Narimani, "High-power wind energy conversion systems: State-of-the-art and emerging technologies", *in Proceedings of the IEEE*, vol. 103, no. 5, pp. 740–788, May 2015.

[10] F. Blaabjerg and K. Ma, "Future on Power Electronics for Wind Turbine Systems", *IEEE Journal of Emerging and Selected Topics in Power Electronics*, vol. 1, no. 3, pp. 139-152, Sept. 2013.

[11] Z. Chen, J. M. Guerrero, and F. Blaabjerg, "A Review of the State of the Art of Power Electronics for Wind Turbines", *IEEE Transactions on Power Electronics*, vol. 24, no. 8, pp. 1859–1875, Aug. 2009.

[12] F. Blaabjerg, M. Liserre, and K. Ma, "Power Electronics Converters for Wind Turbine Systems", *IEEE Transactions on Industry Applications*, vol. 48, no. 2, pp. 708–719, March-April 2012.

[13] F. Blaabjerg and K. Ma, "Wind Energy Systems", *in Proceedings of the IEEE*, vol. 105, no. 11, pp. 2116–2131, Nov. 2017.

[14] M. Kazmierkowski and L. Malesani, "Current control techniques for three-phase voltage-source PWM converters: a survey", *IEEE Transactions on Industrial Electronics*, vol. 45, no. 5, pp. 691–703, Oct. 1998.

[15] M. Kazmierkowski, R. Krishnan, and F. Blaabjerg, Control in Power Electronics: Selected Problems, *San Diego, USA: Academic Press*, 2002.

[16] V. Yaramasu and B. Wu, Model Predictive Control of Wind Energy Conversion Systems, *Wiley-IEEE Press*, 2017.

[17] A. Timbus, M. Liserre, R. Teodorescu, P. Rodriguez, and F. Blaabjerg, "Evaluation of Current Controllers for Distributed Power Generation Systems", *IEEE Transactions on Power Electronics*, vol. 24, no. 3, pp. 654–664, March 2009.

[18] M. Morari and J. H. Lee, "Model predictive control: past, present and future", *Computers and Chemical Engineering*, vol. 23, no. 4, pp. 667–682, 1999.

[19] R. Kennel, " Prädiktives Führungsverfahren für Stromrichter", PhD thesis, University of Kaiserslautern, 1984.

[20] P. Cortes, M. Kazmierkowski, R. Kennel, D. Quevedo, J. Rodriguez, "Predictive Control in Power Electronics and Drives", *IEEE Trans. on Industrial Electronics*, vol. 55, no. 12, pp. 4312–4324, Dec. 2008.

[21] A. Linder, R. Kanchan, R. Kennel, and P. Stolze, Model-Based Predictive Control of Electric Drives, *Göttingen, Germany: Cuvillier Verlag*, 2010.

[22] S. Kouro, P. Cortes, R. Vargas, U. Ammann, J. Rodriguez, "Model Predictive Control–A Simple and Powerful Method to Control Power Converters", *IEEE Trans. on Industrial Electronics*, vol. 56, no. 6, pp. 1826–1838, June 2009.

[23] J. Rodriguez and P. Cortes, Predictive Control of Power Converters and Electrical Drives, 1^{st} *edition New York: Wiley-IEEE Press*, 2012.

[24] S. Vazquez, J. Leon, L. Franquelo, J. Rodriguez, H. Young, A. Marquez, P. Zanchetta, "Model Predictive Control: A Review of Its Applications in Power Electronics", *IEEE Industrial Electronics Magazine*, vol. 8, no. 1, pp. 16–31, March 2014.

[25] T. Burton, D. Sharpe, N. Jenkins, and E. Bossanyi, *Wind Energy Handbook*, Wiley, 2001.

[26] T. Ackermann, *Wind Power in Power System*, Wiley, 2005

[27] B. Wu, Y. Lang, N. Zargari, and S. Kouro, *Power conversion and control of wind energy systems*, Wiley-IEEE Press, 2011.

[28] J. Yuz and G. Goodwin, On sampled-data models for nonlinear systems, *IEEE Transaction on Automatic Control*, vol. 50, no. 10, pp. 1477–1489, 2005.

[29] C. Silva and J. Yuz, On sampled-data models for model predictive control, *in Proc. IEEE Ind. ELectron. Soc. AnnuaL Con (IECON)*, pp. 2966–2971, 2010.

[30] P. Vaclavek and P. Blaha, PMSM model discretization for Model Predictive Control algorithms, *International Symposium on System Integration*, pp. 13–18, 2013.

[31] C. Dirscherl, C. Hackl, and K. Schechner, “Modellierung und Regelung von modernen Windkraftanlagen: Eine Einführung”, pp. 1540–1614 (Chapter 24) in D. Schröder (Ed.), *Elektrische Antriebe – Regelung von Antriebssystemen*, Springer-Verlag, 2015.

[32] C.M. Hackl, “Non-identifier based adaptive control in mechatronics: Theory and application”, Springer International Publishing, 2017.

[33] S. Heier, “Grid Integration of Wind Energy Conversion Systems”, John Wiley & Sons Ltd, 1998.

[34] M. Abdelrahem, C. Hackl, and R. Kennel, “Model Predictive Control of Permanent Magnet Synchronous Generators in Variable-Speed Wind Turbine Systems”, *in Proceedings of Power and Energy Student Summit (PESS 2016)*, Aachen, Germany, 19-20 January 2016.

[35] G. Abad, J. López, M. Rodríguez, L. Marroyo, G. Iwanski, “ Doubly Fed Induction Machine: Modeling and Control for Wind Energy Generation Applications”, Wiley-IEEE Press, 2011.

[36] R. Pena, J. Clare, and G. Asher, Doubly fed induction generator using back-to-back PWM converters and its application to variable-speed wind-energy generation, *IEE Proceedings on Electric Power Applications*, vol. 143, no. 3, pp. 231–241, 1996.

[37] C. Hackl, M. Kamper, J. Kullick, and J. Mitchel, “Current control of reluctance synchronous machines with online adjustment of the controller parameters”, *in Proceedings of the 2016 IEEE International Symposium on Industrial Electronics (ISIE 2016)*, Santa Clara, USA, p. 153–160, 2016.

[38] W. Leonhard, “Field-orientation for controlling AC machines-principle and application”, *Third International Conference on Power Electronics and Variable-Speed Drives*, London, UK, 1988, pp. 277–282.

[39] W. Leonhard, Control of Electrical Drives, New York, Springer, 1997.

[40] M. Kazmierkowski, L. Franquelo, J. Rodriguez, M. Perez, and J. Leon, “High-Performance Motor Drives”, *IEEE Industrial Electronics Magazine*, vol. 5, no. 3, pp. 6–26, Sept. 2011.

[41] M. Chinchilla, S. Arnaltes, and J. C. Burgos, “Control of permanent magnet generators applied to variable-speed wind-energy systems connected to the grid”, *IEEE Transactions on Energy Conversion*, Vol. 21, No. 1, pp. 130–135, March 2006.

[42] S. Li, T. A. Haskew, R. P. Swatloski, and W. Gathings, “Optimal and Direct-Current Vector Control of Direct-Driven PMSG Wind Turbines”, *IEEE Transactions on Power Electronics*, vol. 27, no. 5, pp. 2325–2337, May 2012.

[43] H. Le-Huy, K. Slimani, and P. Viarouge, “Analysis and implementation of a real-time predictive current controller for permanent-magnet synchronous servo drives”, *IEEE Transactions on Industrial Electronics*, vol. 41, no. 1, pp. 110–117, Feb. 1994.

[44] Hyung-Tae Moon, Hyun-Soo Kim and Myung-Joong Youn, "A discrete-time predictive current control for PMSM", *IEEE Transactions on Power Electronics*, vol. 18, no. 1, pp. 464–472, Jan 2003.

[45] F. Morel, X. F. Lin-shi, and J. M. Retif, "A comparative study of predictive current control schemes for a permanent magnet synchronous machine drive", *IEEE Transactions on Industrial Electronics*, vol. 56, no. 7, pp. 2715—2728, Jul. 2009.

[46] M. Abdelrahem, C. Hackl, R. Kennel, "Simplified Model Predictive Current Control without Mechanical Sensors for Variable-Speed Wind Energy Conversion Systems", *Electrical Engineering*, vol. 99, no. 1, pp. 367–377, 2017.

[47] M. Abdelrahem, C. Hackl, Z. Zhang, R. Kennel, "Robust Predictive Control for Direct-Driven Surface-Mounted Permanent-Magnet Synchronous Generators Without Mechanical Sensors", *IEEE Transactions on Energy Conversion*, vol. 33, no. 1, pp. 179–189, March 2018.

[48] M. Abdelrahem, C. Hackl, R. Kennel, "Encoderless Model Predictive Control of Doubly-Fed Induction Generators in Variable-Speed Wind Turbine Systems", *in Proceedings of The Science of Making Torque from Wind (TORQUE 2016) Conference*, Munich, 5–7 October 2016.

[49] M. Abdelrahem, R. Kennel, "Efficient Direct Model Predictive Control for Doubly-Fed Induction Generators", *Electric Power Components and Systems*, vol. 45, no. 5, pp 574–587, 2017.

[50] M. Abdelrahem, C. Hackl, Z. Zhang, and R. Kennel, "Sensorless Control of Permanent Magnet Synchronous Generators in Variable-Speed Wind Turbine Systems", *in Proceedings of Power and Energy Student Summit (PESS 2016)*, Aachen, Germany, 19–20 January 2016, pp. 1–8.

[51] M. Abdelrahem, C. Hackl, R. Kennel, "Implementation of Extended Kalman Filter for PMSG Considering the Dynamics of the Mechanical System", *in proceedings of International Conference for Power Electronics, Intelligent Motion, Renewable Energy and Energy Management (PCIM)*, 16-18 May 2017, Nuremberg, Germany, pp. 1214–1221.

[52] M. Abdelrahem, P. Catterfeld, C. Hackl, and R. Kennel, "A Sliding-Mode-Observer for Encoderless Direct Model Predictive Control of PMSGs", *in proceedings of International Exhibition and Conference for Power Electronics, Intelligent Motion, Renewable Energy and Energy Management (PCIM)*, Nuremberg, Germany, 2018, pp. 1–8.

[53] Y. Zhao, C. Wei, Z. Zhang, and W. Qiao, "A Review on Position/Speed Sensorless Control for Permanent-Magnet Synchronous Machine-Based Wind Energy Conversion Systems", *IEEE Journal of Emerging and Selected Topics in Power Electronics*, vol. 1, no. 4, pp. 203–216, Dec. 2013.

[54] R. Kumar, S. Das, P. Syam, and A. Chattopadhyay, "Review on model reference adaptive system for sensorless vector control of induction motor drives", *IET Electric Power Applications*, vol. 9, no. 7, pp. 496–511, 8 2015.

[55] C. Schauder, "Adaptive speed identification for vector control of induction motors without rotational transducers", *IEEE Trans. on Industrial Applications*, vol. 28, no. 5, pp. 1054–1061, Sep./Oct. 1992.

[56] G. D. Andreescu, "Position and Speed Sensorless Control of PMSM Drives Based on Adaptive Observer", *in proceedings of EPE'99*, Lausanne, pp. 1–10.

[57] R. Cardenas, R. Pena, S. Alepuz, and G. Asher, "Overview of Control Systems for the Operation of DFIGs in Wind Energy Applications", *IEEE Trans. on Industrial Electronics*, vol. 60, no. 7, pp. 2776–2798, July 2013.

[58] R. Cardenas, R. Pena, J. Clare, G. Asher and J. Proboste, "MRAS Observers for Sensorless Control of Doubly-Fed Induction Generators", *IEEE Trans. on Power Electronics*, vol. 23, no. 3, pp. 1075–1084, May 2008.

[59] M. Abdelrahem, C. Hackl, and R. Kennel, "Sensorless Control of Doubly-Fed Induction Generators in Variable-Speed Wind Turbine Systems", *in Proceedings of the* 5^{th} *International Conference on Clean Electrical Power (ICCEP)*, Taormina, Italy, 16-18 June 2015, pp. 406–413.

[60] M. Abdelrahem, C. Hackl, R. Kennel, "Implementation and experimental investigation of a sensorless field-oriented control scheme for permanent-magnet synchronous generators", *Electrical Engineering*, vol. 100, no. 2, pp. 849–856, June 2018.

[61] M. Nasir Uddin and N. Patel, "Maximum Power Point Tracking Control of IPMSG Incorporating Loss Minimization and Speed Sensorless Schemes for Wind Energy System", *IEEE Trans. on Industry Applications*, vol. 52, no. 2, pp. 1902–1912, March-April 2016.

[62] M. Elbuluk, L. Tong, and I. Husain, "Neural-network-based model reference adaptive systems for high-performance motor drives and motion controls", *IEEE Trans. on Industry Applications*, vol. 38, no. 3, pp. 879–886, May-June 2002.

[63] M. Cirrincione and M. Pucci, "An MRAS-based sensorless high-performance induction motor drive with a predictive adaptive model", *IEEE Trans. on Industrial Electronics*, vol. 52, no. 2, pp. 532–551, April 2005.

[64] S. Maiti, V. Verma, C. Chakraborty and Y. Hori, "An Adaptive Speed Sensorless Induction Motor Drive With Artificial Neural Network for Stability Enhancement", *IEEE Trans. on Industrial Informatics*, vol. 8, no. 4, pp. 757–766, Nov. 2012.

[65] S. M. Gadoue, D. Giaouris, and J. W. Finch, "A new fuzzy logic based adaptation mechanism for MRAS sensorless vector control induction motor drives", *in Proceedings of IET Conference on Power Electronics, Machines and Drives (PEMD'2008)*, 2008, pp. 179–183.

[66] A. Samat, D. Ishak, S. Iqbal and A. Tajudin, "Implementation of Sugeno FIS in model reference adaptive system adaptation scheme for speed sensorless control of PMSM", *IEEE International Conference on Control System, Computing and Engineering (ICCSCE)*, Batu Ferringhi, 2014, pp. 652–657.

[67] M. Jain, M. Singh, A. Chandra, and S. S. Williamson, "Sensorless control of permanent magnet synchronous motor using ANFIS based MRAS", *IEEE International Electric Machines & Drives Conference (IEMDC)*, Niagara Falls, ON, 2011, pp. 599–606.

[68] S. M. Gadoue, D. Giaouris and J. W. Finch, "MRAS Sensorless Vector Control of an Induction Motor Using New Sliding-Mode and Fuzzy-Logic Adaptation Mechanisms", *IEEE Trans. on Energy Conversion*, vol. 25, no. 2, pp. 394–402, June 2010.

[69] M. Comanescu and L. Xu, "Sliding-mode MRAS speed estimators for sensorless vector control of induction Machine", *IEEE Trans. on Industrial Electronics*, vol. 53, no. 1, pp. 146–153, Feb. 2006.

[70] H. B. Azza, N. Zaidi, M. Jemli, and M. Boussak, "Development and Experimental Evaluation of a Sensorless Speed Control of SPIM Using Adaptive Sliding Mode-MRAS Strategy", *IEEE Journal of Emerging and Selected Topics in Power Electronics*, vol. 2, no. 2, pp. 319–328, June 2014.

[71] J. Yan, H. Lin, Y. Feng, X. Guo, Y. Huang, and Z. Q. Zhu, "Improved sliding mode model reference adaptive system speed observer for fuzzy control of direct-drive permanent magnet synchronous generator wind power generation system", *IET Renewable Power Generation*, vol. 7, no. 1, pp. 28–35, February 2013.

[72] S. Golestan, M. Monfared, F. D. Freijedo, and J. M. Guerrero, "Design and tuning of a modified power-based PLL for single-phase grid connected power conditioning systems", *IEEE Trans. Power Electron.*, vol. 27, no. 8, pp. 3639–3650, Aug. 2012.

[73] Y. Park, S. K. Sul, W. C. Kim, and H. Y. Lee, "Phase-Locked Loop Based on an Observer for Grid Synchronization", *IEEE Transactions on Industry Applications*, vol. 50, no. 2, pp. 1256–1265, March-April 2014.

[74] T. V. Tran, T. W. Chun, H. H. Lee, H. G. Kim, and E. C. Nho, "PLL-based seamless transfer control between grid-connected and islanding modes in grid-connected inverters", *IEEE Trans. Power Electron.*, vol. 29, no. 10, pp. 5218–5228, Oct. 2014.

[75] S. Golestan, J. M. Guerrero, and J. C. Vasquez, "Three-Phase PLLs: A Review of Recent Advances", *IEEE Transactions on Power Electronics*, vol. 32, no. 3, pp. 1894–1907, March 2017.

[76] M. Comanescu and L. Xu, "An improved flux observer based on PLL frequency estimator for sensorless vector control of induction motors", *IEEE Transactions on Industrial Electronics*, vol. 53, no. 1, pp. 50–56, Feb. 2006.

[77] L. Sun, Z. Wu, F. Xiao, X. Cai, and S. Wang, "Design of the PLL for the speed sensorless stator-flux-oriented control of induction motors", *18th International Conference on Electrical Machines and Systems (ICEMS)*, Pattaya, 2015, pp. 1913–1918.

[78] Y. Beddiaf, L. Chrifi-Alaoui, F. Zidani, and S. Drid, "Modified speed sensorless indirect field-oriented control of induction motor using PLL", *15th International Conference on Sciences and Techniques of Automatic Control and Computer Engineering (STA)*, Hammamet, 2014, pp. 135–141.

[79] S. Shinnaka, "A New Speed-Varying Ellipse Voltage Injection Method for Sensorless Drive of Permanent-Magnet Synchronous Motors With Pole Saliency–New PLL Method Using High-Frequency Current Component Multiplied Signal", *IEEE Transactions on Industry Applications*, vol. 44, no. 3, pp. 777–788, May-june 2008.

[80] Z. Chen, X. Cai, R. Kennel, and F. Wang, "Enhanced sensorless control of SPMSM based on Stationary Reference Frame High-Frequency Pulsating Signal injection", *IEEE 8th International Power Electronics and Motion Control Conference (IPEMC-ECCE Asia)*, Hefei, 2016, pp. 885–890.

[81] Z. Chen, J. Gao, F. Wang, Z. Ma, Z. Zhang, and R. Kennel, "Sensorless Control for SPMSM With Concentrated Windings Using Multisignal Injection Method", *IEEE Transactions on Industrial Electronics*, vol. 61, no. 12, pp. 6624–6634, Dec. 2014.

[82] G. Wang, Z. Li, G. Zhang, Y. Yu, and D. Xu, "Quadrature PLL-Based High-Order Sliding-Mode Observer for IPMSM Sensorless Control With Online MTPA Control Strategy", *IEEE Transactions on Energy Conversion*, vol. 28, no. 1, pp. 214–224, March 2013.

[83] G. Wang, H. Zhan, G. Zhang, X. Gui, and D. Xu, "Adaptive Compensation Method of Position Estimation Harmonic Error for EMF-Based Observer in Sensorless IPMSM Drives", *IEEE Transactions on Power Electronics*, vol. 29, no. 6, pp. 3055–3064, June 2014.

[84] X. Song, J. Fang, B. Han, and S. Zheng, "Adaptive Compensation Method for High-Speed Surface PMSM Sensorless Drives of EMF-Based Position Estimation Error", *IEEE Transactions on Power Electronics*, vol. 31, no. 2, pp. 1438–1449, Feb. 2016.

[85] G. Zhang, G. Wang, D. Xu, and N. Zhao, "ADALINE-Network-Based PLL for Position Sensorless Interior Permanent Magnet Synchronous Motor Drives", *IEEE Transactions on Power Electronics*, vol. 31, no. 2, pp. 1450–1460, Feb. 2016.

[86] S. Bolognani, S. Calligaro, and R. Petrella, "Design Issues and Estimation Errors Analysis of Back-EMF-Based Position and Speed Observer for SPM Synchronous Motors", *IEEE Journal of Emerging and Selected Topics in Power Electronics*, vol. 2, no. 2, pp. 159–170, June 2014.

[87] L. Tong and et al., "An SRF-PLL-Based Sensorless Vector Control Using the Predictive Deadbeat Algorithm for the Direct-Driven Permanent Magnet Synchronous Generator", *IEEE Transactions on Power Electronics*, vol. 29, no. 6, pp. 2837–2849, June 2014.

[88] M. Preindl and E. Schaltz, "Sensorless Model Predictive Direct Current Control Using Novel Second-Order PLL Observer for PMSM Drive Systems", *IEEE Transactions on Industrial Electronics*, vol. 58, no. 9, pp. 4087–4095, Sept. 2011.

[89] V. Kaura, and V. Blasko, "Operation of a phase locked loop system under distorted utility conditions", *IEEE Trans. on Industry Applications*, vol. 33, no. 1, pp. 58–63, Jan/Feb 1997.

[90] M. Abdelrahem, C. Hackl, R. Kennel, "Finite Position Set-Phase Locked Loop for Sensorless Control of Direct-Driven Permanent-Magnet Synchronous Generators", *IEEE Transactions on Power Electronics*, *IEEE Transactions on Power Electronics*, vol. 33, no. 4, pp. 3097–3105, April 2018.

[91] Y. B. Zbede, S. M. Gadoue, and D. J. Atkinson, "Model Predictive MRAS Estimator for Sensorless Induction Motor Drives", *IEEE Trans. on Industrial Electronics*, vol. 63, no. 6, pp. 3511–3521, June 2016.

[92] M. Abdelrahem, C. Hackl, A. Farhan, and R. Kennel, "Finite-Set MRAS Observer for Encoderless Control of PMSGs in Wind Turbine Applications", *accepted for publication in proceedings of IEEE Conference on Power Electronics and Renewable Energy (CPERE)*, Aswan, Egypt, 23-25 October 2019.

[93] M. Abdelrahem, C. Hackl, R. Kennel, and J. Rodriguez, "MRAS Observers based finite-position-set for sensorless control of PMSGs/DFIGs in wind energy conversion systems", *Energies*, under preparation, 2019.

[94] T. Shi, Z. Wang and C. Xia, "Speed Measurement Error Suppression for PMSM Control System Using Self-Adaption Kalman Observer", *IEEE Trans. on Industrial Electronics*, vol. 62, no. 5, pp. 2753–2763, May 2015.

[95] M. Abdelrahem, C. Hackl, R. Kennel, "A Robust Encoderless Predictive Current Control Using Novel MRAS Observer for Surface-Mounted Permanent-Magnet Synchronous Generators", *in proceedings of International Conference for Power Electronics, Intelligent Motion, Renewable Energy and Energy Management (PCIM)*, 16-18 May 2017, Nuremberg, Germany, pp. 113–120.

[96] M. Abdelrahem, A. E. Hafni, R. Kennel and C. M. Hackl, "Predictive phase locked loop for sensorless control of PMSG based variable-speed wind turbines", *IEEE International Symposium on Sensorless Control for Electrical Drives (SLED)*, Catania, 2017, pp. 151–156.

[97] M. Abdelrahem, C. Hackl, M. Dal, R. Kennel and J. Rodriguez, "Efficient Finite-Position-Set MRAS Observer for Encoder-less Control of DFIGs", *in IEEE International Symposium on Predictive Control of Electrical Drives and Power Electronics (PRECEDE)*, Quanzhou, China., 2019, pp. 1–6.

[98] M. Abdelrahem, C. Hackl, R. Kennel and J. Rodriguez, "Computationally Efficient Finite Position Set-Phase Locked Loop for Encoderless Control of PMSGs in Wind Turbine Applications", *IEEE Transactions on Power Electronics*, under preparation, 2019.

[99] J. F. Stumper, V. Hagenmeyer, S. Kuehl, and R. Kennel, "Deadbeat Control for Electrical Drives: A Robust and Performant Design Based on Differential Flatness", *IEEE Transactions on Power Electronics*, vol. 30, no. 8, pp. 4585–4596, Aug. 2015.

[100] Y. Mohamed and E. El-Saadany, "Robust High Bandwidth Discrete-Time Predictive Current Control with Predictive Internal Model-A Unified Approach for Voltage-Source PWM Converters", *IEEE Transactions on Power Electronics*, vol. 23, no. 1, pp. 126–136, Jan. 2008.

[101] P. Cortes, J. Rodriguez, C. Silva and A. Flores, "Delay Compensation in Model Predictive Current Control of a Three-Phase Inverter", *IEEE Transactions on Industrial Electronics*, vol. 59, no. 2, pp. 1323–1325, Feb. 2012.

[102] V. Léchappé and et al., "Delay Estimation and Predictive Control of Uncertain Systems With Input Delay: Application to a DC Motor", *IEEE Transactions on Industrial Electronics*, vol. 63, no. 9, pp. 5849–5857, Sept. 2016.

[103] X. Zhang, B. Hou, and Y. Mei, "Deadbeat Predictive Current Control of Permanent-Magnet Synchronous Motors with Stator Current and Disturbance Observer", *IEEE Transactions on Power Electronics*, vol. 32, no. 5, pp. 3818–3834, May 2017.

[104] M. Abdel-Salam, A. Ahmed, and M. Abdel-Sater, "Harmonic Mitigation, Maximum Power Point Tracking and Dynamic Performance of Variable Speed Grid Connected Wind Turbine", *Journal of Electric Power Component and Systems*, Vol. 39, pp. 176–190, 2011.

[105] M. Habibullah, D.D–C. Lu, "A Speed-Sensorless FS-PTC of Induction Motors Using Extended Kalman Filters", *IEEE Transactions on Industrial Electronics*, Vol. 62, No. 11, pp. 6765–6778, Nov. 2015.

[106] L. Idkhajine, E. Monmasson, and A. Maalouf, "Fully FPGA-Based Sensorless Control for Synchronous AC Drive Using an Extended Kalman Filter", *IEEE Transactions on Industrial Electronics*, vol. 59, no. 10, pp. 3908–3918, Oct. 2012.

[107] N. K. Quang, N. T. Hieu, and Q. P. Ha, "FPGA-Based Sensorless PMSM Speed Control Using Reduced-Order Extended Kalman Filters" *IEEE Transactions on Industrial Electronics*, vol. 61, no. 12, pp. 6574–6582, Dec. 2014

[108] G. Rigatos, P. Siano and N. Zervos, "Sensorless Control of Distributed Power Generators With the Derivative-Free Nonlinear Kalman Filter", *IEEE Transactions on Industrial Electronics*, vol. 61, no. 11, pp. 6369-6382, Nov. 2014.

[109] M. Benadja and A. Chandra, "Adaptive Sensorless Control of PMSGs-Based Offshore Wind Farm and VSC-HVdc Stations", *IEEE Journal of Emerging and Selected Topics in Power Electronics*, vol. 3, no. 4, pp. 918–931, Dec. 2015.

[110] Q. Huang and Z. Pan, "Sensorless control of permanent magnet synchronous generator in direct-drive wind power system", *in proceedings of International Conference on Electrical Machines and Systems (ICEMS)*, Beijing, 2011, pp. 1–5.

[111] Kyeong-Hwa Kim and Myung-Joong Youn, "A simple and robust digital current control technique of a PM synchronous motor using time delay control approach", *IEEE Transactions on Power Electronics*, vol. 16, no. 1, pp. 72–82, Jan 2001.

[112] H. Eldeeb, C.M. Hackl, L. Horlbeck, and J. Kullick, "A unified theory for optimal feed-forward torque control of anisotropic synchronous machines", *International Journal of Control*, vol. 91, no. 10, pp. 2273–2302, 2018.

[113] S. Bolognani, L. Tubiana, and M. Zigliotto, "Extended Kalman filter tuning in sensorless PMSM drives", *IEEE Transactions on Industry Applications*, vol. 39, no. 6, pp. 1741–1747, November 2003.

[114] K. Reif, S. Gunther, E. Yaz and R. Unbehauen, "Stochastic stability of the discrete-time extended Kalman filter", *IEEE Transactions on Automatic Control*, vol. 44, no. 4, pp. 714–728, Apr 1999.

[115] K. Reif, S. Gunther, E. Yaz and R. Unbehauen, "Stochastic stability of the continuous-time extended Kalman filter", *IEE Proceedings - Control Theory and Applications*, vol. 147, no. 1, pp. 45–52, Jan 2000

[116] C. De Wit, A. Youssef, J. Barbot, P. Martin, F. Malrait, "Observability conditions of induction motors at low frequencies", *Proceedings of the* 39^{th} *IEEE Conference on Decision and Control*, Vol. 3, pp. 2044–2049, 2000.

[117] S. Vazquez, J. Rodriguez, M. Rivera, L. G. Franquelo, and M. Norambuena, "Model Predictive Control for Power Converters and Drives: Advances and Trends", *IEEE Transactions on Industrial Electronics*, vol. 64, no. 2, pp. 935–947, Feb. 2017.

[118] A. Calle-Prado, S. Alepuz, J. Bordonau, P. Cortes, and J. Rodriguez, "Predictive Control of a Back-to-Back NPC Converter-Based Wind Power System", *IEEE Transactions on Industrial Electronics*, vol. 63, no. 7, pp. 4615–4627, July 2016.

[119] K. A. Islam, M. Abdelrahem, and R. Kennel, "Efficient finite control set-model predictive control for grid-connected photovoltaic inverters", *in proceedings of IEEE International Symposium on Industrial Electronics (INDEL)*, Banja Luka, 2016, pp. 1–6.

[120] H. Young, M. Perez, and J. Rodriguez, "Analysis of Finite-Control-Set Model Predictive Current Control With Model Parameter Mismatch in a Three-Phase Inverter", *IEEE Transactions on Industrial Electronics*, vol. 63, no. 5, pp. 3100–3107, May 2016.

[121] C. Lin, T. Liu, J. Yu, L. Fu, and C. Hsiao, "Model free predictive current control for interior permanent-magnet synchronous motor drives based on current difference detection technique", *IEEE Transactions on Industrial Electronics*, vol. 61, no. 2, pp. 667–681, Feb. 2014.

[122] C. Lin, J. Yu, Y. Lai, and H. Yu, "Improved model-free predictive current control for synchronous reluctance motor drives", *IEEE Transactions on Industrial Electronics*, vol. 63, no. 6, pp. 3942–3953, Jun. 2016.

[123] M. Siami, D. A. Khaburi, A. Abbaszadeh, and J. Rodriguez, "Robustness improvement of predictive current control using prediction error correction for permanent magnet synchronous machines", *IEEE Transactions on Industrial Electronics*, vol. 63, no. 6, pp. 3458–3466, Jun. 2016.

[124] M. Siami, D. A. Khaburi and J. Rodriguez, "Torque Ripple Reduction of Predictive Torque Control for PMSM Drives With Parameter Mismatch", *IEEE Transactions on Power Electronics*, vol. 32, no. 9, pp. 7160–7168, Sept. 2017.

[125] S. Kwak, U. Moon, and J. Park, "Predictive-Control-Based Direct Power Control With an Adaptive Parameter Identification Technique for Improved AFE Performance", *IEEE Transactions on Power Electronics*, vol. 29, no. 11, pp. 6178–6187, Nov. 2014.

[126] M. Abdelrahem, C. Hackl, R. Kennel, “Finite set model predictive control with on-line parameter estimation for active frond-end converters”, *Electrical Engineering*, vol. 100, no. 3, pp. 1497–1507, September 2018.

[127] N. Stati, M. Abdelrahem, M. H. Mobarak, and R. Kennel, “Finite control set-model predictive control with on-line parameter estimation for variable-speed wind energy conversion systems”, *IEEE International Symposium on Industrial Electronics (INDEL)*, Banja Luka, 2016, pp. 1–6.

[128] T. Boileau, N. Leboeuf, B. Nahid-Mobarakeh and F. Meibody-Tabar, “Online Identification of PMSM Parameters: Parameter Identifiability and Estimator Comparative Study”, *IEEE Transactions on Industry Applications*, vol. 47, no. 4, pp. 1944–1957, July-Aug. 2011.

[129] H. Kim, M. Youn, K. Cho and H.-S. Kim, “Nonlinearity estimation and compensation of PWM VSI for PMSM under resistance and flux linkage uncertainty”, *IEEE Transactions on Control Systems Technology*, vol. 14, no. 4, pp. 589–601, July 2006.

[130] K. Liu, Q. Zhang, J. Chen, Z. Q. Zhu and J. Zhang, “Online Multiparameter Estimation of Nonsalient-Pole PM Synchronous Machines With Temperature Variation Tracking”, *IEEE Transactions on Industrial Electronics*, vol. 58, no. 5, pp. 1776–1788, May 2011.

[131] Z. H. Liu, H. L. Wei, Q. C. Zhong, K. Liu, X. S. Xiao, and L. H. Wu, “Parameter Estimation for VSI-Fed PMSM Based on a Dynamic PSO With Learning Strategies”, *IEEE Transactions on Power Electronics*, vol. 32, no. 4, pp. 3154–3165, April 2017.

[132] Z. Chen, J. Qiu, and M. Jin, “Adaptive finite-control-set model predictive current control for IPMSM drives with inductance variation”, *IET Electric Power Applications*, vol. 11, no. 5, pp. 874–884, may 2017.

[133] O. Sandre-Hernandez, R. Morales-Caporal, J. Rangel-Magdaleno, H. Peregrina-Barreto, and J. N. ernandez-Perez, “Parameter Identification of PMSMs Using Experimental Measurements and a PSO Algorithm”, *IEEE Transactions on Instrumentation and Measurement*, vol. 64, no. 8, pp. 2146–2154, Aug. 2015.

[134] C. Xia, M. Wang, Z. Song, and T. Liu, “Robust Model Predictive Current Control of Three-Phase Voltage Source PWM Rectifier With Online Disturbance Observation”, *IEEE Transactions on Industrial Informatics*, vol. 8, no. 3, pp. 459–471, Aug. 2012.

[135] B. Wang, X. Chen, Y. Yu, G. Wang and D. Xu, "Robust Predictive Current Control With Online Disturbance Estimation for Induction Machine Drives," *in IEEE Transactions on Power Electronics*, vol. 32, no. 6, pp. 4663–4674, June 2017.

[136] Kyeong-Hwa Kim and Myung-Joong Youn, “A simple and robust digital current control technique of a PM synchronous motor using time delay control approach”, *IEEE Transactions on Power Electronics*, vol. 16, no. 1, pp. 72–82, Jan 2001.

[137] M. Abdelrahem, Z. Zhang, R. Kennel, H. Eldeeb and C. Hackl, “Simple and robust direct-model predictive current control technique for PMSGs in variable-speed wind turbines”, *in IEEE International Symposium on Predictive Control of Electrical Drives and Power Electronics (PRECEDE)*, Pilsen, 2017, pp. 1–6.

[138] K. h. Kim, "Model reference adaptive control-based adaptive current control scheme of a PM synchronous motor with an improved servo performance", *IET Electric Power Applications*, vol. 3, no. 1, pp. 8–18, January 2009.

[139] Y. Mohamed and E. El-Saadany, "Robust High Bandwidth Discrete-Time Predictive Current Control with Predictive Internal Model-A Unified Approach for Voltage-Source PWM Converters", *IEEE Transactions on Power Electronics*, vol. 23, no. 1, pp. 126–136, Jan. 2008.

[140] X. Zhang, L. Zhang, and Y. Zhang, "Model Predictive Current Control for PMSM Drives with Parameter Robustness Improvement", *in IEEE Transactions on Power Electronics*, vol. 34, no. 2, pp. 1645–1657, Feb. 2019.

[141] J. Wang, F. Wang, G. Wang, S. Li and L. Yu, "Generalized Proportional Integral Observer-Based Robust Finite Control Set Predictive Current Control for Induction Motor Systems with Time-Varying Disturbances", *in IEEE Transactions on Industrial Informatics*, vol. 14, no. 9, pp. 4159–4168, Sept. 2018

[142] J. Wang, F. Wang, Z. Zhang, S. Li, and J. Rodriguez, "Design and Implementation of Disturbance Compensation-Based Enhanced Robust Finite Control Set Predictive Torque Control for Induction Motor Systems", *IEEE Transactions on Industrial Informatics*, vol. 13, no. 5, pp. 2645–2656, Oct. 2017.

[143] L. Yan, M. Dou, H. t. Zhang, Z. Hua and J. Yang, "Robustness Improvement of FCS-MPTC for Induction Machine Drives Using Disturbance Feedforward Compensation Technique", *IEEE Transactions on Power Electronics*, vol. 34, no. 3, pp. 2874–2886, March 2019.

[144] W. H. Chen, J. Yang, L. Guo and S. Li, "Disturbance-Observer-Based Control and Related Methods–An Overview', *IEEE Transactions on Industrial Electronics*, vol. 63, no. 2, pp. 1083–1095, 2016.

[145] J. Yang et al., "Disturbance/Uncertainty estimation and attenuation techniques in PMSM drives–A survey", *IEEE Transactions on Industrial Electronics*, vol. 64, no. 4, pp. 3273–3285, Apr. 2017.

[146] M. Abdelrahem, C. Hackl, R. Kennel and J. Rodriguez, "Efficient Direct-Model Predictive Control with Discrete-Time Integral Action for PMSGs", *IEEE Transactions on Energy Conversion*, vol. 34, no. 2, pp. 1063–1072, June 2019.

[147] I. Takahashi and T. Noguchi, "A New Quick-Response and High-Efficiency Control Strategy of an Induction Motor", *IEEE Transactions on Industry Applications*, vol. IA-22, no. 5, pp. 820–827, Sept. 1986.

[148] M. Depenbrock, "Direct self-control (DSC) of inverter-fed induction machine", *IEEE Transactions on Power Electronics*, vol. 3, no. 4, pp. 420–429, Oct. 1988.

[149] L. Zhong, M. F. Rahman, W. Y. Hu, and K. W. Lim, "Analysis of direct torque control in permanent magnet synchronous motor drives", *IEEE Transactions on Power Electronics*, vol. 12, no. 3, pp. 528–536, May 1997.

[150] F. Niu, et. al., "Comparative Evaluation of Direct Torque Control Strategies for Permanent Magnet Synchronous Machines", *IEEE Transactions on Power Electronics*, vol. 31, no. 2, pp. 1408–1424, 2016.

[151] T. G. Habetler, F. Profumo, M. Pastorelli, and L. M. Tolbert, "Direct torque control of induction machines using space vector modulation" *IEEE Transactions on Industry Applications*, vol. 28, no. 5, pp. 1045–1053, Sept.-Oct. 1992.

[152] Lixin Tang, Limin Zhong, M. F. Rahman, and Y. Hu, "A novel direct torque controlled interior permanent magnet synchronous machine drive with low ripple in flux and torque and fixed switching frequency", *IEEE Transactions on Power Electronics*, vol. 19, no. 2, pp. 346–354, March 2004.

[153] Z. Zhang, R. Tang, B. Bai, and D. Xie, "Novel Direct Torque Control Based on Space Vector Modulation With Adaptive Stator Flux Observer for Induction Motors", *IEEE Transactions on Magnetics*, vol. 46, no. 8, pp. 3133–3136, Aug. 2010.

[154] Z. Zhang, Y. Zhao, W. Qiao, and L. Qu, "A Space-Vector-Modulated Sensorless Direct-Torque Control for Direct-Drive PMSG Wind Turbines" *IEEE Transactions on Industry Applications*, vol. 50, no. 4, pp. 2331–2341, July-Aug. 2014.

[155] T. Geyer, G. Papafotiou, M. Morari, "Model Predictive Direct Torque Control–Part I: Concept, Algorithm, and Analysis", *IEEE Transactions on Industrial Electronics*, vol. 56, no. 6, pp. 1894–1905, 2009.

[156] F. Wang, S. Li, X. Mei, W. Xie, J. Rodriguez, and R. Kennel, "Model-Based Predictive Direct Control Strategies for Electrical Drives: An Experimental Evaluation of PTC and PCC Methods", *IEEE Transactions on Industrial Informatics*, vol. 11, no. 3, pp. 671–681, June 2015.

[157] M. Abdelrahem, C. Hackl, B. Kahia, and R. Kennel, "Predictive Direct Torque Control Strategy for Surface-Mounted Permanent-Magnet Synchronous Generators", *in Conference on sustainable energy supply and energy storage systems (NEIS)*, Hamburg, Germany, 21-22 September 2017, pp. 1–6.

[158] M. Mokhtari Vayeghan and S. A. Davari, "Torque ripple reduction of DFIG by a new and robust predictive torque control method", *IET Renewable Power Generation*, vol. 11, no. 11, pp. 1345–1352, Sept. 2017.

[159] P. Cortes and et al., "Guidelines for weighting factors design in Model Predictive Control of power converters and drives", *IEEE International Conference on Industrial Technology*, Gippsland, VIC, pp. 1–7, 2009.

[160] S. A. Davari, D. A. Khaburi, and R. Kennel, “An Improved FCS-MPC Algorithm for an Induction Motor With an Imposed Optimized Weighting Factor”, *IEEE Transactions on Power Electronics*, vol. 27, no. 3, pp. 1540–1551, March 2012.

[161] F. Villarroel, et. al. “Multiobjective Switching State Selector for Finite-States Model Predictive Control Based on Fuzzy Decision Making in a Matrix Converter”, *IEEE Transactions on Industrial Electronics*, vol. 60, no. 2, pp. 589–599, Feb. 2013.

[162] C. A. Rojas, et. al. “Predictive torque and flux control without weighting factors”, *IEEE Trans. Ind. Electron.*, vol. 60, no. 2, pp. 681–690, Feb. 2013.

[163] V. P. Muddineni, A. K. Bonala, and S. R. Sandepudi, “Enhanced weighting factor selection for predictive torque control of induction motor drive based on VIKOR method”, *IET Electric Power Applications*, vol. 10, no. 9, pp. 877–888, Nov. 2016.

[164] S. A. Davari, D. A. Khaburi, and R. Kennel, “Using a weighting factor table for FCS-MPC of induction motors with extended prediction horizon”, 38^{th} *Annual Conference on IEEE Industrial Electronics Society (IECON)*, Montreal, QC, pp. 2086–2091, 2012.

[165] L. Guo, X. Zhang, S. Yang, Z. Xie, L. Wang, and R. Cao, “Simplified model predictive direct torque control method without weighting factors for permanent magnet synchronous generator-based wind power system”, *IET Electric Power Applications*, vol. 11, no. 5, pp. 793–804, May 2017.

[166] M. Norambuena, J. Rodriguez, Z. Zhang, F. Wang, C. Garcia, and R. Kennel, “A Very Simple Strategy for High-Quality Performance of AC Machines Using Model Predictive Control”, *IEEE Transactions on Power Electronics*, vol. 34, no. 1, pp. 794–800, Jan. 2019.

[167] M. Abdelrahem, H. Eldeeb, C. Hackl, R. Kennel and J. Rodriguez, “Computationally Efficient Predictive Direct Torque Control Strategy for PMSGs without Weighting Factors”, *in proceedings of International Exhibition and Conference for Power Electronics, Intelligent Motion, Renewable Energy and Energy Management (PCIM)*, Nuremberg, Germany, 2018, pp. 133–140.

[168] H. A. Young, M. A. Perez, J. Rodriguez and H. Abu-Rub, "Assessing Finite-Control-Set Model Predictive Control: A Comparison with a Linear Current Controller in Two-Level Voltage Source Inverters," in IEEE Industrial Electronics Magazine, vol. 8, no. 1, pp. 44–52, March 2014.

[169] C. Garcia, J. Rodriguez, C. Silva, C. Rojas, P. Zanchetta, and H. Abu-Rub, “Full Predictive Cascaded Speed and Current Control of an Induction Machine”, *IEEE Transactions on Energy Conversion*, vol. 31, no. 3, pp. 1059–1067, Sept. 2016.

[170] K. Belda and D. Vosmik, “Explicit Generalized Predictive Control of Speed and Position of PMSM Drives”, IEEE Transactions on Industrial Electronics, vol. 63, no. 6, pp. 3889–3896, June 2016.

[171] M. Preindl and S. Bolognani, "Model Predictive Direct Speed Control with Finite Control Set of PMSM Drive Systems", *IEEE Transactions on Power Electronics*, vol. 28, no. 2, pp. 1007–1015, Feb. 2013.

[172] P. Kakosimos and H. Abu-Rub, "Predictive Speed Control With Short Prediction Horizon for Permanent Magnet Synchronous Motor Drives", *IEEE Transactions on Power Electronics*, vol. 33, no. 3, pp. 2740–2750, March 2018.

[173] E. J. Fuentes, C. A. Silva and J. I. Yuz, "Predictive Speed Control of a Two-Mass System Driven by a Permanent Magnet Synchronous Motor",*IEEE Transactions on Industrial Electronics*, vol. 59, no. 7, pp. 2840–2848, July 2012.

[174] A. Formentini, A. Trentin, M. Marchesoni, P. Zanchetta and P. Wheeler, "Speed Finite Control Set Model Predictive Control of a PMSM Fed by Matrix Converter", *IEEE Transactions on Industrial Electronics*, vol. 62, no. 11, pp. 6786–6796, Nov. 2015.

[175] H. Abu-Rub, M. Malinowski, and K. Al-Haddad, "Power electronics for renewable energy systems, transportation and industrial applications", John Wiley & Sons, 2014.

[176] X. Xu, J. Sun, C. Yan, and J. Zhao, "Model predictive direct speed control of interior permanent magnet synchronous motor", *in proceedings of* 29^{th} *Chinese Control And Decision Conference (CCDC)*, Chongqing, 2017, pp. 392–397.

[177] X. Xu, J. Sun, C. Yan, and J. Zhao, "Predictive speed control of interior permanent magnet synchronous motor with maximum torque per ampere control strategy", *in proceedings of* 36^{th} *Chinese Control Conference (CCC)*, Dalian, 2017, pp. 4847–4852.

[178] X. Gao, M. Abdelrahem, C. Hackl, Z. Zhang, and R. Kennel, "Direct Predictive Speed Control With a Sliding Manifold Term for PMSM Drives", *IEEE Journal of Emerging and Selected Topics in Power Electronics*, early access, 2019, doi: 10.1109/JESTPE.2019.2923285.

[179] M. Abdelrahem, C. Hackl, R. Kennel and J. Rodriguez, "Sensorless Predictive Speed Control of Permanent-Magnet Synchronous Generators in Wind Turbine Applications", *in proceedings of International Exhibition and Conference for Power Electronics, Intelligent Motion, Renewable Energy and Energy Management (PCIM 2019)*, Nuremberg, Germany, 2019, pp. 1–8.

[180] T. Geyer, N. Oikonomou, G. Papafotiou, and F. Kieferndorf, "Model Predictive Pulse Pattern Control", *IEEE Transactions on Industry Applications*, vol. 48, no. 2, pp. 663–676, March-April 2012.

[181] M. Tomlinson, H. Mouton, R. Kennel, and P. Stolze, "A Fixed Switching Frequency Scheme for Finite-Control-Set Model Predictive Control—Concept and Algorithm", *IEEE Transactions on Industrial Electronics*, vol. 63, no. 12, pp. 7662–7670, Dec. 2016.

[182] F. Sebaaly, H. Vahedi, H. Y. Kanaan, and K. Al-Haddad, "Novel Current Controller Based on MPC With Fixed Switching Frequency Operation for a Grid-Tied Inverter", *IEEE Transactions on Industrial Electronics*, vol. 65, no. 8, pp. 6198–6205, Aug. 2018.

[183] L. Tarisciotti, P. Zanchetta, A. Watson, J. Clare, M. Degano, and S. Bifaretti, "Modulated Model Predictive Control for a Three-Phase Active Rectifier", *IEEE Transactions on Industry Applications*, vol. 51, no. 2, pp. 1610–1620, March-April 2015.

[184] L. Tarisciotti and et al., "Model Predictive Control for Shunt Active Filters With Fixed Switching Frequency", *IEEE Transactions on Industry Applications*, vol. 53, no. 1, pp. 296–304, Jan.-Feb. 2017.

[185] H. Mahmoudi, M. Aleenejad, and R. Ahmadi, "A New Multiobjective Modulated Model Predictive Control Method With Adaptive Objective Prioritization", *IEEE Transactions on Industry Applications*, vol. 53, no. 2, pp. 1188–1199, March-April 2017

[186] M. Vijayagopal, P. Zanchetta, L. Empringham, L. de Lillo, L. Tarisciotti, and P. Wheeler, "Control of a Direct Matrix Converter With Modulated Model-Predictive Control", *IEEE Transactions on Industry Applications*, vol. 53, no. 3, pp. 2342–2349, May-June 2017.

[187] L. Tarisciotti and et al., "Modulated Predictive Control for Indirect Matrix Converter", *IEEE Transactions on Industry Applications*, vol. 53, no. 5, pp. 4644–4654, Sept.-Oct. 2017.

[188] S. S. Yeoh, T. Yang, L. Tarisciotti, C. I. Hill, S. Bozhko, and P. Zanchetta, "Permanent-Magnet Machine-Based Starter–Generator System With Modulated Model Predictive Control", *IEEE Transactions on Transportation Electrification*, vol. 3, no. 4, pp. 878–890, Dec. 2017.

[189] S. Vazquez, C. Montero, C. Bordons and L. G. Franquelo, "Model predictive control of a VSI with long prediction horizon", *IEEE International Symposium on Industrial Electronics*, Gdansk, 2011, pp. 1805–1810.

[190] T. Geyer, "Computationally Efficient Model Predictive Direct Torque Control", *IEEE Transactions on Power Electronics*, vol. 26, no. 10, pp. 2804–2816, Oct. 2011.

[191] T. Geyer and D. E. Quevedo, "Multistep Finite Control Set Model Predictive Control for Power Electronics", *IEEE Transactions on Power Electronics*, vol. 29, no. 12, pp. 6836–6846, Dec. 2014.

[192] T. Geyer and D. E. Quevedo, "Performance of Multistep Finite Control Set Model Predictive Control for Power Electronics", *IEEE Transactions on Power Electronics*, vol. 30, no. 3, pp. 1633–1644, March 2015.

[193] P. Karamanakos, T. Geyer, and R. P. Aguilera, "Long-Horizon Direct Model Predictive Control: Modified Sphere Decoding for Transient Operation", *IEEE Transactions on Industry Applications*, vol. 54, no. 6, pp. 6060–6070, Nov.-Dec. 2018.

[194] A. Ayad, P. Karamanakos, and R. Kennel, "Direct Model Predictive Current Control Strategy of Quasi-Z-Source Inverters", *IEEE Transactions on Power Electronics*, vol. 32, no. 7, pp. 5786–5801, July 2017.

[195] H. Fang, Z. Zhang, X. Feng, and R. Kennel, "Ripple-reduced model predictive direct power control for active front-end power converters with extended switching vectors and time-optimised control", *IET Power Electronics*, vol. 9, no. 9, pp. 1914–1923, 27 7 2016.

[196] Z. Zhang, H. Fang, F. Gao, J. Rodriguez, and R. Kennel, "Multiple-Vector Model Predictive Power Control for Grid-Tied Wind Turbine System With Enhanced Steady-State Control Performance", *IEEE Transactions on Industrial Electronics*, vol. 64, no. 8, pp. 6287–6298, Aug. 2017.

[197] Y. Zhang, D. Xu, and L. Huang, "Generalized Multiple-Vector-Based Model Predictive Control for PMSM Drives", *IEEE Transactions on Industrial Electronics*, vol. 65, no. 12, pp. 9356–9366, Dec. 2018.

[198] Y. Zhang, Y. Bai, and H. Yang, "A Universal Multiple-Vector-Based Model Predictive Control of Induction Motor Drives", *IEEE Transactions on Power Electronics*, vol. 33, no. 8, pp. 6957–6969, Aug. 2018.

[199] Y. Zhang, W. Xie, Z. Li, and Y. Zhang, "Low-Complexity Model Predictive Power Control: Double-Vector-Based Approach", *IEEE Transactions on Industrial Electronics*, vol. 61, no. 11, pp. 5871–5880, Nov. 2014.

[200] Y. Zhang, J. Hu, and J. Zhu, "Three-Vectors-Based Predictive Direct Power Control of the Doubly Fed Induction Generator for Wind Energy Applications", *IEEE Transactions on Power Electronics*, vol. 29, no. 7, pp. 3485–3500, July 2014.

[201] S.Vasquez, J.I. Leon, L.G. Franquelo, J.M. Carrasco, O. Martinez, J. Rodriguez, P. Cortes and S. Kouro, *Model Predictive Control with Constant Switching Frequency Using a Discrete Space Vector Modulation with Virtual State Vectors*, IEEE International Conference on Industrial Technology, 2009. ICIT 2009.

[202] M. Abdelrahem, F. Hamadto, A. Garikapati, and R. Kennel, "Multiple-Vector Direct Model Predictive Control for Grid-Connected Power Converters with Reduced Calculation Burden", *in IEEE International Symposium on Predictive Control of Electrical Drives and Power Electronics (PRECEDE)*, Quanzhou, China., 2019, pp. 1–6.

[203] P. Antoniewicz and M. Kazmeirkowski, Virtual-flux-based predictive direct power control of ac/dc converters with online inductance estimation, *IEEE Transactions on Industrial Electronics*, Vol. 55, No. 12, Dec. 2008, pp. 4381–4390.

[204] J. Norniella and et al., New strategies for estimating the coupling inductance in grid-connected direct power control-based three-phase active rectifiers, *in Proc. IEEE PES*, Jul. 2013, pp. 1–5.

[205] F. Huerta and et al., Novel control of three-phase active-front-end rectifier with compensation of unknown grid-side inductance, *IEEE Transactions on Industrial Electronics*, Vol. 58, No. 8, Aug. 2011, pp. 3275–3286.

[206] A. Timbus, P. Rodriguez, R. Teodorescu, and M. Ciobotaru, Line impedance estimation using active and reactive power variations, *in Proc. of IEEE Power Electron. Spec. Conf.*, Jun. 2007, pp. 1273–1279.

[207] B. Arif, and et al., Grid Parameter Estimation Using Model Predictive Direct Power Control, *in IEEE Transactions on Industry Applications*, Vol. 51, No. 6, Nov.-Dec. 2015, pp. 4614–4622.

[208] M. Mehreganfar and S. A. Davari, "Sensorless predictive control method of three-phase AFE rectifier with MRAS observer for robust control", 2017 IEEE International Symposium on Predictive Control of Electrical Drives and Power Electronics (PRECEDE), Pilsen, 2017, pp. 107–112.

[209] N. Hoffmann and F. Fuchs, Minimal invasive equivalent grid impedance estimation in inductive–resistive power networks using extended Kalman filter, *IEEE Transactions on Power Electronics*, Vol. 29, No. 2, Feb. 2014, pp. 631–641.

[210] M. Abdelrahem, C. Hackl, and R. Kennel, "Application of Extended Kalman Filter to Parameter Estimation of Doubly-Fed Induction Generators in Variable-Speed Wind Turbine Systems", *in Proceedings of the* 5^{th} *International Conference on Clean Electrical Power (ICCEP)*, Taormina, Italy, 16-18 June 2015, pp. 226–233.

[211] I. Hammoud, K. Morsy, M. Abdelrahem, and R. Kennel, "Computationally Efficient Model Predictive Direct Power Control with Online Finite Set Model Inductance Estimation Technique for Grid-Connected Photovoltaic Inverters", *in IEEE International Symposium on Predictive Control of Electrical Drives and Power Electronics (PRECEDE)*, Quanzhou, China., 2019, pp. 1–6.

[212] IEEE Recommended Practice and Requirements for Harmonic Control in Electric Power Systems, *in IEEE Std 519-2014 (Revision of IEEE Std 519-1992)*, pp. 1–29, 2014.

[213] M. Tsili and S. Papathanassiou, "A review of grid code technical requirements for wind farms", *IET Renewable Power Generation*, vol. 3, no. 3, pp. 308–332, Sept. 2009.

[214] I. Erlich and U. Bachmann, "Grid code requirements concerning connection and operation of wind turbines in Germany", *in proceedings of IEEE Power Engineering Society General Meeting*, San Francisco, CA, 2005, pp. 1253–1257.

[215] I. Erlich, W. Winter, and A. Dittrich, "Advanced grid requirements for the integration of wind turbines into the German transmission system", *in proceedings of IEEE Power Engineering Society General Meeting*, Montreal, Que., 2006.

[216] Grid Connection Regulations fo High and Extra High Voltage, *E. ON Netz GmbH*, 2006, available at: https://www.nerc.com, viewed at 02 July 2019.

[217] M. Nasiri, J. Milimonfared, S.H. Fathi, "A review of low-voltage ride-through enhancement methods for permanent magnet synchronous generator based wind turbines", *Renewable and Sustainable Energy Reviews*, vol. 47, pp. 399–415, 2015.

[218] J. Conroy, R. Watson, "Low-voltage ride-through of a full converter wind turbine with permanent magnet generator", *IET Renewable Power Generation*, vol. 1, pp. 182–189, 2007.

[219] V. Mendes, F. Matos, S. Liu, A. Cupertino, H. Pereira, C. De Sousa, "Low Voltage Ride-Through Capability Solutions for Permanent Magnet Synchronous Wind Generators", *Energies*, vol. 9, pp. 1–19, 2016.

[220] N. Heng, L. Jiao, Z. Peng, H. Yikang, "Improved control strategy of an active crowbar for directly-driven PM wind generation system under grid voltage dips", *in Proceedings of International Conference on Electrical Machines and Systems(ICEMS*), Wuhan, 17-20 October 2008.

[221] T. Nauyen, D. Lee, "Ride-through technique for PMSG wind turbines using energy storage systems", *Journal of Power Electronics*, vol. 10, pp. 733-738, 2010.

[222] B. Bolund, H. Bernhoff, M. Leijon, "Flywheel energy and power storage systems", *Renewable & Sustainable Energy Reviews*, vol. 11, pp. 235-258, 2007.

[223] G. Xu, L. Xu, D. Morrow, "Wind turbines with energy storage for power smoothing and FRT enhancement", *in Proceedings of IEEE power and energy society general meeting*, San Diego, CA, 24-29 July 2011.

[224] Y. Peng, Y. Li, Z. Xu, M. Wen, L. Luo, Y. Cao, Z. Leonowicz, "Power Quality Improvement and LVRT Capability Enhancement of Wind Farms by Means of an Inductive Filtering Method", *Energies*, vol. 9, 302, 2016.

[225] SW. Mohod, MV. Aware, "A STATCOM-control scheme for grid connected wind energy system for power quality improvement", *IEEE Systems Journal*, vol. 4, **2010**, pp. 346–52, 2010.

[226] L. Wang, DN. Truong, "Dynamic stability improvement of four parallel-operated PMSG-based offshore wind turbine generators fed to a power system using a STATCOM", *IEEE Transaction on Power Delivery*, vol. 28, pp. 111–119, 2013.

[227] K. Goweily, M. El Moursi, M. Abdel-Rahman, M. Badr, "Voltage booster scheme for enhancing the fault ride-through of wind turbines", *IET Power Electronics*, vol. 8, pp. 1853–1863, 2015.

[228] A. Causebrook, DJ. Atkinson, AG. Jack, "Fault ride-through of large wind farms using series dynamic braking resistors", *IEEE Transaction in Power Systems*, vol. 22, pp. 966–75, 2007.

[229] J. Tongzhou, H. Xiongfeng, L. Xianyun, L. Kun, Z. Mei, "Performance analysis and research on LVRT of PMSG wind power system with SDBR", *in proceedings of the* 33^{rd} *Chinese control conference*, Nanjing, 28-30 July 2014.

[230] Z. Wu, X. Dou, J. Chu, M. Hu, "Operation and Control of a Direct-Driven PMSG-Based Wind Turbine System with an Auxiliary Parallel Grid-Side Converter", *Energies*, vol. 6, no. 7, pp. 3405–3421, 2013.

[231] H. Huang, C. Mao, J. Lu, D. Wang, "Electronic Power Transformer Control Strategy in Wind Energy Conversion Systems for Low Voltage Ride-through Capability Enhancement of Directly Driven Wind Turbines with Permanent Magnet Synchronous Generators (D-PMSGs)", *Energies*, vol. 7, pp. 7330-7347, 2014.

[232] Z. Liu, C. Liu, G. Li, "Power coordinated control of wind turbines with permanent magnet synchronous generator for low voltage ride through", *in proceedings of IEEE Power & Energy Society General Meeting*, National Harbor, MD, 27-31 July 2014.

[233] AD. Hansen, G. Michalke, "Modelling and control of variable-speed multi-pole permanent magnet synchronous generator wind turbine", *Wind Energy*, vol. 11, pp. 537–554, 2008.

[234] S. Alepuz, A. Calle, S. Busquets-Monge, S. Kouro, B. Wu, "Use of Stored Energy in PMSG Rotor Inertia for Low-Voltage Ride-Through in Back-to-Back NPC Converter-Based Wind Power Systems", *IEEE Transactions on Industrial Electronics*, vol. 60, pp. 1787–1796, 2013.

[235] V. Yaramasu, B. Wu, S. Alepuz, S. Kouro, "Predictive Control for Low-Voltage Ride-Through Enhancement of Three-Level-Boost and NPC-Converter-Based PMSG Wind Turbine", *IEEE Transactions on Industrial Electronics*, vol. 61, pp. 6832–6843, 2014.

[236] J. Morren, and S. Haan, "Ride through of wind turbines with doubly-fed induction generator during a voltage dip", *IEEE Transaction on Energy Conversion*, vol. 20, no. 2, pp. 435–441, Jun. 2005.

[237] C. Wessels, F. Gebhardt, and F. Fuchs, "Fault ride-through of a DFIG wind turbine using a dynamic voltage restorer during symmetrical and asymmetrical grid faults", *IEEE Transaction Power Electrons*, vol. 26, no. 3, pp. 807–815, Mar. 2011.

[238] X. Yan, G. Venkataramanan, Y. Wang, Q. Dong, and B. Zhang, "Grid fault tolerant operation of a DFIG wind turbine generator using a passive resistance network", *IEEE Transaction Power Electrons*, vol. 26, no. 10, pp. 2896–2905, Oct. 2011.

[239] P. Flannery, and G. Venkataramanan, "A fault tolerant doubly fed induction generator wind turbine using a parallel grid side rectifier and series grid side converter", *IEEE Transaction Power Electrons*, vol. 23, no. 3, pp. 1126–1135, May 2008.

[240] V. Mendes, C. de Sousa, S. Silva, J. Rabelo, and W. Hofmann, "Modeling and ride-through control of doubly fed induction generators during symmetrical voltage sags", *IEEE Transaction Energy Conversion*, vol. 26, no. 4, pp. 1161–1171, Dec. 2011.

[241] J. da Costa, H. Pinheiro, T. Degner, and G. Arnold, "Robust controller for DFIGs of grid-connected wind turbines", *IEEE Transaction on Industrial Electrons*, vol. 58, no. 9, pp. 4023–4038, Sep. 2011.

[242] D. Xie, Z. Xu, L. Yang, J. Østergaard, Y. Xue, and K. P. Wong, "A Comprehensive LVRT Control Strategy for DFIG Wind Turbines With Enhanced Reactive Power Support", *IEEE Transactions on Power Systems*, vol. 28, no. 3, pp. 302–3310, Aug. 2013.

[243] M. Abdelrahem, R. Kennel, "Fault-Ride through Strategy for Permanent-Magnet Synchronous Generators in Variable-Speed Wind Turbines", *Energies*, vol. 9, no. 12, pp. 1–15, 2016.

[244] M. H. Mobarak, M. Abdelrahem, N. Stati and R. Kennel, "Model predictive control for low-voltage ride-through capability improvement of variable-speed wind energy conversion systems", *in proceedings of IEEE International Symposium on Industrial Electronics (INDEL)*, Banja Luka, 2016, pp. 1–6.

[245] M. Abdelrahem, M. Mobarak, R. Kennel, "Realization of Low-Voltage Ride Through Requirements for PMSGs in Wind Turbines Systems Using Generator-Rotor Inertia", *in proceedings of IEEE* 9^{th} *International Conference on Electrical and Computer Engineering (ICECE)*, Dhaka, Bangladesh, 20-22 December 2016.

[246] M. Abdelrahem, M. H. Mobarak, and R. Kennel, "Model Predictive Control for Low-Voltage Ride Through Capability Enhancement of DFIGs in Variable-Speed Wind Turbine Systems", *in proceedings of IEEE* 9^{th} *International Conference on Electrical and Computer Engineering (ICECE 2016)*, 20-22 December 2016, Dhaka, Bangladesh, pp. 70–73.

[247] M. Abdelrahem, R. Kennel, "Direct-Model Predictive Control for Fault Ride-Through Capability Enhancement of DFIG", *in proceedings of International Conference for Power Electronics, Intelligent Motion, Renewable Energy and Energy Management (PCIM)*, 16-18 May 2017, Nuremberg, Germany, pp. 1917–1924.